



The  
University  
Of  
Sheffield.

*Towards more sustainable cement production: a  
no-combustion approach for the decarbonisation  
of CaCO<sub>3</sub>*

Marco Simoni

A thesis submitted in partial fulfilment of the requirement  
for the degree of Doctor of Philosophy

Department of Materials Science & Engineering

The University of Sheffield

13<sup>th</sup>, May 2022

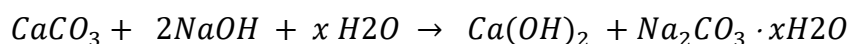
## Abstract

The decarbonisation of calcium carbonate ( $\text{CaCO}_3$ ) to obtain lime ( $\text{CaO}$ ) is a crucial step for a wide range of major industrial processes, most noticeably in Portland Cement (PC) production; from 1 tonne of  $\text{CaCO}_3$  approximately 0.44 tonnes of embodied  $\text{CO}_2$  is released to produce ~560 kg of  $\text{CaO}$ . With a global use of ~3 billion tonnes per year of calcined calcium carbonate, this makes the decarbonisation of  $\text{CaCO}_3$  one of the major contributors to global  $\text{CO}_2$  emissions. The  $\text{CO}_2$  released from  $\text{CaCO}_3$  alone accounts for ~6 % of global  $\text{CO}_2$  emissions.

In the conventional calcination process, the decarbonisation of  $\text{CaCO}_3$  occurs at temperatures above  $950^\circ\text{C}$ , resulting in the  $\text{CO}_2$  emissions both from  $\text{CaCO}_3$  and the combustion of the fuels necessary to provide the required energy. The  $\text{CO}_2$  released from  $\text{CaCO}_3$  represents the main challenge for the industrial sectors using  $\text{CaO}$ , as it is not replaceable. The thermal calcination of  $\text{CaCO}_3$  is currently considered unavoidable, and therefore, the release of  $\text{CO}_2$  from feed  $\text{CaCO}_3$  could not be avoided.

To address this, this project proposes a decarbonisation of  $\text{CaCO}_3$  at ambient conditions without combustion but by reaction with concentrated  $\text{NaOH}$  solutions. While producing  $\text{Ca}(\text{OH})_2$  which may be used, for example to produce cement clinkers, the  $\text{CO}_2$  from  $\text{CaCO}_3$  is sequestered within the stable by-product  $\text{Na}_2\text{CO}_3 \cdot x\text{H}_2\text{O}$  ( $x=0, 1$ ). Therefore, it would avoid both the combustion and process  $\text{CO}_2$  from the decarbonisation of feed  $\text{CaCO}_3$ . The reduction of the process  $\text{CO}_2$  is particularly meaningful as it has not been achieved by the conventional high temperature decarbonisation of  $\text{CaCO}_3$ . The by-product  $\text{Na}_2\text{CO}_3$  can offer a safer alternative for  $\text{CO}_2$  storage compared with the geological  $\text{CO}_2$  storage. Alternatively, it could be either used to regenerate  $\text{NaOH}$  or as another commodity.

Firstly, reagent grade  $\text{CaCO}_3$  was used as reactant to identify the optimal conditions allowing for a maximised yield of products,  $\text{Ca}(\text{OH})_2$  and  $\text{Na}_2\text{CO}_3$  or  $\text{Na}_2\text{CO}_3 \cdot \text{H}_2\text{O}$ .



A wide range consisting of 71 starting compositions ( $\text{CaCO}_3 + \text{NaOH} + \text{H}_2\text{O}$ ) was investigated, and the maximum yield of  $\text{Ca}(\text{OH})_2$  with 96 %  $\text{CaCO}_3$  conversion was achieved in the system with 8.1 wt.%  $\text{CaCO}_3$ , 37.2 wt.%  $\text{NaOH}$  and 54.7 wt.%  $\text{H}_2\text{O}$ . Higher  $\text{NaOH}$  concentrations were generally enhancing the conversion of  $\text{CaCO}_3$ , for a specific water-to-solid ratio.

Longer reaction times were found to increase the conversion of  $\text{CaCO}_3$  up to five minutes, beyond which the system indicated little improvement in production of  $\text{Ca}(\text{OH})_2$ . It was also discovered that, in batch conditions, the reaction was enhanced at a slower stirring speed.

The computational investigation also suggested that the activity of water in the system, highly dependent on the concentration of NaOH, decide the formation of either  $\text{Na}_2\text{CO}_3$  or  $\text{Na}_2\text{CO}_3 \cdot \text{H}_2\text{O}$ . This information helps to establish the extent of the reaction based on the balance between  $\text{Na}_2\text{CO}_3$  or  $\text{Na}_2\text{CO}_3 \cdot \text{H}_2\text{O}$  in the reaction products, in addition to providing essential knowledge for the subsequent separation process of the reaction products.

At short residence times, the reaction was in accordance with Arrhenius equation, reflecting its enhanced efficiencies at higher processing temperatures, within the mild range of 45 – 80 °C. For a prolonged contact between the reactants, a higher temperature did not lead to significant improvements in terms of decarbonisation of  $\text{CaCO}_3$ .

In the third part of the project, the reaction was tested using industrial grade materials with different characteristics, to assess the feasibility of the developed technology on a wider range of materials used in the real industry.

Limestone (96 wt.%  $\text{CaCO}_3$ ) and chalk (74 wt.%  $\text{CaCO}_3$ ), provided by the industrial collaborator of the project, were tested, and maximum  $\text{CaCO}_3$  conversion yields of 49 % and 79 % were recorded, respectively. This is likely linked to the smaller average particle size of the chalk compared with the limestone, resulting in an enhanced contact surface. The effects of impurities, such as silica within the chalk, were also investigated.

The results o demonstrated promising prospects of the process developed, since very mild conditions are required for the reaction to occur, i.e., short residence times, slow stirring speeds, and ambient conditions. The implementation of this technology could prevent the lime and cement industry from completely relying on the development of CCS technologies, offering a valid alternative to achieve a sustainable industry.

I strongly believe that the alternative route for  $\text{CaCO}_3$  decarbonisation proposed can have a great impact on the cement and concrete research community and industry worldwide, inspiring further investigation and eventual industrial application. The outcomes of my project suggest that, with a totally different approach to the issue known worldwide, the process  $\text{CO}_2$  could be avoided, as well as the technological complications linked to  $\text{CO}_2$  capture in the conventional processes.

## Acknowledgments

Despite the writing of all the sections included in this thesis has been challenging, this one has been the hardest to fulfil by far. I was wondering how I could compress all the “thank you” I owe in a few words, and I accepted the fact that I will never be able to fully express my gratitude. I have also been wondering who I should thank the most, but that is an impossible task as well, since all the events happening in the past four years have been crucial for the achievement of this coveted goal.

My first and mandatory “thank you” goes to my beloved family, I would literally be nothing without my mom, dad, sister, and little brother. They have always believed in me, even when I went through situations I did not think I could manage. Even when I thought to abandon everything and everybody after the accident that nearly killed me. Even when I decided to leave Rome to travel the world. They have always been there for me, and if there is one thing I will always be certain of is that they will keep doing it, no matter what.

My second “thank you” goes to my girlfriend Laura, who has always supported me throughout the PhD. She has been providing that certainty and peace of mind that everybody needs when it comes to put an end to a four-years task.

The third place is for my amazing friend and supervisor Theo. He’s such passionate and energetic in everything he does, that he managed to pass me the enthusiasm with which I tackled research. I will always be there for him, Minerva, Xander and Theon.

Another gigantic “thank you” goes to my supervisors Hajime and John. They’ve always been so kind and helpful to me, allowing me to think and operate independently with complete trust. They helped me during the first impact with the UK, and throughout these past four years, providing experience knowledge and priceless tips.

It is now time to acknowledge all those wonderful friends which made my life so amazing these years; despite all the countless people I met on the way, these friends of mine have been (and still are) a milestone for me. I will never forget any of them, and I will keep being in touch with every last of them. I am talking about Cucciola, TT, Cas, Francesca, Georgie, Katie, Edo, Mat, Cucciolo, Kurwino, Imad, Ben, Panos, Tom, Soheil, Sasso, Dodi, and Gabri. Thank you all for being so special!

Sometimes, your office life is as important as your day-to-day life, and I will never forget all the ISL members I have been chatting and spending quality time with, especially: Dan, Josh, Lewis, Bern, Shaun, Chris, Hannah and Dan. Thank you all, you made my office days so special!

Finally, despite they have not been physically with me during the PhD, my old friends from Rome were always there when it came to helping and supporting me. I am talking about Marco, Scriccio, Giulio, Pirone, Frollo, Cakki, Davide, Patate, Mastro, Mimmo, Francesco, Giulio, Alessio, Mirko...and many others.

To conclude, I thank every one of the above-mentioned people again, and the University of Sheffield for allowing me to undertake and conclude this wonderful journey in the best possible way.

## Publications

Being an industry-funded project, and due to issues with the patent ownership, majority of my PhD data has been confidential for the main part of my project period. As a result, I was not able to publish my research outcomes until recently. Therefore, I volunteered to be involved in different side projects so that I could develop my necessary academic and professional skills to write papers and give presentations at international conferences. In the side projects, I have been investigating 1) Calcium Aluminate Phosphate cements (CAP) for the immobilisation of radioactive  $^{90}\text{Sr}$  and 2) adjustment of the clinkering conditions and phases co-existence for alinite-based cements. My publications related to these projects are listed below.

- Main PhD project:
  - Hanein, T., Simoni, M., Woo, C. L., Provis, J. L., and Kinoshita, H., "Decarbonisation of calcium carbonate at atmospheric temperatures and pressures, with simultaneous  $\text{CO}_2$  capture, through production of sodium carbonate", *Energy & Environmental Science*, 14.12 (2021): 6595-6604.
  - Simoni, M., Hanein, T., Woo, C.L., Tyrer, M., Nyberg, M., Martinez, J.C., Quintero-Mora, N.I., Provis, J.L., and Kinoshita, H., "Decarbonisation of calcium carbonate in sodium hydroxide solutions at ambient conditions: effect of residence time and mixing rates", *Physical Chemistry Chemical Physics*.
  - Simoni, M., Wilkes, M.D., Brown, S., Provis, J.L., Kinoshita, H., and Hanein, T., "Decarbonising the lime industry: state-of-the-art", *Renewable & Sustainable Energy Reviews*, 168, p. 112765.
  - Simoni, M., Hanein, T., Woo, C.L., Provis, J. and Kinoshita, H., "Effect of Impurities on the Decarbonization of Calcium Carbonate Using Aqueous Sodium Hydroxide", *ACS Sustainable Chemistry & Engineering*, 26.08.2022.
  - Simoni, M., Hanein, T., Woo, C.L., Nyberg, M., Tyrer, M., Provis, J.L., and Kinoshita, H., "Synthesis of  $\text{Ca}(\text{OH})_2$  and  $\text{Na}_2\text{CO}_3$  through anion exchange between  $\text{CaCO}_3$  and  $\text{NaOH}$ : effect of reaction temperature ", *RCS Advances*, 15.09.2022, Under review.

- Side projects:
  - Simoni, M., Ball, H. E., Burgos, C., Garcia-Lodeiro, I., Hanein, T., Kinoshita, H., "Interaction of strontium chloride solution with calcium aluminate phosphate (CAP) system", *39<sup>th</sup> Cement and Concrete Science Conference 2019 Proceedings*, Cement and Concrete Science (CCS), 11.09.2019, pp. 135 – 137, ISBN no. 9780861972012.
  - Simoni, M., Hanein, T., Duvallet, T. Y., Jewell, R. B., and Kinoshita, H., "Continuous production of alinite in a laboratory-scale rotary kiln", *40<sup>th</sup> Cement and Concrete Science Conference Proceedings*, Cement and Concrete Science (CCS), 2020.
  - Simoni, M., Hanein, T., Duvallet, T. Y., Jewell, R. B., Provis, J. L., and Kinoshita, H., "Producing cement clinker assemblages in the system: CaO-SiO<sub>2</sub>-Al<sub>2</sub>O<sub>3</sub>-SO<sub>3</sub>-CaCl<sub>2</sub>-MgO", *Cement and Concrete Research*, 144, (2021): 106418.
- Others:
  - Zeppilli, M., Simoni, M., Paiano P., and Majone, M., "Two-side cathode microbial electrolysis cell for nutrients recovery and biogas upgrading", *Chemical Engineering Journal*, 370, (2019): 466-476.
  - Ogden, M.D., Robshaw, T.J., Kearney, S., Turner, J.R., Simoni, M., Baidak, A., Sharrad, C.A. and Walkley, B., "Radioiodine Abatement–Development of Radioiodine Targeting Strategies in the Light of Zero Emission", Available at SSRN 4103257.

## Awards and Prizes

- *Dr. Jeff Wadsworth – Battelle Fellowship* (12,160.00£), Battelle Organisation & Ohio State University, issued on 23.04.2019.
- *Armourers and Brasiers' Conference Travel Grant Program* (600.00£), The Armourers and Brasiers' Company, issued on 24.03.2020.
- Shortlisted finalist for the *Adam Neville PhD Prize for Cement and Concrete 2021 at the Neville Centre of Excellence in Cement and Concrete Engineering Symposium*.

## Attendances and presentations

For the same reasons stated above in “Publications”, the items reported in the following list refer to projects different from my PhD topic. Here is a list of the conferences attended, with respective conference proceedings.

- 5<sup>th</sup> International Workshop on “Mechanisms and Modelling of Waste / Cement Interactions, 25 – 27<sup>th</sup> March, 2019, Karlsruhe (Germany).
- IOM3 – Thermodynamics of Materials Symposium, “*Alinite calcium sulfoaluminate cement production: configuration entropy calculations*”, University of Birmingham, Birmingham (United Kingdom), 4<sup>th</sup> July, 2019.
- 39<sup>th</sup> Cement and Concrete Science, 9 – 10<sup>th</sup> September, 2019, University of Bath, Bath (United Kingdom).
- 43<sup>rd</sup> Annual Symposium on the Scientific Basis for Nuclear Waste Management, “*Interaction of strontium chloride solution with calcium aluminate phosphate (CAP) system*”, 21 – 24<sup>th</sup> October, 2019, Wien (Austria).
- 74<sup>th</sup> RILEM Annual Week & 40<sup>th</sup> Cement and Concrete Science Conference, “*Continuous production of alinite in a laboratory-scale rotary kiln*”, 31<sup>st</sup> August – 4<sup>th</sup> September, 2020, Sheffield (United Kingdom).
- LOWC3 2020 Conference, “*On cement clinker assemblages containing alinite, calcium sulfoaluminate and calcium aluminates*”, 5 – 6<sup>th</sup> October, 2020, Lexington (KY, USA).

## Notes on thesis structure

The format of this thesis deviates from a conventional structure, seeing that most of the work has already been published, or is in the process of being reviewed for journal publication. Specifically, a brief introduction (Section 1) defines the main topic of the thesis, including the relevant industries for the manufacturing of caustic soda and soda ash. The following review paper (Section 2) focuses on the traditional calcination of  $\text{CaCO}_3$ , and it aims to compare the state-of-the-art process with unconventional routes which might lead to a low-carbon transition of the cement industry. The following sections adapt to a step-by-step characterisation of the reaction at different conditions, to highlight the potential for industrial application of the novel route. In fact, since the project was partially funded by the industrial partner CEMEX, those parameters which might affect the technical feasibility and the economic return of the process are studied. These experimental outcomes are presented as part of published, and therefore peer-reviewed journal articles, preceded by a brief overview of the work also outlining the publication status. Following, Section 8 comprises a brief summary of the experimental outcomes while further outlining the potential impact of the proposed process. The subsequent Section 9 (Appendix 1) highlights additional experimental outcomes which have been interrupted because of the pandemic, but that have been reported for the sake of completion. The numbering of figures, tables, and references is independent for Sections 2 – 6, whereas the order is consecutive for Sections 1, 7, 8, and 9. The format of all the sections has been kept homogeneous to ease the reading.

# INDEX

1. Introduction.....	10
1.1. The decarbonisation of CaCO <sub>3</sub> .....	10
1.2. Linked industries.....	13
2. Literature Review.....	18
2.1. Decarbonising the lime industry: state-of-the-art.....	19
3. Alternative decarbonisation route: effect of ternary composition and process feasibility.....	55
3.1. Decarbonisation of calcium carbonate at atmospheric temperatures and pressures, with simultaneous CO <sub>2</sub> capture, through production of sodium carbonate.....	56
4. Alternative decarbonisation route: effect of stirring rate and residence time.....	79
4.1. Decarbonisation of calcium carbonate in sodium hydroxide solutions at ambient conditions: effect of residence time and mixing rate.....	80
5. Alternative decarbonisation route: effect of temperature.....	111
5.1. Effect of processing temperatures on decarbonisation of calcium carbonate in sodium hydroxide solutions at ambient conditions.....	112
6. Alternative decarbonisation route: effect of impurities content.....	143
6.1. Effect of the calcareous source and impurities on the decarbonisation reaction of calcium carbonate in aqueous sodium hydroxide solutions.....	144
7. Concluding remarks and recommendations for future work.....	180
8. Appendix 1.....	183

# 1. Introduction

## 1.1. The decarbonisation of $\text{CaCO}_3$

The concentration of  $\text{CO}_2$  in the atmosphere has been dangerously increasing in the past four decades. A study conducted by Luthi et al. [1] about the air trapped in ice cores from Antarctica aimed to measure the  $\text{CO}_2$  concentration in the earth history, revealing a sharp increase after human civilisation started, especially after the Industrial Revolution. As a result, the temperature has also increased, especially over the past 50 years [2-9], leading to evident and significant changes to our environment. Both the trends mentioned are reported in Figure 1, referring to a period ranging between 1880 and 2020; as shown, a  $\text{CO}_2$  concentration over 400 ppm and a  $+1^\circ\text{C}$  temperature raise have been achieved today [1, 10].

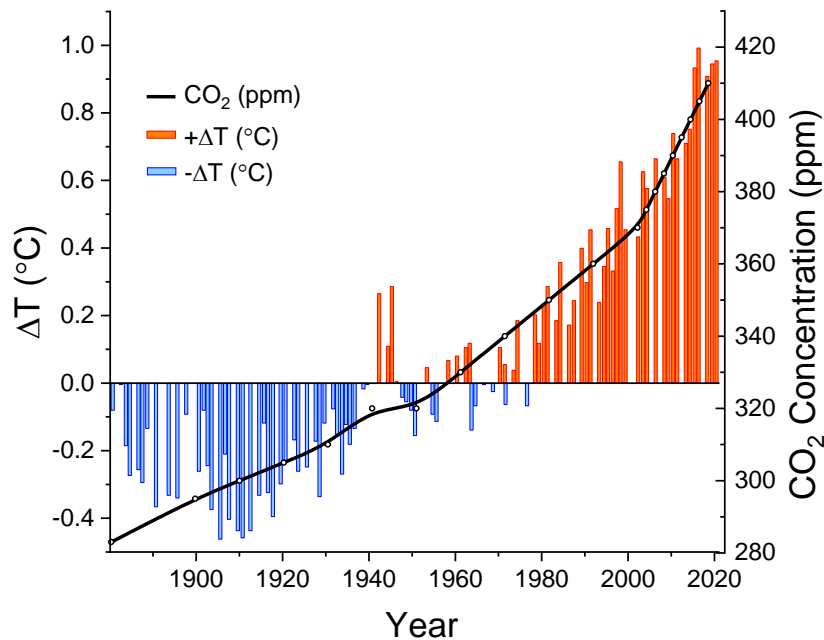


Figure 1: Historical trend of  $\text{CO}_2$  concentration in the atmosphere (ppm), source NOAA Global Monitoring Lab, and temperature over the period 1880 – 2020 [1, 10].

$\text{CO}_2$  represents the main component among the other greenhouse gases [11] and it arises from different carbon anthropogenic sources, i.e., combustion of fossil fuels, deforestation and mineral sources of  $\text{CO}_2$  such as  $\text{CaCO}_3$  [12]. Also, another study conducted by Wei et al. [13] showed that developed countries contributed for about the 60-80% of the total  $\text{CO}_2$  emissions, whereas the developing ones were responsible for the remaining 20-40%, since 1990. According to the Intergovernmental Panel on Climate Change (2007) [14] the global temperatures have increased by over  $0.74^\circ\text{C}$  in the last century and by  $0.33^\circ\text{C}$  1990 [15].

In order to achieve a competitive low-carbon economy by 2050, and thus to limit the rise of  $\text{CO}_2$  emissions observed in the past decade (2.7% annually) [16], the roadmap proposed in

2011 by the European Commission provided the required sector-specific CO<sub>2</sub> emission reductions. Specifically, emission reductions of 80, 60, 90 and 80% are expected from the power generation and distribution, transport, building and industry sectors, respectively [17]. Such values were set in order to limit the global average temperature raise by 2050 by 1.5°C; to do so, it was estimated that an overall 50% emission cut would be necessary. Among the others, the energy intensive industry sector would be expected to meet a 80% CO<sub>2</sub> emissions reduction by 2050; furthermore, it was decided that Carbon Capture and Storage (CCS) technologies [18-21] will be applied to those industries unable to make cuts in any other way by 2035 [17]. Summarizing, the transition to a low-carbon society is considered feasible and affordable, but it would require important innovations and investments; infact, the EU would be expected to invest an additional €270 billion over the next 4 decades [17]. The matter was further discussed during the Paris Climate Change Conference in 2015, where parties to the UNFCCC reached a landmark agreement, the so-called Paris agreement, to contrast climate change. Again, a global temperature rising well below 1.5°C above pre-industrial levels by 2050 was the goal set during the conference. The agreement effectively entered into force on 4th November 2016, bringing all the nations into a common cause for the first time in order to achieve the fixed goal. A global periodic check (the first will be in 2023) has been set every 5 years, in order to assess the collective progresses done, which will be presented through the National Determined Contribution (NDC) of each member party [22]. Lately, during the UN Climate Change Conference (COP26) held in Glasgow (31<sup>st</sup> October 12<sup>th</sup> November 2021), the same goals were confirmed. The milder expected environmental crisis at a temperature rising of 1.5°C respect with 2.0°C was highlighted [23], with China and U.S. also agreeing on giving their contribution for the switching to renewables.

Portland Cement (PC) is the generally employed hydraulic cement for the construction of our infrastructure and it currently is the most manufactured material worldwide. The production of cement was over 4.2 billion metric tonnes in 2016 [24] and it is expected to grow by 2.9% per year up to 2050 [25]. Almost the totality of the cement produced is used to make concrete, which is the most energy- and carbon-efficient material based on a volume basis among all man-made materials; concrete is obtained by blending the cement paste and aggregates, which bond together chemically and result in optimal rheological characteristics. Due to its high demand, cement production represents a very significant anthropogenic CO<sub>2</sub> emission source [26], and it is believed to be responsible for about 5-8% of the worldwide CO<sub>2</sub> emissions [27]; therefore, it significantly impacts the environment in terms of greenhouse gases (GHG).

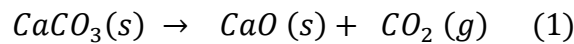
The cement production process consists of a number of steps which transform the raw materials (limestone, clays and shales) into clinker; following, clinker is blended with gypsum in order to obtain the final cement powder. Nowadays, the dry process represents the best available technique in terms of energy efficiency [28].

The dry process is very energy-intensive, both in terms of electrical and thermal energy consumption (Table 1) [29], and it may be summarised in three main steps: raw materials preparation, clinkerisation within a rotary kiln and cement making. The clinkerisation represents the most energy-intensive step, and accounts for about the 70-80% of the overall energy usage [12].

*Table 1: Specific electrical consumption (SEC) and specific thermal consumption (STC) according to a dry process cement plant operating in Germany [15].*

	<b>SEC (MJ/kg<sub>Cement</sub>)</b>	<b>STC (MJ/kg<sub>Clinker</sub>)</b>
<i>Low consumption</i>	$\leq 0.37$	$\leq 3.80$
<i>Medium consumption</i>	$0.37 \leq SEC \leq 0.38$	$3.80 \leq STC \leq 4.10$
<i>High consumption</i>	$0.38 \leq SEC \leq 0.39$	$4.10 \leq STC \leq 4.40$

The calcination reaction itself accounts for about the 60% of the overall CO<sub>2</sub> emissions [30]; as shown in Equation 1 below, calcium carbonate converts to free lime and gaseous CO<sub>2</sub> upon heating around 800°C.



To form the targeted clinker phases, a temperature of about 1450°C is required within the kiln [31-34]; therefore, the combustion of the fuel and the electricity required in the process are responsible for the remaining 40% of the CO<sub>2</sub> emissions coming from the kiln [30]. By considering the overall process, 0.8 tonnes of CO<sub>2</sub> are released in the atmosphere by producing 1 tonne of cement [35]; considering the over 4 Gt of PC globally produced, over 3 billion tonnes of CO<sub>2</sub> are released to the atmosphere annually.

The proposed work develops a novel route for the decarbonisation of limestone for subsequent use in the PC manufacturing process. The decarbonisation of limestone is carried out at low temperature (30-120°C) by mixing with concentrated NaOH solutions rather than by calcination at high temperature. Calcium carbonate would be converted to portlandite Ca(OH)<sub>2</sub> and sodium carbonate Na<sub>2</sub>CO<sub>3</sub> and/or thermonatrite Na<sub>2</sub>CO<sub>3</sub>·H<sub>2</sub>O (Equation 2). While Ca(OH)<sub>2</sub> may be mildly dried to CaO (310 – 470°C) and directly used for cement production, the sequestration of the process CO<sub>2</sub> would also occur by trapping in sodium carbonate/thermonatrite [36].



In Section 2, a deeper insight of the conventional calcination route for  $\text{CaCO}_3$  is presented, reflecting a strong base for the upcoming discussion. The following Sections 3, 4, 5, and 6 will discuss in detail the experimental outcomes gained and the accordance with data in literature, also outlining those aspects which would further improve the potential for industrial applicability. Section 7 briefly introduces those two industrial realities strictly influenced by a significant application of the alternative decarbonization route, such as soda ash ( $\text{Na}_2\text{CO}_3$ ) and caustic soda ( $\text{NaOH}$ ).

## 1.2. Linked Industries

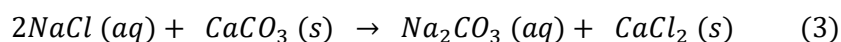
### 1.2.1. Soda ash $\text{Na}_2\text{CO}_3$

Soda ash or sodium carbonate ( $\text{Na}_2\text{CO}_3$ ), the added value by-product of the proposed decarbonisation reaction, is a white, crystalline and hygroscopic powder. It is an important industrial compound in terms of chemicals manufacturing, such as: glass, pulp and paper, soaps and detergents, and many other familiar consumer products. Light and dense soda are the other forms of sodium carbonate available, and they only differ in terms of granular sizes (the former is smaller than the latter). Impurities may include water (<1.5wt.%), sodium chloride (<0.5wt.%), sulphate (<0.1wt.%), calcium (<0.1wt.%), magnesium (<0.1wt.%) and iron (<0.004wt.%). The purity and the impurity profiles depend on the composition of the raw materials and the contamination involved in the production. Over 50 Mt of soda ash have been produced worldwide in 2014, and China was the main producer country, followed by the U.S. (Table 5). According to the data registered by the U.S. market between 2010 and 2014, the average price of soda ash on the market was 150.7 \$/metric tonne and no significant changes are expected in the following years [37].

Table 5: Main worldwide countries producers of soda ash, expressed in thousand metric tonnes [38].

<b>Country</b>	<b>2010</b>	<b>2011</b>	<b>2012</b>	<b>2013</b>	<b>2014</b>
<i>China</i>	20,3	22,9	24,0	24,3	24,5
<i>U.S.</i>	10,6	10,7	11,1	11,5	11,7
<i>Russia</i>	2,7	2,8	2,8	2,5	2,6
<i>Germany</i>	2,5	2,6	2,6	2,5	2,5
<i>India</i>	2,3	2,3	2,5	2,4	2,4
<i>Poland</i>	1,0	1,1	1,1	1,0	1,1

The Soda Solvay process has been used since the 19<sup>th</sup> century to produce sodium carbonate and sodium bicarbonate; owing to high efficiency, it has never been replaced by other processes since then [39]. In this process, calcium carbonate and sodium chloride are reacted together (1:1 molar ratio) in a coal-fed combustion chamber, which provides both the heat and the excess CO<sub>2</sub>, necessary to enhance the reaction (Equation 3), which is endothermic.



For the coal combustion, the calcination of limestone (or 2 moles of CaCO<sub>3</sub>, ΔH<sub>f</sub><sup>0</sup> =+178 kJ mol<sup>-1</sup>) requires the combustion of 1 mole of coal. As a consequence, this step accounts for about the 26% and 9% of the total thermal and electrical total process energy consumption, respectively [40]. Even though the Soda Solvay process should be neutral and resulting in zero emissions in principle, the combustion of the metallurgical coal (about 7% of limestone weight) provides excess CO<sub>2</sub> than required for the stoichiometric reaction, as previously mentioned. As a result, about 0.2 – 0.4t of CO<sub>2</sub> are emitted into the atmosphere for each tonne of sodium carbonate produced [41]. The U.S. currently produces sodium carbonate through a different and less energy-intensive process, but this requires the large amounts of natural trona [42], and therefore it is not easily feasible in other locations worldwide.

### 1.2.2. Caustic soda – NaOH

The production of caustic soda was approximately 65 million tons in 2015 and it is expected to increase up to 82 million tonnes by 2020 [43]. The chlor-alkali process accounts for over 99% of the overall NaOH production [44]. It dates back over 100 years, originating from the electrolysis of brine using mercury (Hg) as cathode, however, the large amounts of mercury dispersed in the environment lead to the switch to the membrane and diaphragm cell process [45, 46]. A scheme of the chlor-alkali membrane cell process can be seen in Figure 4. As shown, a concentrated NaCl solution (brine) enters the anodic cell, where chloride ions Cl<sup>-</sup> are oxidized to chlorine gas Cl<sub>2</sub>(g). Meanwhile, the anode operates the electrolysis of water which results in the generation of hydroxide ions OH<sup>-</sup> and the production of hydrogen gas H<sub>2</sub>(g). Dissolved sodium ions Na<sup>+</sup> can pass the cathode through a cathodic membrane called Nafion; once in the cathode, they can react with the hydroxide ions to form caustic soda (32 – 35w%).

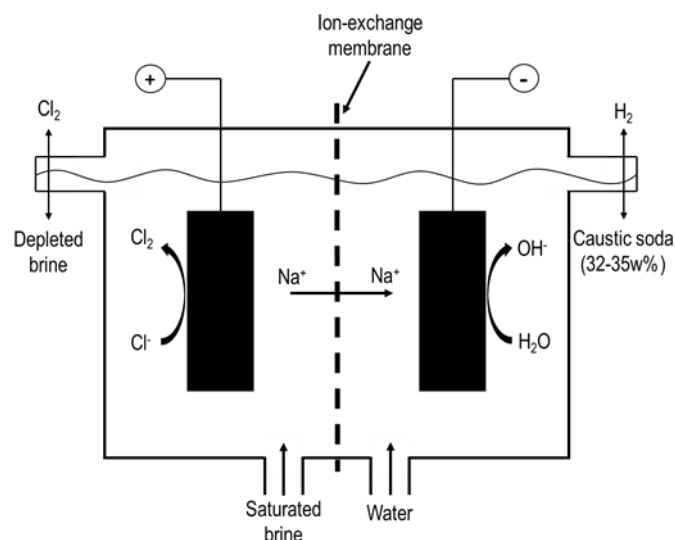


Fig. 4. Diagram of the chlor-alkali ion-exchange membrane process.

Table 3 summarizes the operating conditions for the current state-of-the-art operating conditions of the chlor-alkali process [44]. There is no possibility of independent control on the products of the process, meaning that the production of these products (NaOH, Cl<sub>2</sub>, H<sub>2</sub>) cannot be performed separately. Specifically, the production consists of 1 tonne of chlorine, 1.1 tonne of caustic soda and 0.03 tonne of hydrogen, traditionally referred as electrochemical unit (ECU). Taking into account the power consumption shown in Table 6, since 0.76 t of CO<sub>2</sub> is emitted to produce 1 kWh of electrical power [47], over 1.6 t of CO<sub>2</sub> is emitted to provide the electricity allowing for the production of 1 metric tonne of NaOH.

Table 6. State-of-the-art operating conditions with the current Chlor-Alkali process using dimensionally stable anodes.

<i>Current density</i>	<i>7 kA m<sup>-2</sup></i>
<i>Cell voltage</i>	<i>3.10</i>
<i>Power consumption</i>	<i>2.130 kW-h per tNaOH</i>
<i>Service life</i>	<i>&gt;4 years</i>

The power generation sector would be expected to cut about the 80% of the total CO<sub>2</sub> emissions by 2050. Since the electrical power represents almost all the total energy consumption in the process, by 2050 the industry will be expected to significantly cut the related emissions.

## References

1. Lüthi, D., et al., High-resolution carbon dioxide concentration record 650,000–800,000 years before present. *Nature*, 2008. **453**(7193): p. 379.
2. Houghton, J.T., G.J. Jenkins, and J.J. Ephraums, *Climate change*. 1990.
3. Change, I.P.O.C., *Climate change 2007: The physical science basis*. Agenda, 2007. **6**(07): p. 333.
4. Stocker, T., *Climate change 2013: the physical science basis: Working Group I contribution to the Fifth assessment report of the Intergovernmental Panel on Climate Change*. 2014: Cambridge University Press.
5. Thuiller, W., *Climate change and the ecologist*. *Nature*, 2007. **448**(7153): p. 550-552.
6. Garnaut, R., *The Garnaut climate change review*. Cambridge, Cambridge, 2008.
7. Weart, S.R., *The discovery of global warming*. 2008: Harvard University Press.
8. Peters, G.P., et al., The challenge to keep global warming below 2°C. *Nature Climate Change*, 2013. **3**(1): p. 4-6.
9. Harvey, L.D.D., *Global warming*. 2018: Routledge.
10. Dunn, R.J.H., et al., *Global climate*. *Bulletin of the American Meteorological Society*, 2020. **101**(101 (8)): p. S9-S127.
11. Rodhe, H., A comparison of the contribution of various gases to the greenhouse effect. *Science*, 1990. **248**(4960): p. 1217-1219.
12. Worrell, E., et al., Carbon dioxide emissions from the global cement industry. *Annual review of energy and the environment*, 2001. **26**(1): p. 303-329.
13. United Nations Environment Programme. Division of Early, W. and Assessment, *UNEP Year Book 2012: Emerging Issues in Our Global Environment*. 2012: UNEP/Earthprint.
14. Change, I.P.O.C., *Climate change 2007: the physical science basis: summary for policymakers*. Geneva: IPCC, 2007.
15. Füssel, H.-M., *The risks of climate change: a synthesis of new scientific knowledge since the finalization of the IPCC Fourth Assessment Report (AR4)*. 2010.
16. Le Quéré, C., et al., Global carbon budget 2013, *Earth Syst. Sci. Data*, 6, 235–263. 2014.
17. Com, E.U., A Roadmap for moving to a competitive low carbon economy in 2050 (COM (2011) 112 final). Commission staff working document Impact assessment, 2011.
18. Schneider, M., et al., Sustainable cement production—present and future. *Cement and Concrete Research*, 2011. **41**(7): p. 642-650.
19. Leung, D.Y.C., G. Caramanna, and M.M. Maroto-Valer, An overview of current status of carbon dioxide capture and storage technologies. *Renewable and Sustainable Energy Reviews*, 2014. **39**: p. 426-443.
20. Liu, H., C. Consoli, and A. Zapantis. *Overview of Carbon Capture and Storage (CCS) Facilities Globally*.
21. Iea, U., *Technology Roadmap Carbon Capture and Storage in Industrial Applications*. International Energy Agency, United Nations Industrial Development Organizations, 2011.
22. Rogelj, J., et al., Paris Agreement climate proposals need a boost to keep warming well below 2 C. *Nature*, 2016. **534**(7609): p. 631.
23. Smith, P., et al., *Essential outcomes for COP26*. *Global change biology*, 2021.
24. Survey, U.S.G. and S. Orienteering, *Mineral Commodity Summaries*, 2009. 2009: Government Printing Office.
25. Taylor, M., C. Tam, and D. Gielen, Energy efficiency and CO<sub>2</sub> emissions from the global cement industry. *Korea*, 2006. **50**(2.2): p. 61-7.
26. Metz, B., *Carbon dioxide capture and storage: special report of the intergovernmental panel on climate change*. 2005: Cambridge University Press.
27. Gartner, E. and H. Hirao, A review of alternative approaches to the reduction of CO<sub>2</sub> emissions associated with the manufacture of the binder phase in concrete. *Cement and Concrete research*, 2015. **78**: p. 126-142.
28. Schorch, F., et al., *Best available techniques (BAT) reference document for the production of cement, lime and magnesium oxide*. European Commission Joint Research Centre Institute for Prospective Technological Studies (Report EUR 26129 EN). Luxembourg: Publications Office of the European Union, 2013.
29. Afkhami, B., et al., Energy consumption assessment in a cement production plant. *Sustainable Energy Technologies and Assessments*, 2015. **10**: p. 84-89.

30. Barcelo, L., et al., Cement and carbon emissions. *Materials and structures*, 2014. **47**(6): p. 1055-1065.
31. Taylor, H.F.W., *Cement chemistry*. 1997: Thomas Telford.
32. Pöllmann, H., *Composition of cement phases. Structure and performance of cements*, 2002. **374**: p. 25-56.
33. Bogue, R.H., *Calculation of the compounds in Portland cement. Industrial & Engineering Chemistry Analytical Edition*, 1929. **1**(4): p. 192-197.
34. Mehta, P.K. and P.J.M. Monteiro, *CONCRETE Microstructure, Properties and Materials*. 2017.
35. Warwick, P.D., et al., US Geological Survey Carbon Sequestration–Geologic Research and Assessments. *Energy Procedia*, 2014. **63**: p. 5305-5309.
36. Hanein, T., et al., Decarbonisation of calcium carbonate at atmospheric temperatures and pressures, with simultaneous CO<sub>2</sub> capture, through production of sodium carbonate. *Energy & Environmental Science*, 2021.
37. Bolen, W.P., 2015 Minerals Yearbook - Soda Ash. November, 2015, USGS: <https://s3-us-west-2.amazonaws.com/prd-wret/assets/palladium/production/mineral-pubs/soda-ash/myb1-2015-sodaa.pdf>.
38. Jewell, S. and S.M. Kimball, *USGS Mineral Commodities Summaries: 2014. US Geological Survey*, <http://minerals.usgs.gov/minerals/pubs/mcs/2014/mcs2014.pdf>, Accessed, 2014. **12**(12): p. 2014.
39. Lister, T., *Sodium Carbonate: A Versatile Material*. 2000: Royal Society of Chemistry.
40. Shipchandler, R., B.K.L. Pun, and M.J. Weiss, *Systems and methods for soda ash production*. 2012, Google Patents.
41. Houghton, J.T., et al., *Revised 1996 IPCC guidelines for national greenhouse gas inventories. v. 1: Greenhouse gas inventory reporting instructions.-v. 2: Greenhouse gas inventory workbook.-v. 3: Greenhouse gas inventory reference manual*. 1997.
42. Eugster, H.P. and L.A. Hardie, *Sedimentation in an ancient playa-lake complex: the Wilkins Peak Member of the Green River Formation of Wyoming. Geological Society of America Bulletin*, 1975. **86**(3): p. 319-334.
43. Du, F., et al., *Sodium Hydroxide Production from Seawater Desalination Brine: Process Design and Energy Efficiency. Environmental science & technology*, 2018. **52**(10): p. 5949-5958.
44. Botte, G.G., *Electrochemical manufacturing in the chemical industry. The Electrochemical Society Interface*, 2014. **23**(3): p. 49-55.
45. Lakshmanan, S. and T. Murugesan, *The chlor-alkali process: work in progress. Clean Technologies and Environmental Policy*, 2014. **16**(2): p. 225-234.
46. Millet, P., *Chlor-alkali technology: fundamentals, processes and materials for diaphragms and membranes*, in *Handbook of Membrane Reactors*. 2013, Elsevier. p. 384-415.
47. European Commission (EC): *Communication from the Commission to the Council and the European Parliament on the comprehensive risk and safety assessments ("stress tests") of nuclear power plants in the European Union; Brussels, 4 October 2012, <https://eur-lex.europa.eu/legal-content/EN/TXT/PDF/?uri=CELEX:52012DC0571&from=EN>*

## 2. Literature review

This work may be intended as a detailed literature review about the main topic of this PhD project, which is the decarbonisation of  $\text{CaCO}_3$ , highlighting the main aspects surrounding the conventional calcination route. Specifically, importance has been given to the specifics of the technologies used and the related environmental footprint, and a deep discussion is also provided about all those solutions which are expected to help mitigate the carbon emissions from the lime/cement industry. Additionally, this review paper introduces two novel decarbonisation routes not involving combustion, and therefore informing the scientific community about other possibilities to investigate. Finally, the work is also intended to enrich the literature about the lime industry, which is usually overshadowed from the cement one; it has been accepted for publication of *Renewable & Sustainable Energy Reviews*. I here certify that I conceptualised and drafted the original manuscript, I replied to the concerns expressed from the journal reviewers, and I took care of the whole submission process.

# Decarbonising the lime industry: state-of-the-art

Marco Simoni<sup>\*1</sup>, Mathew D. Wilkes<sup>2</sup>, Solomon Brown<sup>2</sup>, John L. Provis<sup>1</sup>, Hajime Kinoshita<sup>1</sup>,  
and Theodore Hanein<sup>1</sup>

Departments of Materials Science & Engineering<sup>1</sup> and Chemical & Biological Engineering<sup>2</sup>, University  
of Sheffield, Sheffield, S1 3JD, United Kingdom.

\* Corresponding author: [marco.simoni.w@gmail.com](mailto:marco.simoni.w@gmail.com), [t.hanein@sheffield.ac.uk](mailto:t.hanein@sheffield.ac.uk)

## Abstract

The thermal treatment of limestone (mainly  $\text{CaCO}_3$ ) to produce lime ( $\text{CaO}$ ) is a major contributor to  $\text{CO}_2$  emissions and the literature on decarbonising the lime industry is scarce. Subsequent hydration of lime would lead to the synthesis of slaked/hydrated lime  $\text{Ca}(\text{OH})_2$ ; the production of a tonne of  $\text{Ca}(\text{OH})_2$  emits  $\sim 1.2$  tonnes of  $\text{CO}_2$  arising mainly from the process chemistry and fossil fuel combustion. Carbon Capture & Storage (CCS) technologies are currently believed to have the highest potential to mitigate these  $\text{CO}_2$  emissions, assuming that the thermal calcination of  $\text{CaCO}_3$  is unavoidable. Despite intensive research efforts and development, CCS technologies cannot be industrially applied yet due to their limited efficiency and the associated capital and operational costs.

In this review, the current state of the lime industry and its processing configurations is visualised. This is followed by a detailed description of the current status of the relevant CCS technologies (including their  $\text{CO}_2$  avoidance costs) and eco-efficient alternative fuels. This work then gives voice to two novel and potentially more sustainable decarbonisation routes that do not involve the thermal calcination of  $\text{CaCO}_3$ , one of which involves simultaneous mineralisation leading to permanent storage of  $\text{CO}_2$ . These technologies are particularly interesting especially if high temperature lime kilns, as we know them, are phased out to meet climate goals. It is revealed that the energy shift to green electricity might lead to a no-carbon lime industry and subsequent carbon neutrality (or negativity) of other hard-to-abate sectors.

**Keywords:** Lime; Sustainable Manufacturing; Industry Decarbonisation; Kiln; Carbon Capture and Storage

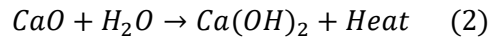
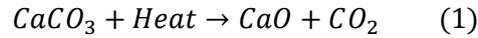
## Notations

2-amino-2-methyl-1-propanol	AMP	Low Emissions Intensity Lime and Cement	LEILAC
Annular Shaft Kiln	ASK	Lime Kiln Dust	LKD
Air Separation Unit	ASU	Long Rotary Kiln	LRK
CO <sub>2</sub> Avoidance Costs	CAC	Molten Carbonate Fuel Cell	MCFC
Calcium Looping	CaL	Monoethanolamine	MEA
Carbon Capture & Storage	CCS	Mixed Feed Shaft Kiln	MFSK
Carbon Capture Utilisation & Storage	CCUS	Natural Gas Combined Cycle	NGCC
CO <sub>2</sub> Purification Unit	CPU	Organic Rankine Cycle	ORC
Concentrated Solar Thermal	CST	Post-Combustion Capture	PCC
CO <sub>2</sub> Separation Unit	CSU	Parallel Flow Regenerative Kiln	PFRK
Direct Air Capture	DAC	Long Rotary Kiln with Pre-heater	PRK
Direct Contact Cooling	DCC	Piperazine	PZ
Calix's Direct Separation	DS	Alstom's Regenerative Calcium Cycle	RCC
Electrochemical Unit	ECU	Residue Derived Fuels	RDF
Electrostatic Precipitation	ESP	Selective Catalytic Reduction	SCR
European Lime Association	EuLA	Solid-Oxide Fuel Cell	SOFC
Flue Gas Desulfurization	FGD	Selective Non-Catalytic Reduction	SNCR
Flue Gas Recycle	FGR	Technology Readiness Level	TRL
Greenhouse Gas	GHG	Thermal Plasma	TP
International Energy Agency – GHG	IEAGHG		

### 1. The slaked lime industry

The term “lime” is usually used to refer to all those products deriving from the calcination of limestone and/or chalk, although they may be classified as: quicklime CaO, hard-burnt lime CaO, slaked/hydrated lime Ca(OH)<sub>2</sub>, and dolomitic lime (e.g., 30wt.% CaO, 21wt.% MgO, and 45wt.% CO<sub>2</sub> in the original limestone [1]). CaO, the direct product of the calcination of limestone, is the most in demand simple oxide worldwide, considering that it is also the essential precursor for the cement industry [2]. Depending on the average diameter size D, different quicklimes may be obtained: large lump lime (D < 20 cm), pebble lime (0.6 cm < D < 2.5 cm), ground lime (D < 0.25 cm), pulverised lime (D < 10-4 cm), and pelletised lime (D ≈ 2.5 cm). Quicklime reacts spontaneously with water, and its transport requires strict safety measures, given the strong exothermicity of its hydration reaction (1.14 MJ released per kg of CaO hydrated [3]). Outside the cement industry, a significant portion of CaO (around 27% in the EU in 2017 [4]) would be hydrated and stored as Ca(OH)<sub>2</sub>, finding application in a wide range of industries, such as: iron and steel manufacturing for the treatment of the acid effluents and heavy metals removal [5], construction [6], soil stabilisation [7], removal of contaminants (e.g. As, F) from potable water [8], low-temperature desulfurization [9] and sulfur scrubbing [10], CO<sub>2</sub> capture [11], wastewater treatment [12], and bulk chemicals [13]. In 2020, out of the 70 Mt globally produced, the EU market accounted for the manufacturing of 17.4 and 4.8 Mt of CaO and Ca(OH)<sub>2</sub>, respectively [4]. The ability and advanced technological understanding of using CaO/Ca(OH)<sub>2</sub> to capture CO<sub>2</sub> makes it useful for enabling net-zero emissions across several industries [14].

The slaked lime manufacturing process involves quarrying, crushing, washing, and stone preparation of the raw limestone prior calcination to CaO (Equation 1) and subsequent hydration to Ca(OH)<sub>2</sub> (Equation 2).



The composition of the limestone fed into the kiln may vary according to the specifics of the desired product, but generally requiring  $\geq 80$  wt.% CaCO<sub>3</sub> + MgCO<sub>3</sub> [15]. About 95% of the total energy input is employed for the calcination, which therefore reflects the key step of the process. In fact, 1.0 – 1.8 tonnes of CO<sub>2</sub> are emitted per tonne of CaO manufactured, with the lime industry (not including cement manufacture) contributing for about 1% to the total CO<sub>2</sub> emitted to the atmosphere annually [16]. The emissions from the hydration step were considered negligible here with respect to the calcination, where CO<sub>2</sub> arises from the process chemistry (68%), fuel combustion (30%) and electricity consumption (2%) [1]. Apart from CO<sub>2</sub>, which represents about the 20 Vol.% of the off-gas stream, Lime Kiln Dust (LKD), NO<sub>x</sub>, and SO<sub>x</sub>, also arise upon calcination, with concentrations ranging between 1.4 – 2 mg/Nm<sup>3</sup> [17], 100 – 2000 mg/Nm<sup>3</sup> [18], and 50 – 400 mg/Nm<sup>3</sup> [17], respectively. While LKD represents a valuable by product which is effectively removed via modern wet scrubbers [19], both NO<sub>x</sub> and SO<sub>x</sub> represent a threat to human health and the environment [20]. The NO<sub>x</sub> emissions may be limited through primary techniques (fuel selection, burner design, air staging) which prevent their formation at all, or by application of secondary ones (Selective Non-Catalytic Reduction (SNCR) and Selective Catalytic Reduction (SCR [21]), transforming the NO<sub>x</sub> species produced into N<sub>2</sub> and H<sub>2</sub>O. The SO<sub>x</sub> emissions may be limited by using fine limestone [18], injecting lime into the combustion air [19], sulfur scrubbing [10], and injecting an absorbent into the exhaust gases [18]. The composition of the exhaust off-gas stream from a lime kiln varies in accordance with the kiln and fuel used for the calcination, but it can be approximated as reported in Table 1 that also shows the cement kiln off-gas, and which are quite similar.

Table 1.

Source	CO <sub>2</sub> (vol.%)	O <sub>2</sub> (vol.%)	N <sub>2</sub> (vol.%)	H <sub>2</sub> O (vol.%)
Lime Kiln Off-Gas	20.6	8.2	63.9	7.3
Cement Kiln Off-Gas	22.8	7.5	62.4	7.3

## 2. The calcination of limestone

### 2.1. Lime Industry

The choice of the kiln design significantly affects the overall cost of lime production [18]; the main features of five types of kiln are reported in Table 2, where the efficiency was calculated by taking into account the theoretical energy required for the thermal dissociation of  $\text{CaCO}_3$  ( $1819.4 \text{ kJ kgCaCO}_3^{-1}$  [22]). A deeper insight into the calcination units commercially available now follows and the technical aspects relevant for this discussion are outlined.

Table 2.

Kiln type	$\eta(\%)$	CO <sub>2</sub> emissions factor ( $t_{\text{CO}_2}/t_{\text{CaO}}$ )	Electricity consumption (kWh/tonne)	Output range (t/d)	Input Grain size (mm)
<i>PFRK</i>	75 – 99	1.0 – 1.2	20 – 40	100 – 600	10 – 200
<i>LRK</i>	35 – 53	1.2 – 1.8	18 – 25	160 – 1500	2 – 60
<i>PRK</i>	41 – 62	1.1 – 1.4	17 – 45	150 – 1500	10 – 60
<i>ASK</i>	65 – 96	1.0 – 1.3	18 – 50	80 – 300	40 – 150
<i>MFSK</i>	68 – 93	1.0 – 1.5	5 – 15	60 – 200	20 – 200

The PFRK design (Figure 1A) represents the most used type of kiln in the EU, counting 158 units in 2013 [18]. It consists of two shaft kilns, both composed of a pre-heating (top), burning (middle), and cooling (bottom) zone. At the burning zone, the two shafts are interconnected by a crossover channel that enables very low specific heat consumption. The fuel is injected through a series of lances vertically placed in the material bed of the burning zone at the top of the first shaft, leading to combustion with the counter-current cooling air blown from the bottom. These combustion gases, together with the process CO<sub>2</sub> released from the burned limestone, enter the crossover channel at a temperature of 1050°C. These streams then flow upwards upon mixing with the cooling air from the bottom of shaft two, heating the limestone in the respective pre-heating zone. The limestone is fed at the top of both shaft kilns and slowly drops by gravity to the bottom of each calcination unit, while converting to CaO. Considering a calcination temperature between 950 and 1050°C, the retention time of the kiln charge accounts to about 8 hours [23], depending on the feeding rate set. A PFRK is suitable for different types of fuel, requiring about 20 – 40 kWh/tonne<sub>CaO</sub> of electrical input [18], and finally leading to a high reactivity and low CO<sub>2</sub> residual quicklime.

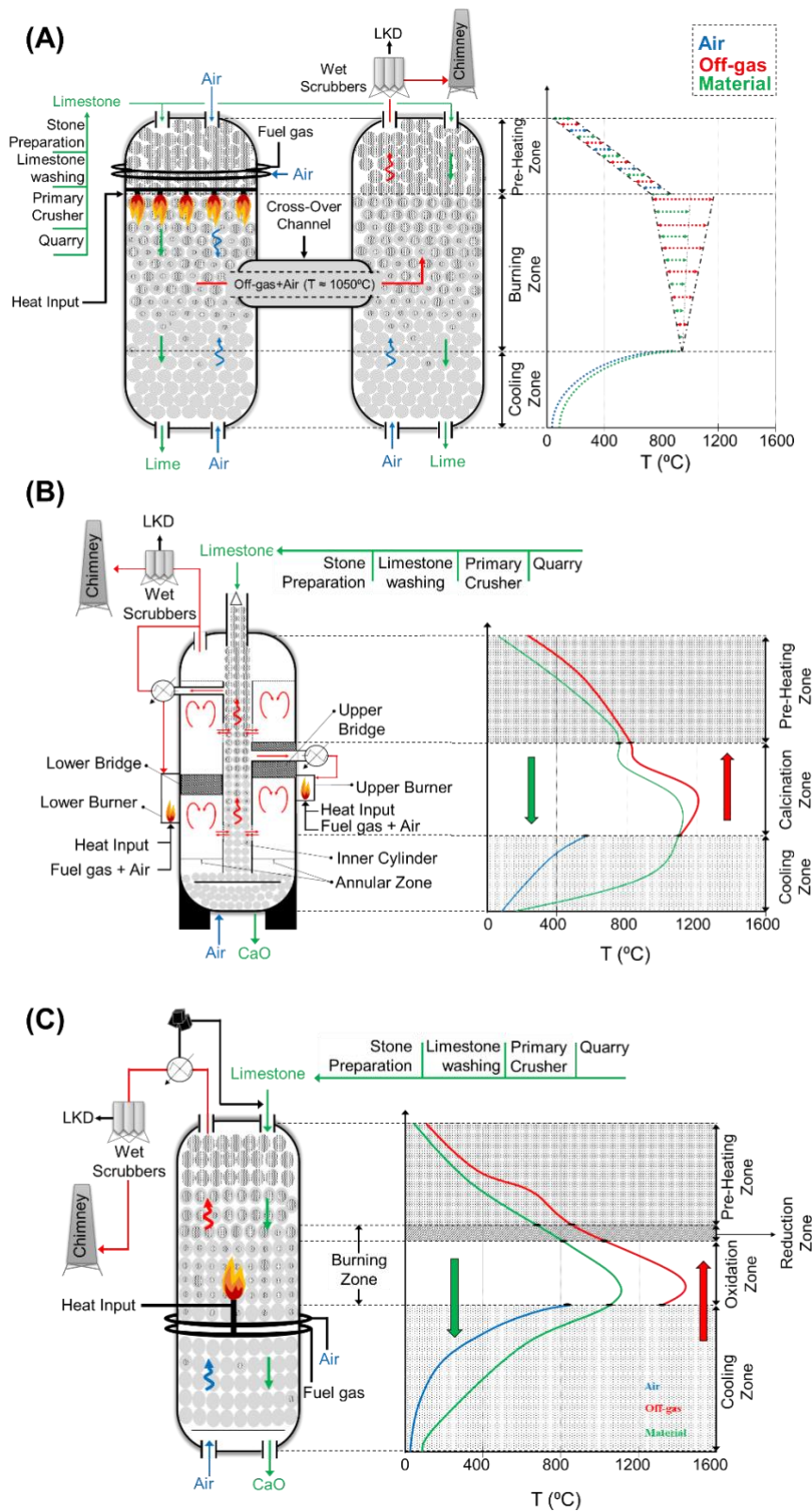


Figure 1.

An ASK design (Figure 1B [24]) can be represented by a central cylinder, within which the limestone advances by gravity towards the bottom, passing through the pre-heating, calcination, and cooling zones. The inner cylinder is physically divided from the external shell by the so-called annular zone [25]. In the pre-heating section, the material is pre-heated by the counter-current flow of the gases arising from the upper burner, followed by proper calcination in the upper calcining zone. In the lower calcining zone, the calcination continues in a co-current flow of the limestone with the combustion gases from the lower burner. Fuel injection occurs at the height of the upper and lower burners, where the heat from the off-gas is also recovered to minimise energy loss. This design allows for lower thermal losses [16], with respect to PRK and LRK configurations, but it also requires longer residence times (8 – 20h [26]) and higher construction costs. The lime produced presents a medium-high reactivity even when produced from a feed with poor  $\text{CaCO}_3$  content, and yields a  $\text{CO}_2$ -rich (29 – 34 vol.%) off-gas. A limestone with average size between 40 and 150 mm is used in an ASK, which may operate continuously only at high air ratios, thereby limiting the temperature rise within the kiln. The electricity consumption is strongly dependent on the grain size, ranging between 18 and 50 kWh/tonne<sub>CaO</sub>. (Table 2). The raw material and the coke are mixed prior to entering the kiln, and therefore leading to a final sulfur-rich quicklime with limited quality but high reactivity.

An MFSK design (Figure 1C) is suitable for a limestone particle size in the range 20 to 200 mm, which moves ( $\sim 2 \text{ m}\cdot\text{h}^{-1}$ ) down the unit together with the slightly smaller and dense grade coke and anthracite, avoiding segregation. After passing through the pre-heating section, where both the temperatures of the bed and the gas are around 800 – 850°C, the feed enters the burning zone which is divided into the excess-air reduction and oxidation sub-sections. The temperatures of the flue gas and the bed range between 1000 – 1400°C and 800 – 1000°C, respectively, in the burning zone, while the cooling leads to a final solid product below 200°C. The lime produced has a low-to-moderate reactivity with a high sulfur retention. Despite the low electrical consumption and construction/maintenance costs, the lifetime of the device is significantly affected by the large size of limestone fed.

The industrial LRK (Figure 2A [27]) is normally a 50 – 225 m long rotating cylinder, 2 – 6 m in diameter, inclined at 1 – 4° to the horizontal, allowing the feed to move throughout the calcination unit. The limestone is fed at the upper end, in counter-current with fuel and combustion air, ensuring effective calcination of  $\text{CaCO}_3$  to  $\text{CaO}$ . Depending on the level of moisture in the feed, the process might be dry or wet; the former would involve the pre-heating and pre-calcination of the stone, and in the latter the stone is fed directly into the rotary kiln upon passage through a chain-zone. A chain system is mainly formed of oval links, ensuring better heat transfer and evaporation, together with an enhanced material transportation and

decrease of dust losses from the unit [28]. Despite the higher energy efficiency linked to the dry process, it is not always convenient for existing wet-process plants to convert to dry operations, also given the humidity of the stone upon quarrying (which can be around 30%). To highlight the temperature profile within the rotary kiln, a wet process is taken into account (Figure 2A [27]). The limestone enters the chain system at ambient temperature and leaves it at around 120 – 150°C, while the temperature of the off-gas is about 600°C. The mean residence time of the solids is 80 – 100 minutes [29], mainly depending on the rotation speed set up. Following calcination through the rotary kiln unit, the solids are collected and cooled down [30] to ambient temperature from about 1150-1200°C with a counter-current ambient air flow in the cooling zone, while the off-gas is used to pre-heat both the limestone in the chain zone and the calciner fuel (shown here in Figure 2A as coal). Strong heat losses (convection and radiation) [31] make this configuration highly energy-intensive and relatively poorly efficient ( $18\% < \eta < 25\%$ ) (Table 2), even taking into account the limited electricity consumption of 18 – 25 kWh/tonne<sub>CaO</sub> [18]. Despite this, the high flexibility and robustness, the possibility to produce limes at varying reactivity, and the feasibility for soft limestone, are possible advantages. The LRK design leads to the incorporation of the sulfur from the fuel into the produced lime, therefore rendering it suitable for a wide range of fuels [18].

A PRK is characterised by the presence of appropriate pre-heaters (cyclones, vertical shafts, and/or travelling gates) prior the entrance of the feed into the calciner. Such a configuration (Figure 2B [32]) ensures lower convective and radial heat losses together with improved heat recovery from the off-gases, which leave the pre-heating tower at around 200 – 300°C. The temperature of the gas and the solids is quite uniform within each of a sequence of cyclones, increasing from around 300°C to above 800°C in the first and last units, respectively, through turbulent mixing. Following this, the solids enter the calciner, where the temperature of the solids is raised up to ~900°C by heat transfer from the flue and coal combustion gas, whose temperature decreases down to around 800°C. The limestone is then fed into the rotary kiln and totally calcined for an average residence time of 30 minutes [33], leading to a final product at about 1150-1200°C which is finally cooled down by heat exchange with a counter-current air flow in the cooling zone. Despite the higher efficiency of the PRK design respect with the LRK (Table 2), higher maintenance costs need to be highlighted. The improved heat recovery within the series of pre-heaters results in a significantly shorter length of the rotating unit (40 – 90 m) respect with a LRK, while a higher electrical consumption is registered (17 – 45 kWh/tonne<sub>CaO</sub>). Higher sulfur contents are detected within the flue-gas of a PRK design respect with LRK; the multiple stages of CaCO<sub>3</sub> calcination, occurring in different units, leads to a poor sulfur uptake within the lime produced. Several adjustments may be made to prevent

excessive emissions of sulfur to the atmosphere, such as ensuring reducing conditions within the kiln, or by addition of finely crushed limestone to preferentially absorb  $\text{SO}_x$ .

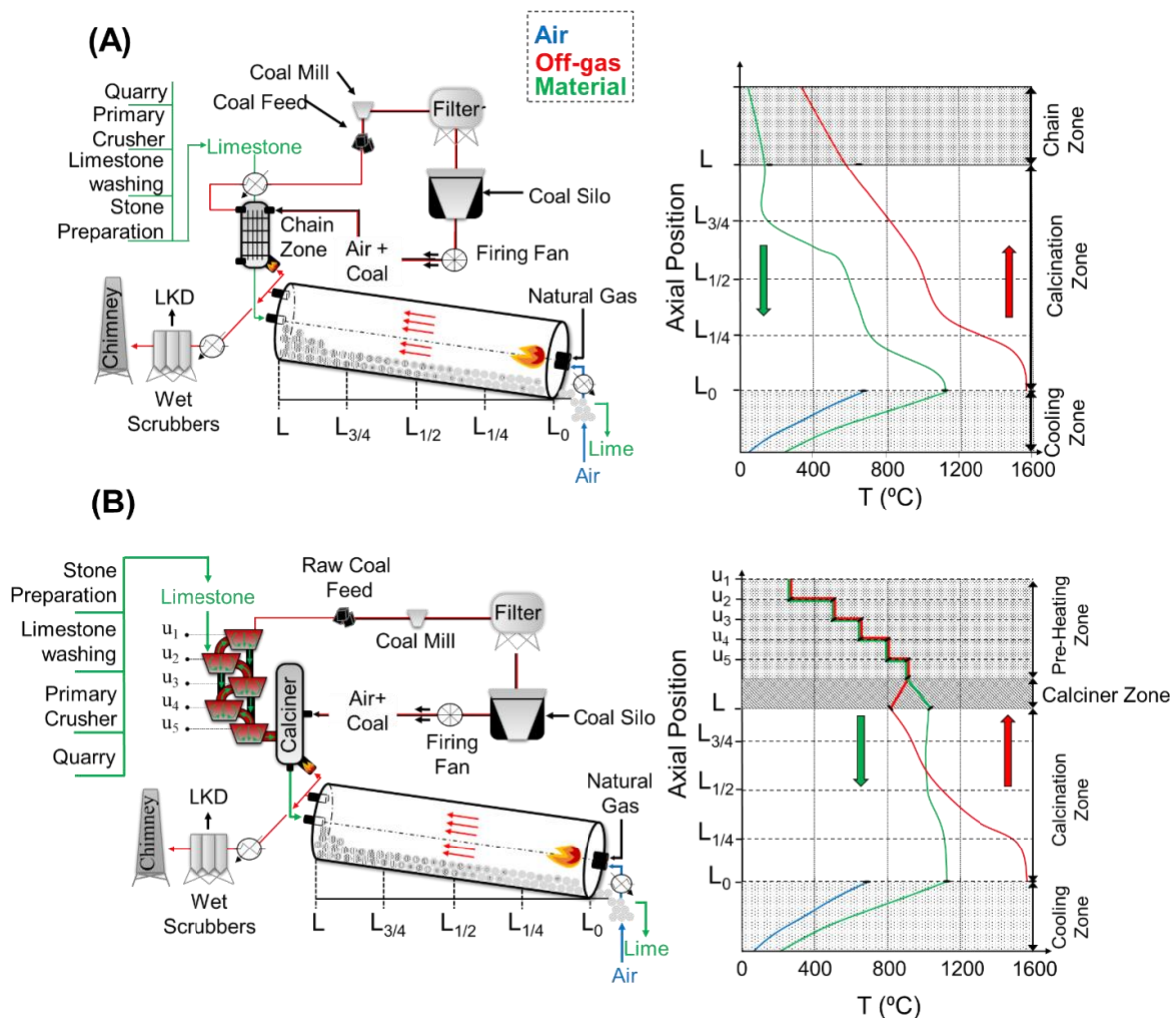


Figure 2.

## 2.2. Cement Industry

The cement industry accounts for over 4 billion tonnes produced worldwide every year, of which 180 Mt are manufactured in the EU [34]. That would account for about 88 Mt of  $\text{CaO}$  produced for cement purposes annually (about four times than the  $\text{CaO}/\text{Ca}(\text{OH})_2$  produced for non-construction purposes), considering a clinker-to-cement ratio of 0.81 and a  $\approx 60$  wt.%  $\text{CaO}$  content in clinker [35]. While lime is mainly produced through the PFRK configuration for the reasons discussed above, cement is mainly manufactured within LRK and PRK units (Fig. 2A and B, respectively). Especially, the PRK configuration reflects the most energy-efficient option for clinkering, which was firstly introduced in the 1960's. Depending on the design considered, such as air-trough or air-separate pre-calciners, up to the 40 and 95% of the raw

feed can be decarbonised prior entering the rotary kiln [36]. It is essential that the formation of the clinker does not occur in the pre-calciner unit; for this reason, around the 70% of the overall amount fuel can be efficiently used in the pre-calciner unit.

Given both the high similarity in off-gas composition (Table 1) and process design, all the considerations discussed below assume a higher-scale importance in terms of impact, considering the much larger market of cement with respect to lime/slaked lime. In other words, a common approach in terms of CO<sub>2</sub> emissions reduction may be likely adopted for the lime and cement industry.

### 3. Quicklime slaking

The hydration of CaO to give Ca(OH)<sub>2</sub> (Equation 2) mainly involves the electrical input necessary for the handling and mixing of CaO into water (approx. 5-30 kWh consumed per tonne of hydrated lime [18]). The heat released by the strongly exothermic hydration of CaO [3] is recovered and exploited in drying the product, to produce Ca(OH)<sub>2</sub> as a powder or putty, depending on the amount of water removed by evaporation. A Ca(OH)<sub>2</sub> powder is obtained when considering a stoichiometric amount of water in the so-called “dry process”. It consists of a pre-hydrator with a double shaft paddle screw geometry, preventing caking of the product, followed by a hydrator where the CaO introduced is fully reacted with water [37]. The quality of the final product mainly depends on the limestone used, but also on the conditions applied during the hydration process [38]. A high Ca/Mg limestone would be generally hydrated under ambient conditions to give a final product with 72 – 74 wt.% CaO and 23 – 24 wt.% chemically-combined water content. Starting from a dolomitic limestone (35 – 46 wt.% MgCO<sub>3</sub>), the hydration may be performed under ambient conditions, but MgO would remain un-hydrated given the lack of medium-to-high alkaline conditions [38].

Conversely, when over-stoichiometric amounts of water are used, a Ca(OH)<sub>2</sub> putty is obtained. Different process designs may be used to perform the slaking: a slurry slaker, paste slaker, ball mill slaker, and batch slaker. A slurry slaker requires initial mixing of quicklime and water (1 to 3.3-5 weight ratio) in the slaking chamber; the paste flows by gravity to the grit removal chamber, where the viscosity of the slurry is reduced by addition of cold water. The grit can thus be separated at the bottom of the chamber by gravity, and finally discharged; the slaked lime will have an overall residence time of ~10 min. A paste slaker involves a lower CaO/water ratio (1:2.5), therefore is compact in size, allowing for a total residence time of ~5 min. The resulting high density requires the use of appropriate rotating paddles which push the paste toward the discharge point; here, it is diluted with four parts of water, allowing for the grit removal by gravity. Ball mill slakers are generally much more expensive than the other types,

but they enable the slaking process to proceed even when the available water is highly concentrated in sulfates. An external classifier separates the slurry from the grit, which is then recirculated into the mill for further grinding and slaking. A batch slaker is a variation of the slurry slaker design, since the size of the batch reactor is predetermined and therefore the corresponding volumes of water and quicklime need to be added in succession. The slurry undergoes mixing until a temperature of 75 – 80°C is achieved, then is dumped into a second tank for grit removal [39]. To prevent the reformation of  $\text{CaCO}_3$  by reaction between  $\text{Ca(OH)}_2$  and atmospheric  $\text{CO}_2$  [40], the final slaked products resulting from all of these processes need to be stored in dry draft-free conditions.

## 4. Sustainable solutions and research gaps

As outlined above, the calcination of  $\text{CaCO}_3$  represents the key reaction for a wide range of industries, particularly lime, slaked lime, and cement. The same chemical reaction (and thus related process engineering) is also highly relevant to the regeneration of spent sorbents in the calcium-looping carbon capture processes [41] described in section 4.1.7.

Several approaches may be considered to make such an emitting step more sustainable, and this work offers the reader an overview of those possible solutions. Significant improvements have already been achieved to cut the  $\text{CO}_2$  emissions arising from fuel combustion, such as fuel switching [42] and Carbon Capture & Storage (CCS) [43].

This review will also promote the counterargument, by identifying some additional routes [44, 45] which do not involve the thermal calcination of  $\text{CaCO}_3$ , still considered unavoidable. Such alternatives did not receive much attention yet, but the current worldwide situation is urgently calling for a net change of mentality to pursue the global decarbonisation. Also, the authors aim to provide a valid and strong base for all those interested in the lime industry, often overshadowed by the cement one [2, 46].

### 4.1. Carbon Capture & Storage

Although the primary focus is on power generation sources [47], CCS technologies are also believed to have a high potential to mitigate the  $\text{CO}_2$  emissions from a wide range of industrial processes, e.g., cement, oil refining, chemicals, glass, paper, iron, and steel production [48, 49]. Post-combustion type  $\text{CO}_2$  capture technologies may be a better fit for the lime industry [50], since they enable the capture of both the raw material and fuel  $\text{CO}_2$ , while pre-combustion technologies could only reduce the latter category of emissions [51]. The following sections provide a detailed overview of the main CCS technologies relevant to the lime industry,

highlighting the energy demand and the resulting cost of CO<sub>2</sub> removal; Table 3 below groups all the main characteristics of each solution discussed.

Table 3.

Technology	Inlet CO <sub>2</sub> concentration	CO <sub>2</sub> capture rate (%)	Specific energy demand (GJ/tCO <sub>2</sub> )	CAC (€/tCO <sub>2</sub> )
Oxy-fuel <sup>[1]</sup>	18-22 mol.%	90	1.6	33 <sup>[2]</sup> - 42 <sup>[3]</sup>
RTI's PEI Solid Sorption <sup>[4]</sup>	15 vol.%	90	2.7	39 - 46
Hollow Fibre Membrane <sup>[5]</sup>	19 mol.%	80	1.2	46 - 48
Veloxotherm™ RAM	-	-	-	50 <sup>[6]</sup>
CaL integrated <sup>[1]</sup>	18-22 mol.%	93	3.2	39 <sup>[7]</sup> - 59 <sup>[3]</sup>
CaL tail-end <sup>[1]</sup>	18-22 mol.%	91	4.01	52 <sup>[3]</sup>
Aker Solutions' ACC™ <sup>[8]</sup>	18 vol%	90	2.8	-
MCFC <sup>[9]</sup>	34 mol.%	31-76	0.4-1.2	-

The avoidance cost (CAC), expressed as the difference of CO<sub>2</sub>-removal costs between a plant with CCS technology and a reference plant without CCS (which may be subject to carbon taxation, although this is not explicitly included in calculations here) [60, 61], is reported for each technology discussed. It is worth noting, there is no standardised method for calculating the (CAC), therefore, we refer the reader to the individual references cited to gain further understanding on the specific assumption used in their respective calculations. The typical method for calculating the CAC is reported in Equation 3 below [54]

$$CAC = \frac{Cost_{CCS} - Cost_{ref}}{e_{eq,ref} - e_{eq,CCS}} \quad (3)$$

Where, Cost<sub>CCS</sub> and Cost<sub>ref</sub> are the costs of the plant with and without CCS, respectively. e<sub>(eq,ref)</sub> and e<sub>(eq,CCS)</sub> are the specific equivalent emissions from the reference plant and the plant with CCS. However, for demonstration purposes, the application of the CCS technologies proposed will be shown for the lime industry by integrating with the PFRK calcination unit reported in detail in Figure 1A.

#### 4.1.1. Physical/chemical absorption

The choice of a physical or chemical absorption process does not affect the quality of the lime produced, as it treats the off-stream gases and with no interaction with the Ca-based solids undergoing processing, either before or after calcination. However, the high capital costs [62].

require a further implementation of the state-of-the-art technology to ensure economic return. A wide range of solvents have been investigated for liquid-phase CO<sub>2</sub> chemical absorption, including piperazine (PZ), 2-amino-2-methyl-1-propanol (AMP), aqueous ammonia (NH<sub>3</sub>), and aqueous potassium carbonate (K<sub>2</sub>CO<sub>3</sub>). Monoethanolamine (MEA) at 30-40 wt.% concentration is usually considered the benchmark solvent for CO<sub>2</sub> removal [47]. Such a design can be used upon removal of SO<sub>x</sub>, NO<sub>x</sub> and particulate matter via flue gas desulfurization (FGD) [18], selective catalytic/non-catalytic reduction (SCR/SNCR) [21], and electrostatic precipitation (ESP) [63], respectively. These impurities, together with water, need to be removed prior stockage of the CO<sub>2</sub>, to prevent corrosion [64]. Moreover, the solubility of SO<sub>x</sub> as H<sub>2</sub>S in MEA and DEA has been assessed 2.4 times higher than CO<sub>2</sub> [65]; a 70% adsorption of NO<sub>x</sub>-derived species, nitrate and nitrite, was observed in [66] at an NO<sub>x</sub> inlet concentration up to 150 ppm for a MEA absorber designed for a 90% CO<sub>2</sub> removal. In other words, the presence of SO<sub>x</sub> and NO<sub>x</sub> in the gaseous off-stream would also lower the adsorption efficiency of the CO<sub>2</sub>, leading to a rise in removal costs. Also, the Direct Contact Cooling (DCC) prevents the degradation of the solvent occurring at the high temperature of the exhaust gases [67]. The schematic in Figure 3A refers to the MEA-based CO<sub>2</sub> capture process for lime production proposed by Choi et al. [46], registering a promising energy consumption of 3.72 GJ/tCO<sub>2</sub> and CAC of 60-90 €/tCO<sub>2</sub>.

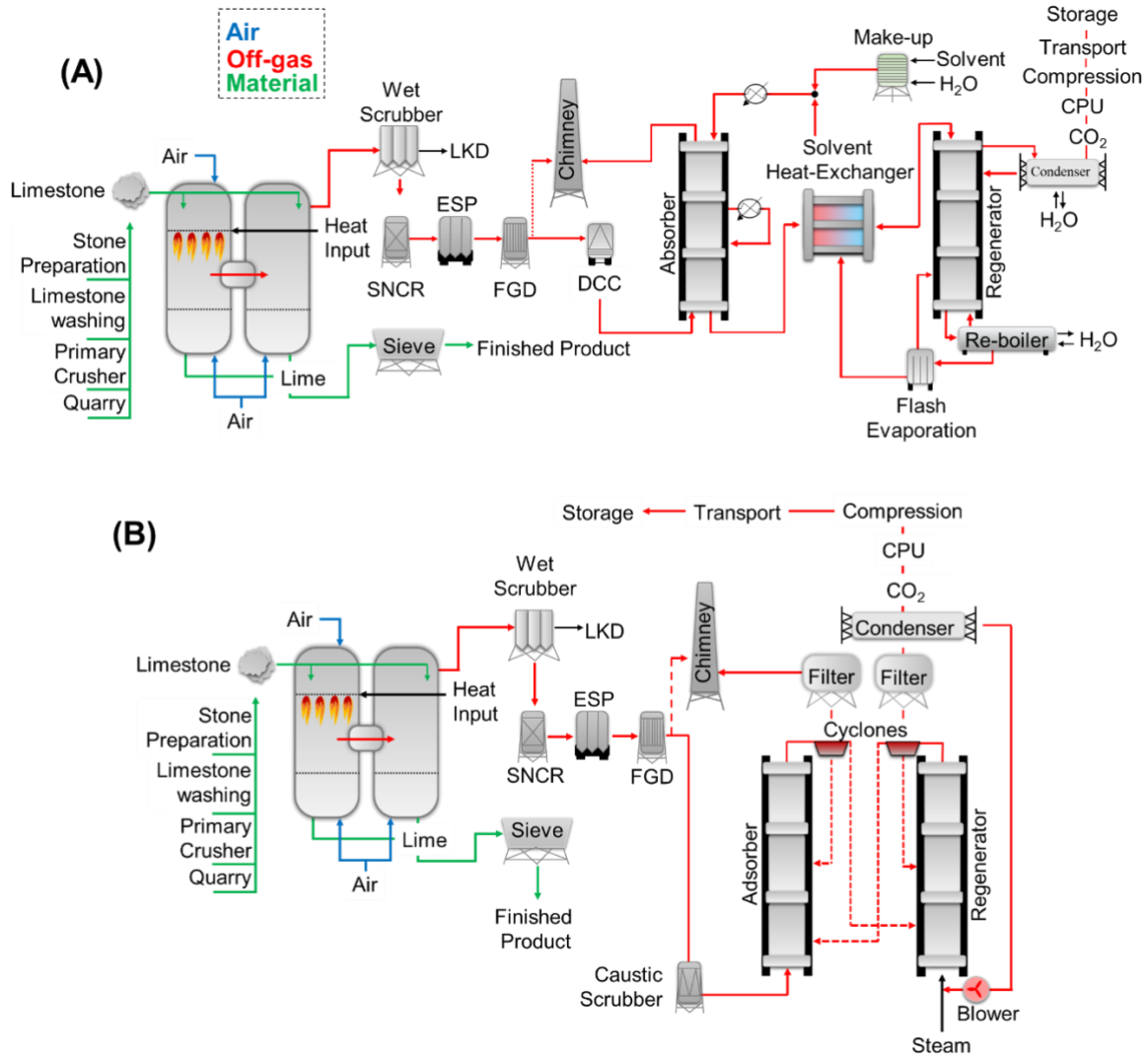


Figure 3.

The off-gas leaves the PFRK unit, and it is pre-treated through wet scrubber, SNCR, ESP, FGD, and DCC, prior to entering the absorbent column as a CO<sub>2</sub>-rich gas; here, the CO<sub>2</sub> dissolves by reaction with MEA. Primary and secondary alkanolamines react with CO<sub>2</sub> to form a zwitterion ( $RNH_2^+ COO^-$  in Equation 4), which instantaneously neutralises to form a carbamate ( $RNHCOO^-$  in Equation 5) [68]. This zwitterion mechanism does not work for tertiary amines as they cannot form a carbamate. For more information on aqueous amine and CO<sub>2</sub> chemistry see [69]. The resulting cleaned off-gas leaves the system at the top, while the CO<sub>2</sub> passes from the gas to the liquid bulk as the ionised species  $HCO_3^-$ .



The CO<sub>2</sub>-rich amine solution is then stripped in the regenerator and the reverse of reaction 4 occurs, to give a regenerated amine solution to recirculate, and a CO<sub>2</sub>-rich gaseous stream; the energy-intensive stripping of CO<sub>2</sub> from RNH<sub>2</sub> [70] is performed through a series of re-

boiling steps. These results are concordant with the 3.1-3.2 GJ/t<sub>CO<sub>2</sub></sub> energy demand outlined from the International Energy Agency – GHG (IEAGHG) when considering the pulp and paper production route [71]. Currently there are no industrial or demonstration scale studies specific to solvent based CO<sub>2</sub> capture from lime kilns, whereas several demonstration-scale tests have been already reported for cement production [50, 58].

The solid sorption technology has been successfully applied at RTI and Norcem's pilot-scale cement facilities, outlining relatively low CAC of 39 - 46 €/t<sub>CO<sub>2</sub></sub> [55], but also efficiency drop at higher (250 mg/Nm<sup>3</sup>) SO<sub>x</sub> concentrations. Also, by only referring to a conventional Natural Gas Combined Cycle (NGCC) power plant, a lower solvent regeneration energy (2.7 GJ/tCO<sub>2</sub> [72]) was outlined with respect to the MEA process just discussed. An example of solid sorption technology integrated with lime production in a PFRK is shown in Figure 3B [72]. The off gas enters an absorber column upon pre-treatment via wet scrubbing, SNCR, ESP, GFD. Following the CO<sub>2</sub>-loading/unloading cycle described above for the MEA process, the CO<sub>2</sub>-rich gas from the top of the regenerator undergoes a final condensation step, leading to pure CO<sub>2</sub> and a gaseous stream which is recirculated at the bottom of the regeneration unit.

#### 4.1.2. Membrane separation

The membrane separation has not been tested yet on the exhaust gas from a lime plant, but other industrial studies highlighted promising outcomes. Specifically, the treatment of a 36 vol.% CO<sub>2</sub> blast furnace gas allowed for the capture of 89% of the total CO<sub>2</sub> for an electrical consumption of 0.6 GJ/t<sub>CO<sub>2</sub></sub> [73]. A good potential was also outlined for eventual application to the cement industry, registering an 80% CO<sub>2</sub> removal at a 40 – 50 €/t<sub>CO<sub>2</sub></sub> CAC when tested at the Norcem's pilot plant [74]. Other studies [56, 75] confirmed the outcomes just reported, while Lidqvist et al. [76] highlighted that the majority of the investment and operating costs of this technology are related to turbomachinery and CO<sub>2</sub> compression. Since the study considered flue gas compositions from the cement industry comparable with lime kiln exhaust gas (Table 1), it highlights the potential applicability to the lime manufacturing process. The flow diagram in Figure 4 was obtained by re-adapting the design in [74] to a PFRK calcination unit.

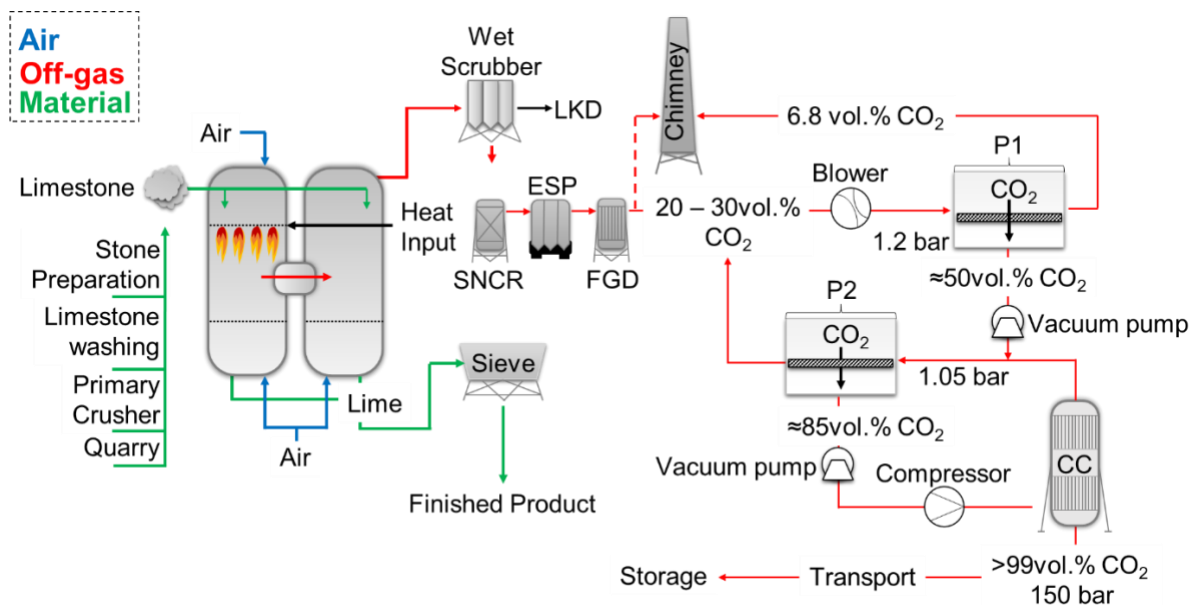


Figure 4.

As reported, the off-gas from the kiln unit undergoes a series of pre-treatments, i.e., SNCR, ESP, and FGD, for the effective removal of water, NO<sub>x</sub>, and SO<sub>x</sub>, which would lower the efficiency of the membranes for competition effect [77]. Following, the primary CO<sub>2</sub> capture step occurs in P1 at 1.2 bar and 20 – 30 vol.% CO<sub>2</sub>. From P1, an approximately 50 vol.% CO<sub>2</sub> gas is fed into the secondary CO<sub>2</sub> capture step P2 at 1.05 bar, while a CO<sub>2</sub>-depleted (~7 vol.%) stream may be emitted through the chimney. At the bottom of P2, 85 vol.% CO<sub>2</sub> is directed to a compressor and finally to a CO<sub>2</sub> Condensation Column CC, from which >99 vol.% CO<sub>2</sub> at 150 bar may be obtained. The CO<sub>2</sub>-depleted gaseous streams from P2 and CC are recirculated into P1 and P2, respectively.

#### 4.1.3. Physical/chemical adsorption

Adsorption-based processes exploit the surface physical reaction between the phases involved [78], i.e. gas and solid/liquid. It is significantly different from absorption, which might be physical [79], where the solvent capacity increases almost linearly with the partial pressure of the gaseous component following Henry's law, or chemical, where a chemical interaction occurs between the reactants [80]. Adsorption-based CO<sub>2</sub> capture systems are currently close to commercialisation, however, Bui et al. [47] state that they are unlikely to out-compete liquid scrubbing systems for large scale operations due to the issues related to the handling of solids. Despite this, adsorption-based systems are economically advantageous as the regeneration of the sorbent can be performed through pressure, temperature, or concentration swings, at a

much lower cost than conventional amine scrubbing technologies [81]. Although no specific study of adsorption-based CO<sub>2</sub> capture systems directly applied to the lime industry could be found in the literature, interesting applications to the cement manufacturing process are reported in [50] and [82].

The CO<sub>2</sub>MENT project led by Svante (formerly known as Inventys) is currently in phase II of operation, aiming to capture CO<sub>2</sub> specifically from cement production, while phase III is demonstrating CO<sub>2</sub> utilisation (injection into cement and fly ash) on-site at LafargeHolcim’s cement plant in British Columbia, Canada [82]. Svante’s Veloxotherm™ Rotatory Adsorption Machine (RAM) uses vacuum-temperature-concentration swing adsorption in a single unit to capture CO<sub>2</sub> from cement kiln exhaust, as illustrated in Figure 5 [82]. The device exploits the heat recovery from the PFRK unit to produce steam, which is fed counter-current with respect to the cooling air entering at the top; as a result, the off-gas entering at the bottom of the unit is split into a CO<sub>2</sub>-rich stream and a cleaned flue-gas stream. The CAC is approximately 43 €/t<sub>CO<sub>2</sub></sub>, and the company aims to demonstrate the first full-cycle CO<sub>2</sub> capture and utilisation attached to a cement plant [50].

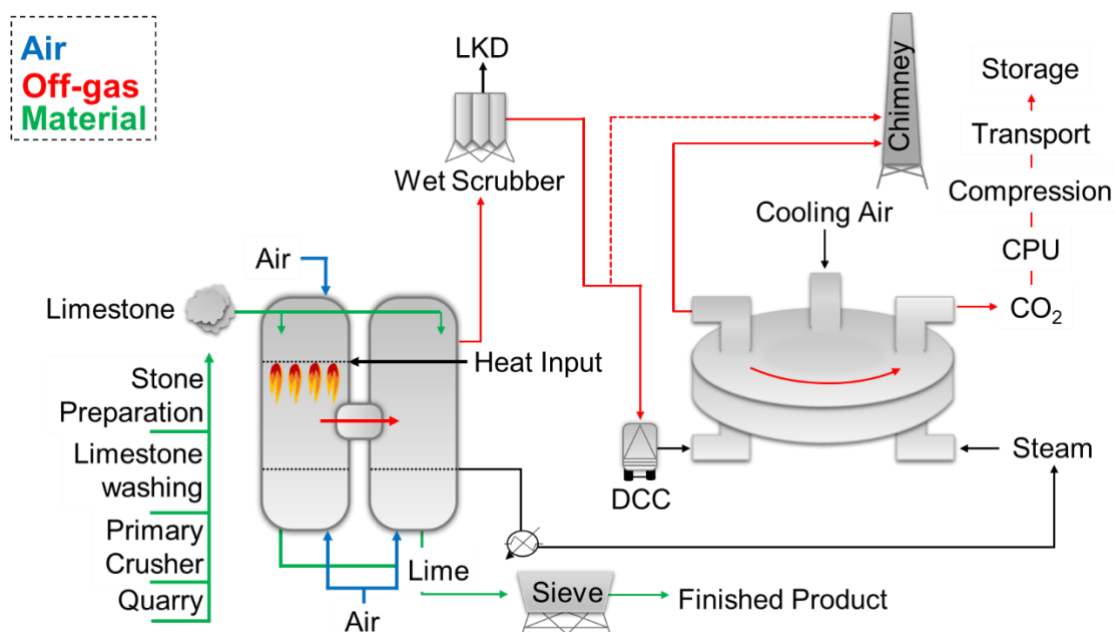


Figure 5.

#### 4.1.4. Direct Separation

This technology, exploiting the separation of the combustion and calcination reactions, has been investigated in the Low Emissions Intensity Lime and Cement (LEILAC) project through Calix’s Direct Separation (DS) technology. Upon integration into the Heidelberg Cement plant in Lixhe, Belgium, CAC around 50 €/t<sub>CO<sub>2</sub></sub> were highlighted [82, 83], therefore suggesting economic feasibility. Figure 6A highlights the Calix DS technology design, where raw materials

enter at the top of the reactor and calcined products exit at the bottom, while the process CO<sub>2</sub> rises in a counter-flow against the raw materials, allowing for the recovery of thermal energy; the resulting CO<sub>2</sub>-rich gaseous stream is cooled and exits the top of the reactor.

The limestone is indirectly heated using fossil fuels, and the remaining emissions from heating can be captured using PCC technologies or oxy-fuel combustion [84]. This innovation looks very promising since it potentially requires minimal changes to the conventional processes involved in the lime industry. The LEILAC1 pilot was completed in 2019, and due to its success [82] the LEILAC2 project plans on scaling up to demonstration scale capturing 100 ktpa of CO<sub>2</sub> [85], while also considering less carbon intensive heat sources, i.e. biomass or electricity. Additionally, grid connectivity enables the potential for this technology to balance electricity demand, stabilising the grid during highly volatile periods [85].

#### 4.1.5. Oxy-fuel

Oxy-fuel technologies are here included as an example of pre-combustion CCS alternatives; combustion is performed with high purity O<sub>2</sub> from an Air Separation Unit (ASU) and produces a CO<sub>2</sub>-rich exhaust gas from the calcination process, enabling a CO<sub>2</sub> Purification Unit (CPU) to purify and compress the CO<sub>2</sub> stream ready for storage or use. Further benefits of this technology are a consequence of: 1) limited NO<sub>x</sub> formation in the O<sub>2</sub>/CO<sub>2</sub> environment, 2) a shorter flame length, 3) an improved flame stability with Flue Gas Recycle (FGR), and 4) increased radiative heat transfer due to higher concentrations of CO<sub>2</sub> and H<sub>2</sub>O [86]. On the other hand, retrofitting plants for oxy-fuel combustion would result in major modifications to key processing units, including the need for greater sealing [87]. These modifications require long shut-down periods affecting reliability of product supply and involve very high investment costs. This last aspect may be observed in Figure 6B, where the oxy-fuel combustion technology is applied to the lime industry via significant changes to the overall configuration together with the addition of a FGR [52]. Despite the expected high investment costs, very promising outcomes may be observed when oxy-fuel technology is coupled with the cement industry [88]; in fact, the oxy-fuel design showed the lowest CAC (33 €/t<sub>CO2</sub>) with the bulk of the cost associated with the ASU and CPU. Similarly, Gardarsdottir et al. [54] highlighted promising performance of the oxy-fuel process (CAC of 42 €/t<sub>CO2</sub>) when economically compared to MEA (CAC of 80 €/t<sub>CO2</sub>) and other CCS technologies, due to the lower variable operating costs and lower clinker cost. Eriksson et al. [88] used a process model to show that oxy-fuel combustion in lime kilns can produce a high-quality product with a lower specific energy demand. Similarly, Granados et al. [86] simulated oxy-fuel combustion in a lime rotary kiln, wherein their one-dimensional model showed improved heat and mass transfer rates

when incorporating low levels (<65%) of FGR, indicating that smaller kiln dimensions can be used to produce the same quantity of product. At 55% FGR the lime production could increase by 13% whilst maintaining baseline operating conditions and 98% conversion. However, there is a balance required between FGR rate and decarbonisation rate, as an increased  $\text{CO}_2$  partial pressure would hinder the conversion of  $\text{CaCO}_3$  to  $\text{CaO}$  [89].

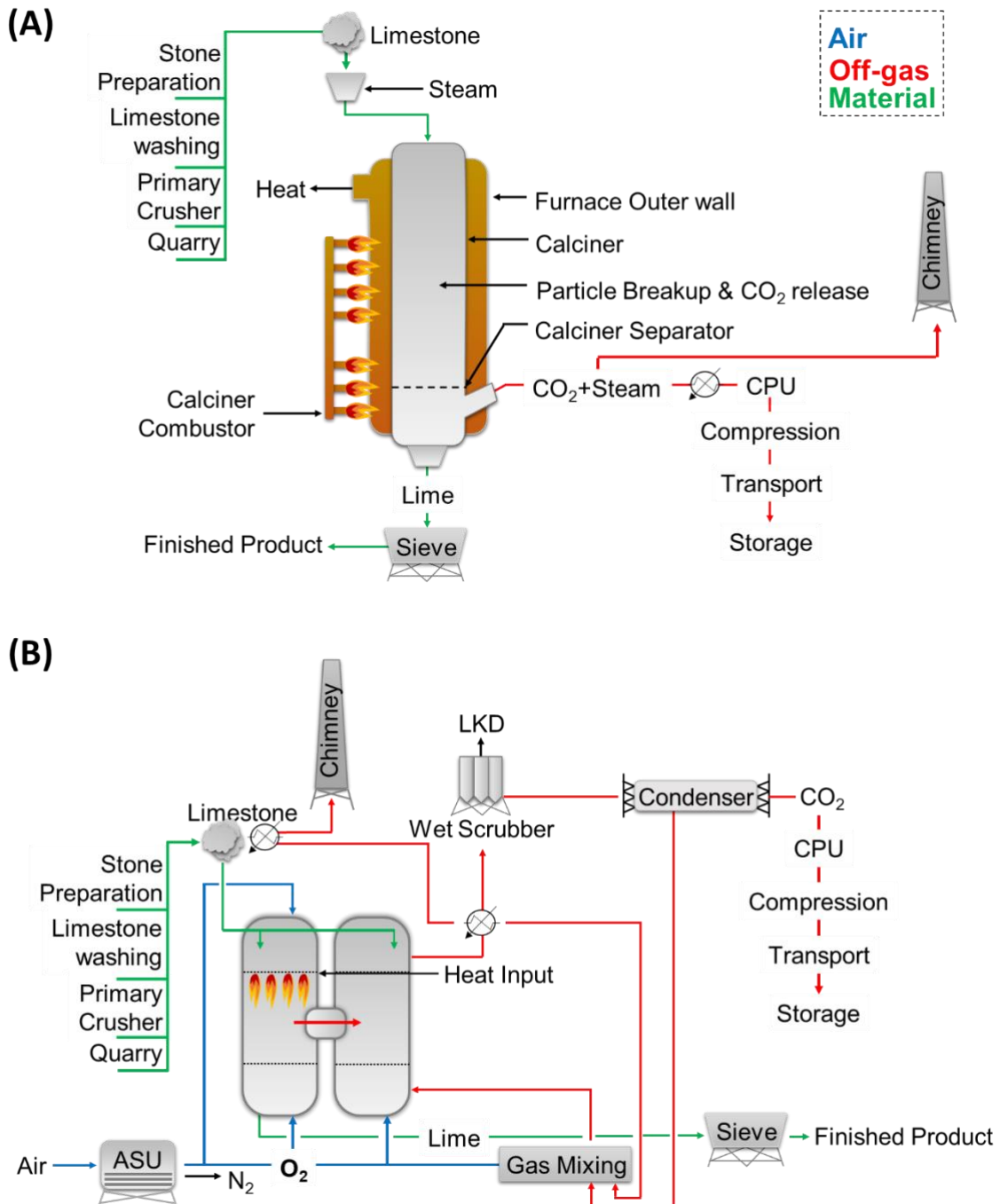
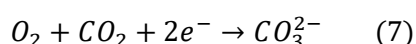
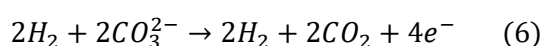


Figure 6.

#### 4.1.6. Fuel cells

High temperature fuel cells, such as Molten Carbonate Fuel Cells (MCFC) and Solid-Oxide Fuel Cells (SOFC), can convert the chemical energy of a fuel directly into electricity through electrochemical energy conversion processes [90]. The applicability of the single-cell MCFC technology to the cement manufacturing process was highlighted by Spinelli et al. [59] (23.9% of the total CO<sub>2</sub> captured at 1.21 GJ/t<sub>CO2</sub>); natural gas is fed to the anode (Equation 6), and the resulting electrical power (8e-) is used at the cathode to convert the off-gas CO<sub>2</sub> (post desulfurization) to CO<sub>3</sub><sup>2-</sup> (Equation 7).



Following this, CO<sub>3</sub><sup>2-</sup> permeates through the electrolyte solution towards the anode, where oxygen recombines with hydrogen to give water and CO<sub>2</sub> is regenerated. A CO<sub>2</sub>-rich stream leaves the anode towards a CO<sub>2</sub> separation unit (CSU), while a CO<sub>2</sub>-poor stream leaves the cathode and is emitted to the atmosphere upon heat recovery. Such a configuration can be considered for application to the lime manufacturing process. For demonstration, the LRK calcination unit considered in [59] is substituted with a PFRK (Figure 7A).

Despite the low capture rate, this technology offers the potential to generate electrical and heat energy that can be internally consumed or exported for profit. When using three fuel cells in series 69.9% of CO<sub>2</sub> emissions could be avoided, with a specific primary energy consumption of 0.9 GJ/tCO<sub>2</sub>; this incorporates the energy generated from the MCFC and Organic Rankine Cycle (ORC), as well as the energy demand from the CO<sub>2</sub> Separation Unit (CSU) and compression [59].

Hanak and Manovic [91] proposed a combined heat and power generation plant using SOFCs integrated with lime production, equipped with Direct Air Capture (DAC) of CO<sub>2</sub>; Figure 7B shows an overview of the poly-generation process proposed. The limestone is fed into the flash calciner, where the decomposition takes place at 900°C under pure CO<sub>2</sub> conditions, ensured by the action of the anodic chamber of the SOFC. The CO<sub>2</sub> produced at the anode (Equation 5) is split into two streams: one is recirculated at the top of the reformer and enters the anode together with the fuel, while the other is fed at the bottom of the flash calciner. Moreover, air and oxygen are also fed at the bottom of the flash calciner, passing through the cathode and a heat exchange unit, respectively. The rising CO<sub>2</sub>-rich stream at the top of the calciner undergoes heat recovery and water separation, while the calcined material is collected upon a series of heat recovery units for the pre-heating of the oxygen, air, and fuel. The heat recovered through the air leaving the cathode ensures a high CO<sub>2</sub> concentration (>90 vol.%) in the resulting gas stream, suitable for geological sequestration [92]. Despite the

high capital cost ( $\sim 850 \text{ €/kW}_{\text{ch}}$  with  $\text{kW}_{\text{ch}}$  identifying the chemical energy input) mainly due to the high cost of the fuel cell, this option may be considered economically feasible by considering the possibility of selling electricity, heat, lime, and potentially  $\text{CO}_2$ .

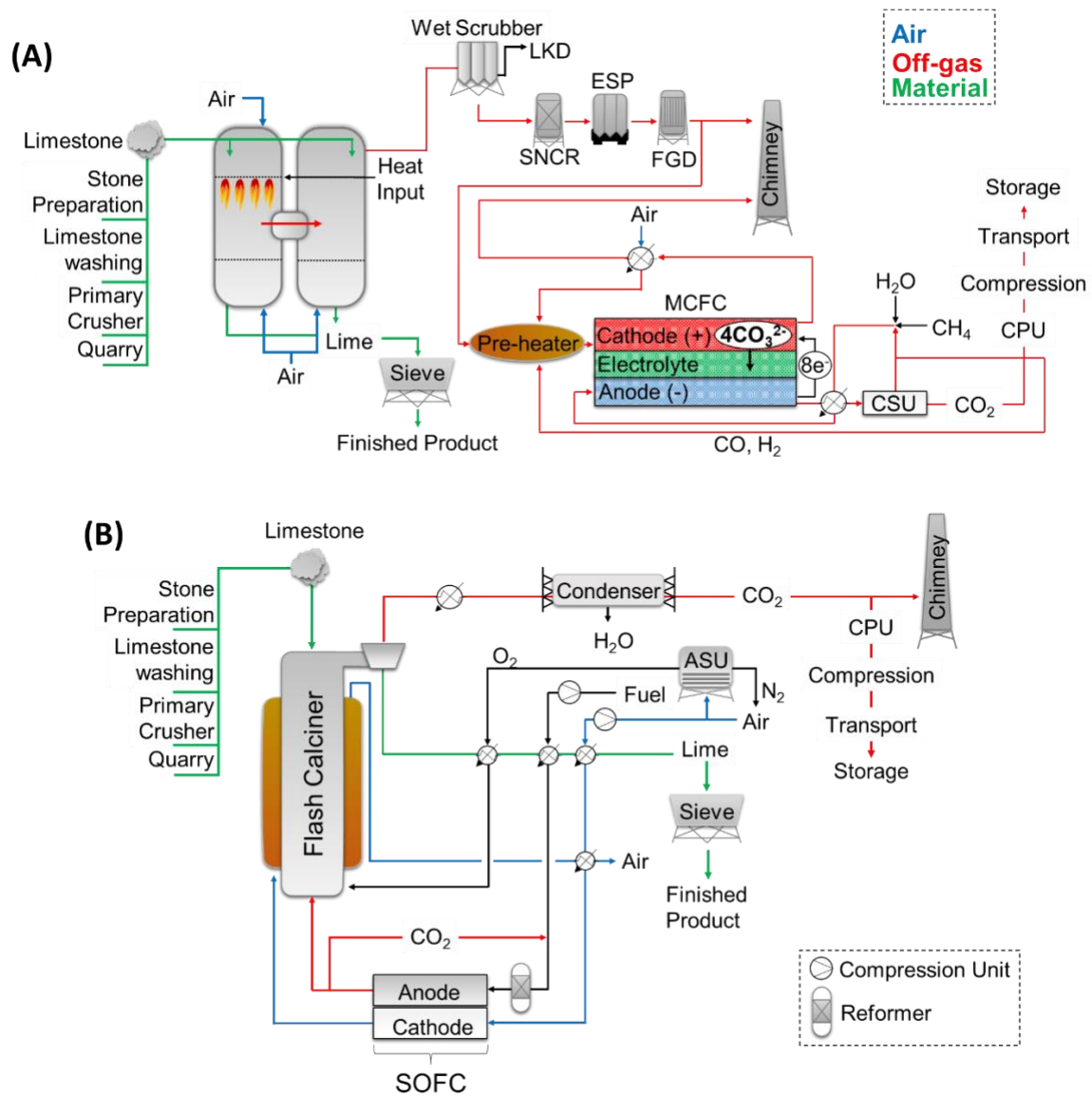


Figure 7.

#### 4.1.7. Calcium looping

Calcium Looping (CaL) is based on the reversible carbonation reaction from  $\text{CaO}$  to  $\text{CaCO}_3$  (Equation 1) and can be used either to remove  $\text{CO}_2$  from the tail-end of the process (Figure 8A) or integrated in the calcination step (Figure 8B), both based on [52].

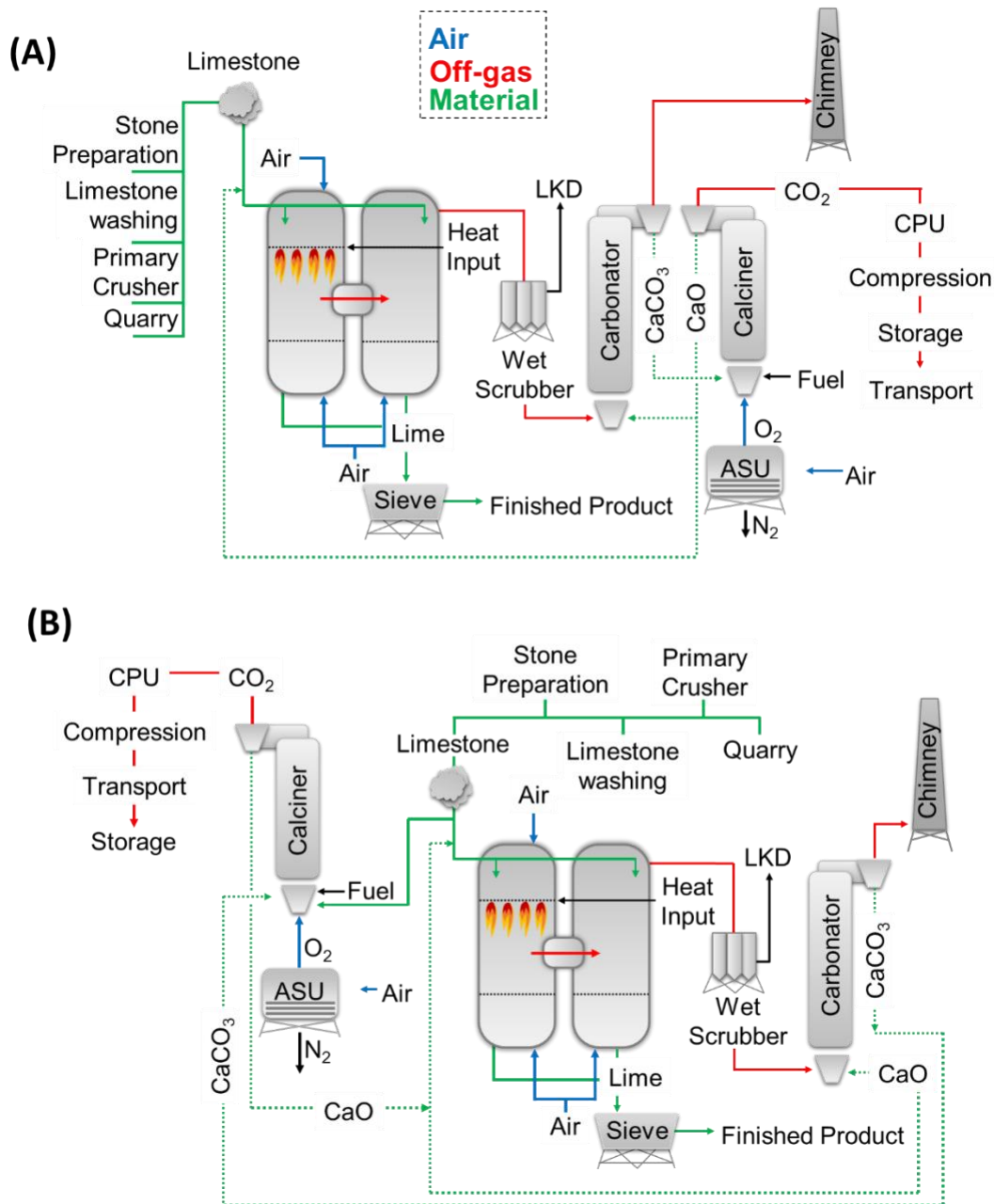


Figure 8.

Additional fuel is required for both configurations, and incorporation of oxy-fuel combustion can be used to produce a purer  $\text{CO}_2$  stream [50]. Both the configurations depicted here have been considered for cement industry by Voldsund et al. [52], highlighting lower energy demands (4.07 and 3.17  $\text{GJ}/\text{t}_{\text{CO}_2}$  for the tail-end and integrated design, respectively) compared to MEA-based capture, but still higher than for oxy-fuel combustion. In their subsequent study [54], the CAC for the tail-end and integrated configurations was reported to be 52 and 59  $\text{€}/\text{t}_{\text{CO}_2}$ , respectively, approximately 10  $\text{€}/\text{t}_{\text{CO}_2}$  more expensive than the oxy-fuel combustion process. However, the calcium looping design benefits from high grade waste heat used in a steam cycle, offsetting the higher CAPEX and greater consumption of fossil fuel. It is worth

noting that the effectiveness of calcium sorbents decreases with each cycle due to particle sintering during the high-temperature calcination step [93]. Such a disadvantage is mitigated with the integrated CaL process (Figure 8B), since certain proportions of fresh  $\text{CaCO}_3$  are fed into the calciner together with the looped  $\text{CaCO}_3$ . The cyclic performance of calcium looping can be improved by incorporating regeneration of deactivated sorbents, thermal pre-treatment, using enhanced synthetic sorbents, modification of precursors, doping and including inert matrices/supports [94].

Fantini [95] investigated the integrated CaL process applied to the cement manufacturing process, as part of the CLEAN clinKER (CLEANKER) project, where a slipstream from the Buzzi Unicem kiln at the Vernasca cement plant (Italy) is used for demonstration. The design allowed for a >90% capture of the process  $\text{CO}_2$  from limestone, with low specific energy demand (below 2 MJLHV/ $t_{\text{CO}_2}$ ) and CAC (below 30 €/ $t_{\text{CO}_2}$ ) [95]. Another industrial demonstration performed at Norcem's Brevik cement plant [96], using GE's RCC tail-end design, reported a higher specific energy demand (3.13 GJ/ $t_{\text{CO}_2}$ ) with respect to the RCC integrated cement production with oxy-fuel combustion (1.45 GJ/ $t_{\text{CO}_2}$ ). The study also highlighted the potential for indirect heating to mitigate the power consumption and cost of the ASU [96].

## 4.2. Fuel switching

Fuel combustion roughly accounts for the 40% of the total  $\text{CO}_2$  emissions from the calcination of limestone [1, 19] (as well as 60% of the overall production costs [18]). Therefore, fuel switching would lead to significant emission reductions from the calcination process, e.g., biomass, but the process  $\text{CO}_2$  produced would not be avoided.

Currently, the lime industry is mainly based on the combustion of fossil fuels, i.e. coal and natural gas [18]. In contrast, many countries already use Residue Derived Fuels (RDF) in cement kilns and municipal waste incinerators, with Germany achieving an over 60% replacement of the fossil-based fuels [97]. In these terms, the biogenic carbon embodied into the waste, not counting as a direct emission since derived from biological sources, is an important factor to consider when defining the overall carbon burden of the RDF used [97]. In contrast, the recent improvements in terms of Food Waste Recycling, for which the anaerobic digestion is recognised to be the most sustainable approach, led to a lower biogenic carbon sent to incinerators and therefore resulting in a heavier carbon impact of the RDF used [98]. Several key aspects must be considered to correctly utilise the waste fuel for limestone calcining. Firstly, solid or liquid fuels may be only used in certain kiln types, e.g. solid lumps are not suitable for a PFRK design [23]. The processing temperature may also affect the

feasibility of a certain waste fuel for a specific kiln; for instance, animal fat would solidify below 40°C, leading potentially to pipe-plugging [99].

Other crucial factors affecting the wide usage of waste fuel for limestone calcination are the calorific power and flame temperature. Calcination requires continuous burning conditions that cannot be met if the combustion of the fuel leads to a varying thermal energy, which may happen if the waste fuel used is not sufficiently homogeneous. The impurity content also needs to be precisely specified, given that 1) limestone and the process combustion atmosphere physically interact, and the properties of the resulting lime vary due to the uptake of impurities upon calcination, and 2) the burning of specific contaminants may require systems for their removal from the off gas if they cannot be emitted to atmosphere. Magnetic separation is usually used for the removal of metal fragments, whose content cannot exceed certain values in the calcined material. For these reasons, the suppliers of waste fuels need to ensure precise treatment to meet relevant regulations for safe industrial use. These pre-treatments often only involve the removal of sediments or water, but in some cases chemical processes are required to remove specific pollutants. However, the gasification of waste fuels is usually performed to achieve stable combustion and avoiding the emission of NO<sub>x</sub> and SO<sub>x</sub> [100].

Finally, an aspect which must not be underestimated is the availability of the waste, since 1) a production stand-by due to an interruption in fuel supply could lead to disadvantageous economic consequences, and 2) different wastes have different calorific power and physical forms (Table 4) [101], and the process might have to be adjusted accordingly, with evident technical difficulties.

Table 4.

<i>Waste Type</i>	<i>Calorific power (MJ/kg)</i>	<i>Physical form</i>
<i>Municipal Solid Waste (MSW)</i>	10.5	Refuse, yard, food, paper and paper-board waste.
<i>Sewage Sludge</i>	3.5	Solid, semi-solid and liquid waste removed during the treatment of municipal wastewater (sewage)
<i>Medical Waste</i>	13.9	General refuse (bedding, gauze, needles), food waste, plastics, chemicals.
<i>Industrial Hazardous Waste</i>	13.9	Liquids, semi-solids, tarry materials, sludge and solids
<i>Organic Fume</i>	1 - 23	Gaseous

Despite these difficulties, the lower cost of purchase (and potentially transport) of the waste fuel compared with fossil ones, and the lower carbon footprint attributed to the energy source, can make the use of waste fuel very attractive. The combustion of wastes as fuel may also help with landfill avoidance and to mitigate waste disposal issues, because the incineration of

waste leads to a 60-80% volume reduction with respect to the initial material [102], and the bottom and fly ashes resulting from the waste combustion may themselves represent a valuable material for construction purposes [103].

Another promising alternative to fossil fuels is renewable sources, which are expected to supply a significant portion of the European energy demand by 2050 [104]. Meier et al. [105] have also demonstrated the feasibility of a solar energy-powered rotary kiln for the production of sustainable quicklime. The configuration, consisting of a multi-tube reaction chamber made from high-temperature SiC panels, allowed for a 20% CO<sub>2</sub> emissions reduction with respect to fossil fuels. The thermal calcination allowed for an overall 30 – 35% efficiency, comparable with the modern devices (Table 2), but the price of the calcined quicklime was about 2 – 3 times higher than the conventionally produced one. Recently, promising results were also obtained by Abanades et al. [89] with a Concentrated Solar Thermal (CST) technology, outlining several advantages such as no contamination from combustion, in an LRK configuration. The latest advancements have also raised other potential alternatives to fossil fuels, such as Thermal Plasma (TP) energy, obtained by passing an electric current through a gas and leading to the formation of free ions and radicals [106], and E-fuels, produced by reacting CO<sub>2</sub> (captured from the atmosphere) with sustainable hydrogen.

Hydrogen is expected to play a crucial role for the green energy transition by 2050, given the high calorific power and the potentially net-zero emissions arising from its combustion. Hydrogen can be distinguished in blue, green, and grey hydrogen, depending on how sustainable the production route is [107]. “Grey” hydrogen arises from natural gas through reforming, with lower emissions with respect to coal, and when the resulting CO<sub>2</sub> is captured and safely stored, making the overall process carbon-neutral, the hydrogen is labelled as “blue”. Finally, “green” hydrogen is completely carbon-neutral, since the electrolysis of water is promoted by sustainable sources. Apart from the widely known safety issues, the high water vapour partial pressure in the lime kiln, resulting from the combustion of hydrogen, might represent a problem in terms corrosion, i.e. acid formation/condensation [108].

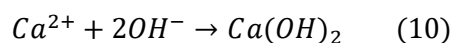
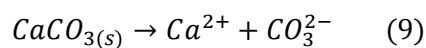
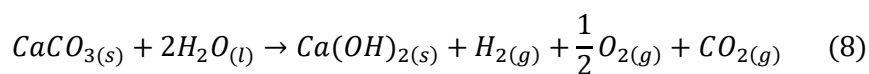
### 4.3. Alternative production routes

The thermal calcination of CaCO<sub>3</sub> is still generally considered to be unavoidable for industrial-scale lime production, and therefore higher-technology readiness level (TRL) research has focused on capturing CO<sub>2</sub> via post- and pre-combustion CCS technologies. However, major challenges need to be overcome in order to successfully apply CCS technologies to industries where the calcination of CaCO<sub>3</sub> represents a key processing step.

In the next sections, we will be exploring novel (lower-TRL) routes for the synthesis of  $\text{Ca(OH)}_2$  that avoid the thermal treatment of  $\text{CaCO}_3$ . The first alternative involves an electrochemical synthesis of  $\text{Ca(OH)}_2$  from  $\text{CaCO}_3$ , with simultaneous production of  $\text{O}_2/\text{CO}_2$  and  $\text{H}_2$  gases; although the process  $\text{CO}_2$  would still be emitted as a gas, the high volumetric concentration would ease its separation from the remaining gases in a CCS process, potentially resulting in a more affordable process. The second alternative route involves a room-temperature liquid-solid reaction between  $\text{CaCO}_3$  and  $\text{NaOH}$  solutions to give the products  $\text{Ca(OH)}_2$  and  $\text{Na}_2\text{CO}_3 \cdot x\text{H}_2\text{O}$  ( $x = 0, 1$ ). In other words, the process  $\text{CO}_2$  from  $\text{CaCO}_3$  would be sequestered in a stable mineral form ( $\text{Na}_2\text{CO}_3 \cdot x\text{H}_2\text{O}$ ), leading to a potential zero-emissions slaked lime production, although the carbon burden linked to  $\text{NaOH}$  usage still needs to be considered in order to assess the environmental impact of the process. Since both the alternative routes mainly rely on electrical power, to be discussed below, the carbon footprint attributed to the generation of electricity will play a key role in determining their sustainability. It is also worth noting that calcination-free production of calcium hydroxide from alkaline waste (e.g., fly ashes and slags) at sub-boiling temperatures has also been developed [109]; however, these sources are in limited supply compared to  $\text{CaCO}_3$  and are being phased out.

### 4.3.1. Electrochemical decarbonisation of $\text{CaCO}_3$

An electrochemical decarbonisation of  $\text{CaCO}_3$  was presented by Ellis et al. [44], who used a water electrolyser and proper chemical reactor to convert  $\text{CaCO}_3$  to  $\text{Ca(OH)}_2$ , under potentiostatic conditions (cell voltage 2.5 V, current 6 mA). The maximum yield (coulombic efficiency) was calculated by considering the molar stoichiometry depicted in Equation 8, and it was assessed to be 0.85. The semi-reactions occurring at the anode and cathode are reported as Equations 9 and 10, respectively.



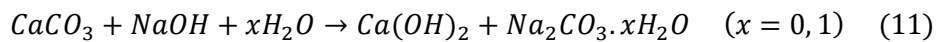
Since 1 mole of  $\text{H}_2$  is produced for each mole of  $\text{CaCO}_3$  initially fed, a large portion of the total energy demand might be fulfilled in situ; this aspect must be clearly assessed, given that it could make the process even more attractive from an industrial point of view.

Although the process  $\text{CO}_2$  could not be avoided, the authors [44] also outlined promising applications allowing for its recovery, together with the co-generated  $\text{O}_2$  and  $\text{H}_2$ . For example, the  $\text{O}_2/\text{CO}_2$  gaseous stream resulting from the anode (67 vol.% $\text{CO}_2$ ) may be applied via oxy-

fuel technology in a conventional lime manufacturing process, leading to lower energy consumptions and NO<sub>x</sub> emissions, as outlined in Section 2.1.6. Such an application would lead to an exhaust kiln gas that is highly concentrated in CO<sub>2</sub>, enabling significant efficiency improvements of the eventual CCS process. Alternatively, those gases could be used to power a SOFC [110], generating electrical energy that is required in other process steps such as mixing and grinding. As a further consequence, the O<sub>2</sub>/CO<sub>2</sub> gas stream would be further enriched in CO<sub>2</sub>, facilitating the separation and compression steps. Although the authors [44] focussed on the potential for cement production, the electrochemical decarbonisation of CaCO<sub>3</sub> also fits the process specifics of the lime industry.

### 4.3.2. Chemical Decarbonisation of CaCO<sub>3</sub>

Another non-combustion route to decarbonisation of CaCO<sub>3</sub> was firstly introduced by Hanein et al. [45], involving the reaction between solid CaCO<sub>3</sub> and NaOH solutions at atmospheric conditions and varying concentrations; the key reaction is reported in Equation 11.



This alternative decarbonisation of CaCO<sub>3</sub> avoids both the fuel and process CO<sub>2</sub> emissions, since no combustion would be required. The CO<sub>2</sub> from CaCO<sub>3</sub> would also be sequestered in a stable mineral form (Na<sub>2</sub>CO<sub>3</sub>/Na<sub>2</sub>CO<sub>3</sub>·H<sub>2</sub>O), and Ca(OH)<sub>2</sub> produced simultaneously in a single step, rather than via CaO. In addition, no additional treatments of CO<sub>2</sub> compression, transport and storage would be required, since most of the CO<sub>2</sub> involved in the process would be solidified as Na<sub>2</sub>CO<sub>3</sub>·xH<sub>2</sub>O. The relatively simple reaction setup offers promising scope for eventual up-scaling, based upon achievement of the highest conversion efficiency (96%) linked to the optimal (CaCO<sub>3</sub>:NaOH:H<sub>2</sub>O) mix design [45]. This alternative route is still at a laboratory level, and an overall reassessment of the markets of Ca(OH)<sub>2</sub> [111], Na<sub>2</sub>CO<sub>3</sub> [112] and NaOH [113] must be achieved for the route to succeed in substituting the calcination of CaCO<sub>3</sub>. Also, it must be mentioned that the chlor-alkali process necessary for the supply of NaOH [114] is currently a carbon-intensive process, since 0.78 tonne of CO<sub>2</sub> per tonne NaOH, if fossil fuels are used in its production [115]. The co-generation of H<sub>2</sub> was already included in the energetic calculation. Therefore, a pre-requisite for feasibility of a “low-carbon” classification for this alternative route to the production of slaked lime will be low emissions from the NaOH industry, which is strongly expected to cut the emissions by using renewable electricity [116] for the sustainment of the chlor-alkali process.

## 5. Concluding remarks and recommendations

The environmental burden attributed to the lime industry is mainly related to the thermal calcination of  $\text{CaCO}_3$  to give  $\text{CO}_2$  that may be distinguished by the nature of its origin: process  $\text{CO}_2$  embodied in  $\text{CaCO}_3$  and released upon thermal degradation (~68%), fuel combustion  $\text{CO}_2$  (~30%), and  $\text{CO}_2$  arising from electricity consumption (~2%). To date, consistent results have been achieved to limit the emissions from the combustion process itself, for instance by design optimisation and process efficiency, to minimise energy wastage, and/or by using alternative fuels with a lower carbon footprint. Despite this, the process  $\text{CO}_2$  remains the main challenge we face to effectively reduce the emissions, as long as the thermal decarbonisation of  $\text{CaCO}_3$  is viewed as the only practical option to obtain  $\text{CaO}$ . In these terms, the application of CCS technologies to treat the arising off-gas stream is considered the best option towards a decarbonised lime industry, but further optimisation is required. If only the CAC and  $\text{CO}_2$  capture rate were to be considered, the Oxy-fuel technology would represent the best option to develop. Despite the Horizon 2020 CEMCAP included Oxy-fuel among those CCS technologies with high potential in retro-fitting [117], its adaptation to the existing lime plants appears unlikely in a short-to-mid-term scenario. In fact, the very high capital costs discourage the prompt dismantling of the state-of-the-art lime plants, whose typical lifetime is between 30-50 years [117]. For this reason, the MEA absorption process is still outcompeting all the other configurations, representing the most solid route with no requirements for design change of the existing plants. The high energy demand required for the regeneration of the solvent requires a strong implementation of the technology, which could consider 1) other solvents with more convenient regeneration conditions or 2) the use of renewable sources and optimised heat recovery from the kiln to minimise the carbon burden linked to the combustion of fuels required for the regeneration step. These obstacles are pushing towards the implementation of the other designs described above, among which the membrane separation and solid adsorption. A high potential is associated with the former option, which has been positively tested for industrial sources with higher (steel) and comparable (cement)  $\text{CO}_2$  concentrations in the off-gas stream, with respect to the lime process. No direct sources for the lime production route could be found, suggesting that a specific case-study should be done in order to test the feasibility for the industry in exam here. The solid adsorption represents a valid alternative to the similarly structured MEA process, given the lower energy required for the regeneration of the adsorbent. Although, the handling of the solids represents an additional energy expenditure, which must be considered by also looking at the service life of the adsorbent, shortened by events of sintering occurring at multiple cycles of regeneration. The same issues can be found for Ca-looping, which offers a valid and retro-fittable alternative for a sustainable lime production, but that still needs to overcome the technical issues linked to a

relatively short service life of the looped  $\text{CaCO}_3/\text{CaO}$  upon sintering and decreasing of the reactive surface. The use of fuel cells also looks promising, given the lowest energy demand detectable among the solutions considered, but the low capture rate requires a series of MFCs for an effective  $\text{CO}_2$  removal. That would increase both the initial investments and the maintenance costs associated with the multiple devices required. Said that, particular attention must be paid prior feeding the flue gas to the fuel cell, in order to avoid issues linked to a high temperature and the presence of foreign species lowering the efficiency and service time of the device.

Consistent investments are required to ease the application of targeted CCS technologies on a short-term basis, whereas the current trend would only allow for a gradual transition towards novel designs. Specifically for the lime industry, more specific pilot-scale research is expected, in order to not rely on the similarities with the cement manufacturing process.

Further possibilities were recently inspired by two independent studies by Ellis et al. [44] and Hanein et al. [45], who conceptualised innovative alternative routes for a no-combustion decarbonisation of  $\text{CaCO}_3$ . Both lines of investigation inspire new points of view on the matter, since the avoidance of the thermal calcination of  $\text{CaCO}_3$  has not previously been demonstrated in a scalable manner, and both processes could allow production of  $\text{H}_2$  as by-product (depending on system boundaries). Both the alternatives may have the potential to influence the future lime and cement supply chain, if deeply investigated and fully scaled-up. Realistically, a total transition towards a no-combustion lime production is strongly unlikely, even from a long-term point of view, but these alternatives might eventually provide a valid alternative for a partial supply of the lime market. While the eventual feasibility of the electrochemical route mainly relies on the cost of electricity, the chemical alternative also depends on other industrial realities, such as soda ash and caustic soda, whose demands would need to be adjusted accordingly. Specifically, an increased caustic soda production will be required to sustain the process, whereas the co-production of sodium carbonate should be translated in a re-sizing of the conventional Solvay manufacturing route. All these assumptions make the evaluation of these alternatives challenging, and it requires the concerted transition of both industrial and energetic markets. However, the further implementation of alternative fuels will be the baseline for the realistic application of the most CCS technologies discussed and will also sustain the novel no-combustion approaches presented here.

This review highlights the potential for alternative approaches to the standard lime manufacturing process, mainly regarding the aspect of the process  $\text{CO}_2$ . A powerful hint has been offered to the scientific community, which is now called upon to prove the techno-economic feasibility of alternative decarbonisation processes, potentially allowing for a net-

zero emissions lime industry. Lime is also a well-known absorbent of CO<sub>2</sub> (as discussed in Sections 1 and 4.1.7); therefore, the no-carbon production of lime can enable carbon neutrality of other hard-to-abate sectors. This is a window of opportunity for the lime industry, as its livelihood may be threatened suddenly if high-temperature kilns, as we know them, are required (by legislation or by societal pressure) to be phased out to reduce impacts of global climate change.

## Captions (in order of appearance)

**Table 1.** Average composition of the exhaust gases from lime and cement kilns.

**Table 2.** Ranges of efficiency  $\eta$ (%), CO<sub>2</sub> emission factor, daily production and optimal feed grain size for the main kiln types used in the EU-27: Parallel Flow Regenerative Kilns (PFRK), Annular Shaft Kilns (ASK), Mixed Feed Shaft Kilns (MFSK), Rotary Kilns with Preheater (PRK), and Long Rotary Kilns (LRK).

**Fig. 1.** Schematic overview of a PFRK (A), ASK (B) and MFSK (C) including the fluxes of the solids and gases involved, along with the temperature profile for the vertical section of the kiln. The black-pattern and light-grey circles denote CaCO<sub>3</sub> and CaO, respectively.

**Fig. 2.** Schematic overview of a LRK (A, top) and PRK (B, bottom) design, including the fluxes of the solids and gases involved, along with the temperature profile throughout the section of the kiln. The black-pattern and light-grey circles denote CaCO<sub>3</sub> and CaO, respectively.

**Table 3.** Overview of the specific energy demand and CAC (where available) for each CO<sub>2</sub> capture technology discussed in section 4.1.

**Fig. 3.** Conceptual design of amine absorption CO<sub>2</sub> capture considered for lime kiln exhaust (A), and of a CO<sub>2</sub> solid sorption process considered for lime kiln exhaust (B), based on RTI and Norcem's cement pilot plant.

**Fig. 4.** Conceptual design of a membrane CO<sub>2</sub> capture considered for lime kiln exhaust, based on Norcem's pilot plant.

**Fig. 5.** Conceptual design of Svante's Veloxotherm™ RAM technology considered for lime kiln exhaust.

**Fig. 6.** Design of Calix's Direct Separation (DS) technology (A), and conceptual design of the Oxy-Fuel technology considered for lime kiln exhaust (B), using a PFRK calcination unit instead of the LRK in that study.

**Fig. 7.** Conceptual design of the MCFC considered for lime kiln exhaust (A), and Lime production integrating waste heat from SOFCs for DAC (B).

**Fig. 8.** Conceptual design of the Tail-end CaL (A) and Integrated CaL (B) technology considered for lime kiln exhaust.

**Table 4.** Calorific power (MJ/kg) and physical form of the most used waste for combustion worldwide.

## Acknowledgements

This work was funded by the Engineering and Physical Science Research Council (EPSRC; EP/R025959/1) and CEMEX. The authors would also like to acknowledge the support of the EPSRC Centre for Doctoral Training in Carbon Capture and Storage and Cleaner Fossil Energy (EP/L016362/1).

## Author's Contribution

Marco Simoni and Mathew D. Wilkes drafted the original manuscript. Theodore Hanein, Hajime Kinoshita, John L. Provis, and Solomon Brown acquired funding, and supervised Marco Simoni and Mathew D. Wilkes. Theodore Hanein, Hajime Kinoshita, John Provis, and Solomon Brown reviewed and edited the manuscript.

## Conflicts of interest

The authors declare that they have no competing interests as defined by Renewable & Sustainable Energy Reviews, or other interests that might be perceived to influence the interpretation of the article.

## References

1. Dowling, A., J. O'Dwyer, and C.C. Adley, *Lime in the limelight*. *Journal of cleaner production*, 2015. 92: p. 13-22.
2. Schneider, M., et al., *Sustainable cement production—present and future*. *Cement and Concrete Research*, 2011. 41(7): p. 642-650.
3. Criado, Y.A., et al., *Experimental investigation and model validation of a CaO/Ca(OH)<sub>2</sub> fluidized bed reactor for thermochemical energy storage applications*. *Chemical Engineering Journal*, 2017. 313: p. 1194-1205.
4. de Vet, J.-M., et al., *Competitiveness of the European Cement and Lime Sectors*. *WIFO Studies*, 2018.
5. Forsido, T., et al., *Neutralisation of acid effluent from steel manufacturing industry and removal of metals using an integrated electric arc furnace dust slag/lime process*. *SN Applied Sciences*, 2019. 1(12): p. 1-6.
6. Ventolà, L., et al., *Traditional organic additives improve lime mortars: New old materials for restoration and building natural stone fabrics*. *Construction and Building Materials*, 2011. 25(8): p. 3313-3318.
7. Locat, J., H. Trembaly, and S. Leroueil, *Mechanical and hydraulic behaviour of a soft inorganic clay treated with lime*. *Canadian geotechnical journal*, 1996. 33(4): p. 654-669.
8. Greenleaf, J.E., J.c. Lin, and A.K. Sengupta, *Two novel applications of ion exchange fibers: Arsenic removal and chemical-free softening of hard water*. *Environmental Progress*, 2006. 25(4): p. 300-311.
9. García-Martínez, J., et al., *SO<sub>2</sub> retention at low temperatures by Ca (OH)<sub>2</sub>-derived CaO: a model for CaO regeneration*. *Fuel*, 2002. 81(3): p. 305-313.
10. Pakrasi, A., et al., *A combined Ca (OH)<sub>2</sub>/NH<sub>3</sub> flue gas desulfurization process for high sulfur coal: results of a pilot plant study*. *Journal of the Air & Waste Management Association*, 1990. 40(7): p. 987-992.
11. Ridha, F.N., et al., *Enhanced CO<sub>2</sub> capture by biomass-templated Ca (OH)<sub>2</sub>-based pellets*. *Chemical Engineering Journal*, 2015. 274: p. 69-75.
12. Grabow, W.O., I.G. Middendorff, and N.C. Basson, *Role of lime treatment in the removal of bacteria, enteric viruses, and coliphages in a wastewater reclamation plant*. *Applied and environmental microbiology*, 1978. 35(4): p. 663-669.
13. Liu, Z., et al., *Isolation and cationization of hemicelluloses from pre-hydrolysis liquor of kraft-based dissolving pulp production process*. *Biomass and Bioenergy*, 2011. 35(5): p. 1789-1796.
14. Skocek, J., M. Zajac, and M. Ben Haha, *Carbon capture and utilization by mineralization of cement pastes derived from recycled concrete*. *Scientific Reports*, 2020. 10(1): p. 1-12.
15. Oates, T., *Lime and limestone*. *Kirk-Othmer Encyclopedia of Chemical Technology*, 2000.
16. Oates, J.A.H., *Lime and limestone: chemistry and technology, production and uses*. 2008: John Wiley & Sons.
17. JRC Reference Report, E.-D.G. *Reference document on BAT in the cement and lime manufacturing industries*. 2007.
18. Schorcht, F., et al., *Best available techniques (BAT) reference document for the production of cement, lime and magnesium oxide*. *European Commission Joint Research Centre Institute for Prospective Technological Studies (Report EUR 26129 EN)*. Luxembourg: Publications Office of the European Union, 2013.
19. Stork, M., et al., *A competitive and efficient lime industry*. *Teknisk rapport*, European Lime Association, 2014.
20. Popp, D., *International innovation and diffusion of air pollution control technologies: the effects of NO<sub>x</sub> and SO<sub>2</sub> regulation in the US, Japan, and Germany*. *Journal of Environmental Economics and Management*, 2006. 51(1): p. 46-71.
21. Schreiber Jr, R.J., C.O. Russell, and J. Evers, *Evaluation of Suitability of Selective Catalytic Reduction and Selective Non-Catalytic Reduction for Use in Portland Cement Industry*. submitted by the Portland Cement Association to the Ozone Transport Commission in, 2006.
22. Stanmore, B.R. and P. Gilot, *calcination and carbonation of limestone during thermal cycling for CO<sub>2</sub> sequestration*. *Fuel processing technology*, 2005. 86(16): p. 1707-1743.
23. Piringer, H., *Lime shaft kilns*. *Energy Procedia*, 2017. 120: p. 75-95.

24. Senegačnik, A., J. Oman, and B. Širok, Analysis of calcination parameters and the temperature profile in an annular shaft kiln. Part 2: Results of tests. *Applied Thermal Engineering*, 2007. 27(8-9): p. 1473-1482.
25. Senegačnik, A., J. Oman, and B. Širok, Annular shaft kiln for lime burning with kiln gas recirculation. *Applied thermal engineering*, 2008. 28(7): p. 785-792.
26. Duan, S., B. Li, and W. Rong, Study on Gas-Solid Heat Transfer and Decomposition Reaction of Calcination Process in an Annular Shaft Kiln Based on the Finite Volume Method. *Processes*, 2022. 10(4): p. 648.
27. Mintus, F., S. Hamel, and W. Krumm, Wet process rotary cement kilns: modeling and simulation. *Clean Technologies and Environmental Policy*, 2006. 8(2): p. 112-122.
28. Atmaca, A. and R. Yumrutaş, Analysis of the parameters affecting energy consumption of a rotary kiln in cement industry. *Applied Thermal Engineering*, 2014. 66(1-2): p. 435-444.
29. Lebas, E., et al., Experimental study of residence time, particle movement and bed depth profile in rotary kilns. *The Canadian Journal of Chemical Engineering*, 1995. 73(2): p. 173-180.
30. Boateng, A.A., *Rotary kilns: transport phenomena and transport processes*. 2015: Butterworth-Heinemann.
31. Hanein, T., F.P. Glasser, and M.N. Bannerman, One-dimensional steady-state thermal model for rotary kilns used in the manufacture of cement. *Advances in Applied Ceramics*, 2017. 116(4): p. 207-215.
32. Mujumdar, K.S., et al., Rotary Cement Kiln Simulator (RoCKS): Integrated modeling of pre-heater, calciner, kiln and clinker cooler. *Chemical Engineering Science*, 2007. 62(9): p. 2590-2607.
33. Newman, J. and B.S. Choo, *Advanced concrete technology set*. 2003: Elsevier.
34. Andrew, R.M., *Global CO<sub>2</sub> emissions from cement production*. *Earth System Science Data*, 2018. 10(1): p. 195-217.
35. Taylor, H.F.W., *Cement Chemistry - 2nd Edition*. 1997.
36. Madlool, N.A., et al., A critical review on energy use and savings in the cement industries. *Renewable and sustainable energy reviews*, 2011. 15(4): p. 2042-2060.
37. SCHAUB. Dry Lime Hydration Plant - Technical Information, [https://www.schaubsystems.com/fileadmin/redaktion/downloads/Produktinformationen/SCHAUB\\_TL\\_Lime\\_hydration\\_plant\\_EN\\_-\\_FO\\_01.pdf](https://www.schaubsystems.com/fileadmin/redaktion/downloads/Produktinformationen/SCHAUB_TL_Lime_hydration_plant_EN_-_FO_01.pdf)
38. Chemical, N.L.A.-T.v.2007, [https://www.lime.org/documents/publications/free\\_downloads/fact-properties2007rev.pdf](https://www.lime.org/documents/publications/free_downloads/fact-properties2007rev.pdf)
39. Hassibi, M. An overview of lime slaking and factors that affect the process, *3rd International Sorbalit Symposium, New Orleans, November, 1999*, (pp. 1-20)
40. Nikulshina, V., M.E. Galvez, and A. Steinfeld, Kinetic analysis of the carbonation reactions for the capture of CO<sub>2</sub> from air via the Ca(OH)<sub>2</sub>-CaCO<sub>3</sub>-CaO solar thermochemical cycle. *Chemical Engineering Journal*, 2007. 129(1-3): p. 75-83.
41. Blamey, J., et al., The calcium looping cycle for large-scale CO<sub>2</sub> capture. *Progress in Energy and Combustion Science*, 2010. 36(2): p. 260-279.
42. Francey, S., H. Tran, and N. Berglin, Global survey on lime kiln operation, energy consumption, and alternative fuel usage. *TAPPI journal*, 2011. 19(8): p. 19-26.
43. Leeson, D., et al., A Techno-economic analysis and systematic review of carbon capture and storage (CCS) applied to the iron and steel, cement, oil refining and pulp and paper industries, as well as other high purity sources. *International Journal of Greenhouse Gas Control*, 2017. 61: p. 71-84.
44. Ellis, L.D., et al., Toward electrochemical synthesis of cement—An electrolyzer-based process for decarbonating CaCO<sub>3</sub> while producing useful gas streams. *Proceedings of the National Academy of Sciences*, 2020. 117(23): p. 12584-12591.
45. Hanein, T., et al., Decarbonisation of calcium carbonate at atmospheric temperatures and pressures, with simultaneous CO<sub>2</sub> capture, through production of sodium carbonate. *Energy & Environmental Science*, 2021.
46. Choi, A.J., et al., Process design and optimization of MEA-based CO<sub>2</sub> capture processes for non-power industries. *Energy*, 2019. 185: p. 971-980.
47. Bui, M., et al., Carbon capture and storage (CCS): the way forward. *Energy & Environmental Science*, 2018. 11(5): p. 1062-1176.
48. Liu, H., C. Consoli, and A. Zapantis. Overview of Carbon Capture and Storage (CCS) Facilities Globally.
49. Iea, U., *Technology Roadmap Carbon Capture and Storage in Industrial Applications*. International Energy Agency, United Nations Industrial Development Organizations, 2011.

50. Plaza, M.G., S. Martínez, and F. Rubiera, *CO<sub>2</sub> Capture, Use, and Storage in the Cement Industry: State of the Art and Expectations*. *Energies*, 2020. 13(21): p. 5692.
51. Naranjo, M., D.T. Brownlow, and A. Garza, *CO<sub>2</sub> capture and sequestration in the cement industry*. *Energy Procedia*, 2011. 4: p. 2716-2723.
52. Voldsund, M., et al., *Comparison of Technologies for CO<sub>2</sub> Capture from Cement Production—Part 1: Technical Evaluation*. *Energies*, 2019. 12(3): p. 559.
53. European Cement Research Academy, *CCS Project: Report on Phase IV.A*. 2016, Duesseldorf, Germany, [https://ecraonline.org/fileadmin/redaktion/files/pdf/ECRA\\_Technical\\_Report\\_CCS\\_Phase\\_IV\\_A.pdf](https://ecraonline.org/fileadmin/redaktion/files/pdf/ECRA_Technical_Report_CCS_Phase_IV_A.pdf)
54. Gardarsdottir, S.O., et al., *Comparison of Technologies for CO<sub>2</sub> Capture from Cement Production—Part 2: Cost Analysis*. *Energies*, 2019. 12(3): p. 542.
55. Nelson, T.O., et al., *RTI's Solid Sorbent-Based CO<sub>2</sub> Capture Process: Technical and Economic Lessons Learned for Application in Coal-fired, NGCC, and Cement Plants*. *Energy Procedia*, 2017. 114: p. 2506-2524.
56. Hägg, B., et al., *Pilot Demonstration-reporting on CO<sub>2</sub> Capture from a Cement Plant Using Hollow Fiber Process*. *Energy Procedia*, 2017. 114: p. 6150-6165.
57. Santos, M.P.S., V. Manovic, and D.P. Hanak, *Unlocking the potential of pulp and paper industry to achieve carbon-negative emissions via calcium looping retrofit*. *Journal of Cleaner Production*, 2021. 280: p. 124431.
58. Knudsen, J.N., et al., *Pilot plant demonstration of CO<sub>2</sub> capture from cement plant with advanced amine technology*. *Energy Procedia*, 2014. 63: p. 6464-6475.
59. Spinelli, M., et al., *Application of Molten Carbonate Fuel Cells in Cement Plants for CO<sub>2</sub> Capture and Clean Power Generation*. *Energy Procedia*, 2014. 63: p. 6517-6526.
60. Rubin, E.S., et al., *A proposed methodology for CO<sub>2</sub> capture and storage cost estimates*. *International Journal of Greenhouse Gas Control*, 2013. 17: p. 488-503.
61. Rubin, E.S., *Understanding the pitfalls of CCS cost estimates*. *International Journal of Greenhouse Gas Control*, 2012. 10: p. 181-190.
62. DNV.GL, P.B., *Industrial Decarbonisation & Energy Efficiency Roadmaps to 2050 - Cement*. 2015, [https://assets.publishing.service.gov.uk/government/uploads/system/uploads/attachment\\_data/file/416674/Cement\\_Report.pdf](https://assets.publishing.service.gov.uk/government/uploads/system/uploads/attachment_data/file/416674/Cement_Report.pdf)
63. Kherbouche, F., et al., *Study of a new electrostatic precipitator with asymmetrical wire-to-cylinder configuration for cement particles collection*. *Journal of Electrostatics*, 2016. 83: p. 7-15.
64. Porter, R.T.J., et al., *The range and level of impurities in CO<sub>2</sub> streams from different carbon capture sources*. *International Journal of Greenhouse Gas Control*, 2015. 36: p. 161-174.
65. Murrieta-Guevara, F., E. Rebolledo-Libreros, and A. Trejo, *Gas solubilities of carbon dioxide and hydrogen sulfide in sulfolane and its mixtures with alkanolamines*. *Fluid phase equilibria*, 1989. 53: p. 1-6.
66. Fine, N.A. and G.T. Rochelle, *Absorption of nitrogen oxides in aqueous amines*. *Energy Procedia*, 2014. 63: p. 830-847.
67. Zoannou, K.-S., D.J. Sapsford, and A.J. Griffiths, *Thermal degradation of monoethanolamine and its effect on CO<sub>2</sub> capture capacity*. *International Journal of Greenhouse Gas Control*, 2013. 17: p. 423-430.
68. Lv, B., et al., *Mechanisms of CO<sub>2</sub> capture into monoethanolamine solution with different CO<sub>2</sub> loading during the absorption/desorption processes*. *Environmental science & technology*, 2015. 49(17): p. 10728-10735.
69. Rochelle, G.T., *Conventional amine scrubbing for CO<sub>2</sub> capture, in Absorption-based post-combustion capture of carbon dioxide*. 2016, Elsevier. p. 35-67.
70. Idem, R., et al., *Pilot plant studies of the CO<sub>2</sub> capture performance of aqueous MEA and mixed MEA/MDEA solvents at the University of Regina CO<sub>2</sub> capture technology development plant and the boundary dam CO<sub>2</sub> capture demonstration plant*. *Industrial & engineering chemistry research*, 2006. 45(8): p. 2414-2420.
71. IEAGHG, *Techno-Economic Evaluation of Retrofitting CCS in a Market Pulp Mill and an integrated Pulp and Board Mill*. 2016: Gloucestershire, England.
72. Nelson, T.O., et al., *Solid Sorbent CO<sub>2</sub> Capture Technology Evaluation and Demonstration at Norcem's Cement Plant in Brevik, Norway*. *Energy Procedia*, 2014. 63: p. 6504-6516.
73. Chung, W., K. Roh, and J.H. Lee, *Design and evaluation of CO<sub>2</sub> capture plants for the steelmaking industry by means of amine scrubbing and membrane separation*. *International Journal of Greenhouse Gas Control*, 2018. 74: p. 259-270.

74. Baker, R.W., et al., CO<sub>2</sub> Capture from Cement Plants and Steel Mills Using Membranes. *Industrial & Engineering Chemistry Research*, 2018. 57(47): p. 15963-15970.
75. Scholes, C.A., et al., Membrane gas separation processes for CO<sub>2</sub> capture from cement kiln flue gas. *International Journal of Greenhouse Gas Control*, 2014. 24: p. 78-86.
76. Lindqvist, K., S. Roussanaly, and R. Anantharaman, Multi-stage Membrane Processes for CO<sub>2</sub> Capture from Cement Industry. *Energy Procedia*, 2014. 63: p. 6476-6483.
77. Scholes, C.A., S.E. Kentish, and G.W. Stevens, Effects of minor components in carbon dioxide capture using polymeric gas separation membranes. *Separation & Purification Reviews*, 2009. 38(1): p. 1-44.
78. Ben-Mansour, R., et al., Carbon capture by physical adsorption: Materials, experimental investigations and numerical modeling and simulations – A review. *Applied Energy*, 2016. 161: p. 225-255.
79. Chiesa, P. and S. Consonni, Shift reactors and physical absorption for low-CO<sub>2</sub> emission IGCCs. 1999.
80. Hill, T.L., Statistical mechanics of multimolecular adsorption II. Localized and mobile adsorption and absorption. *The Journal of Chemical Physics*, 1946. 14(7): p. 441-453.
81. J.P. Birat, e.a., *Global Technology Roadmap for CCS in Industry - Steel Sectoral Report*. 2010.
82. Svante, *Inventys Partners with Total Lafarge to bring Carbon Capture Program to British Columbia*. 2019: Vancouver, BC, Canada, [https://svanteinc.com/wp-content/uploads/2019/05/NR\\_2019-05-28\\_Project-CO2MENT\\_FINAL.pdf](https://svanteinc.com/wp-content/uploads/2019/05/NR_2019-05-28_Project-CO2MENT_FINAL.pdf).
83. *Low Emission Intensity Lime and Cement Project, Public LEILAC Feed Summary Report*. July, 2017, file:///C:/Users/Marco/Downloads/Attachment\_0.pdf
84. Hodgson, P., et al. Direct separation calcination technology for carbon capture: demonstrating a low cost solution for the lime and cement industries in the LEILAC project.
85. *Low Emission Intensity Lime and Cement Project, LEILAC2 Demonstration Plant's Preliminary Front End Engineering Design (Pre-FEED) Report*, 2020, [https://www.project-leilac.eu/\\_files/ugd/ce8a5c\\_9980e75a76cb45d48f9225a68cb9daa1.pdf](https://www.project-leilac.eu/_files/ugd/ce8a5c_9980e75a76cb45d48f9225a68cb9daa1.pdf)
86. Granados, D.A., F. Chejne, and J.M. Mejía, Oxy-fuel combustion as an alternative for increasing lime production in rotary kilns. *Applied Energy*, 2015. 158: p. 107-117.
87. Gerbelová, H., M. Van Der Spek, and W. Schakel, Feasibility assessment of CO<sub>2</sub> capture retrofitted to an existing cement plant: post-combustion vs. oxy-fuel combustion technology. *Energy Procedia*, 2017. 114: p. 6141-6149.
88. Eriksson, M., B. Hökfors, and R. Backman, Oxyfuel combustion in rotary kiln lime production. *Energy Science & Engineering*, 2014. 2(4): p. 204-215.
89. Abanades, J.C., The maximum capture efficiency of CO<sub>2</sub> using a carbonation/calcination cycle of CaO/CaCO<sub>3</sub>. *Chemical Engineering Journal*, 2002. 90(3): p. 303-306.
90. Sharaf, O.Z. and M.F. Orhan, An overview of fuel cell technology: Fundamentals and applications. *Renewable and sustainable energy reviews*, 2014. 32: p. 810-853.
91. Hanak, D.P. and V. Manovic, Combined heat and power generation with lime production for direct air capture. *Energy Conversion and Management*, 2018. 160: p. 455-466.
92. Aminu, M.D., et al., A review of developments in carbon dioxide storage. *Applied Energy*, 2017. 208: p. 1389-1419.
93. Coppola, A., et al., Performance of natural sorbents during calcium looping cycles: a comparison between fluidized bed and thermo-gravimetric tests. *Energy & fuels*, 2013. 27(10): p. 6048-6054.
94. Pawlak-Kruczek, H. and M. Baranowski, Effectiveness of CO<sub>2</sub> Capture by Calcium Looping with Regenerated Calcium Sorbents–Last Step Calcination. *Energy Procedia*, 2017. 105: p. 4499-4512.
95. Martina Fantini, et al., *CLEANKER - Clean clinker by Calcium Looping process for low CO<sub>2</sub> cement production*. 2018.
96. Balfe, M.C., et al., Alstom's Regenerative Calcium Cycle-Norcem Derisking Study: Risk Mitigation in the Development of a 2nd Generation CCS Technology. *Energy Procedia*, 2014. 63: p. 6440-6454.
97. (Ed.), V.D.Z.e.V., *Environmental data of the German cement industry 2020*. July, 2021.
98. Paritosh, K., et al., Food waste to energy: an overview of sustainable approaches for food waste management and nutrient recycling. *BioMed research international*, 2017. 2017.
99. Malloi, C., S.M. Mentzer, and C.E. Miller, Combustion features. *Archaeological soil and sediment micromorphology*, 2017: p. 299-330.
100. Emmanuel, A.C., et al., Second pilot production of limestone calcined clay cement in India: the experience. *Indian Concr. J*, 2016. 90(5): p. 57-63.

101. Seeker, W.M.R. *Waste combustion. Elsevier, Symposium (International) on Combustion. Vol. 23. No. 1.*
102. Buekens, A., *Incineration technologies. 2013: Springer Science & Business Media.*
103. Yin, K., A. Ahamed, and G. Lisak, *Environmental perspectives of recycling various combustion ashes in cement production—A review. Waste Management, 2018. 78: p. 401-416.*
104. European Commission, *A european strategic long-term vision for a prosperous, modern, competitive and climate neutral economy. 28.11.2018.*
105. Meier, A., et al., *Solar chemical reactor technology for industrial production of lime. Solar Energy, 2006. 80(10): p. 1355-1362.*
106. Samal, S., *Thermal plasma technology: The prospective future in material processing. Journal of Cleaner Production, 2017. 142: p. 3131-3150.*
107. Dawood, F., M. Anda, and G.M. Shafiullah, *Hydrogen production for energy: An overview. International Journal of Hydrogen Energy, 2020. 45(7): p. 3847-3869.*
108. Sequeira, C.A.C., *High temperature corrosion: fundamentals and engineering. 2019: John Wiley & Sons.*
109. Castano, S.V., et al., *Calcination-free production of calcium hydroxide at sub-boiling temperatures. RSC Advances, 2021. 11(3): p. 1762-1772.*
110. Singhal, S.C. and K. Kendall, *High-temperature solid oxide fuel cells: fundamentals, design and applications. 2003: Elsevier.*
111. ReportLinker, *Global Calcium Hydroxide Industry. October, 2020, [https://www.reportlinker.com/p05956205/GlobalCalciumHydroxideindustry.html?utm\\_source=GNW](https://www.reportlinker.com/p05956205/GlobalCalciumHydroxideindustry.html?utm_source=GNW)*
112. Survey, U.S.G., *Mineral commodity summaries 2020: National Minerals Information Center. 2019.*
113. Du, F., et al., *Sodium hydroxide production from seawater desalination brine: process design and energy efficiency. Environmental science & technology, 2018. 52(10): p. 5949-5958.*
114. Botte, G.G., *Electrochemical manufacturing in the chemical industry. The Electrochemical Society Interface, 2014. 23(3): p. 49-55.*
115. Moreno Ruiz, E., et al., *Documentation of changes implemented in the ecoinvent database v3.8 (2021.09.21). 2021, <https://ecoinvent.org/wp-content/uploads/2021/09/Change-Report-v3.8.pdf>: Zurich, Switzerland.*
116. Rogelj, J., et al., *Paris Agreement climate proposals need a boost to keep warming well below 2°C. Nature, 2016. 534(7609): p. 631.*
117. Jordal, K., et al., *CEMCAP – making CO<sub>2</sub> capture retrofittable to cement plants. Energy Procedia, 2017. 114: p. 6175-6180.*

### 3. Alternative decarbonisation route: effect of ternary composition and process feasibility

This work is the first manuscript of the series, published on *Energy & Environmental Science*, which introduces the alternative approach to the decarbonisation of  $\text{CaCO}_3$ . Scientific discussion is carried out by taking into account preliminary experiments which allowed to assess the feasibility of the reaction on both reagent and industrial grade  $\text{CaCO}_3$ . By summarising, the work aims to assess the potential impact of the novel decarbonisation route on the cement industry, also highlighting the possible production schemes without taking into account any life-cycle assessment yet. I here certify that I performed 64 out of 71 samples, taking also care of their characterisation (XRD, TG analysis); also, I provided the main author Theodore Hanein with detailed written reports summarising the experimental results.

# Decarbonisation of calcium carbonate at atmospheric temperatures and pressures, with simultaneous CO<sub>2</sub> capture, through production of sodium carbonate

Theodore Hanein\*, Marco Simoni, Chun Long Woo, John L. Provis, and Hajime Kinoshita\*

*Department of Materials Science & Engineering, University of Sheffield, Sheffield S1 3JD, UK*

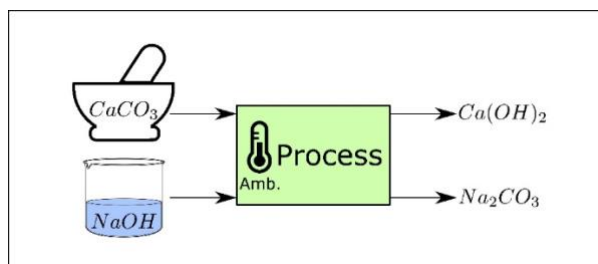
\*Corresponding authors: [t.hanein@sheffield.ac.uk](mailto:t.hanein@sheffield.ac.uk) and [h.kinoshita@sheffield.ac.uk](mailto:h.kinoshita@sheffield.ac.uk)

## Abstract

The calcination of calcium carbonate (CaCO<sub>3</sub>) is a major contributor to carbon dioxide (CO<sub>2</sub>) emissions that are changing our climate. Moreover, the calcination process requires high temperatures (~900°C). A novel low-temperature process for the decarbonisation of CaCO<sub>3</sub> is tested whereby the CO<sub>2</sub> is directly sequestered/mineralised in sodium carbonate. CaCO<sub>3</sub> is reacted with an aqueous sodium hydroxide solution by mixing under atmospheric temperatures and pressures. The reaction products are calcium hydroxide (hydrated lime; Ca(OH)<sub>2</sub>) and sodium carbonate (soda ash; Na<sub>2</sub>CO<sub>3</sub>). For the first time, the extent of this reaction at ambient conditions is studied along with the NaOH requirements. Conceptual process designs, which include procedures to separate and recover material, as well as energy calculations, are also presented to demonstrate technical/industrial feasibility of the process. The technology is also successfully tested on industrially sourced limestone chalk, and the silica impurity remains inert throughout the process. This technology will enable industrial symbiosis by combining the high-temperature lime and sodium carbonate manufacturing processes into a single low-temperature process and greatly reduce the chemical (raw material) CO<sub>2</sub> emissions associated with the production of cement and lime.

**Keywords:** Calcium carbonate; Decarbonisation; Sodium carbonate; Sodium hydroxide; Low-carbon technology; Manufacturing; Cement; Lime; Soda ash

## Abstract Graphic



Novel low-temperature process that, with the availability of green electricity, enables the production of carbon-neutral cement, lime, and soda ash.

## Statement

Global annual  $CO_2$  emissions from limestone (mainly  $CaCO_3$ ) decarbonisation are ~2.3 billion tonnes; this is 7% of global emissions resulting mainly from the cement industry. The  $CO_2$  emissions from the decarbonisation of  $CaCO_3$  stem from both the material breakdown and the fossil fuels used to reach decomposition temperatures (~900°C). A novel process/concept is presented to decarbonise  $CaCO_3$  at atmospheric temperatures and pressures. The core reaction is:  $CaCO_3 + 2NaOH \rightarrow Ca(OH)_2 + Na_2CO_3$ , which is the reverse of the well-known causticization reaction, but has never been assessed for industrial exploitation in this direction. The simplicity of this reaction and its familiarity to industry make it appealing for wide-scale application. This process not only combines  $CaCO_3$  decarbonisation and carbon capture into a single-stage low-temperature process, but also captures/locks the  $CO_2$  in a stable mineral/product, micrometres in size, instead of gaseous form; this allows for simpler and safer use or storage as required. The availability of sodium is not an issue, but the bottleneck of this process is the energy requirements for  $NaOH$  production, which may be resolved by provision of green electricity. The process co-produces  $Na_2CO_3$  and is also an alternative, novel, and viable route to producing soda ash.

# 1. Introduction

Limestone, which makes up 1.5% of the Earth's crust [1] and is geographically widespread, is among the world's most essential resources since it is primarily composed of the mineral calcite ( $\text{CaCO}_3$ ) and finds use in major industries: 1) the construction industry as a key ingredient for cement [2, 3], 2) the metallurgical industry for the refinement of steel through the production of slags [4, 5], 3) the chemical industry for the neutralisation/capture of gaseous effluents (including  $\text{CO}_2$ ) [6], and 4) the food industry for the separation of impurities during sugar refining [7]. These major industrial applications of limestone involve its calcination which leads to the liberation of embodied carbon dioxide and yields CaO (lime):  $\text{CaCO}_3 \xrightarrow{700-900\text{ }^\circ\text{C}} \text{CaO} + \text{CO}_2$ . The calcination process is usually conducted in directly fired furnaces, releasing a flue gas containing relatively dilute  $\text{CO}_2$ . The process of capturing this  $\text{CO}_2$  is challenging because of its small size and non-polar nature;  $\text{CO}_2$  capture can also require the use of other bulk chemicals and is expensive.  $\text{CO}_2$  storage is also complicated due to large availability, while long-term storage without leakage is not proven [8, 9].

Global production of calcined limestone as lime is ~400 Mt annually [10], but the most prominent use is in cement manufacture. More than 4 Gt of cement is produced annually [10], making it a major global  $\text{CO}_2$  emitter. Approximately 60% [2] of these emissions are chemical  $\text{CO}_2$ , originating from the limestone, and are estimated to be 1.45 Gt per year [11]. This translates to ~4 % of global anthropogenic  $\text{CO}_2$  emissions which are gradually warming our planet and changing our climate [12, 13]. This is in addition to the  $\text{CO}_2$  emitted due to the, near-universal, reliance on fossil-fuels in this process, which are required to achieve the high calcination temperatures. Therefore, radical industry transformation is required to accomplish climate goal compliant  $\text{CO}_2$  emissions reduction in the cement industry [14].

Ellis et al. [15] demonstrated an ambient-temperature electrochemical method that decarbonizes  $\text{CaCO}_3$  to produce solid  $\text{Ca}(\text{OH})_2$ . Because this method also generates  $\text{H}_2$  gas and an  $\text{O}_2/\text{CO}_2$  gas mixture,  $\text{CO}_2$  will still need to be separated and sequestered using additional processes. Also, it is still not proven whether the process can be scaled up, and a tailored industrial electrolyser will need to be developed. It is additionally important that such processes are tested on industrial grade calcareous sources, which will contain several impurities. Moreover, further alternatives to calcination and decarbonisation of calcium carbonate are necessary to improve industrial sustainability. Nonetheless, Ellis et al. [15] showed that  $\text{Ca}(\text{OH})_2$  can be used to produce alite, the main mineral in traditional Portland cement, at standard cement clinkering temperatures.

On the other hand, soda ash ( $\text{Na}_2\text{CO}_3$ ) is an essential raw material to the glass, detergent, and chemical industries. Natural soda ash is manufactured from trona while synthetic soda ash is currently industrially produced using the Solvay process. In many regions, such as in Europe, soda ash manufacture is entirely through the Solvay process, due to the lack of trona deposits [16]. The manufacture of synthetic soda ash is a complex and energy-intensive process that involves the use of high temperatures ( $\sim 900^\circ\text{C}$ ) for the calcination of limestone (as the carbon dioxide source). The process emits 200 – 400 kg  $\text{CO}_2$  per tonne of soda ash, and the carbon footprint of the manufacture of natural soda ash is in fact similar [16, 17]. The Solvay process however has limited material efficiency and produces a by-product ( $\text{CaCl}_2$ ) as well as a post-soda lime waste stream.

The present study establishes a method/technology that co-produces lime and sodium carbonate in a single process; thus, inhibiting chemical  $\text{CO}_2$  emissions from the decarbonisation of a calcareous source, by simultaneously sequestering the  $\text{CO}_2$  in a stable and economically desirable mineral. The scalable process occurs at low temperature; thus, the fuel-derived  $\text{CO}_2$  emissions that often originate from achieving the required temperature for  $\text{CaCO}_3$  calcination are also reduced, while the quality of heat (temperature) required is greatly lowered. The  $\text{CaCO}_3$  is decarbonised via reaction with  $\text{NaOH}$  in the presence of necessary water to produce  $\text{Ca}(\text{OH})_2$ , and the  $\text{CO}_2$  is sequestered/mineralised as  $\text{Na}_2\text{CO}_3 \cdot x\text{H}_2\text{O}$  ( $x = 0$  or  $1$ ) simultaneously; this is the reverse of the well-known causticisation reaction. The process efficiency is examined in terms of starting material concentrations, and the feasibility of the process on industrial grade calcium carbonate is demonstrated. Methods to separate the products are also outlined, along with two conceptual process designs and energy performance calculations.

## 2. Methods

### 2.1 Experimental procedure

The starting mix proportions of  $\text{CaCO}_3$ ,  $\text{NaOH}$ , and  $\text{H}_2\text{O}$  are critical to the reaction progress, and are investigated to identify a working envelope that can achieve sufficient conversion of  $\text{CaCO}_3$  into  $\text{Ca}(\text{OH})_2$ . Starting compositions were tested using reagent grade ( $>99\%$  pure)  $\text{CaCO}_3$  (calcite) with an average particle size of approximately  $35 \mu\text{m}$ ;  $\text{NaOH}$  beads ( $\geq 97\%$ ) were also used, along with distilled water. Laboratory-grade methanol ( $>99\%$ ) was used for dissolution/separation of  $\text{NaOH}$ . Furthermore, a limestone chalk with high quantity of impurities was tested to assess the industrial applicability of the decarbonisation technique.

The chalk is 73 wt.% CaCO<sub>3</sub> (thermogravimetric analysis) and the particle size was <200 μm; the other major phase (21 wt.%) in the limestone is silica (quartz).

For each experiment, a sodium hydroxide solution was first prepared at a pre-defined concentration. The decarbonisation reaction was then carried out by mixing a specified amount of CaCO<sub>3</sub> with the solution. All tested systems contained sufficient NaOH for the CaCO<sub>3</sub> in the system to react stoichiometrically. The reaction was carried out in a 250 mL PTFE<sup>1</sup> beaker, filled as indicated in Supplementary Table S1, and mixed for 5 minutes using a Heidolph R2020 overhead mixer equipped with a PTFE centrifugal stirrer shaft (40 mm diameter) set at 1050 rpm. The experiments were conducted at laboratory room temperature (~20°C); however, the dissolution of NaOH in water is an exothermic reaction, which resulted in an initial solution temperature of up to 90°C. The temperature gradually decreased during the five-minute long experiments at a rate of ~5°C per min. Double the required amount of methanol was then used to dissolve the residual NaOH; the methanol was mixed into the slurry for a further 5 minutes. The solid products (and unreacted CaCO<sub>3</sub>) are practically insoluble in methanol; therefore, unreacted NaOH can be separated from the remaining solid mix by filtration. A vacuum assisted Büchner funnel was used for filtration, where the retentate was collected on a Whatman Grade 1 (90mm) filter paper. The retentate was then dried in an oven at 35°C for 30 mins to remove traces of water and methanol. The dried products were then characterised through X-ray diffraction (to identify the products) and thermogravimetric analysis (to quantify the extent of the decarbonisation reaction).

## 2.2 Characterisation techniques

X-ray diffraction (XRD) was used to identify reaction products in selected samples. The analyses were performed using a Bruker D2 PHASER X-ray diffractometer in Bragg-Brentano geometry, with Cu-Kα radiation (30 kV, 10 mA), a one-dimensional LYNXEYE detector and a 1 mm divergence slit. Samples were ground to powders and backloaded into sample holders, 2.5 cm in diameter and 1 mm in depth. Each diffraction pattern was recorded from 5 – 80° 2θ with a step size of 0.02° at 0.5 seconds per step. To improve counting statistics, the stage was set to rotate at 15 rpm. Qualitative phase identification was carried out using the DIFFRAC.EVA V3.1 software and the PDF2019 database.

Thermogravimetric analysis (TGA) was carried out on all samples. Approximately 40 mg of sample was analysed on a PerkinElmer TGA 4000 from 30 – 800°C at a heating rate of 10° C/min under a nitrogen flow of 40 mL/min. The sample was then held at 800°C for 1 hour to

---

<sup>1</sup> PTFE (Teflon) is suitable for mixing in hyper-alkaline environments and is stable up to ~250 °C.

ensure complete loss of CO<sub>2</sub> from CaCO<sub>3</sub> without melting and/or weight loss from Na<sub>2</sub>CO<sub>3</sub>. A Hiden mass spectrometer (HPR-20 GIC EGA) was coupled with the thermogravimeter to analyse the flue gas, recording signals for H<sub>2</sub>O, CO<sub>2</sub>, O<sub>2</sub>, and H<sub>2</sub>. As observed in the thermogravimetric data, and confirmed through XRD and mass spectroscopy, the weight loss due to release of water at 310 – 470°C can be attributed to the dehydroxylation of Ca(OH)<sub>2</sub>, while weight loss at 560 – 800°C can be attributed to the decomposition of calcium carbonate to release CO<sub>2</sub>. The conversion is then calculated from these values, while the uncertainty contributed to this calculation by TG instrument error has been measured to be ±0.2%.

X-ray fluorescence (XRF) spectroscopic analysis was carried out on the limestone chalk, using a PANalytical Zetium instrument operated with PANalytical SuperQ software. The WROXI (wide-ranging oxides) calibration was used to determine the elemental concentrations. The fused 40 mm bead used for measurements was prepared with a Claisse LeNeo Fluxer by mixing 10 g of lithium tetraborate (with 0.5% Lil) flux with 1 g of sample. The measurement was conducted three times and the average compositional values recorded.

### 3. Results and Discussion

Our decarbonisation process is based on the reaction:  $\text{CaCO}_3 (\text{s}) + 2\text{NaOH} (\text{aq}) + x\text{H}_2\text{O} \rightarrow \text{Ca}(\text{OH})_2 + \text{Na}_2\text{CO}_3 \cdot x\text{H}_2\text{O}$  ( $x = 0$  or  $1$ ) which occurs in the presence of necessary water. The reaction can proceed at atmospheric temperature and pressure and reaches effective completion within five minutes; the sodium carbonate precipitates as Na<sub>2</sub>CO<sub>3</sub> and/or Na<sub>2</sub>CO<sub>3</sub>·H<sub>2</sub>O.

#### 3.1 The reaction: CaCO<sub>3</sub> (s) + 2NaOH (aq)

The extent of reaction progression is highly dependent on the initial ratios of CaCO<sub>3</sub>, NaOH, and H<sub>2</sub>O. Seventy-one variations tested are presented in Figure 1 and Supplementary Table S1 as conversion and NaOH consumption efficiency. A maximum conversion of 96% (Sample 1; 54.6 wt.% H<sub>2</sub>O, 37.3 wt.% NaOH, and 8.1 wt.% CaCO<sub>3</sub>) is achieved, clearly indicating the feasibility of this reaction to obtain Ca(OH)<sub>2</sub> from CaCO<sub>3</sub>. A conversion of 86% was also achieved by using 4 – 5 times less NaOH and water for the same amount of CaCO<sub>3</sub> (Sample 5; 40.6 wt.% H<sub>2</sub>O, 32.4 wt.% NaOH, and 27.0 wt.% CaCO<sub>3</sub>).

Figure 1a summarises the conversion achieved at different starting compositions. Both high and low H<sub>2</sub>O:NaOH ratios can result in reduced conversion. The highest conversions are generally achieved at higher ratios of NaOH solution to CaCO<sub>3</sub>. However, Figure 1b shows that at these higher ratios, more NaOH remains unreacted, which will need to be separated

and recycled. There does exist a region where both conversion and NaOH consumption efficiency are high, such as Samples 5 and Sample 6 (see Table S1).

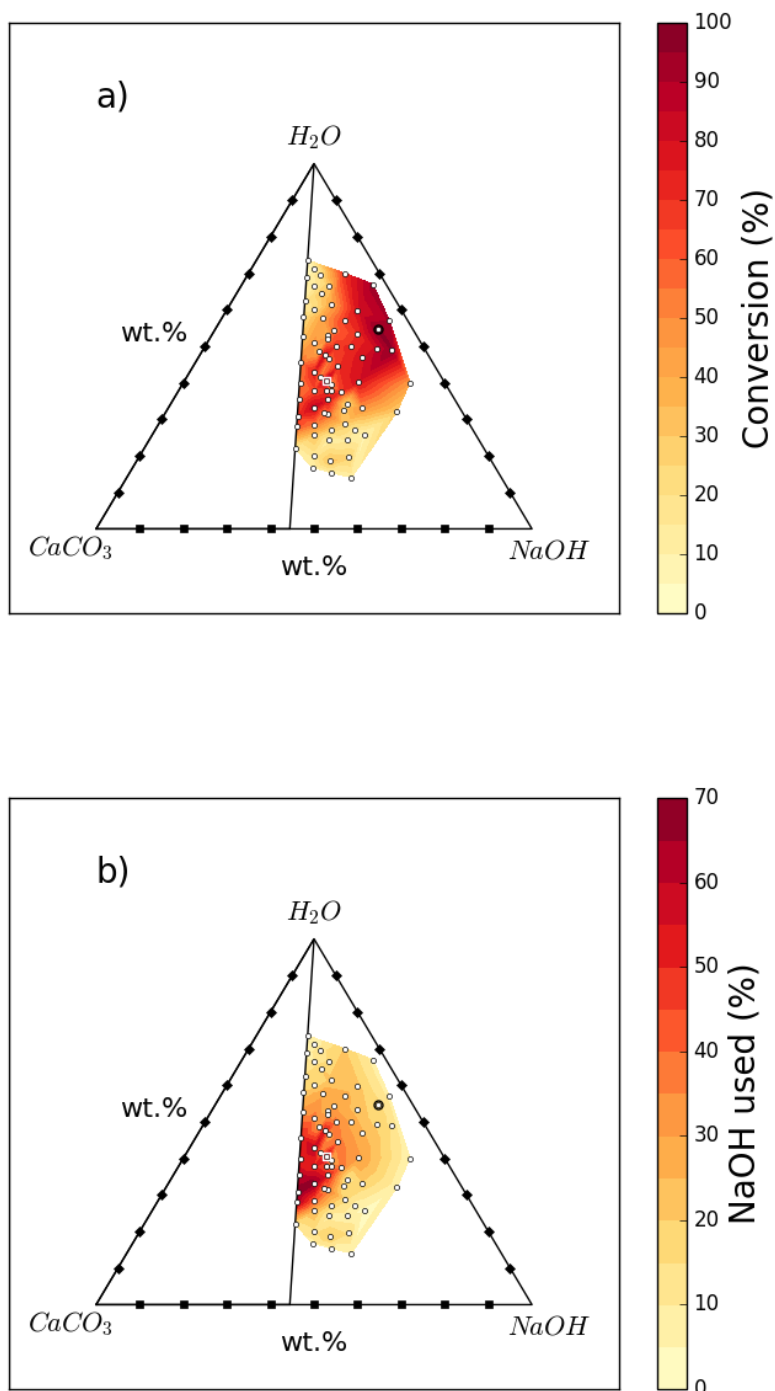


Fig. 1.

As shown in Figure 2, the  $NaOH/CaCO_3$  molar ratios investigated were showing a similar bell-shaped trend in terms of conversion as a function of  $H_2O/NaOH$  molar ratios. With an increase

in NaOH/CaCO<sub>3</sub> molar ratio, the maximum conversion increases up to a certain extent before decreasing; all the maximum conversions for all NaOH/CaCO<sub>3</sub> ratios studied were detected in a H<sub>2</sub>O/NaOH range between 2.0 – 3.0. The maxima were both preceded and followed by lower reaction efficiencies. The lower conversions registered at milder NaOH concentrations, can be attributed to the lower ionic strength of the solutions. On the other hand, low conversions registered at higher NaOH concentrations may be attributed to the scarcity of H<sub>2</sub>O, leading to denser solutions and a hindered physical contact between the reactants. Moreover, the very high ionic strength of these solutions might prevent supersaturation conditions of the products Ca(OH)<sub>2</sub> and Na<sub>2</sub>CO<sub>3</sub>·xH<sub>2</sub>O, hindering their precipitation [18].

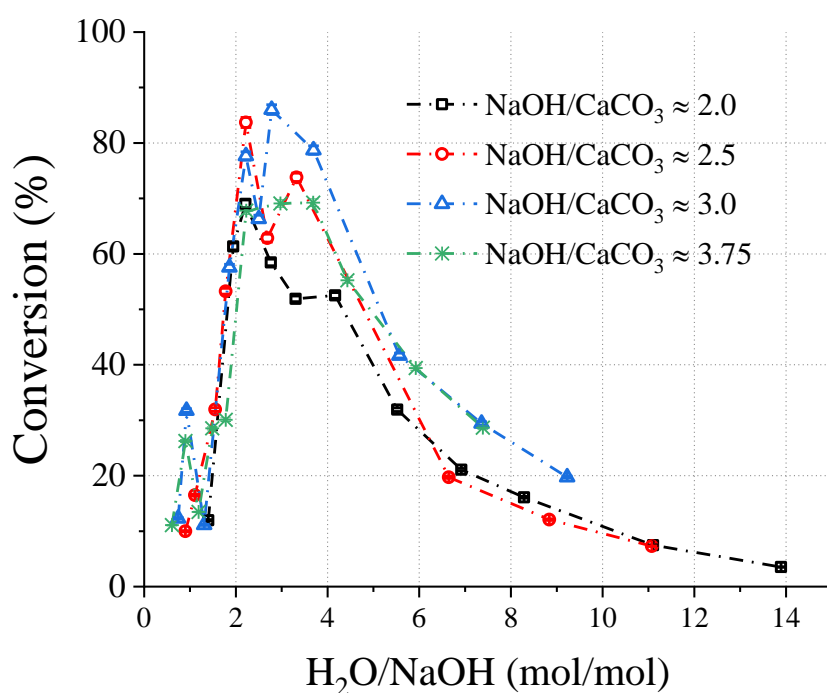


Fig. 2.

The XRD patterns for samples 1 and 5, shown in Figure 3, confirm that the major phases in the solid product are Ca(OH)<sub>2</sub>, Na<sub>2</sub>CO<sub>3</sub>·H<sub>2</sub>O, and CaCO<sub>3</sub>; however, the CaCO<sub>3</sub> peaks in Sample 1 exhibit a low intensity as it is almost completely consumed, which is in agreement with the TG/conversion data. In some samples (not shown here) Na<sub>2</sub>CO<sub>3</sub> was also present and it is concluded that the CO<sub>2</sub> is sequestered as either Na<sub>2</sub>CO<sub>3</sub> or Na<sub>2</sub>CO<sub>3</sub>·H<sub>2</sub>O depending on the temperature, water activity, and NaOH concentration [19-21]. As shown in Figure 3, main peaks of Na<sub>2</sub>CO<sub>3</sub> do overlap with those of Na<sub>2</sub>CO<sub>3</sub>·H<sub>2</sub>O, and both may be existing simultaneously. The possibility of methoxide formation was also investigated and discarded through analyses of XRD and TG data.

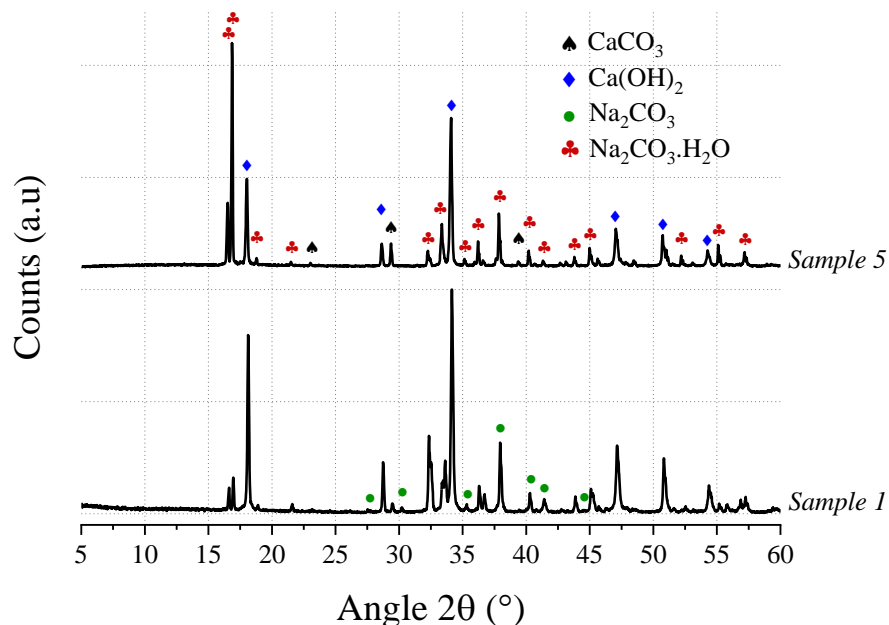


Fig.3.

### 3.2 Applicability to industrial grade calcium carbonate

Calcium carbonate in nature is generally found as limestone rock which also contains other phases (mainly quartz) and impurities. For industrialisation of a decarbonisation process, it is essential that the developed technology is applicable to such raw materials. Therefore, an industrial grade limestone chalk containing a high quantity of impurities was tested. The oxide composition of the limestone chalk is presented in Table 1 and shows the presence of 21 wt. %  $\text{SiO}_2$  as well as other minor impurities.

Table 1.

$\text{Al}_2\text{O}_3$	$\text{CaO}$	$\text{Fe}_2\text{O}_3$	$\text{K}_2\text{O}$	$\text{MgO}$	$\text{Na}_2\text{O}$	$\text{P}_2\text{O}_5$	$\text{SiO}_2$	$\text{SrO}$	$\text{TiO}_2$	Others	LOI
2.9	43.8	1.1	0.7	0.3	0.2	0.1	21.0	0.1	0.2	0.2	29.4

Thermogravimetric analysis of the limestone chalk (not shown here) indicated that the  $\text{CaCO}_3$  content was 73 wt.%, suggesting that some of the Ca is present as silicates, when comparing with XRF data in Table 1. Samples 1L and 5L (Table 2) were prepared with the same compositions as Samples 1 and 5, respectively, but using the chalk instead of the reagent grade  $\text{CaCO}_3$  and correcting for the  $\text{CaCO}_3$  content of the chalk to maintain the same  $\text{NaOH}/\text{CaCO}_3$  ratios as Samples 1 and 5. The starting compositions and resulting conversions (obtained from the TG data shown in Figure 4) are also shown in Table 2. A drop in conversion is observed when using limestone chalk, from 96% (Sample 1) and 86% (Sample 5) to 72%

(Sample 1L) and 61% (Sample 5L), respectively. The XRD (Figure 5) analyses also revealed that the SiO<sub>2</sub>/quartz remained unreacted.

Table 2.

ID	Chalk (g)	NaOH (g)	H <sub>2</sub> O (g)	Chalk (wt.%)	NaOH (wt.%)	H <sub>2</sub> O (wt.%)	Conversion (%)	NaOH used (%)
1L	10.00	33.60	49.20	10.8	36.2	53.0	71.8	12.5
5L	10.07	8.77	11.01	33.7	29.4	36.9	60.9	40.8

### 3.3 Separation of the products

After the decarbonisation reaction, the major constituents of the mixture can include: CaCO<sub>3</sub>, Ca(OH)<sub>2</sub>, NaOH, Na<sub>2</sub>CO<sub>3</sub> and/or Na<sub>2</sub>CO<sub>3</sub>·H<sub>2</sub>O, along with unreacted SiO<sub>2</sub> (when using industrial grade material). Table 3 shows the solubility of these phases, at close to room temperature, in water, methanol, and ethanol. It is deduced that alcohols can be used as selective dissolution media to separate, and recover, unreacted/excess NaOH. Na<sub>2</sub>CO<sub>3</sub> can then be separated from the calcium-containing components and silica, utilising the differences in their solubilities in water as the driving force for separation.

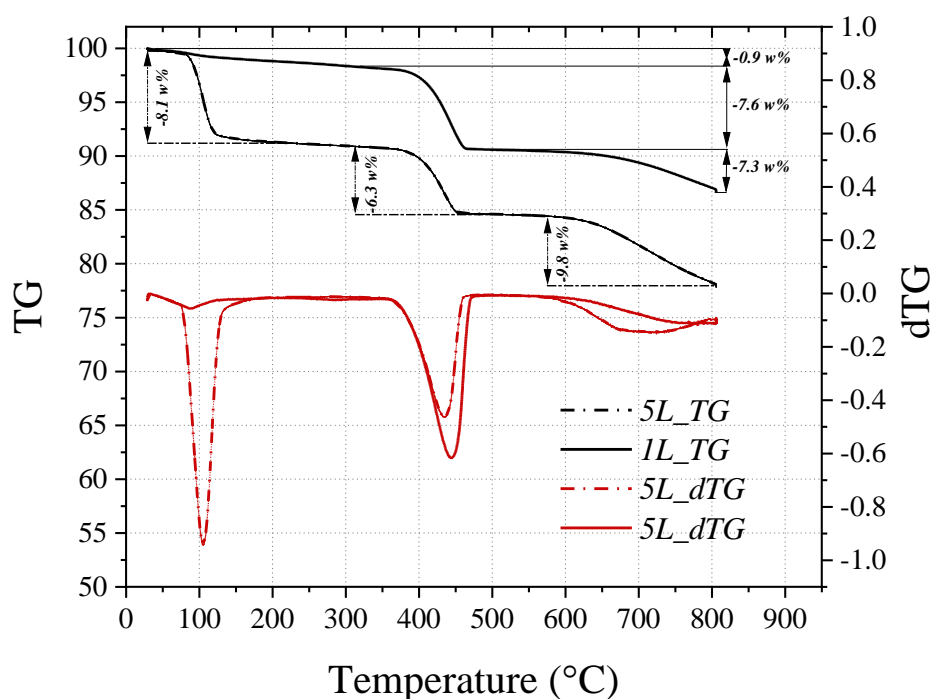


Fig. 3.

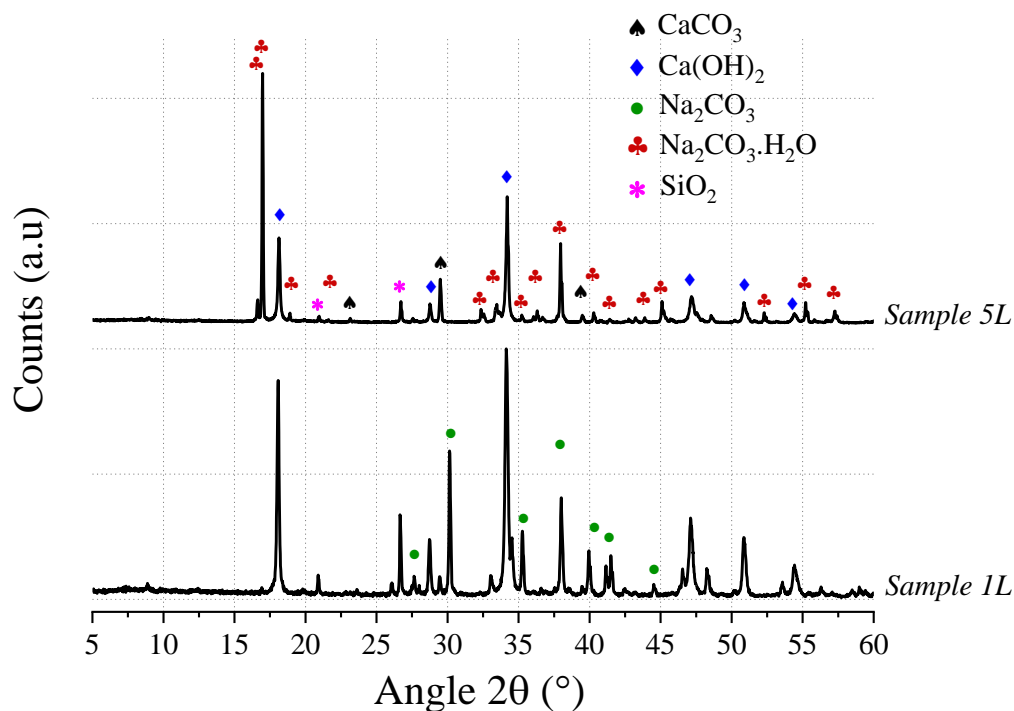


Fig. 4.

Table 3.

	CaCO <sub>3</sub>	Ca(OH) <sub>2</sub>	Na <sub>2</sub> CO <sub>3</sub>	SiO <sub>2</sub>	NaOH
g /100 g of <b>Water</b>	0.0014	0.155	29.4	0.0006	113
g /100 g of <b>Methanol</b>	-	-	0.604	-	31 (28°C)
g /100 g of <b>Ethanol</b>	-	-	0.24	-	17.3 (28°C)

### 3.4 Conceptual process design

The process for industrial decarbonisation of calcium carbonate with simultaneous production of sodium carbonate is now conceptualised and including separation procedures. The major reaction can proceed with high (e.g. Sample 1) or low (e.g. Sample 5) amounts of initial NaOH solution. These two scenarios encouraged us to design and create process flow diagrams for two processes which cover realistic situations, hereby named Process A (Figure 6) and Process B (Figure 7). When low amounts of solution are used initially, or the water is evaporated after the reaction, NaOH can be separated from Na<sub>2</sub>CO<sub>3</sub> before separation from calcium compounds and silica (such as in Process A). When high amounts of solution are added initially, most sodium compounds can dissolve together, leaving behind mainly the calcium compounds and silica as undissolved solids (such as in Process B). Process A may also be adopted for high amounts of solution and vice versa.

In Process A, NaOH is first separated from the main reaction products; while in Process B, NaOH and Na<sub>2</sub>CO<sub>3</sub> are jointly separated. Different steps in the process are presented as unit operations (UO). The first unit operation (UO1) in both flowsheets (highlighted green in Figures 6 and 7) is the heart of the process and is where the reaction between CaCO<sub>3</sub>, NaOH, and H<sub>2</sub>O occurs. At atmospheric pressure, this reaction can be carried out at temperatures up to the boiling point of the NaOH solution; ~170°C [22]. At higher pressures, where the aqueous solution is stable, the reaction may also occur at higher temperatures. In the flowsheets, all UOs that may require thermal energy input are highlighted pink. This thermal energy may be used to evaporate liquids or to control the reaction equilibrium. In both flowsheets, the alcohol and unreacted NaOH can be recirculated. In UO10 of Process A and UO8 of Process B, hydrated sodium carbonate will convert to anhydrous above ~90°C [7]. In UO2 of Process B it is proposed that additional NaOH can also be added at this stage, along with water and temperature control, to shift chemical equilibrium if necessary.

The energy performance of Processes A and B will depend mainly (~80%) on overcoming the latent heats of water and alcohol for evaporation. The minimum vaporisation energy requirements per kg of Ca(OH)<sub>2</sub> production are calculated for all samples, and shown in Table S1, using the heats of vaporisation of water and methanol from Ref. [23] as well as solubility data in Table 3 (to calculate required heat of vaporisation); selected calculations are shown in Figure 8. Up to 1.43 kg of Na<sub>2</sub>CO<sub>3</sub> is produced alongside every kg of Ca(OH)<sub>2</sub>; if the conventional processes is used, the production of these combined can demand 23,648 kJ (13,600 kJ/kg\_Na<sub>2</sub>CO<sub>3</sub> x 1.43 kg\_Na<sub>2</sub>CO<sub>3</sub> + 4,200 kJ/kg\_Ca(OH)<sub>2</sub> x 1.00 kg\_Ca(OH)<sub>2</sub>) [24, 25]. Using the technology presented in this work, the energy requirements for Sample 1 in Process B is 42,201 kJ and for Sample 5 in Process A is 19,400 kJ. The latter is comparable with existing technologies but, along with simultaneous raw-material CO<sub>2</sub> sequestration, the novel process also allows for use of lower-grade heat that could be generated renewably or sourced from waste heat sources, and avoids the high temperatures required for CaCO<sub>3</sub> calcination. The energy performance of the developed technology can also improve when the initial compositions of NaOH and H<sub>2</sub>O are low (see Samples 6 and 19 in Table S1), albeit at the cost of a lower conversion.

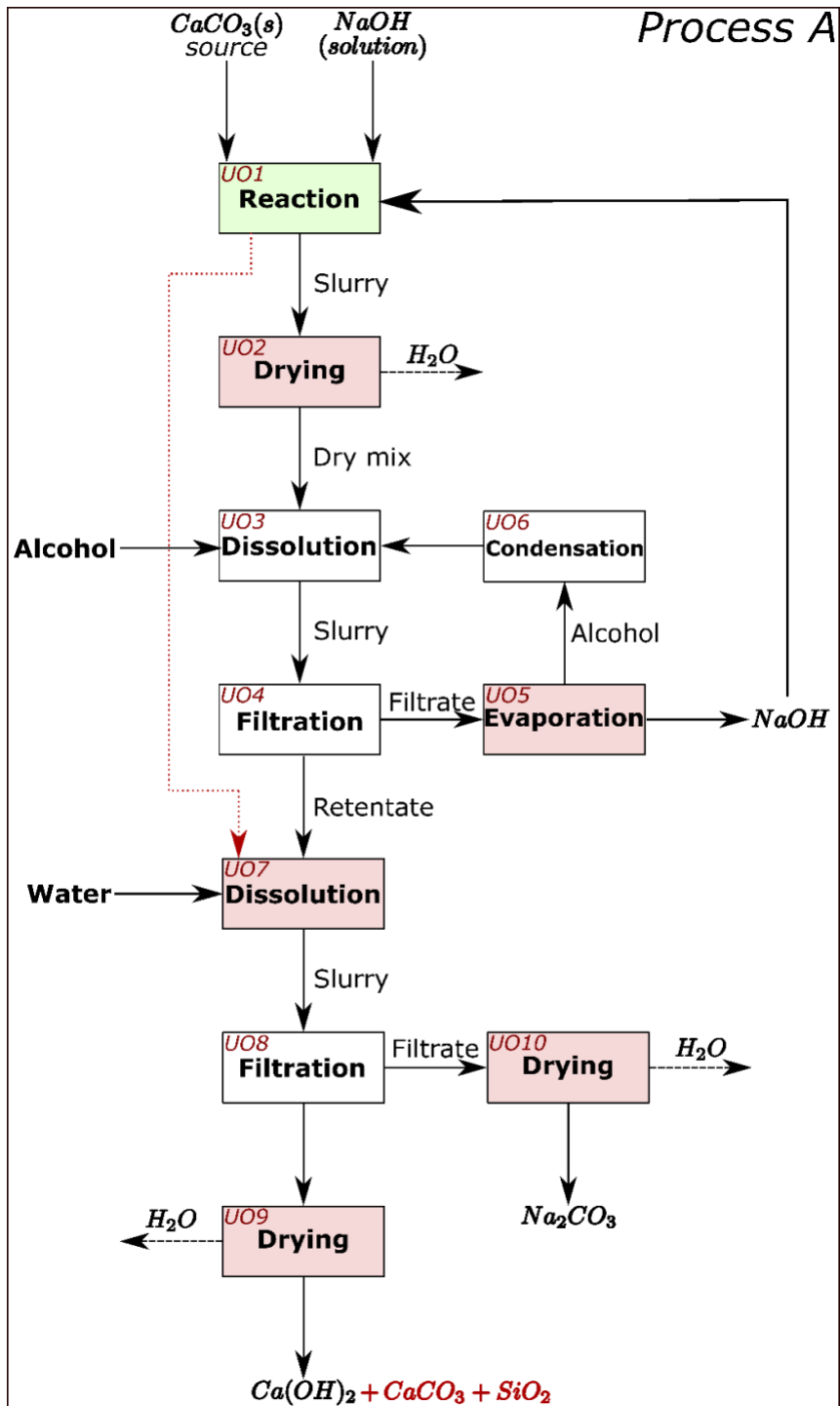


Fig. 5.

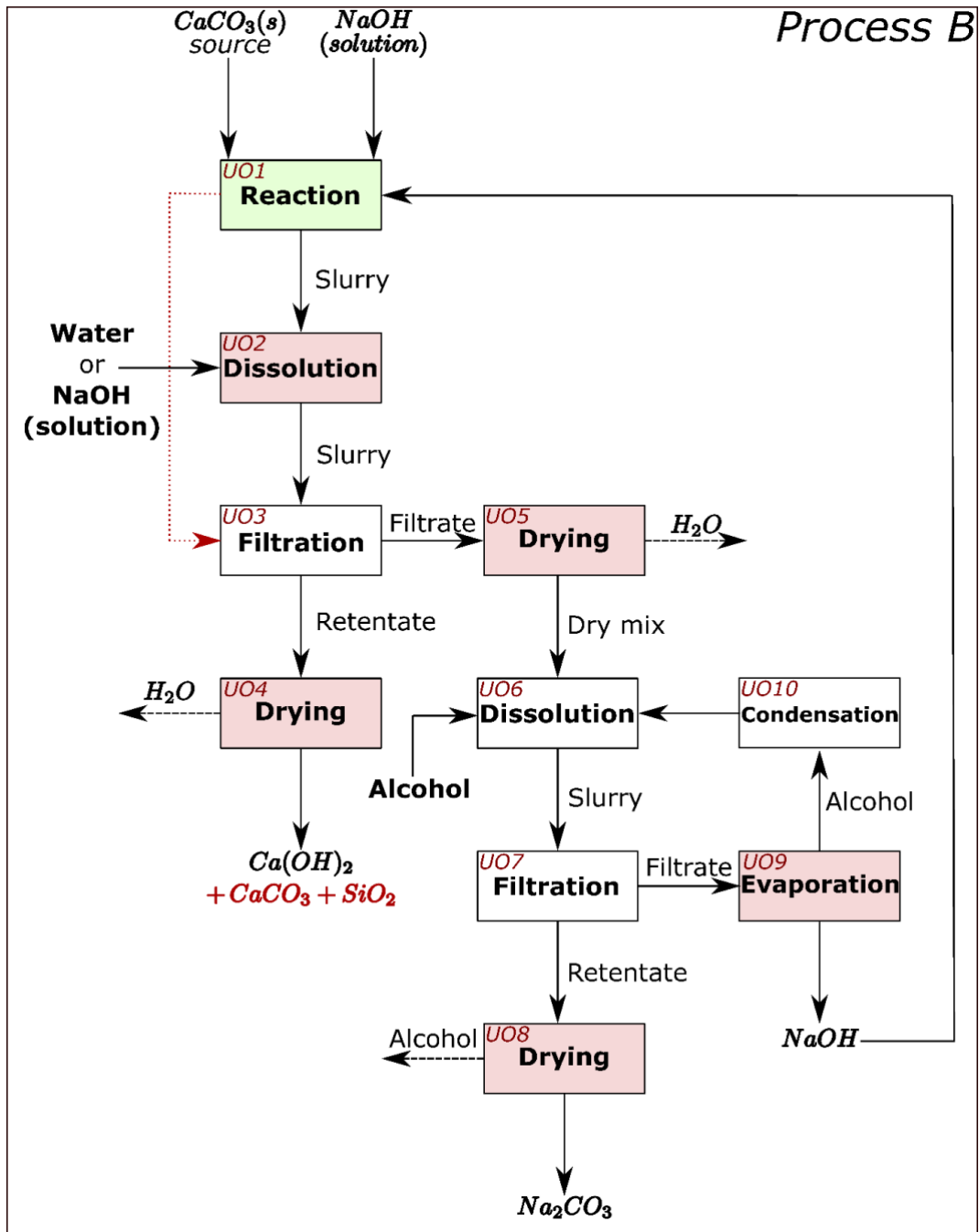


Fig. 6.

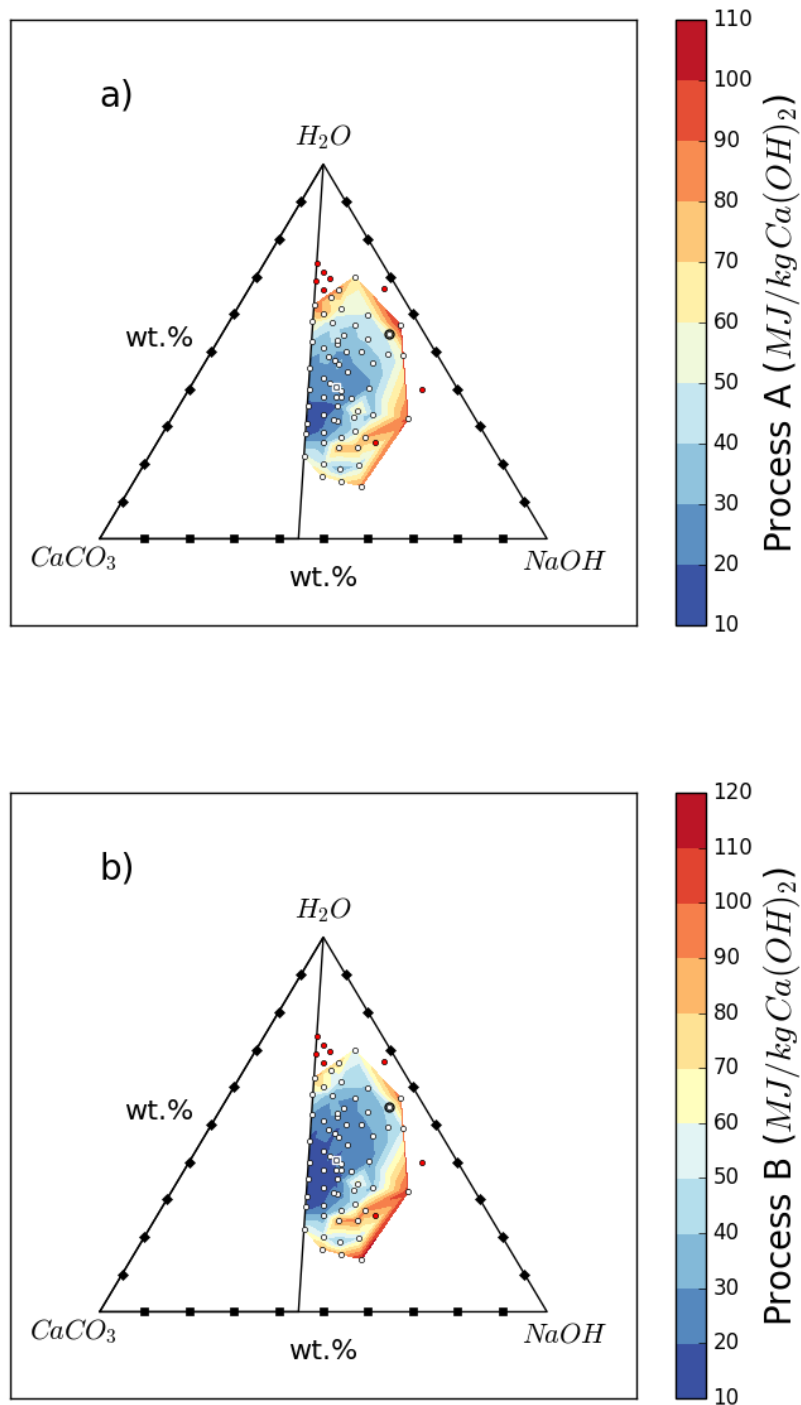


Fig. 7.

#### 4. Additional Discussion

It is generally believed that the calcination of limestone is unavoidable in cement clinker manufacture [14, 26, 27]; however, the obtained calcium compounds from our process (mainly  $\text{Ca(OH)}_2$ ), which may also contain silica, can be used to produce cement clinker when mixed

with appropriate raw materials and thermally treated [15, 28]. In fact, in modern precalciner cement kiln configurations, the limestone is already calcined to form CaO before reaching the rotary kiln where clinker is formed [29]. Any impurities contained in the products of our process are originated from the limestone, and thus, are exactly the same as in the conventional cement manufacture, except that they may contain slightly more sodium depending on separation efficiency. Otherwise, the only compositional difference between the limestone and the products of our process is that the CO<sub>2</sub> component has been replaced with H<sub>2</sub>O. The cement can be manufactured in existing cement plants by replacing the limestone in the raw meal of conventional clinker manufacture with the products from our decarbonisation process. This will enable reduced fuel consumption in the pre-calciner which uses more than 60% of the energy in pyro processing, or allow the pre-calciner part of the kiln configuration to become redundant and repurposed, e.g., for the calcination of clay to produce blended cements such as LC<sup>3</sup> which are currently being commercialised at a global scale [30-32]. The Ca(OH)<sub>2</sub> from our process can also be used to produce lime pozzolan cements (without the need for clinkering), as well as to capture carbon from other processes.

For every tonne of CaCO<sub>3</sub> converted to Ca(OH)<sub>2</sub>, in the here-developed process, an almost equal quantity of sodium carbonate is produced, and this can be advantageous. Annual production of natural soda ash (sodium carbonate) is currently 58 million tonnes, but global reserves are limited and not geographically widespread [10]. Industrially, Na<sub>2</sub>CO<sub>3</sub> is mainly produced through the Solvay process which requires large amount of thermal energy and CaCO<sub>3</sub> calcination [33]. The produced Na<sub>2</sub>CO<sub>3</sub> can have several uses in the industry: 1) for flue gas CO<sub>2</sub> sequestration through the production of NaHCO<sub>3</sub> [34, 35], 2) as an alkali activator for cements, either directly or in the production of activators such as sodium silicates [36, 37], 3) in the production of precipitated calcium carbonate from brine for use as a cement admixture [38], 4) to regenerate the necessary NaOH [21, 39-41], and/or 5) sold for the manufacture of other commodities (e.g. glass). The challenge is that overall demand for Na<sub>2</sub>CO<sub>3</sub> is currently smaller than that for cement in two orders of magnitude; therefore, the use of Na<sub>2</sub>CO<sub>3</sub> has to be increased to maximise the incentive of the proposed process for global industrial implementation. It should be noted, however, that the excess Na<sub>2</sub>CO<sub>3</sub> can also be stored, thus sequestering CO<sub>2</sub> in this stable mineral form without a risk of leakage.

NaOH can have a high carbon footprint, which originates from electricity use during its manufacture via electrolysis of seawater [42, 43]; however, with the use of green electricity (e.g., wind turbines), this method of decarbonisation may offer negligible overall CO<sub>2</sub> emissions. The availability of NaOH is not intrinsically limited, since NaOH can be manufactured through electrolysis of sea water, and the seas and oceans of Earth contain

$\sim 2 \times 10^{16}$  tonnes of Na; the limitation here is the energy demand of the chlor-alkali process (which can be met by renewables) and the utilisation of the very large quantity of  $\text{Cl}_2$  that would be produced as a co-product (but diminishing the  $\text{CaCl}_2$  co-product from soda ash manufacture). The issue associated with  $\text{Cl}_2$  may also be reduced by adopting new technologies such as electrolysis of sea water that produces HCl rather than  $\text{Cl}_2$  [44], as HCl can be widely used for water and wastewater treatment.

Today, most of the  $\text{Cl}_2$  produced in the world is used to make four plastics: Polyvinyl chloride (PVC), epoxies, polycarbonate, and polyurethane [45]. PVC, which contains 60% chlorine by weight, is the most produced out of these, and although some industrial uses of chlorine decline due to environmental health concerns and regulations, that of PVC is increasing. The total global production volume of PVC in 2018 amounted to 44 Mt. It is forecasted that the global market size of PVC will grow to nearly 60 Mt in 2025 [46]. The construction industry is the most significant consumer of PVC, as most is used to manufacture building products; thus, the construction industry drives chlorine production [45]. Nonetheless, PVC is associated with adverse environmental and health impacts during its production, while in use, and after use; thus, posing concern in its use in sustainable construction [47]. Consequently, also due to the large difference in demand between cement and PVC, the wide scale industrial application of our technology may be constrained until development of regeneration processes of NaOH from  $\text{Na}_2\text{CO}_3$ , alternative NaOH production processes, or increased demand for  $\text{Cl}_2/\text{HCl}$ . Nonetheless, limited replacement of global manufacturing with our technology is still feasible in current market demands.

Future work around this technology should focus on optimisation of the novel decarbonisation process, further development of the separation techniques, testing various cements produced from the separated lime products, enhanced utilization of sodium carbonate in cementitious materials, and routes for the regeneration of NaOH from  $\text{Na}_2\text{CO}_3$  as well as novel NaOH production processes. This should be followed by scale-up through pilot demonstration trials and retrofit or grass-root industrial cement process and plant designs.

## 5. Conclusions

The feasibility of a novel method to decarbonise calcium carbonate and co-produce sodium carbonate through simultaneous sequestration of  $\text{CO}_2$ , and under ambient conditions, is established. The core of the process involves the reaction of calcium carbonate with a sodium

hydroxide aqueous solution to produce calcium hydroxide and sodium carbonate. A range of conditions have been identified to achieve 70 – 80% conversion and the reaction is fast ( $\leq 5$  min). The technique is also proven on natural limestone, and the silica in the limestone remained unreacted; thus, demonstrating industrial applicability. The products and unreacted reactants can be separated through selective dissolution, using water and alcohol. The feasibility of scale-up is also demonstrated through encouraging energy performance calculations with two conceptual process designs. The presented technology can offer a route for diminishing the substantial raw-material  $\text{CO}_2$  emissions associated with the calcination of limestone.

The largest environmental impact of this work can be achieved through adoption of the presented technology in the cement industry. To achieve climate goals, the cement industry requires radical transformation within the next few decades. The process presented here can enable carbon neutrality in cement and lime manufacturing, while avoiding post-combustion  $\text{CO}_2$  capture. However, the environmental benefits may only be realised if there is availability of green electricity to supply the necessary sodium hydroxide, or development of new sodium hydroxide production processes. The process presented here is also an alternative to the Solvay process and a novel and viable route to producing soda ash.

## Captions (in order of appearance)

**Fig. 8.** Influence on reaction progression of different starting mix compositions of  $H_2O$ ,  $CaCO_3$ , and  $NaOH$ ; the 71 white dots represent the measured data points while the sample highlighted with a black circle is “Sample 1” and that highlighted with a white square is “Sample 5”. (a) shows the conversion of  $CaCO_3$  to  $Ca(OH)_2$  for different starting mix compositions. (b) shows the amount of  $NaOH$  consumed for different starting mix compositions.

**Fig. 9.** Chart showing the conversion vs  $H_2O/NaOH$  molar ratio for selected  $NaOH/CaCO_3$  molar ratios. A molar ratio of  $NaOH/CaCO_3 = 2$  is the stoichiometric for the decarbonisation reaction and the  $CaCO_3$  content in all experiments presented was constant. The sample information is shown in Supplementary Table S1 and those presented here are where  $NaOH/CaCO_3$  is: 2; Samples 19, 24, 26, 33, 30, 45, 54, 71, 64, 68, 59, 2.5; Samples 6, 13, 23, 29, 44, 57, 58, 63, 67, 69, 3; Samples 5, 8, 12, 22, 27, 40, 46, 48, 56, 62, 65, and 3.75; Samples 17, 18, 20, 28, 42, 47, 49, 50, 53, 61, 66.

**Fig.3.** X-ray diffractograms of Samples 1 and 5, showing the presence of  $Ca(OH)_2$  and  $Na_2CO_3 \cdot H_2O$  resulting from the de-carbonisation of the calcium carbonate via reaction with an aqueous  $NaOH$  solution.

**Table 1.** XRF analysis of the limestone chalk, shown as major oxide composition in weight %. Only components  $>0.1\%$  are presented.

**Table 2.** Starting material compositions for samples 1L and 5L produced from industrial grade limestone chalk. The conversion (X) values calculated from thermogravimetric analysis are also shown.

**Fig. 10.** Thermogravimetric and derivative thermogravimetric analyses of the Samples 1L (solid lines) and 5L (dashed lines).

**Fig. 11.** X-ray diffractograms of Samples 1L and 5L revealing the presence of  $Ca(OH)_2$  and  $Na_2CO_3 \cdot xH_2O$  (where  $x = 0$  and/or 1) and confirming applicability of the technology to industrial grade calcareous sources.  $SiO_2$  (quartz) remains inert through the reaction.

**Table 3.** Solubility data of the various associated compounds in water, methanol, and ethanol. All values are at  $25^\circ C$  unless otherwise stated. Data are taken from: <http://chemister.ru/Database/search-en.php>.

**Fig. 12.** Conceptual process flow diagram/scheme for Process A. The dashed black arrows represent mass leaving the system which may also be recovered if desired.

**Fig. 13.** Conceptual process flow diagram/scheme for Process B. The dashed black arrows represent mass leaving the system which may also be recovered if desired.

**Fig. 14.** Minimum vaporisation energy requirements for the various starting mix compositions of  $H_2O$ ,  $CaCO_3$ , and  $NaOH$  to produce 1 kg of  $Ca(OH)_2$ . Note that up to 1.4 kg of  $Na_2CO_3$  is produced along with every kg of  $Ca(OH)_2$ . Methanol is the alcohol used in separation and the heats of vaporisation of methanol and water are taken from Ref. [23]. Solubility data from Table S4 are also used for the calculations. The 63 white dots represent the data points while the sample highlighted with a black circle is “Sample 1” and that highlighted with a white square is “Sample 5”. In order to visualize the spread, eight of the most energy intensive samples from Table S1 were excluded from the energy plot; these are the samples in which both Process A and Process B require  $>100$  MJ/kg  $Ca(OH)_2$  and are shown as red circles in the figures. (a) shows the energy requirements for Process A. (b) shows the energy requirements for Process B.

## Supporting information/Associated content

*Supplementary Table S1: The starting compositions of H<sub>2</sub>O, NaOH, and CaCO<sub>3</sub> in each sample tested. The calculated conversion is also presented as well as the amount (%) of NaOH used. The minimum energy requirements per kg Ca(OH)<sub>2</sub>, calculated from the heats of vaporisation of water and alcohol (methanol), for Processes A and B are also shown. Note that up to 1.4 kg of Na<sub>2</sub>CO<sub>3</sub> is produced alongside 1 kg of Ca(OH)<sub>2</sub>. This data set was used to generate Figures 1 and 8 in the manuscript.*

ID	H <sub>2</sub> O (g)	NaOH (g)	CaCO <sub>3</sub> (g)	X (%)	NaOH used %	ID	H <sub>2</sub> O (g)	NaOH (g)	CaCO <sub>3</sub> (g)	X (%)	NaOH used %
1	67.53	46.05	10.03	95.96	16.71	37	25.01	11.99	12.03	46.06	36.93
2	63.02	56.04	10.02	95.59	13.66	38	15.04	13.09	10.02	45.86	28.06
3	223.32	100.02	10.00	92.97	7.43	39	50.03	64.99	10.00	45.40	5.58
4	135.03	92.17	10.00	90.63	7.86	40	30.06	11.99	10.00	41.67	27.77
5	15.04	12.01	9.98	86.03	57.14	41	20.00	11.04	10.05	40.84	29.72
6	10.03	10.03	10.06	83.70	67.10	42	40.16	15.05	10.04	39.43	21.03
7	45.04	36.08	10.06	81.11	18.08	43	26.05	13.02	10.02	38.23	23.52
8	20.06	12.06	10.00	78.73	52.18	44	7.02	10.07	10.02	31.94	25.40
9	20.08	19.98	9.89	78.49	31.05	45	20.01	8.05	10.02	31.91	31.75
10	30.04	24.03	9.97	78.10	25.90	46	5.02	12.06	10.02	31.76	21.09
11	60.03	30.07	10.08	78.10	20.92	47	12.05	15.05	10.09	30.09	16.12
12	12.07	12.07	10.00	77.66	51.43	48	40.05	12.08	10.07	29.44	19.62
13	15.04	10.05	9.98	73.81	58.59	49	50.02	15.03	10.07	28.67	15.35
14	30.01	20.04	10.00	70.59	28.15	50	10.03	15.00	10.01	28.54	15.22
15	40.04	25.04	10.06	69.97	22.47	51	21.35	35.33	10.03	27.69	6.28
16	87.53	27.51	10.02	69.30	20.17	52	10.04	15.00	12.09	26.72	17.21
17	25.00	15.06	10.03	69.23	36.85	53	6.06	14.98	10.00	26.25	14.01
18	20.06	14.98	10.08	69.09	37.16	54	25.05	8.04	10.14	21.08	21.25
19	8.02	8.06	10.02	69.02	68.58	55	13.51	15.98	9.98	20.73	10.35
20	15.05	15.01	9.99	67.80	36.06	56	50.00	12.03	9.99	19.75	13.11
21	40.00	20.01	9.97	67.44	26.86	57	30.02	10.03	10.04	19.73	15.79
22	13.50	11.99	10.03	66.34	44.35	58	5.02	10.05	10.01	16.50	13.13
23	12.09	9.99	9.97	62.84	50.12	59	30.01	8.04	9.99	16.11	16.00
24	7.03	8.03	10.02	61.35	61.19	60	10.06	16.95	10.03	15.37	7.27
25	14.06	12.98	9.99	59.56	36.64	61	8.04	15.04	9.99	13.47	7.15
26	10.02	8.05	10.03	58.46	58.21	62	4.03	12.06	10.02	12.31	8.17
27	10.05	12.00	10.02	57.58	38.43	63	40.04	10.06	10.03	12.08	9.62
28	30.02	15.04	10.01	55.24	29.38	64	5.06	8.03	10.04	11.96	11.95
29	8.06	10.07	10.07	53.26	42.57	65	7.07	11.99	9.98	11.14	7.41
30	15.03	8.01	9.98	52.51	52.29	66	4.10	15.02	10.01	11.08	5.90
31	20.02	13.02	10.04	52.22	32.18	67	4.03	9.96	10.05	9.99	8.05
32	15.09	11.06	10.04	51.91	37.67	68	40.00	8.00	9.99	7.46	7.45
33	12.02	8.08	10.03	51.90	51.50	69	50.03	10.03	10.05	7.29	5.84
34	9.98	11.44	10.00	51.07	35.68	70	10.12	19.00	10.03	7.24	3.06
35	15.02	20.06	10.01	48.45	19.32	71	50.00	7.99	10.00	3.54	3.54
36	25.01	13.00	10.05	47.42	29.30						

## Acknowledgements

The authors would like to acknowledge the financial support of the Engineering and Physical Sciences Research Council (grant EP/R025959/1) and CEMEX Asia Research AG. The XRF analysis was performed at HADES/MIDAS facility at the University of Sheffield established with financial support from EPSRC and BEIS (grant EP/T011424/1). The authors would also like to thank the advisory group who contributed to this work: Alan Maries, Mark Tyrer, John Stennett, Nestor-Isaias Quintero-Mora, Magnus Nyberg, Olga Chowaniec, and Juan-Carlos Martinez.

## References

1. Kolb, H. Preparation of carbonates. *ZKG. INT.*, **54(5)**, 262 (2001).
2. Scrivener, K. L., John, V. M., & Gartner, E. M. Eco-efficient cements: Potential economically viable solutions for a low-CO<sub>2</sub> cement-based materials industry. *CEMENT CONCRETE RES.* **114**, 2-26 (2018).
3. Taylor, H.F.W., *Cement Chemistry* (Telford, London, 1997).
4. Ghosh, A. & Chatterjee A., *Iron Making and Steelmaking: Theory and Practice* (PHI Learning Pvt. Ltd, New Delhi, 2008).
5. Fisher, L.V. & Barron A. R. The recycling and reuse of steelmaking slags - A review. *RESOUR. CONSERV. RECY.* **146**, 244-255 (2019).
6. Manovic, V. & Anthony E.J. Lime-based sorbents for high-temperature CO<sub>2</sub> capture - A review of sorbent modification methods. *INT. J. ENV. RES. PUB. HE.* **7(8)**, 3129-3140 (2010).
7. Shearon, W.H., Louviere, W.H. & Laperouse, R.M. Cane sugar refining. *IND. ENG. CHEM.* **43(3)**, 552-563 (1951).
8. Anderson, S.T. Cost implications of uncertainty in CO<sub>2</sub> storage resource estimates: A review. *NAT. RESOUR. RES.* **26(2)**, 137-159 (2017).
9. Middleton, R.S. & Yaw S. The cost of getting CCS wrong: Uncertainty, infrastructure design, and stranded CO<sub>2</sub>. *INT. J. GREENH. GAS. CON.* **70**, 1-11 (2018).
10. U.S. Geological Survey, 2019, Mineral commodity summaries 2020: National Minerals Information Center. <https://www.usgs.gov/centers/nmic/mineral-commodity-summaries>
11. Andrew, R.M. Global CO<sub>2</sub> emissions from cement production. *EARTH SYST. SCI. DATA.* **10(1)**, 195 (2018).
12. Stocker, T.F., et al., *Climate Change 2013: The Physical Science Basis. Contribution of working group I to the fifth assessment report of the intergovernmental panel on climate change* (Cambridge University Press, New York, 2013).
13. Friedlingstein, P. et al. Global carbon budget 2019. *EARTH SYST. SCI. DATA.* **11(4)**, 1783 -1838 (2019).
14. Habert, G et al. Environmental impacts and decarbonization strategies in the cement and concrete industries. *NAT. REV. EARTH. ENVIRON.* (2020). <https://doi.org/10.1038/s43017-020-0093-3>
15. Ellis, L. D., Badel, A. F., Chiang, M. L., Park, R. J. Y., & Chiang, Y. M. Toward electrochemical synthesis of cement - An electrolyzer-based process for decarbonating CaCO<sub>3</sub> while producing useful gas streams. *P. NATL. ACAD. SCI.* **117(23)**, 12584-12591 (2020).
16. European Commission, 2007, *Integrated Pollution Prevention and Control (IPCC) - Reference Document on Best Available Techniques in the Large Volume Inorganic Chemicals - Solids and Others industry.*
17. United States Environmental Protection Agency (EPA), 2009, *Technical Support Document for the Soda Ash Manufacturing Sector: Proposed Rule for Mandatory Reporting of Greenhouse Gases: Washington D.C.*
18. Nancollas, G.H. & N. Purdie, The kinetics of crystal growth *Q REV CHEM SOC*, **18(1)**, 1-20. (1964).
19. Eugster, H.P. & Smith G.I. Mineral equilibria in the Searles Lake evaporites, California. *J. PETROL.* **6(3)**, 473-522 (1965).
20. Monnin, C. & Schott J. Determination of the solubility products of sodium carbonate minerals and an application to trona deposition in Lake Magadi (Kenya). *GEOCHIM. COSMOCHIM. AC.* **48(3)**, 571-581 (1984).
21. Mahmoudkhani, M. & Keith D.W. Low-energy sodium hydroxide recovery for CO<sub>2</sub> capture from atmospheric air - Thermodynamic analysis. *INT. J. GREENH. GAS. CON.* **3(4)**, 376-384 (2009).
22. Lach, A., et al. A new Pitzer parameterization for the binary NaOH-H<sub>2</sub>O and Ternary NaOH-NaCl-H<sub>2</sub>O and NaOH-LiOH-H<sub>2</sub>O Systems up to NaOH Solid Salt Saturation, from 273.15 to 523.15K and at saturated vapor pressure. *J. SOLUTION CHEM.* **44(7)**, 1424-1451 (2015).
23. McBride, B.J. *NASA Glenn Coefficients for Calculating Thermodynamic Properties of Individual Species (National Aeronautics and Space Administration, John H. Glenn Research Center at Lewis Field, 2002).*
24. Wu, Y., Xie, H., Liu, T., Wang, Y., Wang, F., Gao, X., & Liang, B. Soda Ash Production with Low Energy Consumption Using Proton Cycled Membrane Electrolysis. *IND. ENG. CHEM. RES.* **58(8)**, 3450-3458 (2019).
25. Schorcht, F., Kourti, I., Scalet, B. M., Roudier, S., & Sancho, L. D. *Best available techniques (BAT) Reference Document for the Production of Cement, Lime and Magnesium Oxide. European*

- Commission Joint Research Centre Institute for Prospective Technological Studies (Report EUR 26129 EN Luxembourg: Publications Office of the European Union, 2013).
26. Schneider, M. Process technology for efficient and sustainable cement production. *CEMENT CONCRETE RES.* **78**, 14-23 (2015).
  27. Schneider, M., Romer, M., Tschudin, M., & Bolio, H. Sustainable cement production—present and future. *CEMENT CONCRETE RES.* **41(7)**, 642-650 (2011).
  28. Hanein, T., F.P. Glasser, & M.N. Bannerman, Thermodynamic data for cement clinkering. *CEMENT CONCRETE RES.* **132**(106043), (2020).
  29. van Oss, H.G. & A.C. Padovani, Cement Manufacture and the Environment: Part I: Chemistry and Technology. *J IND ECOL.* **6(1)**, 89-105 (2002).
  30. Zunino, F., Martirena F., & Scrivener, K. Limestone Calcined Clay Cements (LC<sup>3</sup>). *ACI MATER J*, **118(3)**, (2021).
  31. Sharma, M., Bishnoi, S., Martirena, F., & Scrivener, K. Limestone calcined clay cement and concrete: A state-of-the-art review. *CEMENT CONCRETE RES.* **149**(106564), (2021).
  32. Hanein, T., Thienel, K.C., Zunino, F., Marsh, A.T.M., Maier, M., Wang, B., Canut, M., Juenger, M.C.G., Ben Haha, M., Al-Jaberi, L.A., Reyes R.S.A., Alujas Díaz, A., Scrivener K. L., Bernal, S.A., Provis, J.L., Sui, T., Bishnoi, S. & J.F.M. Hernández. Clay Calcination Technology: State-of-the-Art Review by the RILEM TC 282-CCL. *MATER STRUCT*, under review (2021).
  33. Rumayor, M., Dominguez-Ramos, A., & Irabien, A. Toward the Decarbonization of Hard-To-Abate Sectors: A Case Study of the Soda Ash Production. *ACS SUSTAIN. CHEM. ENG.* **8(32)**, 11956-11966 (2020).
  34. Nelson, T. O., Coleman, L. J., Green, D. A., & Gupta, R. P. The dry carbonate process: carbon dioxide recovery from power plant flue gas. *ENRGY. PROCED.* **1(1)**, 1305-1311 (2009).
  35. Lee, J. H., Lee, D. W., Kwak, C., Kang, K., & Lee, J. H. Technoeconomic and Environmental Evaluation of Sodium Bicarbonate Production Using CO<sub>2</sub> from Flue Gas of a Coal-Fired Power Plant. *IND. ENG. CHEM. RES.* **58(34)**, 15533-15541 (2019).
  36. Shaqour, F., Ismeik, M., & Esaifan, M. Alkali activation of natural clay using a Ca (OH)<sub>2</sub>/Na<sub>2</sub>CO<sub>3</sub> alkaline mixture. *CLAY MINER.* **52(4)**, 485-496 (2017).
  37. Provis, J.L. & Van Deventer J.S.J. Alkali Activated Materials: State-of-the-Art Report (RILEM TC 224-AAM. Vol. 13. Springer Science & Business Media 2013).
  38. McDonald, L., Glasser, F. P., & Imbabi, M. S. A New, Carbon-Negative Precipitated Calcium Carbonate Admixture (PCC-A) for Low Carbon Portland Cements. *MATERIALS*, **12(4)**, 554 (2019).
  39. Simon, A., Fujioka, T., Price, W. E., & Nghiem, L. D. Sodium hydroxide production from sodium carbonate and bicarbonate solutions using membrane electrolysis: SEP PURIF TECHNOL. **127**, 70-76 (2014).
  40. Liu, J. et al. Hydrogen-motivated electrolysis of sodium carbonate with extremely low cell voltage. *CHEM. COMMUN.* **54(29)**, 3582-3585 (2018).
  41. Fedyaeva, O. N., & Vostrikov, A. A. Processing of pulp and paper industry wastes by supercritical water gasification. *RUSS. J. PHYS. CHEM. B.* **13(7)**, 1071-1078 (2019).
  42. Garcia-Herrero, I., Margallo, M., Onandía, R., Aldaco, R., & Irabien, A. Life Cycle Assessment model for the chlor-alkali process: A comprehensive review of resources and available technologies. *SUSTAIN. PROD. CONSUM.* **12**, 44-58 (2017).
  43. Hong, J., Chen, W., Wang, Y., Xu, C., & Xu, X. Life cycle assessment of caustic soda production: a case study in China. *J. CLEAN. PROD.* **66**, 113-120 (2014).
  44. Lin, H. W., Cejudo-Marín, R., Jeremiasse, A. W., Rabaey, K., Yuan, Z., & Pikaar, I. Direct anodic hydrochloric acid and cathodic caustic production during water electrolysis. *SCI. REP.* **6(1)**, 1 – 4 (2016).
  45. Vallette, J., Murtagh, C., Dedeo M., & Stamm, R. Chlorine and Building Materials A Global Inventory of Production Technologies, Markets, and Pollution Phase 1: Africa, The Americas, and Europe. Healthy Building Network: Washington DC. (2018)
  46. Garside, M., Plastic industry worldwide: Statista Dossier on the global plastic industry. (2020)
  47. Petrović, E.K. & L.K. Hamer, Improving the Healthiness of Sustainable Construction: Example of Polyvinyl Chloride (PVC). *BUILDINGS*, **8(2)**, 28 (2018).

#### 4. Alternative decarbonisation route: effect of residence time and stirring speed

This work aims to assess the efficiency of the reaction depending on fundamental processing conditions, such as stirring rate and residence time. In fact, those parameters may lead to enhanced or contained economic efforts for any industrial process, and defining the system behaviour when these conditions vary is crucial as preliminary information for industrial applicability. The work is totally based on experimental data, and the outcomes suggest high potential for industrial feasibility. It has been already accepted for publication to *Physical Chemistry Chemical Physics* journal. I here certify that I conceptualised and performed all the experiments, including the characterisation, I drafted the original manuscript, replied to the concerns expressed by the peer-reviewers, and took care of the whole submission process.

# Decarbonisation of calcium carbonate in sodium hydroxide solutions at ambient conditions: effect of residence time and mixing rates

Marco Simoni<sup>1</sup>, Theodore Hanein<sup>1\*</sup>, Chun Long Woo<sup>1</sup>, Mark Tyrer<sup>2</sup>, Magnus Nyberg<sup>3</sup>, Juan-Carlos Martinez<sup>3</sup>, Nestor I. Quintero-Mora<sup>4</sup>, John L. Provis<sup>1</sup>, and Hajime Kinoshita<sup>1\*</sup>.

<sup>1</sup> University of Sheffield, Department of Materials Science & Engineering, S1 3JD, Sheffield, UK

<sup>2</sup> Collegium Basilea, Institute of Advanced Study, Hochstrasse 51, 4053 Basel, Switzerland

<sup>3</sup> CEMEX Asia Research AG, Römerstrasse 13, 2555 Brugg, Switzerland

<sup>4</sup> CEMEX Operaciones Mexico, Constitution 444 pte. Monterrey, Mexico

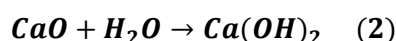
\* Corresponding authors: [t.hanein@sheffield.ac.uk](mailto:t.hanein@sheffield.ac.uk), [h.kinoshita@sheffield.ac.uk](mailto:h.kinoshita@sheffield.ac.uk), [marco.simoni.w@gmail.com](mailto:marco.simoni.w@gmail.com)

## Abstract

The decarbonisation of  $\text{CaCO}_3$  is essential for the production of lime ( $\text{Ca(OH)}_2$  and  $\text{CaO}$ ), which is a commodity required in several large industries and the main precursor for cement production.  $\text{CaCO}_3$  is usually decarbonised at high temperatures, generating gaseous  $\text{CO}_2$  which will require post-process capture to minimise its release into the environment. We have developed a new process that can decarbonise  $\text{CaCO}_3$  under ambient conditions, while sequestering the  $\text{CO}_2$  as  $\text{Na}_2\text{CO}_3 \cdot \text{H}_2\text{O}$  or  $\text{Na}_2\text{CO}_3$  in the same stage. Here, the effects of increasing stirring rates and residence times on reaction efficiency of the key reaction occurring between  $\text{CaCO}_3$  and  $\text{NaOH}$  solution are studied. It is shown that the reaction is enhanced at lower stirring rates and longer residence times up to 300 seconds of contact between the reactants. The mass balance performed for Ca and  $\text{CO}_2$  revealed that up to the 95% of the process  $\text{CO}_2$  embodied in  $\text{CaCO}_3$  was sequestered, with maximum capture rate assessed at  $n$  moles  $\text{CO}_2$  captured per second of reaction progress. A deeper insight into the precipitation of  $\text{Na}_2\text{CO}_3 \cdot \text{H}_2\text{O}$  or  $\text{Na}_2\text{CO}_3$  under different reaction conditions was gained, and SEM-EDX analysis enabled the observation of the reaction front by detection of Na migrating towards inner regions of partially-reacted limestone chalk particles.

# 1. Introduction

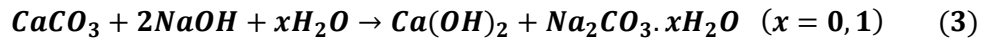
Lime (CaO) or slaked lime (Ca(OH)<sub>2</sub>) are essential components for a wide range of industries and applications worldwide [1], such as: steel manufacturing, construction, water treatment, mineral processing, and others. Given its very low toxicity and mild basic properties [2, 3], Ca(OH)<sub>2</sub> is also widely used in the food industry [4]. The production of Ca(OH)<sub>2</sub> is currently performed through a two-step process, involving 1) the calcination of limestone to give lime, CaO (Equation 1) [5], and 2) its subsequent hydration “slaking” (Equation 2) [1, 6].



In the slaked lime manufacturing process, the calcination of limestone represents the most energy-demanding and CO<sub>2</sub> emitting step; it is conducted in several types of firing kilns [1], and it leads to the release of the process CO<sub>2</sub> from the decarbonisation stoichiometry (Equation 1), and fuel-derived CO<sub>2</sub> by combustion of fossil fuels used to heat the kiln to provide the firing temperature required (between 800 and 1200°C) [7, 8]. The following Step 2 (Equation 2) mainly requires electrical energy input, to handle and mix the reactants and products of this exothermic hydration process [1]. Therefore, the efficiency linked to the energy usage within a given kiln plays a crucial role in defining the overall sustainability of the process; multiple factors may influence the energy input and the resulting efficiency for a given kiln type, such as the quality and the particle size of the limestone feed, the degree of conversion desired, and the moisture [9]. About 1.0-1.8 kg of CO<sub>2</sub> are emitted per kg of lime produced [1], and given the worldwide annual production (over 70 Mt in 2020 [10]), the lime industry is a significant emitter of greenhouse gases (GHG) which are the main contributors to global warming.

Intense efforts and significant investment from this industry are needed to mitigate the emissions of CO<sub>2</sub> to the atmosphere. Considering the calcination of limestone in a broader sense, such a process is also the basis of the Portland cement production industry; over 6 Gt of limestone are annually processed to satisfy the cement market (over 4 Gt in 2018 [11]), resulting in about 3-4 Gt of CO<sub>2</sub> emitted from chemical and fuel contributions combined (≈4% of the total anthropogenic emissions [12, 13]). Given the size of both the lime and cement market worldwide, the validation of a more sustainable limestone decarbonisation route would be a significant contribution to meet the goal (overall 86% CO<sub>2</sub> emissions cut by 2050) set and agreed by the United Nations [8, 14, 15].

Our previous work demonstrated the technical feasibility of an alternative route to decarbonisation of limestone, achieved at ambient conditions without heating [16]. The process is based on the reaction between  $\text{CaCO}_3$  particles and highly concentrated NaOH solutions to produce  $\text{Ca(OH)}_2$  and  $\text{Na}_2\text{CO}_3 \cdot \text{H}_2\text{O}$  or  $\text{Na}_2\text{CO}_3$ , allowing for the decarbonisation directly from the solid limestone and simultaneous sequestration of  $\text{CO}_2$  into stable mineral forms (Equation 3).



This process is particularly beneficial because it does not require the combustion of fuels and avoids the associated  $\text{CO}_2$  emissions, while the process  $\text{CO}_2$  embodied in  $\text{CaCO}_3$  is sequestered as  $\text{Na}_2\text{CO}_3 \cdot \text{H}_2\text{O}$  or  $\text{Na}_2\text{CO}_3$ . Our previous study also highlighted the feasibility of applying this process to impure industrial grade limestone with significant silica content [16].

It is well known that the overall reaction rate in heterogeneous systems would depend on the reaction rate of the involved chemical reactions and the thickness of the product surface layer [17], according to the un-reacted core model [18, 19]. Both the residence time and the mixing rate might affect the reaction kinetic, since a longer contact between the reactants and a higher turbulence would generally enhance the efficacy of a reaction. It is also true that a greater centrifugal force on the solid particles compared with the liquid phase may also affect the overall reactivity of the components [20], due to a separation of the phases resulting in a lower contact surface [21-23]. Given that, this work aims to clarify the dependence of the system studied on the stirring rate and residence time, in order to optimise the process with a view toward its industrialisation. It must be mentioned that such a study only represents a preliminary step towards the scale-up of the process, which needs to take into account evident technical difficulties before considering industrial applicability. These issues are mainly linked to the handling of highly-corrosive NaOH solutions, the management of chlorine gas deriving from the enhanced production of the required chemical NaOH, and the adjustment of the processing conditions in accordance with the scaling-up. Although, the liquid stream from the solid chlor-alkali process is a  $\approx 32$  wt.% NaOH solution (approximately 12 M) [24], comparable with the concentrations used here. Moreover, the excess of chlorine gas may be water scrubbed, and the resulting solutions may be used for the production of Cl-containing cements [25] for non-reinforced concrete. Considering that over the 60% of the concrete worldwide is unreinforced [26], significant proportions of the toxic chlorine gas from the chlor-alkali process might be immobilised upon cementation. Despite the title study aims to investigate the effect of crucial processing conditions, the authors are fully aware that the presented outcomes might fail in

representing the system behaviour at larger scale. Although, this preliminary investigation offers that fundamental basic starting point for a more detailed investigation targeting the proper scale-up of the process.

The present study also aims to clarify the equilibrium between the species  $\text{Na}_2\text{CO}_3\cdot\text{H}_2\text{O}$  and  $\text{Na}_2\text{CO}_3$  at the processing conditions considered, since the co-production of  $\text{Ca}(\text{OH})_2$  and  $\text{Na}_2\text{CO}_3\cdot\text{H}_2\text{O}$  implies the need for a following separation of the products, crucial for their individual sale or use, not discussed here. For instance, high Na contents (above 2 wt.%) would prevent the use of  $\text{Ca}(\text{OH})_2$  for cement production [27, 28], limiting the applicability of this novel technology. Since the solubility of the different species here involved would likely play a key-role for their effective separation, the present study also assessed the precipitation of the by-product  $\text{Na}_2\text{CO}_3\cdot\text{H}_2\text{O}$  or  $\text{Na}_2\text{CO}_3$  ( $x = 0, 1$  in Equation 3, respectively) depending on the reaction conditions used. Finally, solid particles of an industrial grade chalk are reacted to quantify the reaction progress by visual tracking of the products surface layer via SEM-EDX analyses.

## 2. Materials and Methods

### 2.1. Materials

The materials used in this work included commercial grade chemicals: Sigma-Aldrich  $\text{CaCO}_3$  ( $\geq 99\%$ ) and Honeywell Fluka NaOH ( $\geq 97\%$ ). Additionally, the same industrial grade chalk used in a previous study were also considered as a source of  $\text{CaCO}_3$  [16]; the oxide elemental composition gained by XRF analysis is reported in Table 1 below. A dry-state Particle Size Distribution (PSD) analysis was chosen for targeted samples, to avoid the dissolution of the solids at any extent. About 10 g of material was used for the analysis, and the value reported for each sample is an average of 10 consecutive measurements.

Table 1.

	<i>CaO</i>	<i>SiO<sub>2</sub></i>	<i>Al<sub>2</sub>O<sub>3</sub></i>	<i>Fe<sub>2</sub>O<sub>3</sub></i>	<i>K<sub>2</sub>O</i>	<i>MgO</i>	<i>Others</i>	<i>LOI%</i>
<i>Wt.%</i>	44.0	21.0	3.0	1.1	0.6	0.3	<2.0%	29.5

### 2.2. Experimental Procedure

Given the high conversion extent observed in a previous study [15] for the ternary system of 27.1 wt.%  $\text{CaCO}_3$ , 32.4 wt.% NaOH, and 40.5 wt.%  $\text{H}_2\text{O}$ , this starting composition was considered in the following experiments to assess the effect of varying selected parameters on the reaction efficiency. First, NaOH was mixed with distilled water, resulting in a temperature increase of the system to  $\sim 80^\circ\text{C}$  due to the exothermic dissolution reaction.

The solutions were then heated to 90°C in a PTFE beaker with a volume of 6.5 cm<sup>3</sup>, to achieve an identical initial temperature for all experimental runs; following this, 10 g of CaCO<sub>3</sub> were introduced and no further temperature control was applied as the reaction was allowed to progress under laboratory ambient conditions (T ≈ 20°C). To ensure mixing, a PTFE centrifugal stirrer shaft (flat propeller, diameter 4 cm) was used with a Heidolph RZR 2020 overhead mixer, rotating in the bottom centre of the PTFE beaker. The use of PTFE was essential to avoid corrosion that may be caused by the hyper-alkaline NaOH solutions used. To study the effect of the mixing rate on the reaction efficiency, a series of experiments were carried out at each of 40, 300, 500, 800 and 2000 rpm for durations of 30, 300, 720, and 1200 s. The conditions used for each sample are reported Supplementary Electronic Material (Table S1). After the desired duration of reaction, 50 mL of methanol was added and the whole paste was stirred for 300 s to wash by dissolving any unreacted NaOH (NaOH solubility in methanol = 238 g/L [29]). The very low solubility of Ca(OH)<sub>2</sub> [3], CaCO<sub>3</sub> [30], Na<sub>2</sub>CO<sub>3</sub>·H<sub>2</sub>O [31], and Na<sub>2</sub>CO<sub>3</sub> [31] in methanol allows these solids to remain in the system without being lost during the washing.

The reagent grade chalk was reacted at slightly milder mixing regime, to better preserve the condition of the products. The reaction was performed in a plastic vessel with a magnetic stirring of 300 rpm for a total residence time of 300 s. 8.4 g of NaOH were added into 12.3 g of H<sub>2</sub>O to form 17 M NaOH solution, and the solution was cooled down to room temperature before adding 2.5 g of chalk, making the initial system of H<sub>2</sub>O (54.7 wt.%), NaOH (37.2 wt.%) and chalk (8.1 wt.%). A significantly high water-to-solid ratio was chosen to ensure a satisfactory mixing of all the reactants, with the less energetic stirring; anyway, the chosen composition has been tested on reagent grade CaCO<sub>3</sub> already, and it led to an almost total conversion to products [16]. After five minutes of reaction, 32 mL of methanol was added to the resulting paste and stirred for five minutes in order to remove any remaining NaOH.

Following their collection by vacuum filtration, all the solid products here discussed were dried in an 80°C oven for 2 hours; following, the samples selected for TG and XRD analyses were finely ground and sieved below 63µm. For the SEM analysis, selected samples were ground or not, to observe the targeted parameters discussed below.

## 2.3. Characterisation Techniques

### 2.3.1. X-Ray Diffraction (XRD)

X-ray diffraction (XRD) was used to qualitatively identify the reaction products of the reaction. The analysis was conducted by using a Bruker D2 PHASER desktop X-ray

diffractometer in Bragg-Brentano geometry, with a Cu-K $\alpha$  radiation source running at 30 kV and 10 mA, a one-dimensional LYNXEYE detector, and a 1 mm divergence slit. All the samples were powders, and they were loaded onto sample holders with a diameter and depth of 2.5 cm and 1 mm, respectively. All the analyses were conducted between 5° and 80° 2 $\theta$ , with a step size of 0.02° at 0.5 seconds per step; the stage was set to rotate at 15 rpm. Qualitative phase identification was carried out using the Highscore-Plus software and the PDF-4 2019 database.

### 2.3.2. Thermogravimetry (TG/DTG)

Thermogravimetric analysis (TGA) was carried out by sampling about 40 mg of products to be analysed on a PerkinElmer TGA 4000 from 30°C to 800°C at a heating rate of 10°C/min with a 40 mL/min N<sub>2</sub> flow. The temperature was kept at 800°C for 1 hour to ensure complete loss of CO<sub>2</sub> from CaCO<sub>3</sub>. To identify evolving gases, a Hiden mass spectrometer (HPR-20 GIC EGA) was used to record the signals for H<sub>2</sub>O and CO<sub>2</sub>, the only gases involved here. The reaction efficiency  $\alpha$ , only reflecting the fraction of CaCO<sub>3</sub> converted to Ca(OH)<sub>2</sub>, was calculated from the weight loss in the temperature ranges for the thermal decomposition of Ca(OH)<sub>2</sub> (310-470 °C [32]) and CaCO<sub>3</sub> (560-800 °C [33]), as reported in Figure 1 and Equation 4.

$$\alpha = \frac{w\%_{[Ca(OH)_2]}}{MW_{Ca(OH)_2}} \bigg/ \left( \frac{w\%_{[Ca(OH)_2]}}{MW_{Ca(OH)_2}} + \frac{w\%_{[CaCO_3]}}{MW_{CaCO_3}} \right) \quad (4)$$

The content of Na<sub>2</sub>CO<sub>3</sub>·H<sub>2</sub>O could similarly be estimated from mass loss in the temperature range 50-130°C [34] (Figure 1). The measurement was repeated 6 times for each sample to estimate the measurement error ( $\pm 0.16$  wt.%,  $\pm 0.10$  wt.% and  $\pm 0.16$  wt.% for Na<sub>2</sub>CO<sub>3</sub>·H<sub>2</sub>O, Ca(OH)<sub>2</sub> and CaCO<sub>3</sub>, respectively).

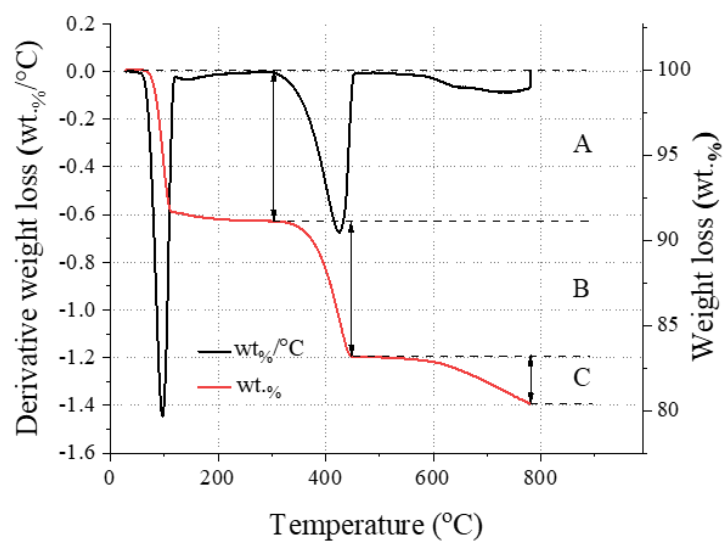


Fig. 1.

### 2.3.3. Scanning Electron Microscopy (SEM)

A Hitachi TM3030 scanning electron microscope with energy-dispersive X-ray spectroscopy (SEM-EDX) was used to gain a deeper insight on the penetration of sodium upon reaction. The solids were mounted in epoxy resin without crushing and left to harden for 72 hours. The analysis surface was ground and polished with progressively finer abrasives, up to a 1  $\mu\text{m}$  finish [35]; in addition, the samples were polished on cashmere polishing cloths by using diamond pastes of 6, 3, 2, 1 and 0.25  $\mu\text{m}$  (MetPrep). The samples then underwent a three-step carbon coating and were back-loaded to a metallic holder. Electrically conductive silver paint (RS Components) was applied at the metallic base-epoxy-resin interface to ensure sufficient conductivity and good quality of the SEM images, collected at a working distance of  $7.4 \pm 0.1$  mm. Separately, selected samples were crushed and sieved to targeted size ranges and attached to conductive carbon adhesive tapes (Agar Scientific).

### 3. Results and Discussion

#### 3.1. Reaction Products

The system under consideration shows a good capability to convert  $\text{CaCO}_3$  to  $\text{Ca(OH)}_2$ ,  $\text{Na}_2\text{CO}_3 \cdot \text{H}_2\text{O}$ , and  $\text{Na}_2\text{CO}_3$  [16]; here, the series of samples mixed at 300 rpm for all the residence times considered was taken as a representative baseline. The XRD analysis (Figure 2) showed the presence of only  $\text{CaCO}_3$ ,  $\text{Ca(OH)}_2$ ,  $\text{Na}_2\text{CO}_3 \cdot \text{H}_2\text{O}$  and  $\text{Na}_2\text{CO}_3$ , with respective main reflection angles  $2\theta$  of  $29.5^\circ$ ,  $18.1^\circ$ ,  $17.1^\circ$ , and  $30.2^\circ$ , within the solid products.

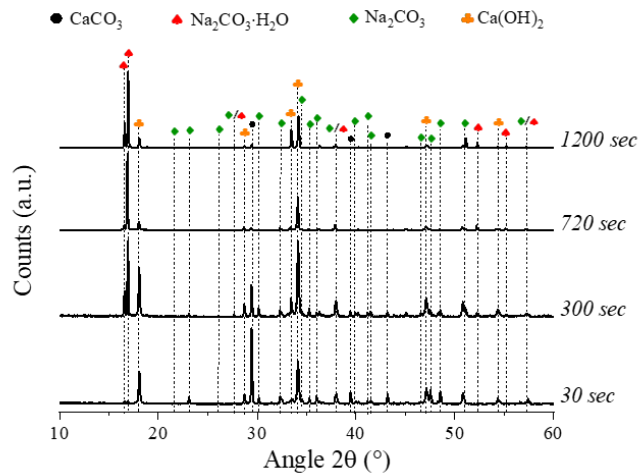


Fig. 2.

Specifically, the intensity of the peaks linked to  $\text{Ca(OH)}_2$  and  $\text{Na}_2\text{CO}_3 \cdot \text{H}_2\text{O}$  was increasing at longer residence times, while  $\text{CaCO}_3$  content appeared to decrease; in addition, the signals linked to  $\text{Na}_2\text{CO}_3$  could be detected at residence times of up to 300 seconds, while at longer ones those were not observable. The relative proportions of  $\text{Na}_2\text{CO}_3 \cdot \text{H}_2\text{O}$  and  $\text{Na}_2\text{CO}_3$  will be discussed in detail in Section 3.3.

In accordance with the XRD outcomes, the TG/dTG analysis of the same baseline samples (Figure 3) showed increasing weight losses in the temperature intervals  $50\text{-}130^\circ\text{C}$  and  $310\text{-}470^\circ\text{C}$ , referring to  $\text{Na}_2\text{CO}_3 \cdot \text{H}_2\text{O}$  [34] and  $\text{Ca(OH)}_2$  [32], respectively, and a decreasing  $\text{CaCO}_3$  content ( $560\text{-}800^\circ\text{C}$  [33]) at longer residence times.

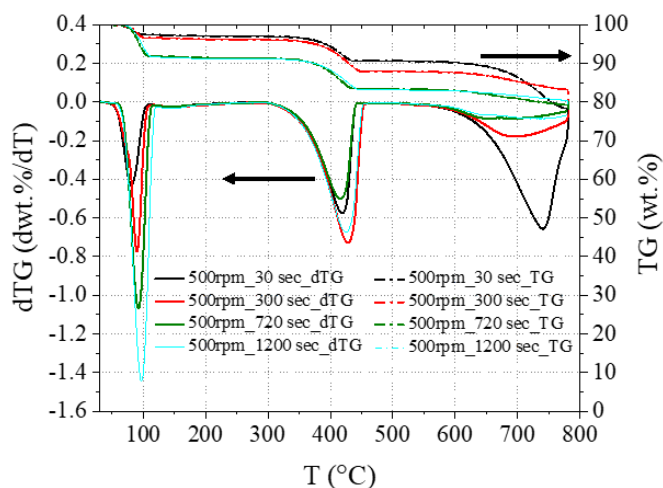


Fig. 3.

The quantification of phases from the TG analysis (Figure 3) is reported in Figure 4A. The amount of  $\text{Na}_2\text{CO}_3$  could not be directly quantified, since its thermal decomposition would occur above  $851^\circ\text{C}$  [36] and the analysis was conducted up to  $800^\circ\text{C}$ . However, the quantification of  $\text{Na}_2\text{CO}_3$  could be performed indirectly by taking into account the difference between the total (100%) and the sum of the other phases ( $\text{CaCO}_3$ ,  $\text{Ca}(\text{OH})_2$ , and  $\text{Na}_2\text{CO}_3 \cdot \text{H}_2\text{O}$ ). This approach could be considered reliable, since the XRD analysis confirmed the presence of the only phases  $\text{CaCO}_3$ ,  $\text{Ca}(\text{OH})_2$ ,  $\text{Na}_2\text{CO}_3 \cdot \text{H}_2\text{O}$ , and  $\text{Na}_2\text{CO}_3$  in the solid system (Figure 2). The XRD analysis also suggested the absence of any amorphous phase since no raised baseline was detected in any pattern (Figure 2). In addition, the weight uptake resulting from the incorporation of  $\text{Na}^+$  and  $\text{OH}^-$  ions from the solution may be used as a further confirmation of the phases detected by XRD and their quantification by TG. This value was calculated for each system by considering the ratio between the final measured weight of the dried products and the initial weight of  $\text{CaCO}_3$ . The weight uptake can represent the extent of reaction, assuming that any residual  $\text{NaOH}$  is removed from the system after washing. Such an assumption appeared to be confirmed by the absence of the  $\text{NaOH}$  characteristic peak at  $2\theta = 16^\circ$  [37] in the XRD analysis reported in Figure 2. Figure 4B shows the experimental weights registered for the representative series of samples, together with the theoretical lines that would result from the quantitative precipitation of  $\text{Na}_2\text{CO}_3 \cdot \text{H}_2\text{O}$  or  $\text{Na}_2\text{CO}_3$ .

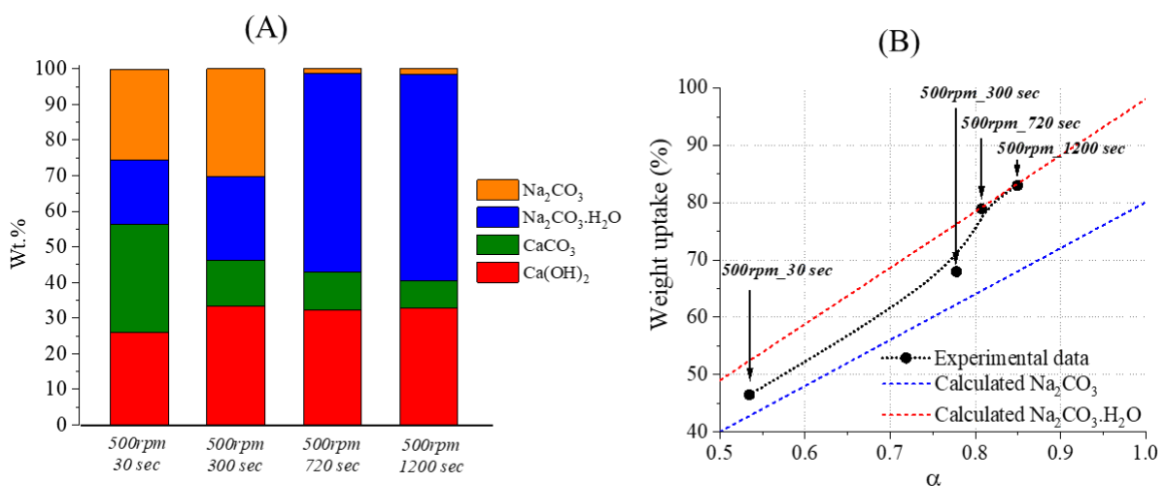


Fig. 4.

### 3.2. Effect of Stirring rate

The characterisation performed on all samples allowed for the determination of the effect on the reaction extent linked to the stirring rate. A Ca mass balance was performed for all the samples discussed here, in order to validate the results from TG analysis; the difference between the inbound (CaCO<sub>3</sub>) and outbound (Ca(OH)<sub>2</sub> and CaCO<sub>3</sub>) calcareous species was considered to do that, revealing errors of ±0.2 g of Ca. The Ca mass balance supported the TG analysis, and the specific values for each sample discussed is reported in S1, alongside an overview of the samples phase compositions gained by TG analysis. The XRD analysis was qualitatively reflecting the quantification performed, considering that the main peak related to CaCO<sub>3</sub> at 2θ = 29.5° was increasing at faster stirring rates, whereas those related to the products Ca(OH)<sub>2</sub>, Na<sub>2</sub>CO<sub>3</sub>.H<sub>2</sub>O, and Na<sub>2</sub>CO<sub>3</sub> were decreasing in intensity (Figure 5).

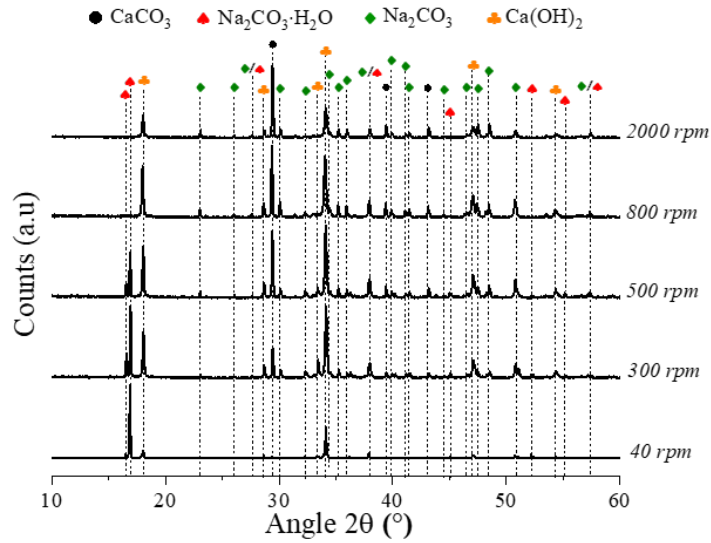


Fig.5.

The TG quantification reported in Figure 6 shows the highest conversion at a stirring rate of 40 rpm, while significant efficiency drops were observed at 2000 rpm. The loss of efficiency at increased stirring rate was most notable in those samples reacted for 30 seconds, with an efficiency drop of 34.1% between 40 and 300 rpm observed for this residence time; the impact was reduced at increasing ones. Generally, the increase in reaction extent above 300 seconds was limited.

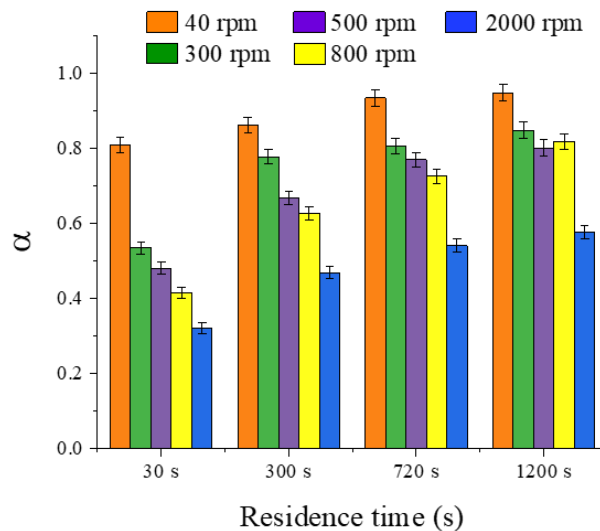


Fig.6.

These outcomes might be justified by physical reasons, as mentioned in Section 1, linked to the significantly different density of a 45 wt.% NaOH solution (1.42 – 1.48 kg/dm<sup>3</sup> [38]) and the reagent grade CaCO<sub>3</sub> (2.93 kg/dm<sup>3</sup> [39]). That would be expected to cause a net separation of the liquid and solid phases within the paste at higher stirring rates due to centrifugation effects, leading to a lower contact between the reactants [21-23] and a resulting hindered conversion, as shown in Figure 7.

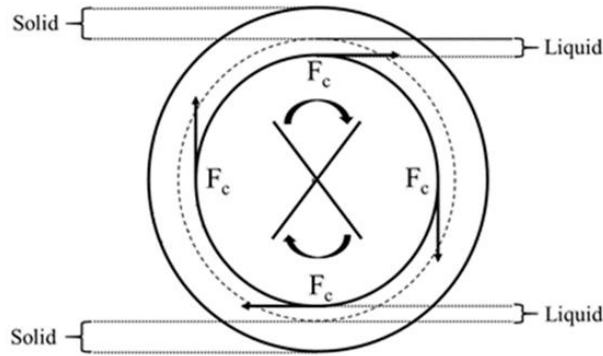


Fig.7.

Alternatively, the lower conversion registered at higher stirring rates may be linked to the main mechanism ruling the reaction progress; several models were considered, including diffusion, and contracting volume or surface, but a nucleation mechanism was strongly suggested. Figure 8 shows the fitting between the whole set of experimental data reported here and the nucleation model proposed by Avrami-Erofeyev [40]; it is reflected in Equation 5, where  $k$  and  $\alpha$  identify the kinetic constant and the conversion extent of the reaction, respectively and its integrated form (Equation 6).

$$f(\alpha) = \left(\frac{1}{k}\right) \left(\frac{\delta\alpha}{\delta t}\right) = 3(1-\alpha) [-\ln(1-\alpha)]^{2/3} \quad (5)$$

$$g(\alpha) = [-\ln(1-\alpha)]^{1/3} = kt \quad (6)$$

The Avrami-Erofeyev model assumes that 1) nucleation occurs randomly within the unreacted material volume, 2) the extent of nucleation does not affect the nucleation rate, and 3) the nucleation growth is homogeneous in any spatial coordinate. Upon formation, the nucleus is unstable; once a wider portion around the nucleus nucleates, the stability increases, and the nucleus becomes a growth one. The nucleation is arrested by events of ingestion and coalescence, which generally imply that the nucleation front of one nucleus collides with another one expanding.

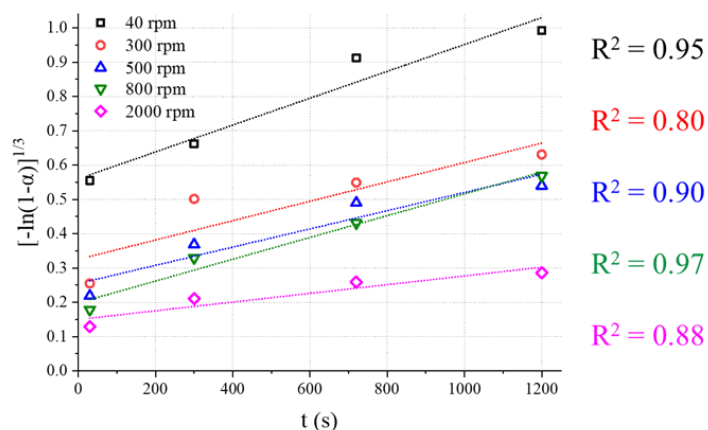


Fig.8.

While  $\alpha$  was calculated from Equation 4, the kinetic constant  $k$  was obtained by dividing  $\alpha$  for the residence time considered; doing this, the kinetic related to the conversion of  $\text{CaCO}_3$  to  $\text{Ca(OH)}_2$  could be outlined, whereas the formation of  $\text{Na}_2\text{CO}_3 \cdot \text{H}_2\text{O}$  and  $\text{Na}_2\text{CO}_3$  was not taken into account here. The decarbonisation rate was significantly decreasing after 30 seconds of reaction, when a maximum rate of  $2.7 \cdot 10^{-3}$  moles of  $\text{CaCO}_3$  converted per second was achieved at 40 rpm, over the double than the kinetics observed at 2000 rpm ( $1.2 \text{ moles CaCO}_3 \cdot \text{s}^{-1}$ ). The slower kinetics registered at different rates confirms the need for a precise optimisation aiming to an eventual scale-up.

Given the heterogeneous reaction taken into account here, a nucleation mechanism involves the primary formation of small crystals of the new product phase within large ones of the reactant; this process is thermodynamically unfavourable at first, given the higher free Gibbs energy  $\Delta G$  [41] linked to the instability of the nuclei formed [42]. Upon achievement of a critical size, the nucleus assumes a more stable configuration, while expanding and incorporating other potential nuclei; nucleation continues until the progression front covers the whole surface of the solid. From here, the nucleation kinetic lowers because of the surface product layer which reduces the contact surface between the reactants.

The effect of stirring rate on the nucleation density and crystal morphology has been empirically accepted in chemical and cast metals industries [43], and the role of convection in single crystals forming has been widely discussed already [44, 45]. Generally, the studies report an enhanced nucleation density in dynamic conditions with respect to static ones [46], leading to shorter residence times required [47]. Taking into account the high  $R^2$  values reported in Figure 8 in correlation with the Avrami-Erofeyev model, the present study would introduce controversial outcomes at first sight. In fact, nucleation appears to be hindered at higher stirring rates, when the collisions between the reactants and the

formation of surface irregularities and cracks should statistically be more frequent. Such a controversial observation might be likely explained by considering an enhanced partition of the solid and liquid bulks at higher stirring rates [22], preventing further contact and reaction progression (Figure 7). In other words, despite the higher turbulence, the entropy of the system would lower as a consequence of the hindered contact between solid and liquid reactants, reflecting a higher  $\Delta G$  at faster stirring rates. Such an effect could be furtherly increased by the eventual distorted expansion of the nuclei undergoing axial centrifugal forces  $F_c$  [48], as also outlined in Figure 9.

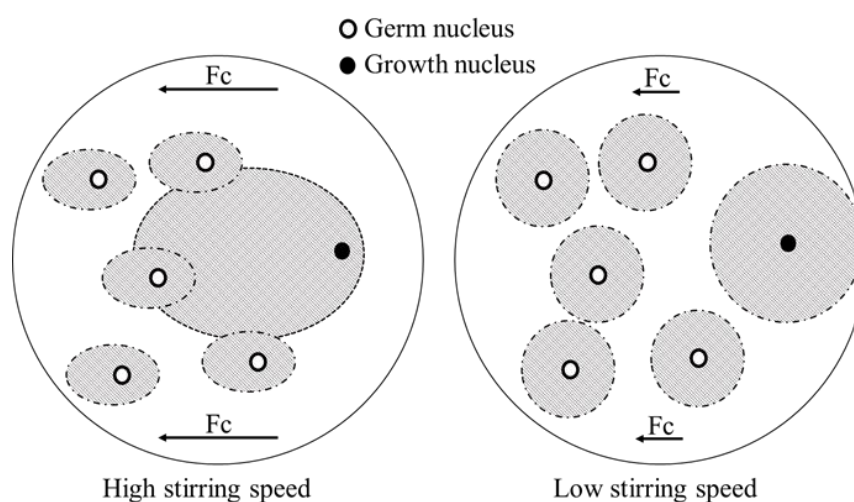
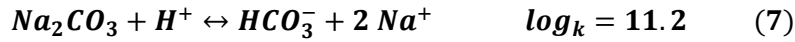


Fig.9.

### 3.3. Equilibrium between $\text{Na}_2\text{CO}_3 \cdot \text{H}_2\text{O}$ and $\text{Na}_2\text{CO}_3$

As mentioned in Section 1, an effective separation of the products will be required upon reaction, and it may likely involve their dissolution in water or solvent. The separation would likely exploit the different solubility of  $\text{Ca}(\text{OH})_2$ ,  $\text{Na}_2\text{CO}_3 \cdot \text{H}_2\text{O}$ , and  $\text{Na}_2\text{CO}_3$ , and the understanding of the equilibrium between  $\text{Na}_2\text{CO}_3 \cdot \text{H}_2\text{O}$  and  $\text{Na}_2\text{CO}_3$  could dictate the optimal processing conditions. The proportioning of  $\text{Na}_2\text{CO}_3 \cdot \text{H}_2\text{O}$  and  $\text{Na}_2\text{CO}_3$  at different stirring rates and residence times has been here assessed, and useful information has been provided for an eventual scale-up of the process. Together with the phase quantification performed by TG, the XRD analysis confirmed the enhanced formation of  $\text{Na}_2\text{CO}_3 \cdot \text{H}_2\text{O}$  with respect to  $\text{Na}_2\text{CO}_3$  up to a stirring rate of 800 rpm (Figure 5) and at increasing residence times (Figure 2). To gain further insight, the behaviour of  $\text{Na}_2\text{CO}_3 \cdot \text{H}_2\text{O}$  and  $\text{Na}_2\text{CO}_3$  in the  $\text{Na}_2\text{CO}_3$ - $\text{NaOH}$ - $\text{H}_2\text{O}$  system was studied using PHREEQC - PH REdox Equilibrium (in C language), a geochemical modelling software simulating a variety of reactions and processes at equilibrium [49], in particular focusing on the activity of water.

The simulation was performed at 20, 60 and 100°C; both Na<sub>2</sub>CO<sub>3</sub>·H<sub>2</sub>O (0.1 mol) and Na<sub>2</sub>CO<sub>3</sub> (0.1 mol) were initially introduced into 100 mL of pure water, and NaOH was added in successive steps up to 20 M; given the high NaOH concentrations taken into account, the Pitzer model was used here [50]. The Na<sub>2</sub>CO<sub>3</sub>·H<sub>2</sub>O and Na<sub>2</sub>CO<sub>3</sub> phases were specified by the equilibria reported below in Equations 7 and 8, respectively, while the total 2 moles of NaOH additions were performed in 20 steps up to a molality of 20 (2 moles NaOH in 0.1 kg H<sub>2</sub>O).



Precipitate compositions were then determined as a function of water activity, Figure 10B, where the highest concentrations of NaOH correspond to the lowest calculated water activities (Figure 10A). The simulation revealed the favourable ranges of the activity of water (*a*<sub>H<sub>2</sub>O</sub>) for the precipitation of Na<sub>2</sub>CO<sub>3</sub>·H<sub>2</sub>O (0.6 < *a*<sub>H<sub>2</sub>O</sub> < 0.8) and Na<sub>2</sub>CO<sub>3</sub> (*a*<sub>H<sub>2</sub>O</sub> < 0.6), as shown in Figure 10B. Increasing NaOH concentrations would lead to a higher viscosity [51, 52] while the activity of water would be significantly reduced [53-55] (Figure 10A).

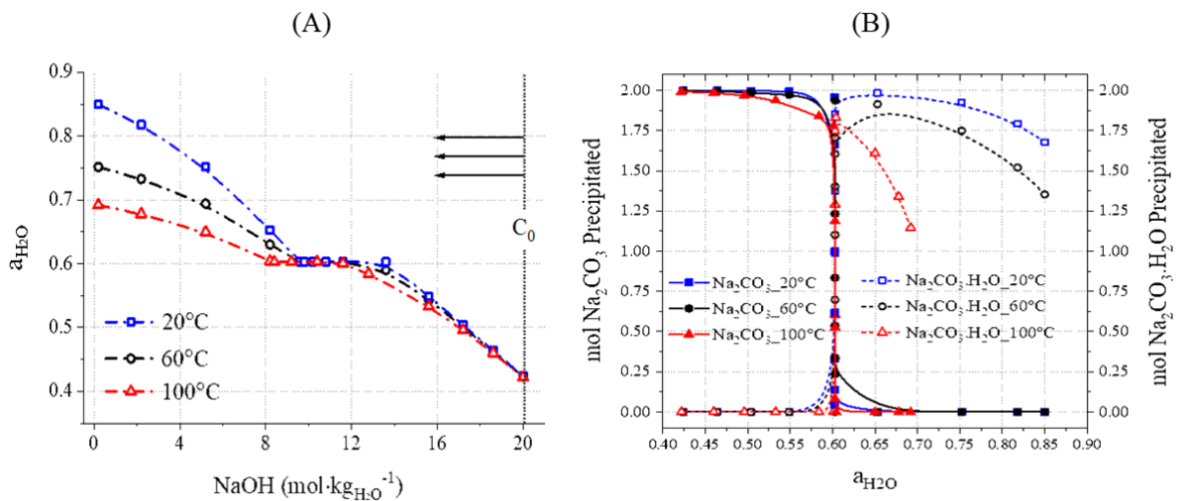


Fig. 10.

Additionally, given the stoichiometry of the reaction (Equation 3), and considering the concentration of dissolved Ca<sup>2+</sup> to be negligible under these highly alkaline conditions due to the limited solubility of Ca(OH)<sub>2</sub>, the final OH<sup>-</sup> concentration would depend on the consumption of NaOH to convert CaCO<sub>3</sub> to products. In other words, a higher conversion

would lead to lower final  $\text{OH}^-$  concentrations, as outlined by the experimental data reported in Figure 11.

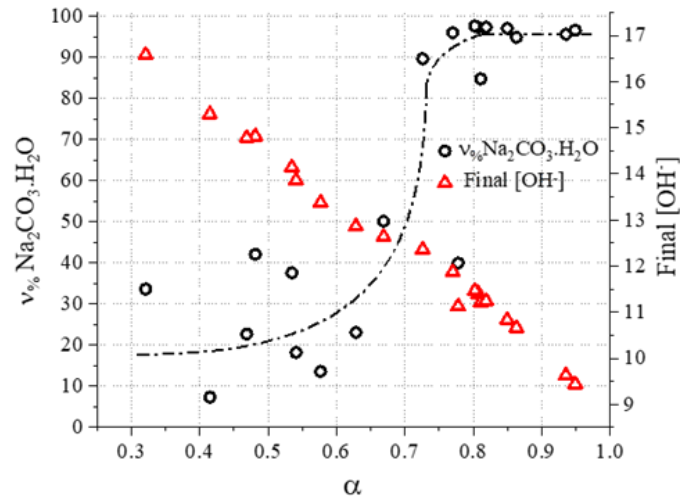


Fig.11.

Following the quantification of the solid phase species within the system, the molar proportion of  $\text{Na}_2\text{CO}_3 \cdot \text{H}_2\text{O}$  formed in the binary system  $\text{Na}_2\text{CO}_3 \cdot \text{H}_2\text{O}/\text{Na}_2\text{CO}_3$  can be calculated. Doing this, it was possible to observe that  $\text{Na}_2\text{CO}_3$  was dominantly forming at the early stage of the reaction (or when the progress of the reaction is limited) because of the low activity of water due to the high concentration of  $\text{NaOH}$  in the system (Figure 11). However, as the reaction progresses, the formation of  $\text{Na}_2\text{CO}_3 \cdot \text{H}_2\text{O}$  may have been enhanced by the rising  $\text{H}_2\text{O}$  activity due to the consumption of  $\text{NaOH}$ , as shown in Equation 3. This would explain the higher contents of  $\text{Na}_2\text{CO}_3$  in the systems with a limited progress of the reaction, corresponding to shorter residence times (Figure 4A) or faster stirring rates (Figure 5). These outcomes are in accordance with the thermodynamic trends reported in Figure 10B.

### 3.4. $\text{CO}_2$ capture

The quantification of  $\text{Na}_2\text{CO}_3 \cdot \text{H}_2\text{O}$  and  $\text{Na}_2\text{CO}_3$  also allowed to calculate the fraction of  $\text{CO}_2$  trapped out of the initial amount introduced as  $\text{CaCO}_3$ , and to outline the  $\text{CO}_2$  capture rate. Equation 9 outlines the mass balance for  $\text{CO}_2$  upon reaction, taking into account the initial  $\text{CO}_2$  introduced with  $\text{CaCO}_3$  ( $g\text{CO}_2, \text{Initial}$ ), the fraction of  $\text{CO}_2$  captured through precipitation of  $\text{Na}_2\text{CO}_3 \cdot \text{H}_2\text{O}$  and  $\text{Na}_2\text{CO}_3$  ( $g\text{CO}_2, \text{Captured}$ ), and the  $\text{CO}_2$  embodied into unreacted  $\text{CaCO}_3$  ( $g\text{CO}_2, \text{Unreacted}$ ). These parameters were calculated by taking into account  $\text{CO}_2$  fractions of

44.0 wt.%, 35.5 wt.% and 41.5 wt.% for  $\text{CaCO}_3$ ,  $\text{Na}_2\text{CO}_3 \cdot \text{H}_2\text{O}$ , and  $\text{Na}_2\text{CO}_3$ , respectively, apart from the sample-specific phase assemblage.

$$g\text{CO}_2, \text{Initial} - g\text{CO}_2, \text{Captured} = g\text{CO}_2, \text{Unreacted} \quad (9)$$

Approximately 4.4 g of  $\text{CO}_2$  are embodied into the initial 10 g of  $\text{CaCO}_3$  powders reacted, and for all the samples the mass balance depicted in equation 9 was respected with uncertainties of  $\pm 0.1$  g. That may be observed in Figure 12A, where  $g\text{CO}_2, \text{Captured}$  and  $g\text{CO}_2, \text{Unreacted}$  are plotted against the residence time for all the samples discussed. It is clear that the reaction between  $\text{CaCO}_3$  and  $\text{NaOH}$  leads to the prompt immobilisation of the process  $\text{CO}_2$  upon precipitation of  $\text{Na}_2\text{CO}_3 \cdot \text{H}_2\text{O}$  and  $\text{Na}_2\text{CO}_3$  (Figure 12A). The rate of  $\text{CO}_2$  capture, expressed as  $\text{mol}_{\text{CO}_2} \text{ captured} \cdot \text{s}^{-1}$ , was reflecting the cumulative precipitation rate of  $\text{Na}_2\text{CO}_3 \cdot \text{H}_2\text{O}$  and  $\text{Na}_2\text{CO}_3$ ; it is formulated in Equation 10, where the subscripts for the variable  $t$  indicate the consecutive intervals considered.

$$k_{\text{CO}_2 \text{ captured}} = \frac{[(g\text{CO}_2, \text{Captured})_{t_{n+1}} - (g\text{CO}_2, \text{Captured})_{t_n}]}{(t_{n+1} - t_n)} \quad (10)$$

The capture rate  $k$ , plotted as  $-\ln k$  in Figure 12B, was decreasing for all the samples at longer residence times, in line with the limited reaction extent registered above 300 seconds (Figure 6). The highest  $\text{CO}_2$  capture rate ( $2.7 \cdot 10^{-3} \text{ mol}_{\text{CO}_2} \text{ s}^{-1}$ ) was registered for the sample reacted at 40 rpm for 30 seconds, and a 94 %  $\text{CO}_2$  capture was achieved after 720 seconds of reaction progress at the same stirring rate. The high resemblance with the trends reported in Figure 6 suggest that the precipitation of  $\text{Ca}(\text{OH})_2$  does not affect the trapping of the process  $\text{CO}_2$  into  $\text{Na}_2\text{CO}_3 \cdot \text{H}_2\text{O}$  nor  $\text{Na}_2\text{CO}_3$ , and also reflecting a high accordance to the stoichiometry depicted in Equation 3.

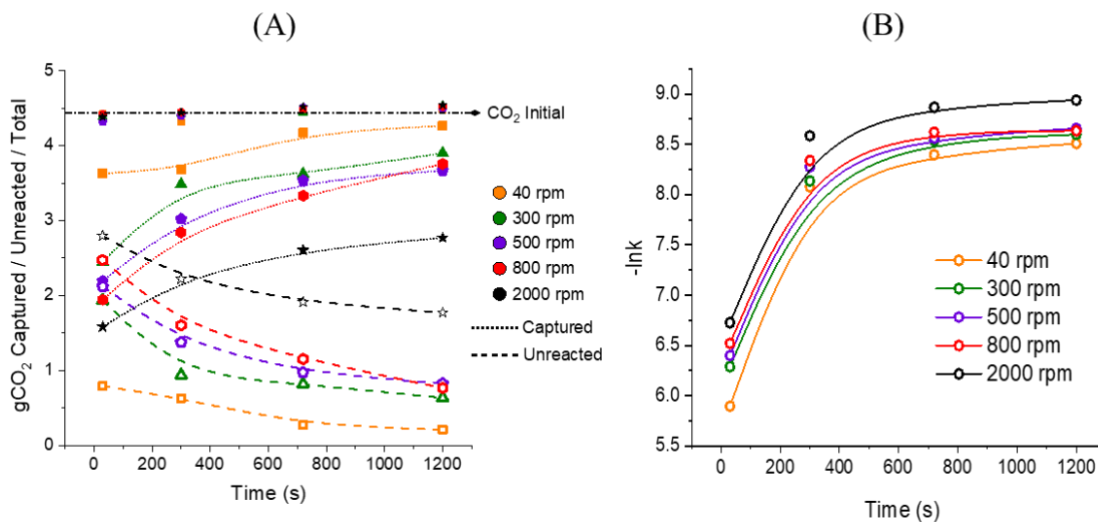


Fig. 12.

### 3.5. Decarbonisation of industrial grade chalk

Chalk with larger particle sizes were subjected to the same reaction, and the size of the reacting solids was chosen upon sieving. The dry PSD analysis revealed a much higher mean particle diameter ( $D_x(50)$  of 1.29 mm, Figure 13B) respect with the reagent grade  $\text{CaCO}_3$  ( $D_x(50)$  of 26.6 $\mu\text{m}$ , Figure 13A); during the analysis, weighted residual and laser obscuration of 3.25% and 2.97%, respectively, were registered. Additionally, both XRF (Table 1) and TG analyses were performed on the solids, upon fine grinding and sieving below 38  $\mu\text{m}$ .

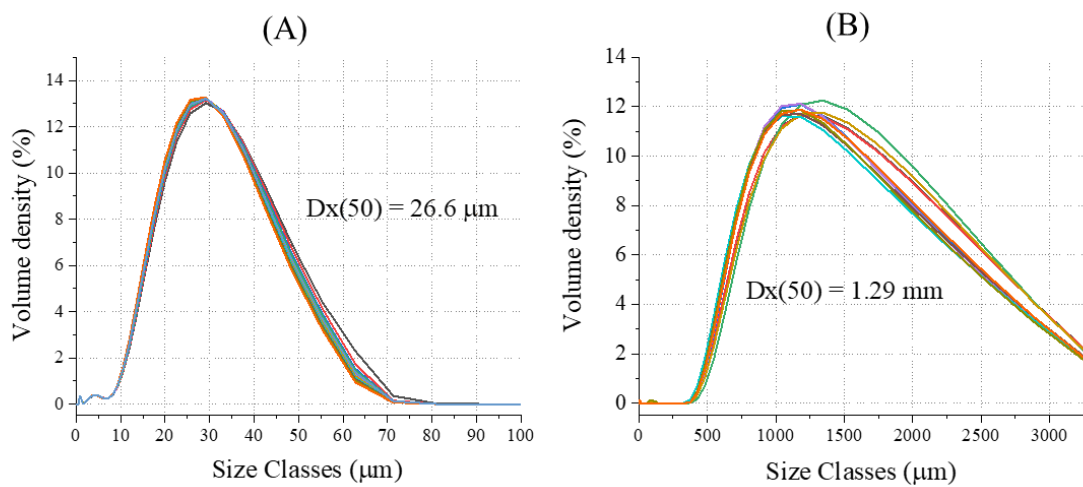


Fig.13.

Figure 14 shows the outcomes of the XRD analysis performed on the ground products; the peaks related to the products  $\text{Ca}(\text{OH})_2$ ,  $\text{Na}_2\text{CO}_3 \cdot \text{H}_2\text{O}$ , and  $\text{Na}_2\text{CO}_3$  could be observed in the reacted solids, together with a slight reduction in intensity of  $\text{CaCO}_3$ .

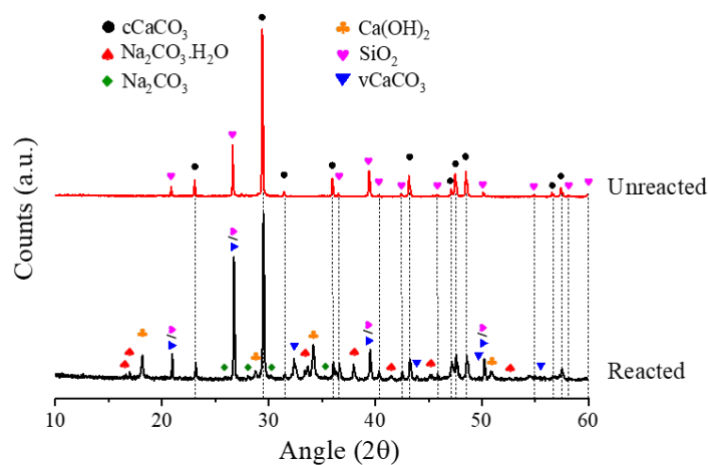


Fig.14.

The TG analysis (Figure 15) reported a total 30.6 wt.% loss for the sample, and the extent of reaction  $\alpha$  was estimated to be 0.3, given the contents of  $\text{CaCO}_3$  (53.8 wt.%) and  $\text{Ca}(\text{OH})_2$  (17.4 wt.%). A 2.3 wt.% loss observed in the temperature range of 50°C-130°C, likely referring to the dehydration of  $\text{Na}_2\text{CO}_3 \cdot \text{H}_2\text{O}$ , whose content was estimated to be 16 wt.%.

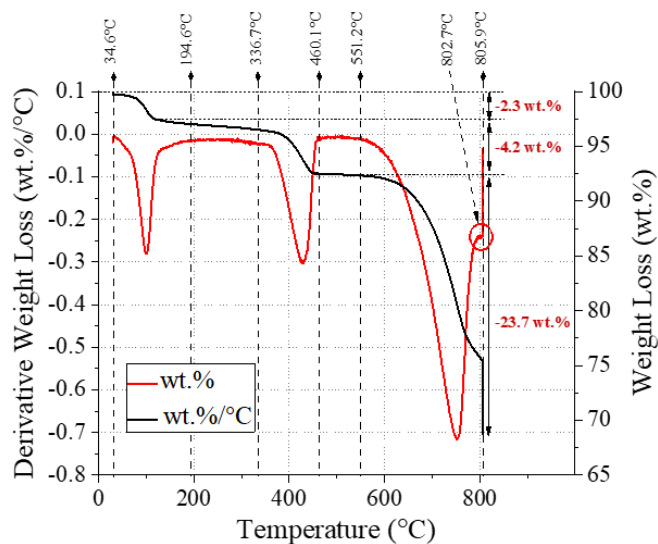


Fig. 15.

The XRD analysis could also reveal traces of  $\text{Na}_2\text{CO}_3$ , which could not be reliably quantified by TG (Section 3.1) because of the significant presence of impurities (Table 1); for the same reason, it was not possible to reliably assess the proportioning between  $\text{Na}_2\text{CO}_3 \cdot \text{H}_2\text{O}$  and  $\text{Na}_2\text{CO}_3$ . It must be mentioned that the large particle size here would significantly affect the yield of the reaction, by largely decreasing the contact surface between the liquid and solid reactants. The DTG curve also shows a small shoulder at 802.7°C. Based on the XRD analysis (Figure 14), this could be assigned to the decarbonisation of vaterite, a metastable polymorph of calcite which is often observed during the synthesis of precipitated calcium carbonate [56-58], and which is seen in the XRD results for the reacted sample in Figure 14. Figures 16A-F show the SEM analysis performed on two representative samples taken from the reacted and unreacted chalk solid particles. As expected, Na could only be detected in the reacted particles (Figure 16B), in line with the formation of  $\text{Na}_2\text{CO}_3 \cdot \text{H}_2\text{O}$  or  $\text{Na}_2\text{CO}_3$ , and higher signals were detected towards the external sections of the solid bead; such a detail will be discussed below, where the EDX analysis of a large number of reacted solid particles is taken into account. Here, the EDX quantification of Na was performed with the software Quantax-70 by considering internal and external sections of the solid particles,

chosen by taking into account the Na mapping in Figure 16B, which highlights a sharp change in Na concentration at a depth of about 200 $\mu$ m.

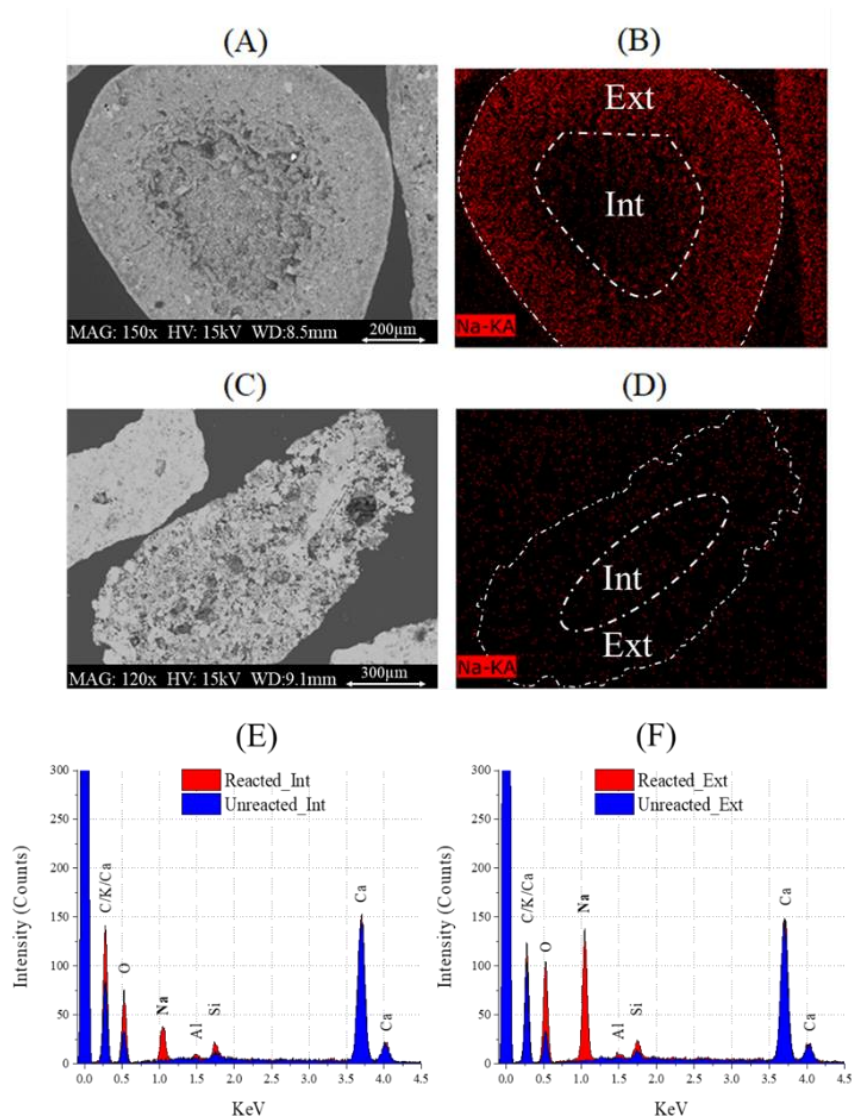


Fig. 16.

Specifically, sodium contents of 18.92 wt.% and 7.32 wt.% were detected in the external and internal sections of the reacted particle, respectively, whereas negligible sodium contents (0.01 – 0.06 wt.%) could be observed in the unreacted chalk. In any case, the sodium peak seen in Figures 15B and D is reflected in Figures 15E and F, where the EDX analysis showed Na signals around 1 KeV; as observed, no signals linked to Na could be detected for the unreacted particle, while a significant gap was observed between the external and internal sections of the reacted one. Moreover, rather homogeneous

distribution of Ca (Figures 17C, D and 18C, D) is observed, with slightly higher contents in the internal regions respect with the external ones.

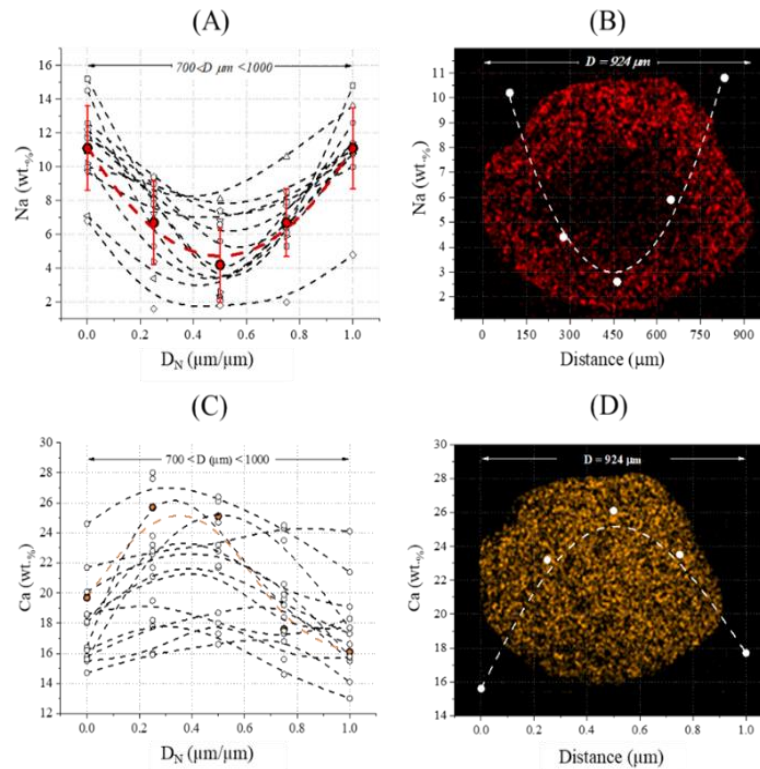


Fig. 17.

That is an expected result, since the stoichiometry of the reaction would lead to an overall weight increase given the reactant ( $\text{CaCO}_3$ ) and products ( $\text{Ca}(\text{OH})_2$ ,  $\text{Na}_2\text{CO}_3 \cdot \text{H}_2\text{O}$ , and  $\text{Na}_2\text{CO}_3$ ) involved (Section 3.1, Figure 4B). Despite Ca should not be lost from the solid surface throughout the reaction, as outlined from the Ca mass balance in S1, the uptake of sodium would result in a final lower Ca proportion in those local regions where the reaction occurred more extensively. As previously mentioned, the particles undergoing SEM analysis were grouped into two sets by their size:  $700 \leq D \leq 1000 \mu\text{m}$  and  $400 \mu\text{m} \leq (D) \leq 700 \mu\text{m}$ .

In both groups, higher contents of Na could be detected in the peripheral regions of each solid particle, at the solid/liquid interface during the reaction. A significant presence of Na was detected within the particles up to a depth of 150-200  $\mu\text{m}$  on average, as shown in Figures 17B and 18B. A normalized radius  $D_N$  was taken into account to display the results, and it was calculated by dividing the length of the radius where the elemental quantification was performed by the total radius of the specific particle. As a  $D_N$  of 0.5 identifies the centre of the particle,  $D_N$  of 0 and 1 reflect its extremes; given that, the Na and Ca contents were detected at  $D_N$  values of 0.0, 0.25, 0.50, 0.75 and 1.0 to better display the gradient observed at gradual depths from the surface. On average of five samples, Na contents

were (wt.%) of  $11.1 \pm 2.5$  (DN = 0) and  $4.2 \pm 2.2$  (DN = 0.5) for the larger group of particles, while  $10.6 \pm 2.0$  (DN = 0) and  $7.2 \pm 2.7$  (DN = 0.5) were observed for the smaller particles. Regarding Ca (Figures 17C, D and 18C, D), slightly higher contents in the inner regions of the solids were observed; the lower local Na content would suggest limited reaction progress into these regions, consistent with the low overall extent of reaction  $\alpha$  of 0.3.

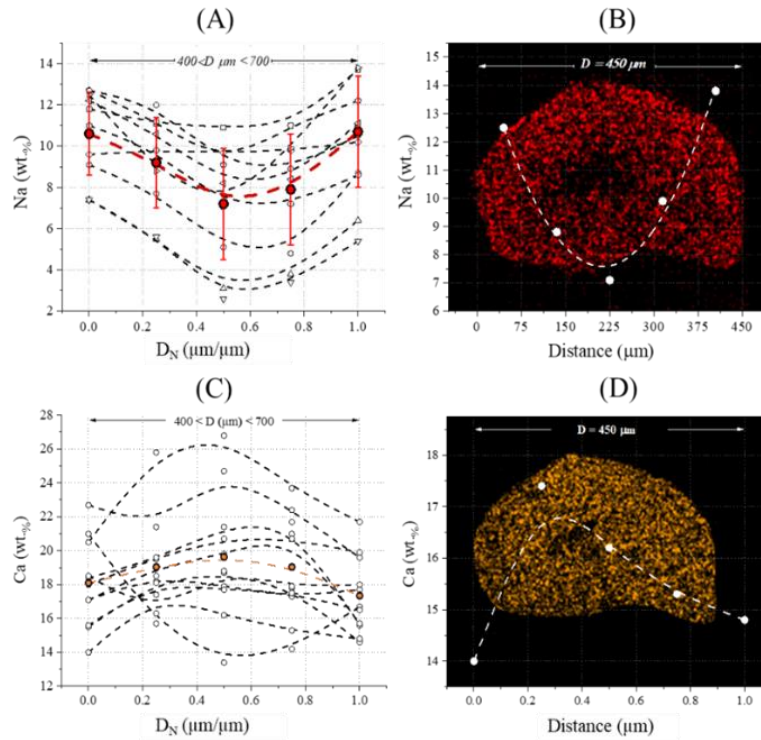
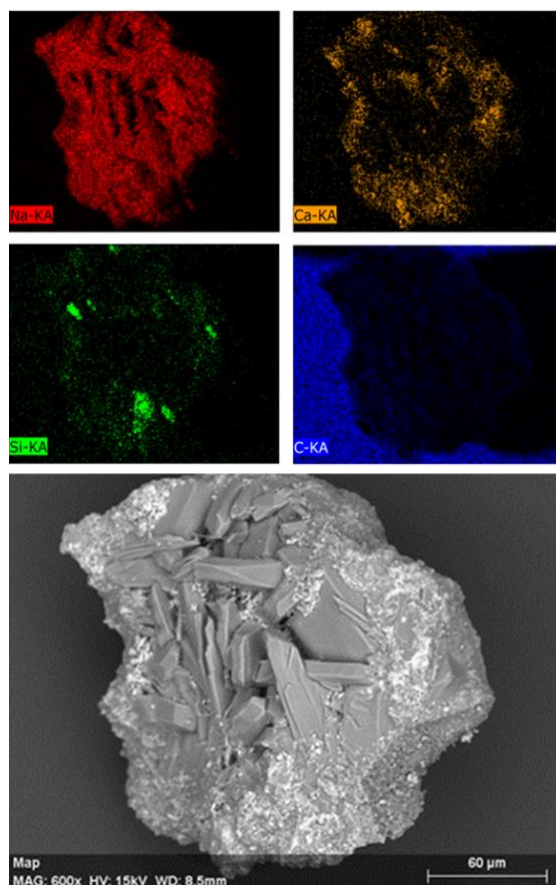


Fig. 18.

Figure 19 shows the SEM-EDX analysis performed on a single reacted chalk bead collected upon grinding and sieving between 150 and 250  $\mu\text{m}$ . Pseudo-hexagonal shaped crystals of  $\text{Na}_2\text{CO}_3 \cdot \text{H}_2\text{O}$  and  $\text{Na}_2\text{CO}_3$  [59] are surrounded by small-sized  $\text{Ca}(\text{OH})_2$  crystals, showing a faceted tetrakaidekahedral morphology [60]. As supported by the XRF and XRD analyses reported in Table 1 and Figure 14, respectively, significant silica agglomerates could also be detected; in the reaction products, those were partially covered by  $\text{Ca}(\text{OH})_2$  layers.



*Fig. 19.*

#### 4. Conclusions

The study of the reaction of  $\text{CaCO}_3$  in  $\text{NaOH}$  solution allowed for the optimisation of processing parameters such as the residence time and the mixing rate. Close to optimum conversion could be obtained after 300 seconds of stirring, while further contact between the reactants did not lead to significant yield improvements. A low stirring rate resulted in enhancing the conversion extent. It is likely that the lower conversion achieved at high stirring rates may be linked to enhanced events of nuclei incorporation or the solid/liquid partition at higher centrifugal force. The proportioning of  $\text{Na}_2\text{CO}_3 \cdot \text{H}_2\text{O}$  and  $\text{Na}_2\text{CO}_3$  was found to be largely affected by the activity of water of the system considered; specifically,  $\text{Na}_2\text{CO}_3 \cdot \text{H}_2\text{O}$  and  $\text{Na}_2\text{CO}_3$  were the favoured species in the final systems at higher and lower water activity, respectively. However, the reaction was effectively capturing the process  $\text{CO}_2$  embodied in  $\text{CaCO}_3$ , up to the 95 % of the total introduced into the system. The comparison between the SEM-EDX analysis of reacted and unreacted chalk samples suggested the possibility of assessing the reaction extent by detection of Na within the solid products. Assuming so, the reaction progression could be visually observed by detection of Na, whose gradient was defined for the solid reacted particles, and whose propagation

was observed up to 150  $\mu\text{m}$  deep from the solid/liquid interface. The lower reaction extent obtained for larger  $\text{CaCO}_3$  solids ( $D \sim 1 \text{ mm}$ ) suggested that this alternative route would require additional grinding to achieve a satisfactory decarbonisation, if compared to the average size of the raw  $\text{CaCO}_3$  feed (2 – 200  $\mu\text{m}$ ) used in a conventional lime or cement plant [1]. Although, we believe that the additional emissions arising from the higher electrical consumption required for a finer  $\text{CaCO}_3$  would be negligible, if compared with the avoided combustion and process  $\text{CO}_2$ .

In conclusion, the chemical decarbonisation of  $\text{CaCO}_3$  allowed for the nearly total capture of the process  $\text{CO}_2$ , while converting  $\text{CaCO}_3$  to the essential lime. These positive outcomes may be obtained relatively simply, given the mild mixing conditions and heating required; despite that, the use of highly-corrosive  $\text{NaOH}$  solutions requires further investigation for an eventual scale-up.

## Captions (in order of appearance)

**Table 1.** Elemental oxide composition (wt.%) of the solid chalk used in the present work, including Loss On Ignition (LOI%) value.

**Fig. 1.** Representative of the temperature-trend from the TG (w%) and DTG (dw%/dt) data, showing the weight loss events of the sample associated with:  $\text{Na}_2\text{CO}_3 \cdot \text{H}_2\text{O}$  (A),  $\text{Ca}(\text{OH})_2$  (B), and  $\text{CaCO}_3$  (C).

**Fig. 2.** XRD patterns of the samples obtained at 300 rpm for all the residence times investigated, highlighting the peaks of all the species detected.

**Fig. 3.** TG and dTG analysis performed on the baseline series 500rpm\_30-1200 sec, showing the weight losses in the regions 50-130°C, 310-470° and 560-800°C which are assigned to  $\text{Na}_2\text{CO}_3 \cdot \text{H}_2\text{O}$ ,  $\text{Ca}(\text{OH})_2$  and  $\text{CaCO}_3$ , respectively. The black arrows clarify the axes referred to the data shown.

**Fig.4.** Phase compositions of the samples reacted at 300 rpm at increasing residence times (A); trend of the weight uptake experimentally observed as a function of conversion (black labels), with lines indicating the relationships that would have been observed if the sodium carbonates were present solely as  $\text{Na}_2\text{CO}_3 \cdot \text{H}_2\text{O}$  (red line), or solely as  $\text{Na}_2\text{CO}_3$  (blue line) (B).

**Fig.5.** XRD patterns for the samples reacted for 300 seconds as a function of stirring rate.

**Fig.6.** Conversion extents obtained at each residence time and stirring rate investigated.

**Fig.7.** Schematic representation of the partition occurring between the solid ( $\text{CaCO}_3$ ) and liquid (NaOH sol.) phases at increasing centrifugal force ( $F_c$ ) or stirring rate.

**Fig.8.** Fitting between the experimental data for all the samples here discussed and the Avrami-Erofeev nucleation model represented by Equation 6; the samples were grouped according to the stirring rate used, and  $R^2$  values are highlighted for each

**Fig.9.** Schematic representation of the nucleation front progression (grey pattern) occurring at high (left) and low (right) stirring rates.

**Fig.10.** PHREEQC simulation showing (A) the activity of water as a function of NaOH molalities at 20, 60 and 100°C in a system with 100 g, 106 g, and 124 g of  $\text{H}_2\text{O}$ ,  $\text{Na}_2\text{CO}_3 \cdot \text{H}_2\text{O}$ , and  $\text{Na}_2\text{CO}_3$ , respectively, and (B) precipitated moles of  $\text{Na}_2\text{CO}_3 \cdot \text{H}_2\text{O}$  and  $\text{Na}_2\text{CO}_3$  at 20, 60 and 100°C; the initial NaOH concentration of the solutions used for this set of samples is labelled as  $C_0$ .

**Fig.11.**  $v\% \text{Na}_2\text{CO}_3 \cdot \text{H}_2\text{O}$  values and final  $\text{OH}^-$  concentration, experimentally determined as a function of conversion.

**Fig. 12.** Trends of  $g\text{CO}_2, \text{Captured}$  and  $g\text{CO}_2, \text{Unreacted}$  at increasing residence times registered for all the samples discussed here (A);  $\text{CO}_2$  capture rate ( $\text{mol}_{\text{CO}_2} \text{Captured} \cdot \text{s}^{-1}$ ) calculated for all the samples from Equation 10.

**Fig.13.** Dry-state Particle Size Distribution (PSD) analysis was performed on reagent grade  $\text{CaCO}_3$  (A) and industrial grade chalk (B); ten measurements per sample were performed, and the average value was considered.

**Fig.14.** XRD patterns of the reacted and unreacted industrial grade chalk, with labelled phases  $c\text{CaCO}_3$  (calcite),  $\text{Ca}(\text{OH})_2$ ,  $\text{Na}_2\text{CO}_3 \cdot \text{H}_2\text{O}$ ,  $\text{Na}_2\text{CO}_3$  and  $v\text{CaCO}_3$  (vaterite).

**Fig.15.** TG (black line) and DTG (red line) trends for the industrial grade chalk reacted here, highlighting the key temperature ranges and the corresponding weight losses observed.

**Fig.16.** SEM images of two representative reacted (A) and unreacted (C) solid chalk particles, with respective Na mapping (red highlighted) in B and D, where the external (Ext) and internal (Int) areas discussed in the body text are displayed in white. Dispersive X-Ray (EDX) analysis performed on the (E) un-reacted and (F) reacted chalk particles, with maps of the elements Na, Si and Ca.

**Fig.17.** Na wt.% and Ca wt.% contents plotted against the normalised particle size considered (DN) for the  $700\mu\text{m} \leq (D) \leq 1000\mu\text{m}$  group (A and C, respectively) and their distribution in a  $D = 924\mu\text{m}$  sample (B and D, respectively).

**Fig.18.** Na wt.% and Ca wt.% contents plotted against the normalised length considered for the  $400\mu\text{m} \leq (D) \leq 700\mu\text{m}$  group (A and C, respectively); specific Na wt.% and Ca wt.% gradients registered for a targeted size ( $D = 450\mu\text{m}$ ) sample (B and D, respectively).

**Fig.19.** SEM images of the reaction products from the chalk upon grinding and sieving between 150 and 250  $\mu\text{m}$ ; the samples were attached on conductive carbon adhesive tapes

## Supplementary Electronic Material

*Table S1. Residence time and stirring rate for each sample produced, linked to the phases compositions gained from TG analysis, and weight uptake observed; the Ca balance, expressed as the difference between the inbound and outbound gram of Ca, is also reported to validate the quantification performed.*

	Residence time (sec)	Stirring rate (rpm)	Wt.% Na <sub>2</sub> CO <sub>3</sub> ·H <sub>2</sub> O	Wt.% Ca(OH) <sub>2</sub>	Wt.% CaCO <sub>3</sub>	Wt.% Na <sub>2</sub> CO <sub>3</sub>	Weight uptake (%)	ΔCa (g)
<i>40rpm_30 sec</i>	30	40	49.6	32.6	10.3	7.6	78.3	0.2
<i>40rpm_300 sec</i>	300	40	53.6	36.2	7.8	2.4	83.6	-0.2
<i>40rpm_720 sec</i>	720	40	59.5	35.0	3.3	2.3	90.9	0.2
<i>40rpm_1200 sec</i>	1200	40	60.8	34.9	2.5	1.8	92.3	0.2
<i>300rpm_30 sec</i>	30	300	18.0	25.9	30.5	25.5	50.5	0.2
<i>300rpm_300 sec</i>	300	300	23.6	33.3	12.8	30.3	75.0	0.2
<i>300rpm_720 sec</i>	720	300	55.8	32.4	10.5	1.3	78.0	0.1
<i>300rpm_1200 sec</i>	1200	300	58.0	32.7	7.8	1.5	82.2	0.2
<i>500rpm_30 sec</i>	30	500	18.9	24.0	35.0	22.1	45.1	0.3
<i>500rpm_300 sec</i>	300	500	27.2	29.8	19.9	23.1	64.0	0.2
<i>500rpm_720 sec</i>	720	500	54.4	31.1	12.6	1.9	74.2	0.1
<i>500rpm_1200 sec</i>	1200	500	56.7	31.6	10.5	1.1	77.5	0.2
<i>800rpm_30 sec</i>	30	800	3.0	22.2	42.2	32.6	38.4	0.2
<i>800rpm_300 sec</i>	300	800	12.1	29.8	23.8	34.3	59.9	0.1
<i>800rpm_720 sec</i>	720	800	49.6	30.2	15.4	4.8	69.8	0.2
<i>800rpm_1200 sec</i>	1200	800	56.9	32.2	9.6	1.3	79.1	0.2
<i>2000rpm_30 sec</i>	30	2000	11.9	17.6	50.4	20.0	29.0	0.3
<i>2000rpm_300 sec</i>	300	2000	10.2	23.7	36.3	29.7	43.9	0.2
<i>2000rpm_720 sec</i>	720	2000	9.2	26.0	29.8	35.1	51.1	0.2
<i>2000rpm_1200 sec</i>	1200	2000	7.1	27.2	27.0	38.6	54.7	0.2

## Author's Contribution

Theodore Hanein and Hajime Kinoshita discovered and conceptualized the technology. Theodore Hanein, Hajime Kinoshita, John L. Provis, and Marco Simoni developed the technology and designed the methodology and experiments. Theodore Hanein, Marco Simoni, and Chun Long Woo carried out experiments. Marco Simoni drafted the original manuscript. Theodore Hanein, Hajime Kinoshita, and John L. Provis acquired funding, and supervised Marco Simoni and Chun Long Woo about authorship. Theodore Hanein, Hajime Kinoshita, John Provis, Mark Tyrer, Juan-Carlos Martinez, Magnus Nyberg, Alan Maries, John Stennet and Nestor I. Quintero-Mora reviewed and edited the manuscript.

## Conflicts of interest

The authors declare that they have no competing interests as defined by Physical Chemistry Chemical Physics, or other interests that might be perceived to influence the interpretation of the article.

## Acknowledgements

This work was funded by the Engineering and Physical Science Research Council (EPSRC) and CEMEX under grant ID EP/R025959/1. The group would also express gratitude to Dr. John Stennet for the support and knowledge received.

## References

1. Schorcht, F., et al., *Best available techniques (BAT) reference document for the production of cement, lime and magnesium oxide*. European Commission Joint Research Centre Institute for Prospective Technological Studies (Report EUR 26129 EN). Luxembourg: Publications Office of the European Union, 2013, [http://eippcb.jrc.ec.europa.eu/reference/BREF/CLM\\_Published\\_def.pdf](http://eippcb.jrc.ec.europa.eu/reference/BREF/CLM_Published_def.pdf), DOI: 10.2788/12850
2. Foreman, P.C. and I.E. Barnes, A review of calcium hydroxide. *International endodontic journal*, 1990. **23**(6): p. 283-297, <https://doi.org/10.1111/j.1365-2591.1990.tb00108.x>.
3. Farhad, A. and Z. Mohammadi, Calcium hydroxide: a review. *International dental journal*, 2005. **55**(5): p. 293-301, <https://doi.org/10.1111/j.1875-595X.2005.tb00326.x>.
4. Dowling, A., J. O'Dwyer, and C.C. Adley, Lime in the limelight. *Journal of cleaner production*, 2015. **92**: p. 13-22, <https://doi.org/10.1016/j.jclepro.2014.12.047>.
5. Habert, G., et al., *Environmental impacts and decarbonization strategies in the cement and concrete industries*. *Nature Reviews Earth & Environment*, 2020: p. 1-15, <https://doi.org/10.1038/s43017-020-0093-3>.
6. Oates, J.A.H., *Lime and limestone: chemistry and technology, production and uses*. 2008: John Wiley & Sons, ISBN 3-527-29527-5.
7. Gutiérrez, A.S., J.B.C. Martínez, and C. Vandecasteele, Energy and exergy assessments of a lime shaft kiln. *Applied Thermal Engineering*, 2013. **51**(1-2): p. 273-280, <https://doi.org/10.1016/j.applthermaleng.2012.07.013>.
8. Barcelo, L., et al., Cement and carbon emissions. *Materials and structures*, 2014. **47**(6): p. 1055-1065, <https://doi.org/10.1617/s11527-013-0114-5>.
9. Boateng, A.A., *Rotary kilns: transport phenomena and transport processes*. 2015: Butterworth-Heinemann, ISBN 978-0-12-803780-5.
10. ReportLinker, *Global Calcium Hydroxide Industry*. October, 2020, [https://www.reportlinker.com/p05956205/?utm\\_source=GNW](https://www.reportlinker.com/p05956205/?utm_source=GNW).
11. Andrew, R.M., *Global CO<sub>2</sub> emissions from cement production*. *Earth System Science Data*, 2018. **10**(1): p. 195-217, <https://doi.org/10.5281/zenodo.831455>.
12. Stocker, T., *Climate change 2013: the physical science basis: Working Group I contribution to the Fifth assessment report of the Intergovernmental Panel on Climate Change*. 2014: Cambridge University Press.
13. Friedlingstein, P., et al., *Global carbon budget 2019*. *Earth System Science Data*, 2019. **11**(4): p. 1783-1838, <https://doi.org/10.5194/essd-11-1783-2019>.
14. Rogelj, J., et al., *Paris Agreement climate proposals need a boost to keep warming well below 2 C*. *Nature*, 2016. **534**(7609): p. 631, <https://doi.org/10.1038/nature18307>.
15. Skea, J., P. Ekins, and M. Winskel, *Energy 2050: Making the transition to a secure low carbon energy system*. 2011: Routledge. ISBN 978-1-84971-084-8.
16. Hanein, T., et al., *Decarbonisation of calcium carbonate at atmospheric temperatures and pressures, with simultaneous CO<sub>2</sub> capture, through production of sodium carbonate*, *Energy & Environmental Science*, 2021, DOI: 10.1039/D1EE02637B17.
18. Homma, S., et al., *Gas–solid reaction model for a shrinking spherical particle with unreacted shrinking core*. *Chemical Engineering Science*, 2005. **60**(18): p. 4971-4980, <https://doi.org/10.1016/j.ces.2005.03.057>.
19. Castellote, M. and C. Andrade, *Modelling the carbonation of cementitious matrixes by means of the unreacted-core model, UR-CORE*. *Cement and concrete research*, 2008. **38**(12): p. 1374-1384, <https://doi.org/10.1016/j.cemconres.2008.07.004>.
20. Soo, S.L., *Fluid dynamics of multiphase systems*. Waltham, Mass, Blaisdell Publishing Co., 1967, OCLC No. 1301193.
21. Yudine, M.I., *Physical considerations on heavy-particle diffusion, in Advances in geophysics*. 1959, Elsevier. p. 185-191, [https://doi.org/10.1016/S0065-2687\(08\)60106-5](https://doi.org/10.1016/S0065-2687(08)60106-5).
22. Micheletti, M., et al., *Particle concentration and mixing characteristics of moderate-to-dense solid–liquid suspensions*. *Industrial & engineering chemistry research*, 2003. **42**(24): p. 6236-6249, <https://doi.org/10.1021/ie0303799>.
23. Tamburini, A., et al., *Dense solid–liquid off-bottom suspension dynamics: simulation and experiment*. *Chemical Engineering Research and Design*, 2009. **87**(4): p. 587-597, <https://doi.org/10.1016/j.cherd.2008.12.024>.

24. Du, F., et al., Sodium Hydroxide Production from Seawater Desalination Brine: Process Design and Energy Efficiency. *Environmental science & technology*, 2018. **52**(10): p. 5949-5958, <https://doi.org/10.1021/acs.est.8b01195>.
25. Neubauer, J. and H. Pöllmann, Alinite—Chemical composition, solid solution and hydration behaviour. *Cement and concrete research*, 1994. **24**(8): p. 1413-1422, [https://doi.org/10.1016/0008-8846\(94\)90154-6](https://doi.org/10.1016/0008-8846(94)90154-6).
26. Scrivener, K.L., V.M. John, and E.M. Gartner, Eco-efficient cements: Potential economically viable solutions for a low-CO<sub>2</sub> cement-based materials industry. *Cement and Concrete Research*, 2018. **114**: p. 2-26, <https://doi.org/10.1016/j.cemconres.2018.03.015>.
27. Leemann, A. and B. Lothenbach, The influence of potassium–sodium ratio in cement on concrete expansion due to alkali–aggregate reaction. *Cement and Concrete Research*, 2008. **38**(10): p. 1162-1168, <https://doi.org/10.1016/j.cemconres.2008.05.004>.
28. Bueno, E.T., et al., A review of ground waste glass as a supplementary cementitious material: A focus on alkali–silica reaction. *Journal of Cleaner Production*, 2020. **257**: p. 120180, <https://doi.org/10.1016/j.jclepro.2020.120180>.
29. Seidell, A., *Solubilities of inorganic and metal organic compounds*. 1940, ISBN: 0598437002, 9780598437006.
30. Morey, G.W., The action of water on calcite, magnesite and dolomite. *American Mineralogist: Journal of Earth and Planetary Materials*, 1962. **47**(11-12): p. 1456-1460.
31. Ellingboe, J.L. and J.H. Runnels, Solubilities of Sodium Carbonate and Sodium Bicarbonate in Acetone-Water and Methanol-Water Mixtures. *Journal of Chemical and Engineering Data*, 1966. **11**(3): p. 323-324.
32. Zelić, J., D. Rušić, and R. Krstulović, Kinetic analysis of thermal decomposition of Ca (OH)<sub>2</sub> formed during hydration of commercial Portland cement by DSC. *Journal of thermal analysis and calorimetry*, 2002. **67**(3): p. 613-622, <https://doi.org/10.1023/A:1014348603686>.
33. Gallagher, P.K. and D.W. Johnson Jr, The effects of sample size and heating rate on the kinetics of the thermal decomposition of CaCO<sub>3</sub>. *Thermochimica Acta*, 1973. **6**(1): p. 67-83, [https://doi.org/10.1016/0040-6031\(73\)80007-3](https://doi.org/10.1016/0040-6031(73)80007-3).
34. Hartman, M., et al., Thermal dehydration of the sodium carbonate hydrates. *Chemical Engineering Communications*, 2001. **185**(1): p. 1-16, <https://doi.org/10.1080/00986440108912851>.
35. Kjellsen, K.O., et al., Preparation of flat-polished specimens for SEM-backscattered electron imaging and X-ray microanalysis—importance of epoxy impregnation. *Cement and concrete research*, 2003. **33**(4): p. 611-616, [https://doi.org/10.1016/S0008-8846\(02\)01029-3](https://doi.org/10.1016/S0008-8846(02)01029-3).
36. Motzfeldt, K., The thermal decomposition. of sodium carbonate by the effusion method. *The Journal of Physical Chemistry*, 1955. **59**(2): p. 139-147.
37. Raymundo-Pinero, E., et al., KOH and NaOH activation mechanisms of multiwalled carbon nanotubes with different structural organisation. *Carbon*, 2005. **43**(4): p. 786-795, <https://doi.org/10.1016/j.carbon.2004.11.005>.
38. Green, D.W. and R.H. Perry, *Perry's Chemical Engineers' Handbook/edición Don W. Green y Robert H. Perry*. 2019.
39. Patnaik, P., *Handbook of inorganic chemicals*. Vol. 529. 2003: McGraw-Hill New York.
40. Khawam, A. and D.R. Flanagan, Solid-state kinetic models: basics and mathematical fundamentals. *The journal of physical chemistry B*, 2006. **110**(35): p. 17315-17328, <https://doi.org/10.1021/jp062746a>.
41. Vekilov, P.G., Nucleation. *Crystal growth & design*, 2010. **10**(12): p. 5007-5019, <https://doi.org/10.1021/cg1011633>.
42. De Yoreo, J.J. and P.G. Vekilov, Principles of crystal nucleation and growth. *Reviews in mineralogy and geochemistry*, 2003. **54**(1): p. 57-93, <https://doi.org/10.2113/0540057>.
43. Mullin, J.W., *Crystallization-4<sup>th</sup> Edition*, 2001: Elsevier, <https://doi.org/10.1021/op0101005>.
44. Brice, J.C., Some thermodynamic aspects of the growth of strained crystals. *Journal of Crystal Growth*, 1975. **28**(2): p. 249-253, [https://doi.org/10.1016/0022-0248\(75\)90241-9](https://doi.org/10.1016/0022-0248(75)90241-9).
45. Weeks, J.D. and G.H. Gilmer, Dynamics of crystal growth. *Adv. Chem. Phys*, 1979. **40**(489): p. 157-227,
46. Hu, H., et al., Nucleation and crystal growth control for scalable solution-processed organic–inorganic hybrid perovskite solar cells. *Journal of Materials Chemistry A*, 2020. **8**(4): p. 1578-1603, <https://doi.org/10.1039/C9TA11245F>.
47. Kouchi, A., A. Tsuchiyama, and I. Sunagawa, Effect of stirring on crystallization kinetics of basalt: texture and element partitioning. *Contributions to Mineralogy and Petrology*, 1986. **93**(4): p. 429-438, <https://doi.org/10.1007/BF00371713>.

48. Garside, J., A. Mersmann, and J. Nývlt, Measurement of crystal growth and nucleation rates. 2002: IChemE.
49. Parkhurst, D.L. and C.A.J. Appelo, Description of input and examples for PHREEQC version 3: a computer program for speciation, batch-reaction, one-dimensional transport, and inverse geochemical calculations. 2013, US Geological Survey, <https://doi.org/10.3133/tm6A43>.
50. Pitzer, K.S., Ion interaction approach: theory and data correlation, in Activity coefficients in electrolyte solutions. 2018, CRC Press. p. 75-153.
51. Miyawaki, O., et al., Activity and activity coefficient of water in aqueous solutions and their relationships with solution structure parameters. *Bioscience, biotechnology, and biochemistry*, 1997. **61**(3): p. 466-469, <https://doi.org/10.1271/bbb.61.466>.
52. Mazurkiewicz, J., P. Tomasik, and J. Zaplotny, Relationships between water activity and viscosity of solutions. *Food hydrocolloids*, 2001. **15**(1): p. 43-46, [https://doi.org/10.1016/S0268-005X\(00\)00048-5](https://doi.org/10.1016/S0268-005X(00)00048-5).
53. Pabalan, R.T. and K.S. Pitzer, Thermodynamics of NaOH (aq) in hydrothermal solutions. *Geochimica et Cosmochimica Acta*, 1987. **51**(4): p. 829-837, [https://doi.org/10.1016/0016-7037\(87\)90295-X](https://doi.org/10.1016/0016-7037(87)90295-X).
54. Balej, J., Water vapour partial pressures and water activities in potassium and sodium hydroxide solutions over wide concentration and temperature ranges. *International journal of hydrogen energy*, 1985. **10**(4): p. 233-243, [https://doi.org/10.1016/0360-3199\(85\)90093-X](https://doi.org/10.1016/0360-3199(85)90093-X).
55. Jiang, J. and S.I. Sandler, A new model for the viscosity of electrolyte solutions. *Industrial & engineering chemistry research*, 2003. **42**(25): p. 6267-6272, <https://doi.org/10.1021/ie0210659>.
56. Kamhi, S.R., On the structure of vaterite CaCO<sub>3</sub>. *Acta Crystallographica*, 1963. **16**(8): p. 770-772, <https://doi.org/10.1107/S0365110X63002000>.
57. Rodriguez-Blanco, J.D., S. Shaw, and L.G. Benning, The kinetics and mechanisms of amorphous calcium carbonate (ACC) crystallization to calcite, via vaterite. *Nanoscale*, 2011. **3**(1): p. 265-271, DOI: 10.1039/C0NR00589D.
58. Spanos, N. and P.G. Koutsoukos, The transformation of vaterite to calcite: effect of the conditions of the solutions in contact with the mineral phase. *Journal of crystal growth*, 1998. **191**(4): p. 783-790, [https://doi.org/10.1016/S0022-0248\(98\)00385-6](https://doi.org/10.1016/S0022-0248(98)00385-6).
59. Yu, S. and C.T. Oguchi, Is sodium sulphate invariably effective in destroying any type of rock? Geological Society, London, Special Publications, 2010. **333**(1): p. 43-58, <https://doi.org/10.1144/SP333.5>.
60. Chen, X., et al., Morphology prediction of portlandite: Atomistic simulations and experimental research. *Applied Surface Science*, 2020. **502**: p. 144296, <https://doi.org/10.1016/j.apsusc.2019.144296>.

## 5. Alternative decarbonisation route: effect of processing temperatures

This work mainly refers to the thermodynamic and kinetic aspects of the interaction between  $\text{CaCO}_3$  and  $\text{NaOH}$  solutions at increasing temperatures and under ambient pressure. Apart from providing essential information about the activation energy necessary to the chemical decarbonisation of  $\text{CaCO}_3$  in comparison with the thermal energy required for the calcination, this work also outlines optimistic outcomes from an economic point of view. In fact, the system was allowing for a quick conversion to products, increasing at higher temperatures. The effect of temperature appeared to be mitigated at longer residence times, and nearly negligible after five minutes of contact time between the reactants. This work has already been submitted to the attention of RSC Advances, and it is currently under review. I here certify that I conceptualised and performed all the experiments, including the characterisation, that I drafted the original manuscript, and took care of the submissions process.

# Synthesis of $\text{Ca}(\text{OH})_2$ and $\text{Na}_2\text{CO}_3$ through anion exchange between $\text{CaCO}_3$ and $\text{NaOH}$ : effect of reaction temperature

Marco Simoni<sup>\*a</sup>, Theodore Hanein<sup>\*a</sup>, Chun Long Woo<sup>a</sup>, Magnus Nyberg<sup>b</sup>, Mark Tyrer<sup>c</sup>, John L. Provis<sup>a</sup>, and Hajime Kinoshita<sup>\*a</sup>.

<sup>a</sup> University of Sheffield, Department of Materials Science & Engineering, S1 3JD, Sheffield, UK

<sup>b</sup> CEMEX Asia Research AG, Römerstrasse 13, 2555 Brügg, Switzerland

<sup>c</sup> Collegium Basilea, Hochstrasse 51, CH-4053 Basel, Switzerland

\* Corresponding authors: [marco.simoni.w@gmail.com](mailto:marco.simoni.w@gmail.com), [t.hanein@sheffield.ac.uk](mailto:t.hanein@sheffield.ac.uk), [h.kinoshita@sheffield.ac.uk](mailto:h.kinoshita@sheffield.ac.uk).

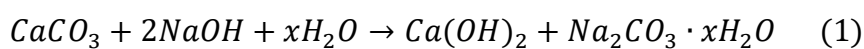
## Abstract

The  $\text{CO}_2$  released upon calcination of limestone accounts for the largest portion of the emissions from the cement, lime, slaked lime, and soda ash manufacturing industries. Our previous works highlighted the possibility for a no-combustion decarbonisation of  $\text{CaCO}_3$  through reaction with  $\text{NaOH}$  solutions to produce  $\text{Ca}(\text{OH})_2$  at ambient conditions, while sequestering the process  $\text{CO}_2$  in a stable mineral  $\text{Na}_2\text{CO}_3 \cdot \text{H}_2\text{O} / \text{Na}_2\text{CO}_3$ . In this study, the effect of temperature was assessed within the range of 45-80°C, highlighting a higher impact at short residence times. The proportioning of the precipitated phases  $\text{Na}_2\text{CO}_3 \cdot \text{H}_2\text{O} / \text{Na}_2\text{CO}_3$  was also assessed at increasing  $\text{NaOH}$  molalities and temperatures, and the data was supported with related simulation. Experiments performed on targeted  $\text{CaCO}_3:\text{NaOH}:\text{H}_2\text{O}$  compositions also allowed for the detection of the Arrhenius parameters characterising each ternary system. An increasing activation energy ( $E_a$ ) was found to be correlated to lower  $\text{NaOH}$  concentrations initially reacting with  $\text{CaCO}_3$ . A preliminary energy balance was performed for the novel decarbonisation route, and the comparison with the conventional one based on thermal calcination is also discussed. The present work offers a further understanding of the effect of temperature on the process with the potential to minimise the emissions from several energy-intensive manufacturing processes, and correctly assess eventual industrial applicability.

**Keywords:** Calcium carbonate, chemical decarbonisation, process  $\text{CO}_2$ ,  $\text{CO}_2$  immobilisation, kinetic, Arrhenius parameters.

# 1. Introduction

The thermal decarbonisation of limestone to give lime ( $\text{CaCO}_3 \rightarrow \text{CaO} + \text{CO}_2$ ) is a crucial step for the production of ordinary Portland Cement (PC), lime (CaO), slaked lime ( $\text{Ca}(\text{OH})_2$ ), and soda ash ( $\text{Na}_2\text{CO}_3$ ), whose worldwide markets exceed 4 Gt [1], ~55 Mt, ~15 Mt [2], and 50 Mt [3] respectively. Given the heavy carbon footprint of such calcination step [4], these industrial realities are responsible for a significant portion of the total CO<sub>2</sub> emissions worldwide [1, 5, 6]. Depending on the targeted product, the very energy-intensive [7] thermal decarbonisation of limestone might occur in different calcination designs [8]. Independently from the final product, the emissions arising from this step are linked to both the process and combustion CO<sub>2</sub>, accounting for 0.8, 1.0 – 1.8, and 0.4 t CO<sub>2</sub>, equivalent for cement, lime/slaked lime, and soda ash, respectively. While the combustion CO<sub>2</sub> results from the stoichiometry of  $\text{CaCO}_3$  decomposition, the latter refers to the combustion of the fuels (primarily fossil fuels) necessary to achieve the calcination temperature (above 900°C) [9]. In order to meet the environmental goals set by the UN in 2015 (at least 80% of CO<sub>2</sub> emission cut from the industry sector by 2050 [10]), a significant contribution is expected from the cement, lime, and soda ash industries. The efficiency enhancement of the existing carbon capture and storage (CCS) technologies [11] and the use of alternative fuels [12] are currently considered in the front line to mitigate these emissions. Despite that, all these solutions start from the assumption that the thermal calcination of limestone is unavoidable, as is the process CO<sub>2</sub>. In contrast to this, recent works [13-16] highlighted the possibility for alternative decarbonisation routes which apply no-combustion approaches for the synthesis of the essential chemical CaO [17] from  $\text{CaCO}_3$ . As far as we are aware, the chemical decarbonisation route here characterised represents the only alternative for the sustainable co-synthesis of  $\text{Ca}(\text{OH})_2$  and  $\text{Na}_2\text{CO}_3$ , and therefore with the potential to supply several large markets. The stoichiometry of the key-reaction developed here is reported in Equation 1; it occurs at ambient conditions and, as reported below, it implies the reaction between  $\text{CaCO}_3$  and concentrated NaOH solutions.



The title study aims to gain a deeper insight into the behaviour of the heterogeneous system considered at increasing temperatures, therefore providing essential information for an eventual scale-up. The full understanding of the system kinetic is a fundamental step towards industrialisation, since it will be crucial to determine the feasibility of the scaled-up process. The reaction velocity may be defined by Equation 2 [18], using the reaction time ( $t$ ), temperature ( $T$ ), and extent of reaction ( $0 < \alpha < 1$ ) [18]. The function  $f(\alpha)$  represents the kinetic

reaction model depending on the mechanism of the process [19], and  $f(T)$  is applied in the Arrhenius equation (Equation 3) that varies with temperature, activation energy ( $E_a$ ) and the pre-exponential factor ( $A$ ).  $E_a$  is the minimal energy that needs to be overcome by the reactants in order for the reaction to occur [20], while the pre-exponential factor provides an estimation of the probability of the collisions between the reactants [21].

$$\frac{\partial \alpha}{\partial t} = f(T) * f(\alpha) \quad (2)$$

$$f(T) = A * e^{\left(-\frac{E_a}{RT}\right)} \quad (3)$$

Although the temperatures here considered (45-80°C) are not very high, keeping the system temperature constant requires an additional energy expenditure, which would increase the operational costs of the process. Therefore, the reaction efficiency was also tested without actively maintaining the temperature after the initial heating of the NaOH solutions to the targeted temperatures. Furthermore, some of the ternary starting compositions tested in our previous study [14] were subjected to the same processing conditions and increasing temperatures here, to obtain the parameters  $E_a$  and  $A$ .

## 2. Materials and Methods

### 2.1. Experimental procedure

The materials used in this work are reagent grade chemicals: Sigma-Aldrich  $\text{CaCO}_3$  ( $\geq 99\%$ ), Honeywell Fluka NaOH ( $\geq 97\%$ ), and distilled water. The starting mixture of  $\text{CaCO}_3$  (26.9 wt.%), NaOH (32.7 wt.%) and distilled water (40.4 wt.%) was first investigated, with the solution having an initial 20 m NaOH molality ( $\text{mol} \cdot \text{kgH}_2\text{O}^{-1}$ ). Such a composition was chosen given the 86% conversion efficiency previously observed [14]. Moreover, the water to solids ratio of 1.5 g/g was ensuring a homogeneous mixing of the solid powders even at milder stirring conditions, as described below, with respect to a previous characterisation [15].

The experimental set up is illustrated in Figure 1. The 20 m NaOH solutions were prepared in a polypropylene PP plastic vessel, and placed in the pre-heated water bath for 30 minutes at the target temperatures of 45°C, 60°C, or 80°C.

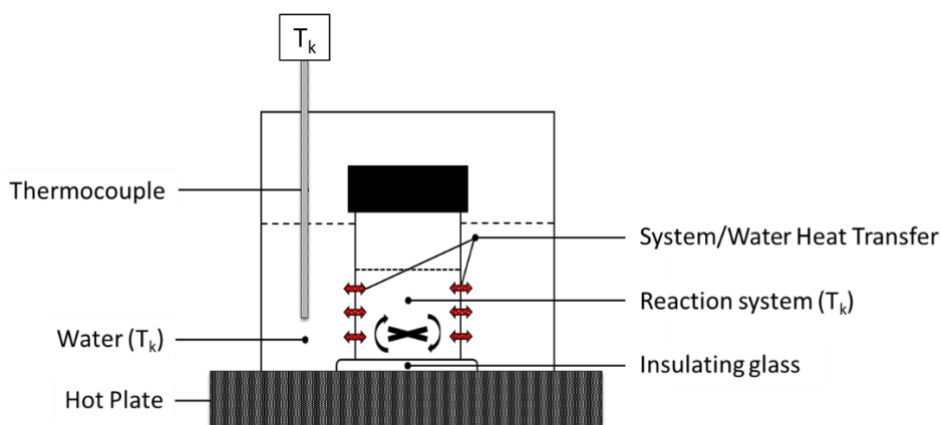


Fig. 1.

The direct contact between the hot plate and the bottom of the reaction vessel was avoided through the placement of an insulating glass disk. The  $\text{CaCO}_3$  powders were also pre-heated at  $80^\circ\text{C}$  for 2 hours to remove any adsorbed water. The  $\text{CaCO}_3$  was then quickly added to the NaOH solutions and manually mixed, at first, to prevent the agglomeration of the solids. Subsequently, the vessel was covered with a lid to minimise the loss of water and heat, and a magnetic stirring of 300 rpm was set up. Isothermal conditions were ensured throughout the residence times investigated: 1, 2, 3, 4 and 5 minutes. Longer residence times were not considered, since our previous study [15] highlighted that negligible reaction progression would occur beyond five minutes of residence time.

The reaction was also performed in non-isothermal conditions, upon initial heating of the NaOH solutions at the targeted temperatures of 45, 60, and  $80^\circ\text{C}$  ( $45^\circ\text{C}_5 \text{ min}_{\text{RT}}$ ,  $60^\circ\text{C}_5 \text{ min}_{\text{RT}}$ , and  $80^\circ\text{C}_5 \text{ min}_{\text{RT}}$ , respectively). A residence time of five minutes was solely considered to produce these samples.

For all systems tested, once the reaction was complete, 30 mL of methanol was added to the system to mix for a further five minutes, ensuring the removal of the unreacted NaOH. The solubility of NaOH in methanol is 238 g/L [22], while the negligible solubility of  $\text{CaCO}_3$  [23],  $\text{Ca}(\text{OH})_2$  [24],  $\text{Na}_2\text{CO}_3$  [25] and  $\text{Na}_2\text{CO}_3 \cdot \text{H}_2\text{O}$  [25] would ensure the same solid phase assemblage remained upon methanol washing. The solid products and the liquid streams could then be collected separately using Buchner filtration. The solids were dried in an  $80^\circ\text{C}$  oven for two hours, before being manually ground and sieved below  $63 \mu\text{m}$  for subsequent characterisation through TG and XRD analysis.

An additional set of experiments was conducted to estimate the activation energy  $E_a$  of the decarbonisation reaction at different starting compositions (Table 1), selected from our previous study [14]. The reaction was conducted at a constant temperature adopting the same procedure described above and all the samples were reacted for one minute at  $30^\circ\text{C}$ ,  $45^\circ\text{C}$ ,

60°C and 70°C. The datasets used and/or analysed during the current study are available from the corresponding author on reasonable request.

Table 1.

ID	NaOH (w%)	CaCO <sub>3</sub> (w%)	H <sub>2</sub> O (w%)	NaOH/CaCO <sub>3</sub> (mol/mol)	H <sub>2</sub> O/CaCO <sub>3</sub> (g/g)	H <sub>2</sub> O/NaOH (mol/mol)	$\alpha$ [10]
NaOH_10m	14.3	14.3	71.4	2.5	3.0	5.5	0.07
NaOH_12m	24.5	24.5	51.0	2.5	2.1	4.6	0.46
NaOH_15m	30.1	20.0	49.9	3.8	2.5	3.7	0.69
NaOH_17m	37.2	8.1	54.7	11.5	6.7	3.3	0.96

## 2.2. Characterisation techniques

### 2.2.1. X-Ray Diffraction (XRD)

The reaction products were qualitatively identified by X-ray diffraction (XRD) and following analysis on the Highscore-Plus software with the PDF-4 2019 database. The measurements were performed using a Bruker D2 PHASER desktop X-ray diffractometer in the Bragg-Brentano geometry equipped with a Cu-K $\alpha$  radiation source running at 30 kV and 10 mA. The instrument is equipped with a one-dimensional LYNXEYE detector and a 1 mm divergence slit. All samples were in a powder form, and they were loaded onto the sample holder with 2.5 cm diameter and 1 mm deep. All the analyses were conducted between 5° and 80° (2 $\theta$ ) with a step size of 0.02° at 0.5 s per step, with the stage rotating at 15 rpm to improve counting statistics.

### 2.2.2. Thermogravimetry (TG/DTG)

A PerkinElmer TGA 4000 was used to provide Thermogravimetric analysis (TGA) for the reaction products; approximately 40 mg of sample were subjected to a temperature ramp from 30°C to 800°C at the heating rate of 10°C/min, with a 40 mL/min of N<sub>2</sub> flow. The heating program was set up to held the sample at 800°C for 1 hour to ensure complete loss of CO<sub>2</sub> from CaCO<sub>3</sub>; the analysis temperature was not exceeding 800°C to avoid the melting or weight loss from Na<sub>2</sub>CO<sub>3</sub>. To identify evolving gases, a Hiden mass spectrometer (HPR-20 GIC EGA) was used to record the signals for CO<sub>2</sub> and H<sub>2</sub>O. An example of TG analysis is presented in Figure 2, where the mass loss events are linked to Ca(OH)<sub>2</sub>, Na<sub>2</sub>CO<sub>3</sub>·H<sub>2</sub>O and CaCO<sub>3</sub>. Together with the weight loss, the DTG trend is also reported to ensure the distinction of eventual overlapping signals. The extent of reaction was calculated based on the amount of

Ca(OH)<sub>2</sub> [26] and unreacted CaCO<sub>3</sub> [27], based on the respective thermal decompositions. The content of Na<sub>2</sub>CO<sub>3</sub>·H<sub>2</sub>O could similarly be estimated in the temperature range 50-130°C [28].

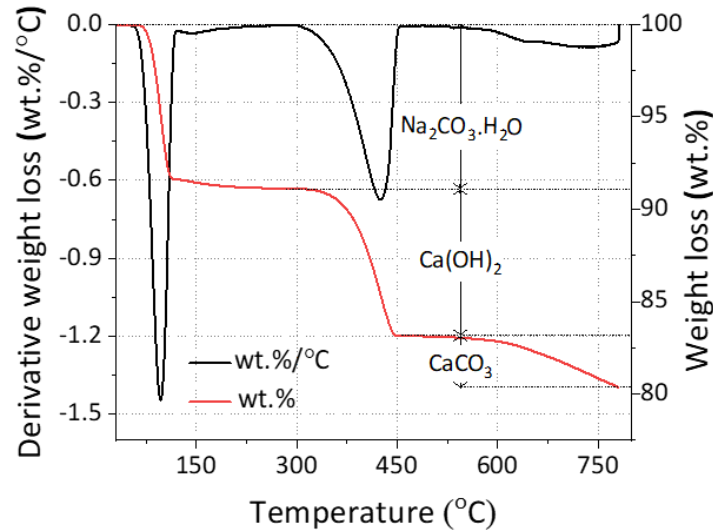


Fig. 2.

The measurement was repeated 6 times for each sample to estimate the measurement error ( $\pm 0.16$  wt.%,  $\pm 0.10$  wt.% and  $\pm 0.16$  wt.% for Na<sub>2</sub>CO<sub>3</sub>·H<sub>2</sub>O, Ca(OH)<sub>2</sub> and CaCO<sub>3</sub>, respectively).

$$\alpha = \frac{w\%_{[Ca(OH)_2]}}{MW_{Ca(OH)_2}} \bigg/ \left[ \frac{w\%_{[Ca(OH)_2]}}{MW_{Ca(OH)_2}} + \frac{w\%_{[CaCO_3]}}{MW_{CaCO_3}} \right] \quad (5)$$

### 3. Theory

This investigation aims to provide the scientific community with a deeper insight into the chemistry and energetic demand of a novel CaCO<sub>3</sub> decarbonisation route [29], with the potential to lead the transition towards sustainable cement, lime, and soda ash industries. To highlight this, an energetic comparison with the state-of-the-art processes is presented in Section 5, highlighting the potential advantages of the alternative one. To do that, the concomitant by-production of soda ash Na<sub>2</sub>CO<sub>3</sub> was also considered, whose conventional manufacturing route through Solvay process requires a high energy supply. This early-stage investigation, together with other ones focussing on the processing conditions [15] and nature of the raw materials used [30], will provide a strong base to the potential scale-up of the process. In these terms, future work will aim to design a laboratory-scale process simulating

the ideal industrial one, providing a stronger dataset to assess the effective energy requirements of the route, and therefore allowing for a proper techno-economic analysis.

## 4. Results and Discussion

### 4.1. Effect of temperature and CO<sub>2</sub> capture

The XRD analysis of the 45°C\_n, 60°C\_n, and 80°C\_n samples, with n indicating the specific residence time, are shown in Figures 3A, B, and C, respectively.

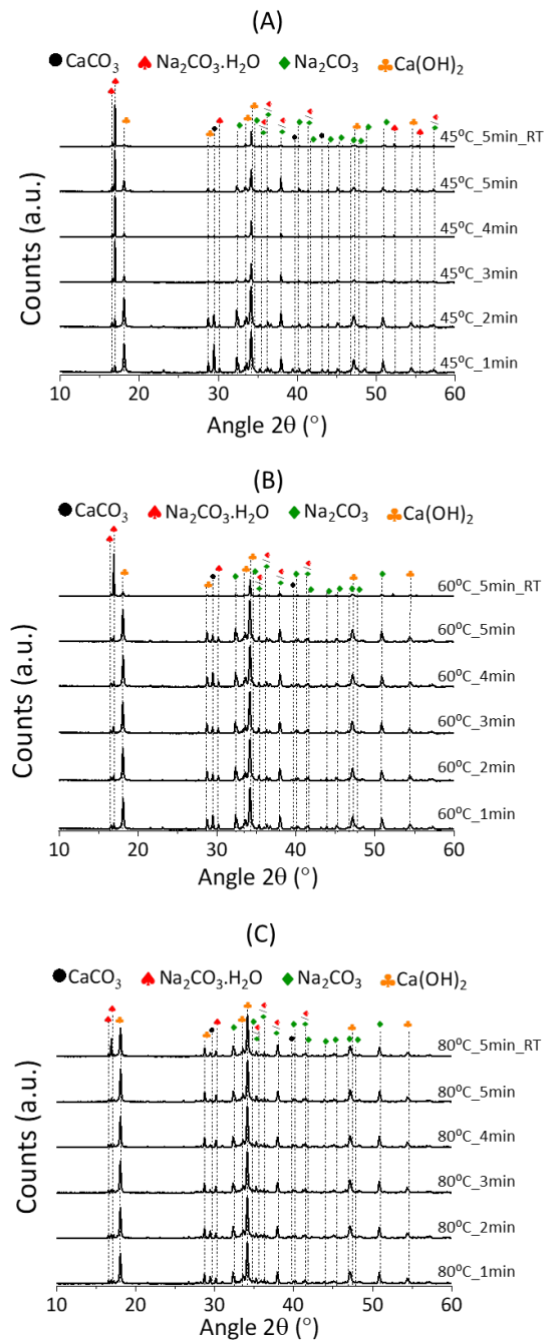


Fig.3.

Upon reaction, only  $\text{Ca}(\text{OH})_2$ ,  $\text{Na}_2\text{CO}_3$ ,  $\text{Na}_2\text{CO}_3 \cdot \text{H}_2\text{O}$  and unreacted  $\text{CaCO}_3$  could be detected, with respective main reflection angles at  $2\theta$  of  $29.5^\circ$  [31],  $34.1^\circ$  [32],  $16.9^\circ$  [33] and  $30.1^\circ$  [34]. No additional phases were detected, suggesting the absence of secondary and competing reactions. The TG data for the  $45^\circ\text{C}_n$ ,  $60^\circ\text{C}_n$  and  $80^\circ\text{C}_n$  series is shown in Figure 4A, B and C, respectively.

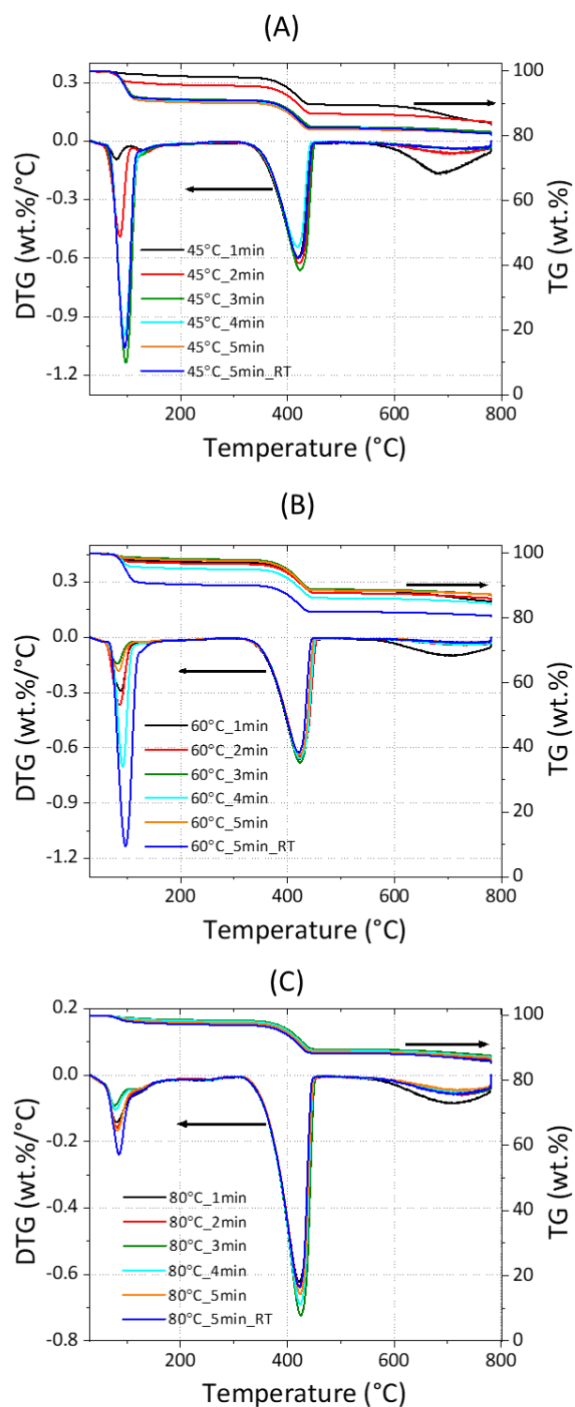


Fig. 4.

The phase quantification could be performed through the weight losses observed in the TG data for  $\text{CaCO}_3$  (at 560-800°C),  $\text{Ca(OH)}_2$  (at 310-470°C) and  $\text{Na}_2\text{CO}_3 \cdot \text{H}_2\text{O}$  (at 50-130°C). The estimated quantities for all the samples discussed are summarised in Table 2, where the processing conditions used are stated in the sample IDs.

Table 2.

Sample ID	$\text{CaCO}_3$ (wt.%)	$\text{Ca(OH)}_2$ (wt.%)	$\text{Na}_2\text{CO}_3 \cdot \text{H}_2\text{O}$ (wt.%)	$\text{Na}_2\text{CO}_3$ (wt.%)	LOI (%)	$\text{Na}_2\text{CO}_3 \cdot \text{xH}_2\text{O} / \text{Ca(OH)}_2$ (mol%/mol%)
45°C_1min	13.7	34.5	6.6	45.2	15.4	1.1
45°C_2min	6.4	35.6	23.6	34.4	14.9	1.1
45°C_3min	4.2	34.3	55.9	5.6	18.3	1.1
45°C_4min	4.8	32.9	59.6	2.7	18.8	1.1
45°C_5min	3.2	33.5	61.6	1.7	18.5	1.1
45°C_RT_5min	4.6	34.7	57.0	3.7	18.7	1.1
60°C_1min	8.9	34.8	15.1	41.2	14.6	1.1
60°C_2min	4.5	36.8	18.0	40.7	13.5	1.1
60°C_3min	4.2	37.7	8.6	49.5	12.2	1.1
60°C_4min	4.3	36.7	8.9	50.1	15.0	1.1
60°C_5min	3.1	37.8	11.1	48.0	12.2	1.1
60°C_RT_5min	3.2	33.5	61.6	1.7	18.5	1.1
80°C_1min	8.5	34.7	11.1	45.7	13.8	1.2
80°C_2min	6.1	35.9	11.0	47.0	13.0	1.2
80°C_3min	5.2	36.1	6.6	52.1	12.0	1.2
80°C_4min	5.5	36.1	7.9	50.5	12.3	1.2
80°C_5min	5.2	35.8	11.2	47.8	12.6	1.2
80°C_RT_5min	6.0	35.2	15.0	43.8	13.4	1.2

It must be mentioned that the content of  $\text{Na}_2\text{CO}_3$  was calculated by subtracting the sum of the other quantified phases  $\text{Ca(OH)}_2$ ,  $\text{CaCO}_3$  and  $\text{Na}_2\text{CO}_3 \cdot \text{H}_2\text{O}$  from the total mass (100%). In fact, since it would start decomposing above 851°C [35], it could not be directly quantified by TG analysis (up to 800°C) through the detection of the relevant peak. A higher content of  $\text{Na}_2\text{CO}_3$  could also be suggested by the lower LOI registered for samples with similar reaction efficiencies (Table 2). This aspect will be extensively discussed in Section 3.2. However, the quantification was considered reliable since the XRD analysis confirmed the absence of any additional phases in the solid products. Moreover, the ratio between the precipitated  $\text{Na}_2\text{CO}_3 \cdot \text{H}_2\text{O} / \text{Na}_2\text{CO}_3$  and  $\text{Ca(OH)}_2$  (mol%/mol%) revealed a good accordance to the stoichiometry expressed in Equation 1 (Table 2). In fact, 1 mol of both  $\text{Ca(OH)}_2$  and

$\text{Na}_2\text{CO}_3 \cdot \text{H}_2\text{O}/\text{Na}_2\text{CO}_3$  should precipitate for each mol of  $\text{CaCO}_3$  reacted, and the resulting molar ratio between  $\text{Na}_2\text{CO}_3 \cdot \text{H}_2\text{O}/\text{Na}_2\text{CO}_3$  and  $\text{Ca}(\text{OH})_2$  was expected to be close to unity. Specifically, the ratios were suggesting a slight over-precipitation of  $\text{Na}_2\text{CO}_3 \cdot \text{H}_2\text{O}$  and  $\text{Na}_2\text{CO}_3$  with respect to  $\text{Ca}(\text{OH})_2$  for all the systems studied and that could possibly be reflecting the distribution of the positive ( $\text{Ca}^{2+}$ ) and negative ( $\text{CO}_3^{2-}$ ) charged sites on the surface of the  $\text{CaCO}_3$ . Statistically, a 27% excess of negatively charged sites may be found on the  $\text{CaCO}_3$  surface [36], justifying the greater affinity of the  $\text{CaCO}_3$  to interact with the cationic species  $\text{Na}^+$  in the liquid bulk to form  $\text{Na}_2\text{CO}_3 \cdot \text{H}_2\text{O}/\text{Na}_2\text{CO}_3$ .

Based on the TG data, the extent of reaction ( $\alpha$ ) was calculated for each system, and the outcomes are reported in Figure 5.

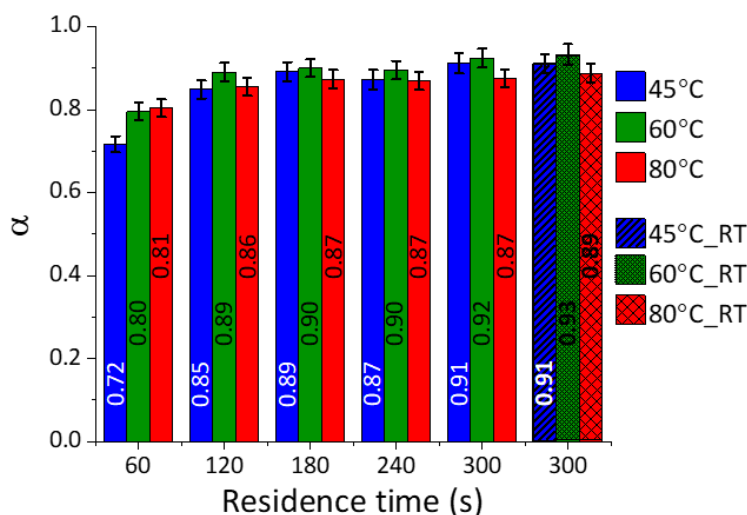


Fig.5.

The conversion of  $\text{CaCO}_3$  was high in the tested reaction conditions, where extents of reaction between 0.7-0.8 were seen. The general trends of the extent of reaction coincides with that of XRD data (Figures 3A, B, and C) which shows progressive decrease in the intensity of the  $\text{CaCO}_3$  main peak at  $29.5^\circ 2\theta$ . In the first 60 seconds, temperature had a significant impact on the extent of reaction, showing enhanced efficiency of  $\text{CaCO}_3$  conversion at higher temperatures, while limited effects of temperature were observed at longer reaction times. This is because the reaction is nearly completed with the longer reaction time even at the lower temperatures. It seems likely that the higher conversion registered at short residence time and higher temperature could be linked to the lower viscosity of the NaOH solutions, favouring the ionic mobility and the enhanced interaction between the dissolved species and the solid surface and bulk.

The efficiency of the system may also be expressed in terms of CO<sub>2</sub> capture, expressed as moles of CO<sub>2</sub> precipitated as Na<sub>2</sub>CO<sub>3</sub>·xH<sub>2</sub>O per second of reaction progression. As reported in Figure 6, the CO<sub>2</sub> capture rate was decreasing from ~ 4.5·10<sup>-4</sup> mol·sec<sup>-1</sup> of CO<sub>2</sub> in the first 60 seconds of reaction down to two orders of magnitude below (~10<sup>-6</sup> mol·sec<sup>-1</sup> of CO<sub>2</sub>) after 300 seconds of contact time. In other terms, around the 80% of the total process CO<sub>2</sub> initially introduced was effectively captured after 60 seconds of reaction.

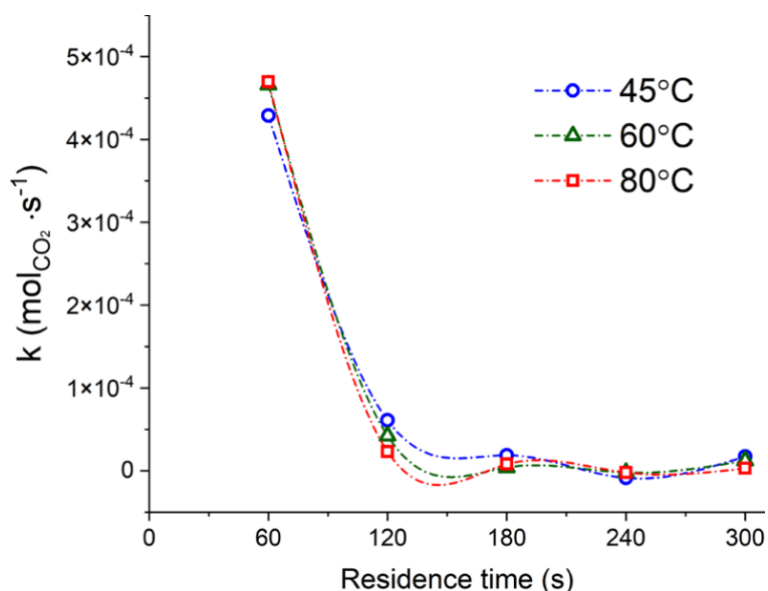


Fig.6.

The samples reacted at ambient conditions (45°C\_5 min\_RT, 60°C\_5 min\_RT, and 80°C\_5 min\_RT) indicated extent of reactions like those reacted at a constant temperature after 300 seconds (Figure 5). Decreasing temperature trends could be detected for 45°C\_5 min\_RT, 60°C\_5 min\_RT, and 80°C\_5 min\_RT, with final temperatures of 21.5, 42.1, and 53.6°C, respectively, after five minutes of residence time. Evidently, the temperature of the system was not significantly influencing the progression of the reaction for a residence time of five minutes.

#### 4.2. Partitioning of Na<sub>2</sub>CO<sub>3</sub>·H<sub>2</sub>O and Na<sub>2</sub>CO<sub>3</sub>

The reaction at different conditions resulted in sequestration of CO<sub>2</sub> by forming Na<sub>2</sub>CO<sub>3</sub>·H<sub>2</sub>O and Na<sub>2</sub>CO<sub>3</sub> in different proportion, with the x value (Equation 1) equal to 1 and 0, respectively. To further study this phenomenon, the proportion between Na<sub>2</sub>CO<sub>3</sub>·H<sub>2</sub>O and Na<sub>2</sub>CO<sub>3</sub> was examined. Based on the data obtained from TGA (Figures 4A, B and C), the molar fraction v of precipitated Na<sub>2</sub>CO<sub>3</sub> was calculated by dividing the moles of Na<sub>2</sub>CO<sub>3</sub> in the samples by the total moles of Na<sub>2</sub>CO<sub>3</sub>·H<sub>2</sub>O and Na<sub>2</sub>CO<sub>3</sub>. As reported in Figure 7, at a constant temperature of

45°C,  $v\text{Na}_2\text{CO}_3$  decreased significantly from 0.88 to 0.11 in the first 3 minutes, whereas the precipitation of  $\text{Na}_2\text{CO}_3$  was dominant at 60 and 80°C for all the residence times investigated.

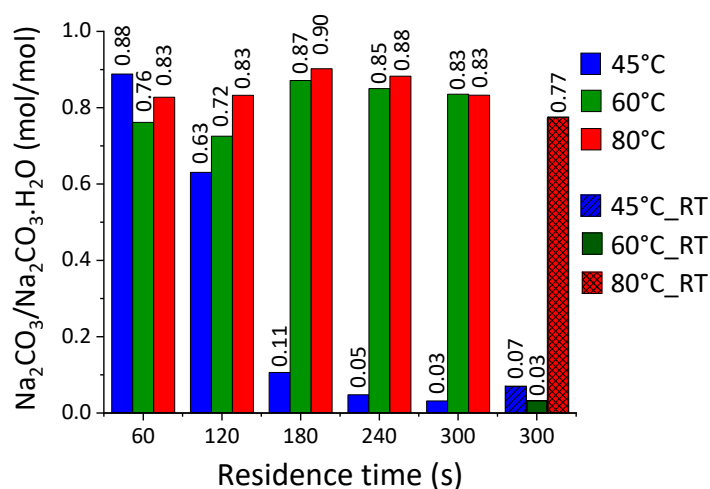


Fig. 7.

The samples reacted at ambient conditions showed enhanced precipitation of  $\text{Na}_2\text{CO}_3 \cdot \text{H}_2\text{O}$  at initial temperatures  $T_i$  of 45 and 60°C. Such a different proportion gained at different values of  $T_i$  might be explained by considering the thermodynamics of the system. Referring to Equation 1 and considering the  $x$  value equal to 0 or 1, the calculation of the reaction standard enthalpy of reaction  $\Delta H_R$  led to values of  $-54.5 \text{ kJ mol}^{-1}$  and  $-69.2 \text{ kJ mol}^{-1}$ , respectively. The calculation was performed by application of the Hess law and considering standard enthalpies of formation of  $-1207.4$ ,  $-426.7$ ,  $-285.8$ ,  $-986.1$ ,  $-1429.7$ , and  $-1129.2 \text{ kJ} \cdot \text{mol}^{-1}$  for  $\text{CaCO}_3$  [37],  $\text{NaOH}$  [38],  $\text{H}_2\text{O}$  [38],  $\text{Ca}(\text{OH})_2$  [38],  $\text{Na}_2\text{CO}_3 \cdot \text{H}_2\text{O}$  [37], and  $\text{Na}_2\text{CO}_3$  [37], respectively. That would suggest that the precipitation of  $\text{Na}_2\text{CO}_3$  would be slightly favoured at higher temperatures with respect to  $\text{Na}_2\text{CO}_3 \cdot x\text{H}_2\text{O}$ , i.e. the reaction with  $x$  equal to 1 shows a slightly more exothermic behaviour. In fact, lower  $\text{Na}_2\text{CO}_3$  contents were measured for those samples reacted at ambient conditions from a  $T_i$  of 45 and 60°C, with respect to those at 80°C, with respective final temperatures  $T_f$  of 21.5°C, 42.1°C and 53.5°C. This reflects somewhat less exothermic behaviour, i.e. higher  $\Delta H_R$ , precipitation of  $\text{Na}_2\text{CO}_3$  respect with  $\text{Na}_2\text{CO}_3 \cdot \text{H}_2\text{O}$ . The results of the TG analysis were supported by the XRD patterns reported in Figures 3A, B and C. In fact, weak signals could be detected at  $2\theta$  of  $16.9^\circ$ , main peak for  $\text{Na}_2\text{CO}_3 \cdot \text{H}_2\text{O}$ , for all the 80°C\_n series, whereas increased intensities were observed for the 45°C\_n series above 2 minutes of residence time and the sample reacted at ambient conditions with  $T_i$  of 60°C.

The equilibrium of  $\text{Na}_2\text{CO}_3 \cdot \text{H}_2\text{O}$  and  $\text{Na}_2\text{CO}_3$  was studied by performing targeted simulations of a simplified system using the PHREEQC software [39] with the PITZER(2018) database, and an overview of the outcomes is reported in Figures 8A and B.

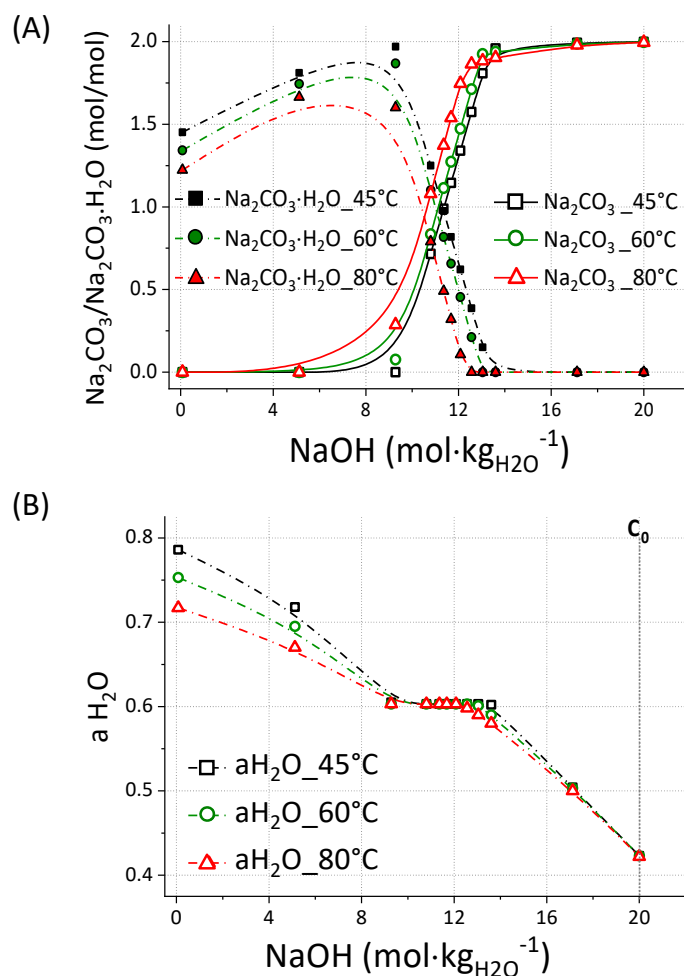


Fig. 8.

The simulation was conducted for a system composed of both 1 mole of  $\text{Na}_2\text{CO}_3 \cdot \text{H}_2\text{O}$  and 1 mole of  $\text{Na}_2\text{CO}_3$  dissolved in 0.1 kg of water at 45, 60 or 80°C, with increasing concentration of NaOH up to 20 m. The simulated system does not contain Ca ions as in the experimentally tested systems but it is useful to understand the general behaviour of  $\text{Na}_2\text{CO}_3 \cdot \text{H}_2\text{O}$  and  $\text{Na}_2\text{CO}_3$  in the aqueous system with the presence of NaOH at high concentrations. As seen in Figure 8A, lower molality of NaOH would lead to the dominant precipitation of  $\text{Na}_2\text{CO}_3 \cdot \text{H}_2\text{O}$  while  $\text{Na}_2\text{CO}_3$  is the major precipitate at higher NaOH molality. In the NaOH concentration range of approximately 10 to 12.5 m, co-precipitation of  $\text{Na}_2\text{CO}_3 \cdot \text{H}_2\text{O}$  and  $\text{Na}_2\text{CO}_3$  occurs. This may explain the data presented in Figure 7 for the samples reacted at 45°C. In fact, a low consumption of NaOH has taken place at the very start of Reaction 1, when the concentration of NaOH is still high (20 m), and  $\text{Na}_2\text{CO}_3$  is the main product. When more NaOH is consumed, at enhanced reaction progression, the precipitation of  $\text{Na}_2\text{CO}_3 \cdot \text{H}_2\text{O}$  is favoured. Although the reaction also produces  $\text{Ca}(\text{OH})_2$ , its solubility is much lower than that of NaOH, and thus, the behaviour of the aqueous system is expected to be dominated by NaOH. Despite the NaOH

concentration, the data for 60 and 80°C presented in Figure 7 indicated that Na<sub>2</sub>CO<sub>3</sub> was the main product throughout the tested period even after significant NaOH consumption. This may be related to the activity of water in the system. As shown in Figure 8B, the activity of water (a<sub>H<sub>2</sub>O</sub>) generally decreases at higher NaOH concentration, in accordance with the literature [40]. The activity of water is lower also when the temperature is higher. By comparing this with Figure 8A, it can be deduced that Na<sub>2</sub>CO<sub>3</sub> forms when the activity of water is lower (the NaOH concentration is higher), and Na<sub>2</sub>CO<sub>3</sub>·H<sub>2</sub>O can form when it is higher (the NaOH concentration is lower). Most likely, in these systems, the reaction temperatures (60 and 80°C) were high enough to maintain the activity of water sufficiently low to form Na<sub>2</sub>CO<sub>3</sub> even after consumption of NaOH. This also suggests that 45°C is not high enough to form Na<sub>2</sub>CO<sub>3</sub>, as confirmed with the experiments conducted at ambient conditions. In fact, the system initially heated at 60°C mostly formed Na<sub>2</sub>CO<sub>3</sub>·H<sub>2</sub>O at the end of the reaction, where the temperature became 42.1°C.

The temperature significantly affects the a<sub>H<sub>2</sub>O</sub> values up to a NaOH molality around 10, and, above such a value, the system assumes a transitional a<sub>H<sub>2</sub>O</sub> value of 0.603. That corresponds to a chemical potential *u* of -241.3 kJ·mol<sup>-1</sup> (Equation 6), where *u*<sub>0</sub> is the standard chemical potential of formation of pure water [41], *R* the gas constant, and *T* the temperature in K.

$$u = u_0 + RT \ln a_w \quad (6)$$

At this point, the transition Na<sub>2</sub>CO<sub>3</sub>·H<sub>2</sub>O / Na<sub>2</sub>CO<sub>3</sub> is swapped (Figure 8A), promoting the precipitation of Na<sub>2</sub>CO<sub>3</sub>·H<sub>2</sub>O and Na<sub>2</sub>CO<sub>3</sub> above and below an activity of water of 0.603, respectively. To explain the constant water activity value of 0.603, the gradual formation of Na<sub>2</sub>CO<sub>3</sub> to the detriment of Na<sub>2</sub>CO<sub>3</sub>·H<sub>2</sub>O must be considered; as a result, water is released into the liquid bulk and it counterbalances the further addition of NaOH. In fact, when all the sodium into the system is converted to Na<sub>2</sub>CO<sub>3</sub> and no more H<sub>2</sub>O is released by the dissolution of Na<sub>2</sub>CO<sub>3</sub>·H<sub>2</sub>O, the activity of water rapidly drops down to just above 0.400 at NaOH 20 m. That corresponds to a higher water activity a<sub>H<sub>2</sub>O</sub> within the liquid phase of the system (Figure 8B), and therefore resulting in a higher proportioning of Na<sub>2</sub>CO<sub>3</sub>·H<sub>2</sub>O with respect to Na<sub>2</sub>CO<sub>3</sub> (Figure 8A).

### 4.3. Calculation of the Arrhenius parameters E<sub>a</sub> and A

An additional set of experiments was conducted to estimate the activation energy E<sub>a</sub> of the decarbonisation reaction at the different starting compositions reported in Table 1, selected from our previous study [14]. Based on the amount of CaCO<sub>3</sub> and Ca(OH)<sub>2</sub> in the reaction products estimated from their TGA data (Supplementary Electronic Information I - IV), the extent of reaction (α) was calculated for each reaction. As reported in Figure 9, beneficial

effects of raising temperatures were observed at different levels depending on the starting composition.

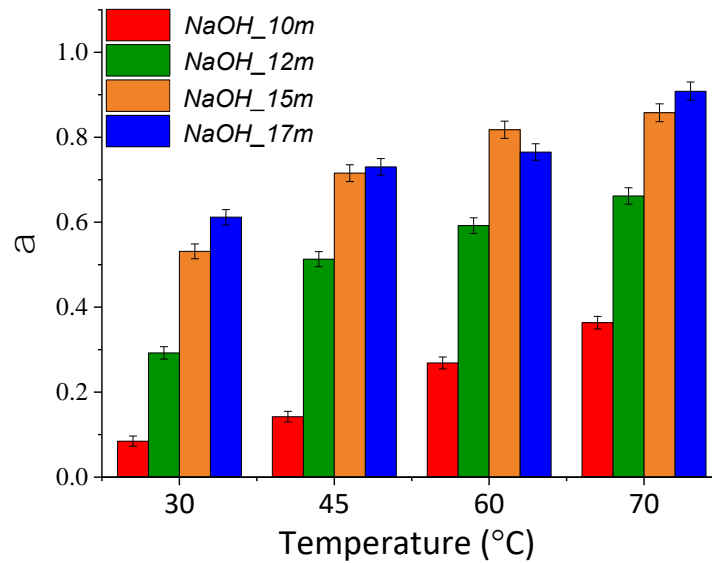


Fig. 9.

In these terms, the effects of temperature (T) is commonly expressed in the reaction rate constant (k) using Arrhenius equation (Equation 7) [42], depending on the pre-exponential factor (A), activation energy ( $E_a$ ) and gas constant (R).

$$k = Ae^{(-E_a/RT)} \quad (7)$$

The rate constant k is a change in the extent of reaction ( $\alpha$ ) per unit time (t). Since the reactions in this sub-set of experiments were all conducted for 1 minute, the extent of reaction obtained (Figure 9) was directly used in Equation 7 as representative of the reaction rate, and thus:

$$\alpha = Ae^{(-E_a/RT)} \quad (8)$$

Taking the natural logarithm, Equation 8 can also be expressed as:

$$\ln \alpha = \ln A - \frac{E_a}{RT} \quad (9)$$

By plotting  $\ln \alpha$  against  $T^{-1}$ , the activation energy  $E_a$  and pre-exponential factor A can be calculated from the slope ( $-E_a/RT$ ) and the intercept at  $T^{-1} = 0$ , respectively.

Figure 10 shows the corresponding plot, together with the linear fitting by the Arrhenius equation (Equation 9) for NaOH\_10m (Equation 10), NaOH\_12m (Equation 11), NaOH\_15m (Equation 12) and NaOH\_17m (Equation 13).

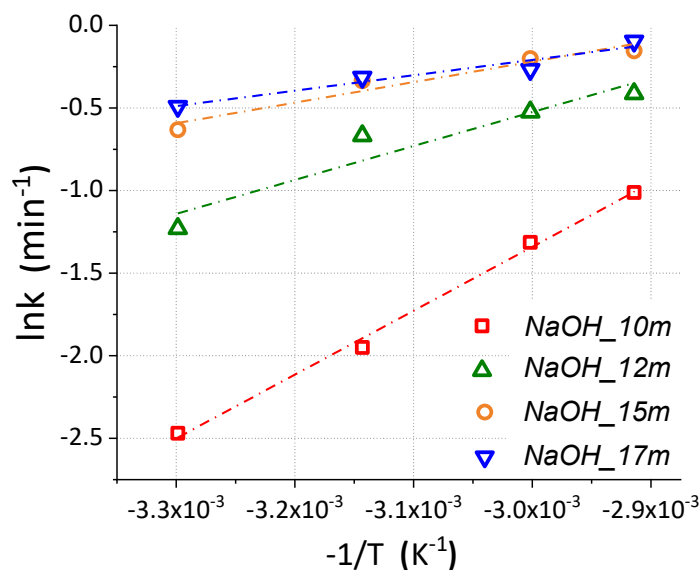


Fig. 10.

$$y = 3865.1x + 10.254 \quad R^2 = 1.00 \quad (10)$$

$$y = 2054.3x + 5.638 \quad R^2 = 0.91 \quad (11)$$

$$y = 1242.1x + 3.507 \quad R^2 = 0.94 \quad (12)$$

$$y = 933.3x + 2.591 \quad R^2 = 0.93 \quad (13)$$

Based on these, the apparent activation energies for NaOH\_10M, NaOH\_12M, NaOH\_15M and NaOH\_17M are estimated as 32.1, 17.1, 10.3 and 7.8 kJ mol<sup>-1</sup>, respectively, and therefore reflecting the limited kinetics at lower NaOH molality.

Despite that, faster kinetics could be observed for all the conditions tested here, with respect to the conventional calcination route of CaCO<sub>3</sub> under inert atmospheres (164 – 225 kJ·mol<sup>-1</sup> [43]) and with varying CO<sub>2</sub> partial pressures (213.3 – 2142.2 kJ·mol<sup>-1</sup> [44]). Since the pre-exponential factor A represents the probability of collisions between the reacting components [45], we expected larger values of the pre-exponential factor for the higher NaOH concentration. However, this trend was not clearly observed in the present analysis, as shown in Figure 11.

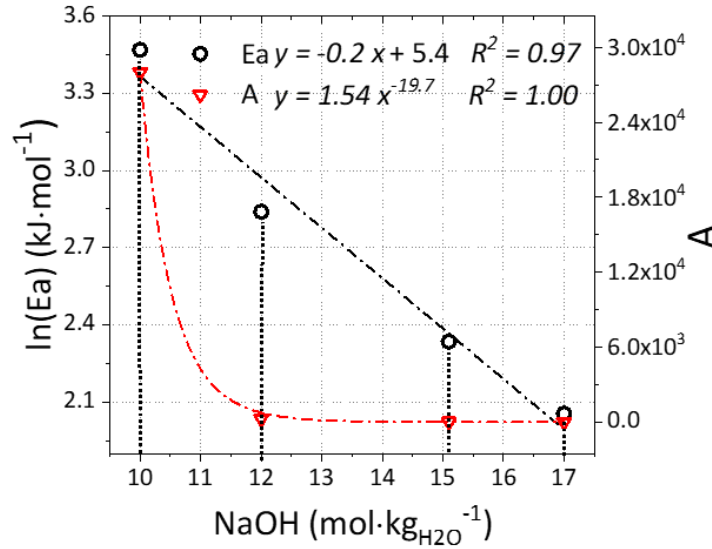


Fig. 11.

Given the lower efficiency reported, it is supposed that such collisions would not allow the activation energy barrier to be overcome. According to this data, a first-order kinetic description, only depending on a single parameter (i.e. NaOH concentration), would be supposed; on the other hand, the results reported by Hanein et al. [14] were also suggesting lower conversions at NaOH concentrations higher than 17.0 M. The other factors, such as the concentration of other reactants and intrinsic properties of both the NaOH solutions [46] used and CaCO<sub>3</sub> [47] may also play a determining role for collision of the reacting components. Previous studies [48-50] already discussed the interaction between solid calcite and dissolved solutes, concluding that the incorporation would occur at the level of the solid surface by adsorption, followed by nucleation/precipitation of the products within the core of solid CaCO<sub>3</sub>. It seems more likely that the system appeared to follow a first-order kinetic from low to medium NaOH concentrations; beyond the optimal NaOH molality, the activity of the Na<sup>+</sup> and OH<sup>-</sup> ions in the liquid bulk would be too low and the reaction progression hindered.

## 5. Industry-oriented considerations

The authors understand that a proper Life-Cycle Assessment needs to be done before assessing the industrial feasibility of the novel route, but this is not the aim of the present investigation. Nevertheless, some crucial considerations are reported below to better highlight the high potential of the decarbonisation route characterised here.

This approach shows considerable potential from an industrial perspective, since it is highlighted that eventual fluctuations of temperature would not negatively affect the reaction yield; moreover, the mild processing conditions required suggest very convenient production costs. On the other hand, the energy input required for the synthesis of the stoichiometric NaOH would represent the major obstacle in sight of an industrial application. In fact, 7,668 GJ is required to produce 1 t of NaOH, which occurs alongside the synthesis of 0.03 t of hydrogen gas and 1.1 t of chlorine gas, through the chlor-alkali process [51]. Such hydrogen is typically wasted and vented to the atmosphere, whereas the in-situ recirculation for power production would lower the energy demand by approximately 34% [52]. In these conditions, about 3,942 GJ of electricity should be supplied through usage of fresh fuel to decarbonise 1 tonne of CaCO<sub>3</sub>. Whereas the conventional cement production route implies the decarbonisation to be carried out at an efficiency between 41 and 62% [53]; considering the theoretical heat of dissociation of CaCO<sub>3</sub> (1819.4 kJ [54]), an energy input of 2,500 – 2,900 GJ per tonne of CaCO<sub>3</sub> to decarbonise is required. At first glance, the novel route does not appear economically feasible, since it requires 1.4 – 1.6 times the energy involved in the conventional one. However, it must be reminded that the co-production of Na<sub>2</sub>CO<sub>3</sub> occurs whilst synthesising Ca(OH)<sub>2</sub>, and important energetic considerations would arise from that. In fact, the production of 1 tonne of Na<sub>2</sub>CO<sub>3</sub> requires 13.6 GJ through the conventional Solvay process [55], which would be completely avoided by supplying the product via the chemical route proposed. According to the stoichiometry depicted in Equation 1, a Na<sub>2</sub>CO<sub>3</sub>/Ca(OH)<sub>2</sub> weight ratio of 1.43 occurs at the end of the reaction, assuming total conversion of CaCO<sub>3</sub>. The following considerations are done by normalising all the calculations with respect to cement, lime, and slaked lime, treating Na<sub>2</sub>CO<sub>3</sub> as an added-value by-product. For the calculations, a 1:1 weight ratio between the decarbonised CaCO<sub>3</sub> and the resulting cement was considered; in fact, the CaO proportion in PC is around 60 – 70% [56], and a 0.56 weight ratio occurs between the produced CaO (upon dehydration of Ca(OH)<sub>2</sub>) and the reacted CaCO<sub>3</sub>. For clarity, these numbers are reported in Table 3, alongside the cases for lime and slaked lime productions.

Table 3.

Production Type	PC	Lime	Slaked Lime	CaCO <sub>3</sub> Reacted	NaOH Reacted	Na <sub>2</sub> CO <sub>3</sub> Produced
PC	1	-	-	1	0.8	1.0
Lime	-	1	-	1.6	1.3	1.8
Slaked Lime	-	-	1	1.2	1.0	1.4

All these considerations were used to produce the energetic comparisons displayed in Figure 12, where the electrical energy input required to produce the stoichiometric NaOH is reported alongside the thermal energy to be supplied to decarbonise CaCO<sub>3</sub> plus the one to produce soda ash. The extremes of the energy efficiencies reported for the PRK design are labelled as “Thermal\_1” ( $\eta= 41\%$ ) and “Thermal\_2” ( $\eta= 62\%$ ) for the PC case, whereas the novel decarbonisation route is displayed as “Chemical” both for PC, lime, and slaked lime. It must be mentioned that the energies outlined were normalised with respect to 1 tonne of PC, according to the stoichiometry just discussed, and therefore expressed in GJ<sub>Equivalent</sub>, i.e., the energy required to produce 1 tonne of PC and the stoichiometric amount of Na<sub>2</sub>CO<sub>3</sub>. Furthermore, the values reported solely refer to the decarbonisation step, without considering additional consumptions associated with the further processing of both reactants and products. As reported, the chemical decarbonisation allows for a ~4 times lower energy consumption with respect to the thermal route, referring to the synthesis of 1 tonne of PC and 1.0 tonnes of Na<sub>2</sub>CO<sub>3</sub> (Table 3). For the calculation of the energy requirement from the chemical route, a 10% surplus was considered to include the handling and separation of the materials.

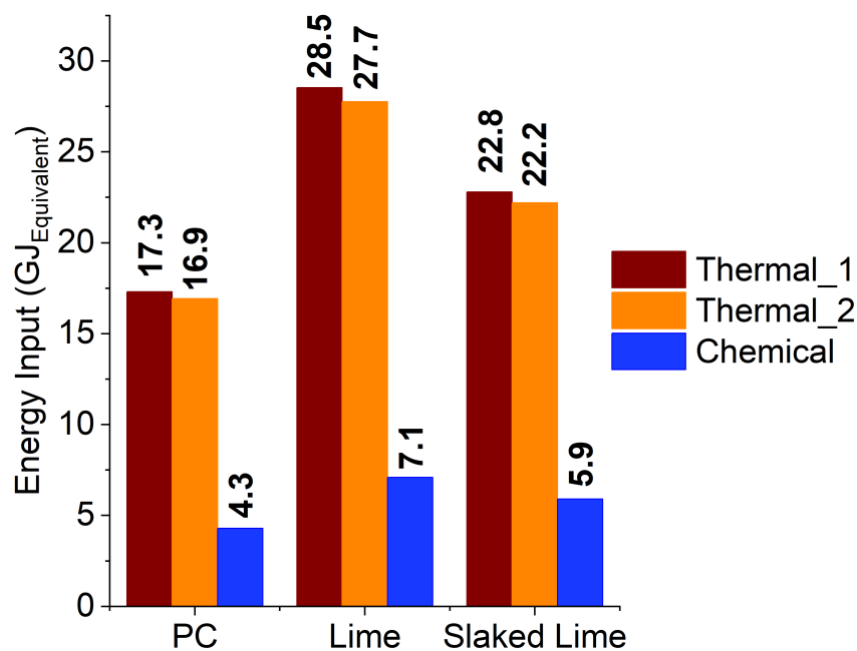


Fig. 12.

Regarding the production of lime, 1.6 tonnes of initial CaCO<sub>3</sub> are required to ensure 1 tonne of product, corresponding to a higher consumption of NaOH with respect to PC. For this reason, the normalisation with respect to lime shows that a higher amount of soda ash is produced, and that is considered for the calculation of the thermal power required from the

conventional route. In these terms, the calcination design adopted in the lime/slaked lime industry allows for higher efficiencies ( $75\% < \eta < 99\%$  [53]); in Figure 12, the labels “Thermal\_1” and “Thermal\_2” refer to the efficiency extremes of 75 and 99%, respectively. The larger consumption of NaOH reflects a higher energy input for the chemical route with respect to PC; despite that, even in this case the thermal route would require ~4 times the energy employed in the chemical decarbonisation, when 1 and 1.8 tonnes of CaO and Na<sub>2</sub>CO<sub>3</sub> are produced, respectively (Table 3). Finally, the case study for slaked lime Ca(OH)<sub>2</sub> highlighted a 3.7 – 3.8 lower energy input for the chemical route with respect to the conventional one for the synthesis of 1 and 1.4 tonnes of slaked lime and soda ash, respectively.

Despite the preliminary energetic balance appears promising from an applicative point of view, the global market demand of the chemicals involved must be considered. In fact, the current global demand for PC and soda ash is 4 Gt [1] and 50 Mt [57], respectively; if the whole global production of PC is performed chemically, an excess production of soda ash would occur. However, the demand for soda ash might significantly increase given the increasing importance of geopolymers in the global perspective, with Na<sub>2</sub>CO<sub>3</sub> widely used as activator to produce these low-carbon binders [58]. Furthermore, in case the excess of soda ash could not be reused, Na<sub>2</sub>CO<sub>3</sub> would represent a safer option for CO<sub>2</sub> storage with respect to the current geological disposal of liquid and compressed CO<sub>2</sub>, whose long-term effects have not been fully understood yet [59].

Another drawback of the chemical route is represented by the emissions of gaseous chloride arising from the chlor-alkali process to produce NaOH [51]; if the size of the market increases to fulfil the demand for cement production, such emissions might have a heavy impact on the environment. The development of chlorine-based binders, such as alinite [60], would help to mitigate the issue; in fact, despite the presence of chlorine leads to the failure of reinforced concrete upon corrosion of steel [61], over 75% of worldwide cement is used for unreinforced purposes [62]. In addition, an enhancement of the chlor-alkali process with in-situ hydrogen processing and re-use would contribute to the mitigation of the drinkable water crisis expected in the next decades [63]. In fact, Na<sup>+</sup> and Cl<sup>-</sup> are removed from the brine (concentrated seawater) fed into the chlor-alkali process, and pure water is a by-product from the reprocessing of hydrogen [64].

Alternatively, both the excess production of soda ash and the increasing emissions of chlorine gas might be limited by solely applying the novel route to produce lime and slaked lime, whose markets (50 Mt and 20Mt, respectively [2]) are currently closer to that of soda ash (50 Mt [57]).

## 6. Conclusions

The effects of temperature on the efficiency of a low temperature alternative decarbonisation process for  $\text{CaCO}_3$  was assessed. The reaction appeared effective for the sequestration of the process  $\text{CO}_2$  partitioned into  $\text{CaCO}_3$ , with over the 80% of it captured within the first 60 seconds of reaction. The laboratory-scale experimental results are promising in terms of scale-up since short residence times and mild heating conditions were found to lead to high conversion degrees of  $\text{CaCO}_3$ . The beneficial effect of a higher temperature was observed at short residence time, whereas the benefits appeared limited at longer ones. The results showed also that the temperature can be controlled only at the beginning of the reaction, and it may not be necessary to actively maintain it throughout the reaction. In fact, the reaction took place rapidly even under ambient conditions, regardless of the initial temperature considered. That would reflect a significant advantage from an industrial point of view, suggesting the process is robust and that no additional costs would be associated with the control of the reaction temperature.

The precipitation of  $\text{Na}_2\text{CO}_3 \cdot \text{H}_2\text{O}$  was found to be the main process  $\text{CO}_2$  sequestration path at milder temperature and pH, but these outcomes appear mainly relevant to the following separation of the reaction products  $\text{Ca}(\text{OH})_2$  and  $\text{Na}_2\text{CO}_3 \cdot x\text{H}_2\text{O}$ . In fact, the solubilities of  $\text{Na}_2\text{CO}_3 \cdot \text{H}_2\text{O}$  and  $\text{Na}_2\text{CO}_3$  are different ( $330$  and  $307 \text{ g} \cdot \text{L}^{-1}$  at  $25^\circ\text{C}$  and  $1 \text{ atm}$ , respectively), and a successful separation of the products requires a precise adjustment of the system considering the phases involved. In these terms, the precipitation of  $\text{Na}_2\text{CO}_3 \cdot \text{H}_2\text{O}$  seems favourable, given the higher gap with the solubility product of  $\text{Ca}(\text{OH})_2$  ( $1.5 \text{ g} \cdot \text{L}^{-1}$  at  $25^\circ\text{C}$  and  $1 \text{ atm}$ ) and therefore suggesting an easier separation of the products.

The Arrhenius parameters  $E_a$  and  $A$  were determined for the four starting mix compositions previously tested. Generally, the activation energy barrier was smaller for the system with the higher initial  $\text{NaOH}$  concentration. However, the decarbonisation route discussed here showed much faster kinetics with respect to the conventional  $\text{CaCO}_3$  calcination for all the conditions tested.

Preliminary energetic considerations were also reported, and the comparison between the thermal and chemical route to produce PC, lime, slaked lime, and soda ash was shown. As outlined, the chemical route was  $\sim 4$  times more convenient in terms of energy input, if only the decarbonisation step of  $\text{CaCO}_3$  is considered. The outcomes were discussed and justified, outlining both the advantages and drawbacks to solve to successfully apply the novel route.

Overall, the alternative decarbonisation of  $\text{CaCO}_3$  investigated in the present work may have the potential to drastically reduce the carbon footprint of the related industries, potentially

removing the need for high temperature calcination. Although, a successful large-scale application would require high investment costs which might potentially be overrun in a short-to-medium period, considering both the lower energetic requirement and carbon footprint. However, the main obstacle to overcome is still represented by the general concept that the thermal decarbonisation of  $\text{CaCO}_3$  is unavoidable, and that a transition would be technically too difficult to operate. Although, the current environmental crisis demands for decisive and optimistic approaches which require desire for real change, opening new paths towards a sustainable world.

## List of Captions

**Table 1.** Starting compositions (w%) and the molar ratio NaOH/CaCO<sub>3</sub> of the samples. The conversion extent  $\alpha$  is defined in Equation 5 below.

**Fig. 1.** Illustration of the experimental set up discussed above, highlighting the indirect temperature control on the reaction system by setting the surrounding water environment at a Tk temperature through external thermocouple.

**Fig. 2.** Generic temperature-trend of the TG data (wt.%) and DTG data (wt.%/°C), red and black lines, respectively, showing the weight loss events of the sample associated with: Na<sub>2</sub>CO<sub>3</sub>·H<sub>2</sub>O, Ca(OH)<sub>2</sub>, and CaCO<sub>3</sub>.

**Fig. 3.** XRD patterns for the 45°C<sub>n</sub> samples produced at a constant temperature of 45°C, 60°C and 80°C and that produced without actively maintaining the temperature after initial heating at 45°C, 60°C and 80°C.

**Fig. 4.** TG/dTG analysis for the samples series 45°C<sub>n</sub> (A), 60°C<sub>n</sub> (B), and 80°C<sub>n</sub> (C,) showing the weight losses in the temperature ranges of 50-130°C, 310-470°C and 560-800°C corresponding to the presence of Na<sub>2</sub>CO<sub>3</sub>·H<sub>2</sub>O, Ca(OH)<sub>2</sub> and CaCO<sub>3</sub>, respectively.

**Table 2.** Processing conditions and phases composition gained from thermogravimetric analysis, together with the Loss On Ignition (LOI) expressed in % and the Na<sub>2</sub>CO<sub>3</sub>·H<sub>2</sub>O/Ca(OH)<sub>2</sub> molar ratio registered for all the samples discussed.

**Fig. 5.** Extent of reaction ( $\alpha$ ) for the samples at different temperatures (45, 60 and 80°C) and increasing residence times, based on TG analysis; the outcomes are also reported for those samples produced without actively maintaining the temperature throughout the reaction.

**Fig. 6.** CO<sub>2</sub> capture rate, expressed in moles of CO<sub>2</sub> precipitated as Na<sub>2</sub>CO<sub>3</sub>·xH<sub>2</sub>O per second of reaction progression, for all the residence times considered at constant temperature; the samples reacted at ambient conditions were not considered for this graph. The lines only work as a guide for the eye.

**Fig. 7.** Molar fraction  $v$  of Na<sub>2</sub>CO<sub>3</sub>, expressed as molar ratio between Na<sub>2</sub>CO<sub>3</sub> and Na<sub>2</sub>CO<sub>3</sub>·H<sub>2</sub>O, for the samples produced at 45, 60 and 80°C at increasing residence times.

**Fig. 8.** PHREEQC simulation showing the molar ratio between the precipitated Na<sub>2</sub>CO<sub>3</sub> and Na<sub>2</sub>CaO<sub>3</sub>·H<sub>2</sub>O (A) and the activity of water  $a_{H_2O}$  (B) at 45, 60 and 80°C and increasing NaOH molalities, up to 20 m; the concentration  $C_0$  (B) indicates the initial NaOH concentration considered for the samples here discussed.

**Fig. 9.** Conversion extent values ( $\alpha$ ) of the samples NaOH\_10m<sub>n</sub>, NaOH\_12m<sub>n</sub>, NaOH\_15m<sub>n</sub> and NaOH\_17m<sub>n</sub> plotted against the temperature initially set up and kept constant throughout the reaction.

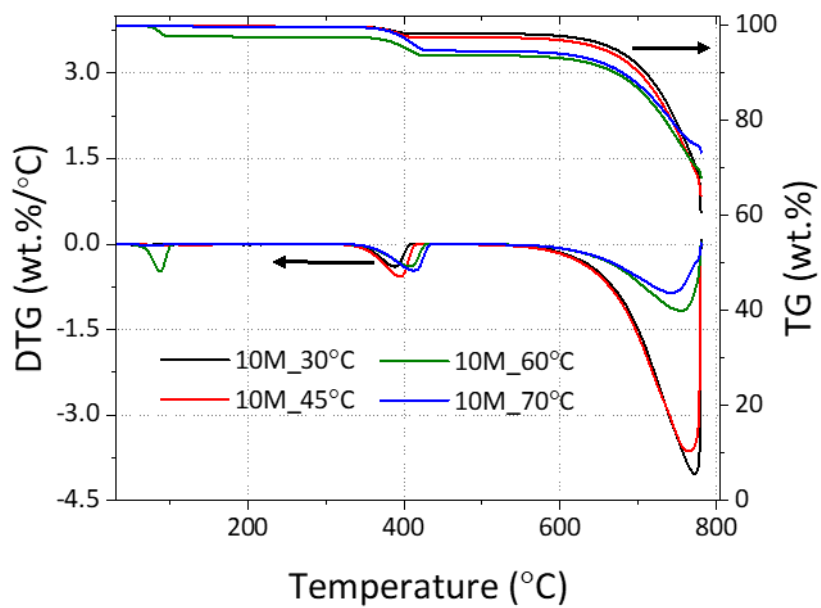
**Fig. 10.** Linearized Arrhenius plot showing the correlation between  $\ln k$  and  $-1/T$  (K<sup>-1</sup>) for the samples series NaOH\_10m<sub>n</sub>, NaOH\_12m<sub>n</sub>, NaOH\_15m<sub>n</sub> and NaOH\_17m<sub>n</sub>, reflected by the equations, 9, 10, 11, and 12, respectively.

**Fig. 11.**  $\ln E_a$  and pre-exponential factor  $A$  values against the NaOH concentration characterising the compositions NaOH\_10m<sub>n</sub>, NaOH\_12m<sub>n</sub>, NaOH\_15m<sub>n</sub> and NaOH\_17m<sub>n</sub> investigated.

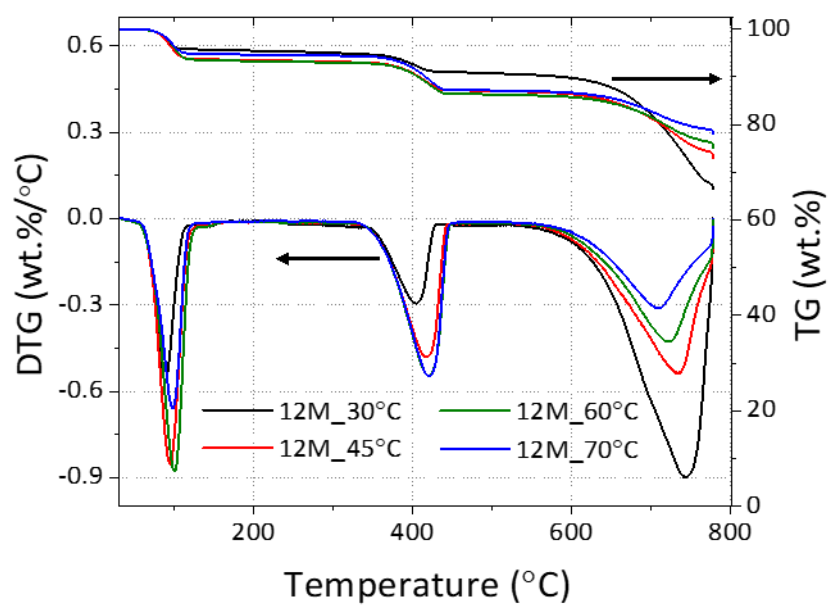
**Table 3.** Amounts of NaOH reacted and Na<sub>2</sub>CO<sub>3</sub> produced through the chemical route by considering the stoichiometry depicted in Equation 1, together with the amount of CaCO<sub>3</sub> required for both the thermal and chemical approach. The values reported refer to the normalisation of the products, case by case, PC, Lime and Slaked lime.

**Fig. 12.** Comparison of the energy consumption between the thermal and chemical approaches to the decarbonisation of  $\text{CaCO}_3$ , referred to the cement, lime and slaked lime industries; the values only depend on the decarbonisation step, considering a PRK design for the thermal calcination in PC production, and PFRK one for lime and slaked lime.

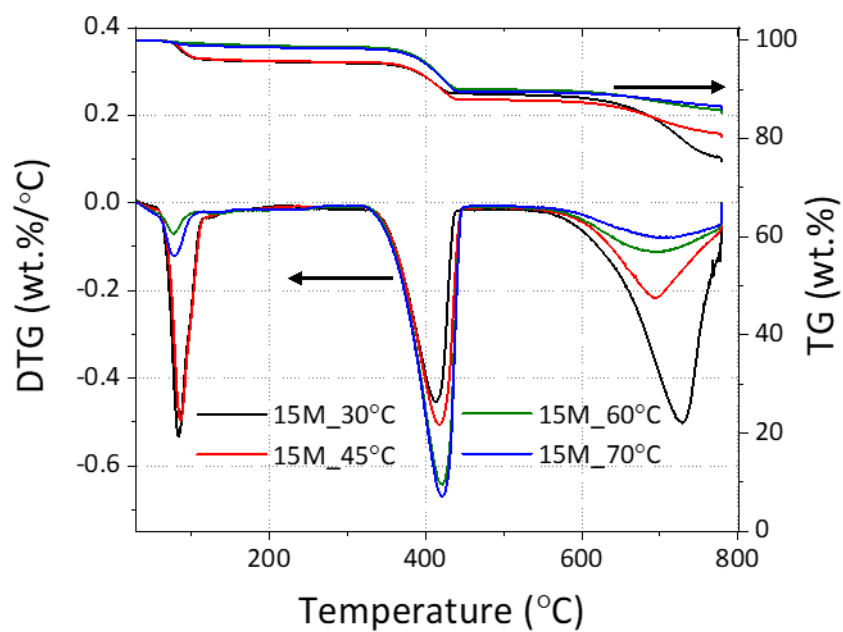
## Supplementary Electronic Information



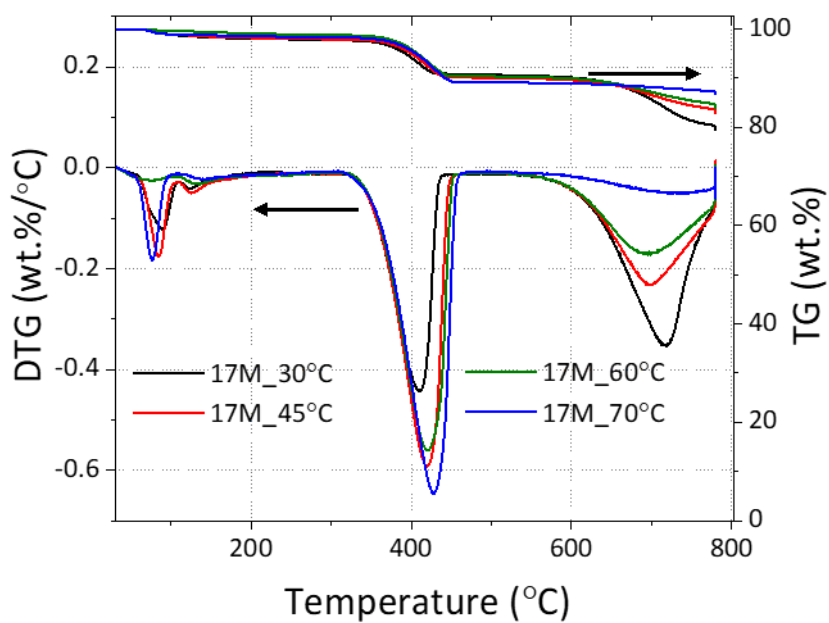
SEI\_I: TG/DTG trends registered for the samples reacted at 30, 45, 60, and 70°C in 10M NaOH solutions.



SEI\_II: TG/DTG trends registered for the samples reacted at 30, 45, 60, and 70°C in 12M NaOH solutions.

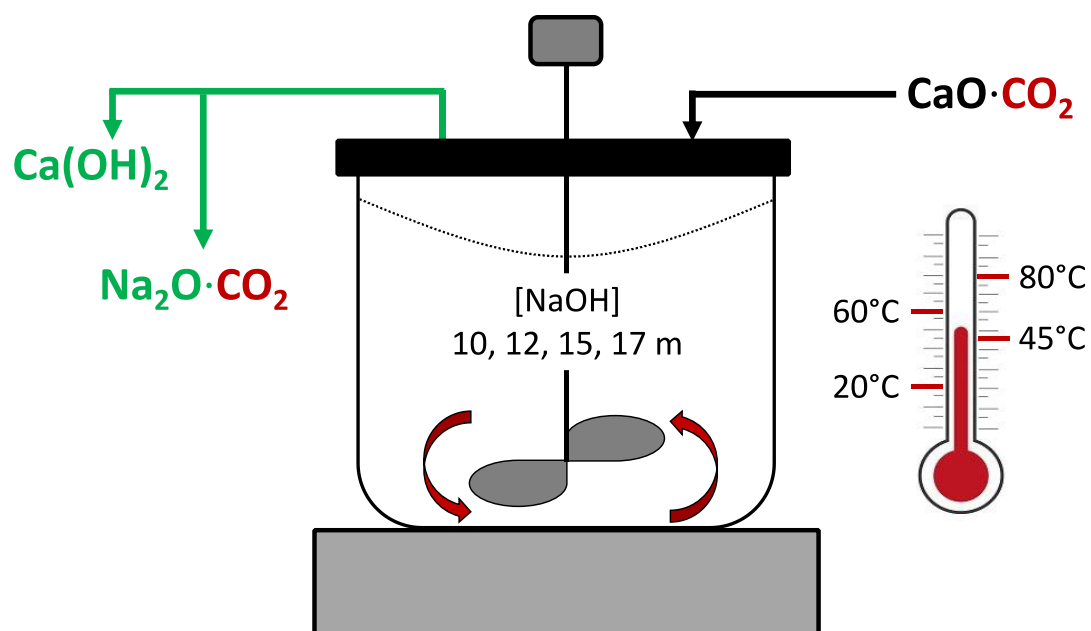


SEI\_III: TG/DTG trends registered for the samples reacted at 30, 45, 60, and 70°C in 15M NaOH solutions.



SEI\_IV: TG/DTG trends registered for the samples reacted at 30, 45, 60, and 70°C in 17M NaOH solutions.

## Graphic Abstract



## Synopsis

The chemical decarbonisation of  $\text{CaCO}_3$  was successfully tested in a range of mild temperatures simulating those oscillations occurring within real industrial processes, and the kinetic parameters were gained.

## Acknowledgements

This work was funded by the Engineering and Physical Science Research Council (EPSRC) and CEMEX under grant ID EP/R025959/1. This research utilised the HADES/MIDAS facility at the University of Sheffield established with financial support from EPSRC and BEIS, under grant EP/T011424/1. The group would also express gratitude to Alan Maries, Juan-Carlos Martinez, John Stennet, and Nestor I. Quintero-Mora for the support and knowledge received.

## Declaration of interest

The authors declare that they have no competing interests as defined by RSC Advances, or other interests that might be perceived to influence the interpretation of the article.

## References

1. Andrew, R.M., *Global CO<sub>2</sub> emissions from cement production*. *Earth System Science Data*, 2018. 10(1): p. 195-217.
2. de Vet, J.-M., et al., *Competitiveness of the European Cement and Lime Sectors*. WIFO Studies, 2018.
3. Bolen, W.P., *Mineral Commodity Summaries—Soda Ash*. United States Geological Survey, Reston, VA, 2015.
4. Warwick, P.D., et al., *US Geological Survey Carbon Sequestration—Geologic Research and Assessments*. *Energy Procedia*, 2014. 63: p. 5305-5309.
5. Gartner, E. and H. Hirao, *A review of alternative approaches to the reduction of CO<sub>2</sub> emissions associated with the manufacture of the binder phase in concrete*. *Cement and Concrete research*, 2015. 78: p. 126-142.
6. Steinhauser, G., *Cleaner production in the Solvay Process: general strategies and recent developments*. *Journal of Cleaner Production*, 2008. 16(7): p. 833-841.
7. Worrell, E., et al., *Carbon dioxide emissions from the global cement industry*. *Annual review of energy and the environment*, 2001. 26(1): p. 303-329.
8. Schorcht, F., et al., *Best available techniques (BAT) reference document for the production of cement, lime and magnesium oxide*. European Commission Joint Research Centre Institute for Prospective Technological Studies (Report EUR 26129 EN). Luxembourg: Publications Office of the European Union, 2013.
9. Barcelo, L., et al., *Cement and carbon emissions*. *Materials and structures*, 2014. 47(6): p. 1055-1065.
10. Rogelj, J., et al., *Paris Agreement climate proposals need a boost to keep warming well below 2 C*. *Nature*, 2016. 534(7609): p. 631.
11. Leeson, D., et al., *A Techno-economic analysis and systematic review of carbon capture and storage (CCS) applied to the iron and steel, cement, oil refining and pulp and paper industries, as well as other high purity sources*. *International Journal of Greenhouse Gas Control*, 2017. 61: p. 71-84.
12. Schneider, M., et al., *Sustainable cement production—present and future*. *Cement and Concrete Research*, 2011. 41(7): p. 642-650.
13. Ellis, L.D., et al., *Toward electrochemical synthesis of cement—An electrolyzer-based process for decarbonating CaCO<sub>3</sub> while producing useful gas streams*. *Proceedings of the National Academy of Sciences*, 2020. 117(23): p. 12584-12591.
14. Hanein, T., et al., *Decarbonisation of calcium carbonate at atmospheric temperatures and pressures, with simultaneous CO<sub>2</sub> capture, through production of sodium carbonate*. *Energy & Environmental Science*, 2021.
15. Simoni, M., et al., *Decarbonisation of calcium carbonate in sodium hydroxide solutions under ambient conditions: effect of residence time and mixing rates*. *Physical Chemistry Chemical Physics*, 2022.
16. Simoni, M., et al., *Effect of Impurities on the Decarbonization of Calcium Carbonate Using Aqueous Sodium Hydroxide*. *ACS Sustainable Chemistry & Engineering*, 2022.
17. Dowling, A., J. O'Dwyer, and C.C. Adley, *Lime in the limelight*. *Journal of cleaner production*, 2015. 92: p. 13-22.
18. Sørensen, O.T. and J. Rouquerol, *Sample controlled thermal analysis: origin, goals, multiple forms, applications and future*. Vol. 3. 2013: Springer Science & Business Media.
19. Levenspiel, O., *Chemical reaction engineering*. 1998: John Wiley & sons.
20. Menzinger, M. and R. Wolfgang, *The meaning and use of the Arrhenius activation energy*. *Angewandte Chemie International Edition in English*, 1969. 8(6): p. 438-444.
21. Vyazovkin, S., et al., *ICTAC Kinetics Committee recommendations for performing kinetic computations on thermal analysis data*. *Thermochimica acta*, 2011. 520(1-2): p. 1-19.
22. Seidell, A., *Solubilities of inorganic and metal organic compounds*. 1940.
23. Morey, G.W., *The action of water on calcite, magnesite and dolomite*. *American Mineralogist: Journal of Earth and Planetary Materials*, 1962. 47(11-12): p. 1456-1460.
24. Farhad, A. and Z. Mohammadi, *Calcium hydroxide: a review*. *International dental journal*, 2005. 55(5): p. 293-301.
25. Ellingboe, J.L. and J.H. Runnels, *Solubilities of Sodium Carbonate and Sodium Bicarbonate in Acetone-Water and Methanol-Water Mixtures*. *Journal of Chemical and Engineering Data*, 1966. 11(3): p. 323-324.
26. Zelić, J., D. Rušić, and R. Krstulović, *Kinetic analysis of thermal decomposition of Ca (OH)<sub>2</sub> formed during hydration of commercial Portland cement by DSC*. *Journal of thermal analysis and calorimetry*, 2002. 67(3): p. 613-622.
27. Gallagher, P.K. and D.W. Johnson Jr, *The effects of sample size and heating rate on the kinetics of the thermal decomposition of CaCO<sub>3</sub>*. *Thermochimica Acta*, 1973. 6(1): p. 67-83.

28. Hartman, M., et al., Thermal dehydration of the sodium carbonate hydrates. *Chemical Engineering Communications*, 2001. 185(1): p. 1-16.
29. Hanein, T., et al., Decarbonisation of calcium carbonate at atmospheric temperatures and pressures, with simultaneous CO<sub>2</sub> capture, through production of sodium carbonate. *Energy & Environmental Science*, 2021. 14(12): p. 6595-6604.
30. Simoni, M., et al., Effect of impurities on the decarbonisation of calcium carbonate using aqueous sodium hydroxide. *ACS Sustainable Chemistry & Engineering*, 2022. Accepted, in the process of publication.
31. Antao, S.M. and I. Hassan, Temperature dependence of the structural parameters in the transformation of aragonite to calcite, as determined from in situ synchrotron powder X-ray-diffraction data. *The Canadian Mineralogist*, 2010. 48(5): p. 1225-1236.
32. Nagai, T., et al., Compression mechanism and amorphization of portlandite, Ca(OH)<sub>2</sub>: structural refinement under pressure. *Physics and Chemistry of Minerals*, 2000. 27(7): p. 462-466.
33. Wu, K.K. and I.D. Brown, A neutron diffraction study of Na<sub>2</sub>CO<sub>3</sub>·H<sub>2</sub>O. *Acta Crystallographica Section B: Structural Crystallography and Crystal Chemistry*, 1975. 31(3): p. 890-892.
34. Arakcheeva, A., et al., The incommensurately modulated structures of natural natrite at 120 and 293 K from synchrotron X-ray data. *American Mineralogist*, 2010. 95(4): p. 574-581.
35. Motzfeldt, K., The thermal decomposition. of sodium carbonate by the effusion method. *The Journal of Physical Chemistry*, 1955. 59(2): p. 139-147.
36. Stipp, S.L. and M.F. Hochella Jr, Structure and bonding environments at the calcite surface as observed with X-ray photoelectron spectroscopy (XPS) and low energy electron diffraction (LEED). *Geochimica et Cosmochimica Acta*, 1991. 55(6): p. 1723-1736.
37. Robie, R.A. and B.S. Hemingway, *Thermodynamic properties of minerals and related substances at 298.15 K and 1 bar (105 Pascals) pressure and at higher temperatures*. Vol. 2131. 1995: US Government Printing Office.
38. Chase Jr, M.W., *NIST-JANAF thermochemical tables fourth edition*. *J. Phys. Chem. Ref. Data, Monograph*, 1998. 9.
39. Parkhurst, D.L. and C.A.J. Appelo, *Description of input and examples for PHREEQC version 3: a computer program for speciation, batch-reaction, one-dimensional transport, and inverse geochemical calculations*. 2013, US Geological Survey.
40. Balej, J., Water vapour partial pressures and water activities in potassium and sodium hydroxide solutions over wide concentration and temperature ranges. *International journal of hydrogen energy*, 1985. 10(4): p. 233-243.
41. Speight, J.G., *Lange's handbook of chemistry*. Vol. 1. 2005: McGraw-Hill New York.
42. Laidler, K.J., The development of the Arrhenius equation. *Journal of chemical Education*, 1984. 61(6): p. 494.
43. Fedunik-Hofman, L., A. Bayon, and S.W. Donne, Kinetics of solid-gas reactions and their application to carbonate looping systems. *Energies*, 2019. 12(15): p. 2981.
44. Caldwell, K.M., P.K. Gallagher, and D.W. Johnson Jr, Effect of thermal transport mechanisms on the thermal decomposition of CaCO<sub>3</sub>. *Thermochimica Acta*, 1977. 18(1): p. 15-19.
45. Renner, T., *Quantities, units and symbols in physical chemistry*. 2007: Royal Society of Chemistry.
46. Imberti, S., et al., Ions in water: The microscopic structure of concentrated hydroxide solutions. *The Journal of chemical physics*, 2005. 122(19): p. 194509.
47. Heberling, F., et al., Reactivity of the calcite–water-interface, from molecular scale processes to geochemical engineering. *Applied geochemistry*, 2014. 45: p. 158-190.
48. Franklin, M.L. and J.W. Morse, The interaction of manganese (II) with the surface of calcite in dilute solutions and seawater. *Marine Chemistry*, 1983. 12(4): p. 241-254.
49. Comans, R.N.J. and J.J. Middelburg, Sorption of trace metals on calcite: Applicability of the surface precipitation model. *Geochimica et cosmochimica acta*, 1987. 51(9): p. 2587-2591.
50. Kornicker, W.A., J.W. Morse, and R.N. Damasceno, The chemistry of Co<sup>2+</sup> interaction with calcite and aragonite surfaces. *Chemical geology*, 1985. 53(3-4): p. 229-236.
51. Lakshmanan, S. and T. Murugesan, The chlor-alkali process: work in progress. *Clean Technologies and Environmental Policy*, 2014. 16(2): p. 225-234.
52. Kumar, A., F. Du, and J.H. Lienhard, Caustic Soda Production, Energy Efficiency, and Electrolyzers. *ACS Energy Letters*, 2021. 6(10): p. 3563-3566.
53. Simoni, M., et al., Decarbonising the lime industry: State-of-the-art. *Renewable and Sustainable Energy Reviews*, 2022. 168: p. 112765.
54. Stanmore, B.R. and P. Gilot, calcination and carbonation of limestone during thermal cycling for CO<sub>2</sub> sequestration. *Fuel processing technology*, 2005. 86(16): p. 1707-1743.

55. *Intergovernmental Panel on Climate, C. and J.T. Houghton, Revised 1996 IPCC Guidelines for National Greenhouse Gas Inventories: Greenhouse Gas Inventory Workbook. 1996: OECD.*
56. *Taylor, H.F.W., Cement Chemistry - 2<sup>nd</sup> Edition. 1997. 0727725920, 9780727725929.*
57. *Jewell, S. and S. Kimball, USGS mineral commodities summaries: 2014. US Geological Survey, <http://minerals.usgs.gov/minerals/pubs/mcs/2014/mcs2014.pdf>, Accessed, 2014. 12(12): p. 2014.*
58. *Provis, J.L. and S.A. Bernal, Geopolymers and related alkali-activated materials. Annual Review of Materials Research, 2014. 44: p. 299-327.*
59. *Tsang, C.-F., J. Birkholzer, and J. Rutqvist, A comparative review of hydrologic issues involved in geologic storage of CO<sub>2</sub> and injection disposal of liquid waste. Environmental Geology, 2008. 54(8): p. 1723-1737.*
60. *Simoni, M., et al., Producing cement clinker assemblages in the system: CaO-SiO<sub>2</sub>-Al<sub>2</sub>O<sub>3</sub>-SO<sub>3</sub>-CaCl<sub>2</sub>-MgO. Cement and Concrete Research, 2021. 144: p. 106418.*
61. *Glass, G.K. and N.R. Buenfeld, The presentation of the chloride threshold level for corrosion of steel in concrete. Corrosion science, 1997. 39(5): p. 1001-1013.*
62. *Environment, U.N., et al., Eco-efficient cements: Potential economically viable solutions for a low-CO<sub>2</sub> cement-based materials industry. Cement and Concrete Research, 2018. 114: p. 2-26.*
63. *Jury, W.A. and H.J. Vaux Jr, The emerging global water crisis: managing scarcity and conflict between water users. Advances in agronomy, 2007. 95: p. 1-76.*
64. *Khasawneh, H., M.N. Saidan, and M. Al-Addous, Utilization of hydrogen as clean energy resource in chlor-alkali process. Energy Exploration & Exploitation, 2019. 37(3): p. 1053-1072.*

## 6. Alternative decarbonisation route: effect of impurities content

The last experimental chapter of this PhD thesis focuses on the characterisation of the reaction specifically for industrial grade materials with different characteristics, to define the system efficiency starting from different calcareous sources. The outcomes suggested that varying contents of impurities would not significantly affect the efficiency of the chemical decarbonisation of limestone. Moreover, the material with higher silica content resulted more reactive than the nearly  $\text{CaCO}_3$  pure one. The work has been completed, and it will be soon submitted to the attention of ACS Sustainable Chemistry & Engineering. I here certify that I conceptualised and performed all the experiments, including the characterisation, I drafted the original manuscript, I replied to the comments raised from the peer-reviewers and that I took care of the whole submission process.

# Effect of impurities on the decarbonisation of calcium carbonate using aqueous sodium hydroxide

Marco Simoni\*, Theodore Hanein\*, Chun Long Woo, John Provis and Hajime Kinoshita\*.

University of Sheffield, Department of Materials Science & Engineering, S1 3JD, Sheffield, UK

\* Corresponding author: [t.hanein@sheffield.ac.uk](mailto:t.hanein@sheffield.ac.uk), [h.kinoshita@sheffield.ac.uk](mailto:h.kinoshita@sheffield.ac.uk), [marco.simoni.w@gmail.com](mailto:marco.simoni.w@gmail.com).

## Abstract

Decarbonising calcium carbonate ( $\text{CaCO}_3$ ) is a crucial step for a wide range of major industrial processes and materials, including Portland Cement (PC) production. Apart from the carbon footprint linked to the fuel combustion, the process  $\text{CO}_2$  embodied within  $\text{CaCO}_3$  represents the main concern for sustainability of the production. Our recent works demonstrated that it is possible to avoid both the fuel and process  $\text{CO}_2$ , by reacting  $\text{CaCO}_3$  with aqueous NaOH system and obtain  $\text{Ca}(\text{OH})_2$  and  $\text{Na}_2\text{CO}_3 \cdot x\text{H}_2\text{O}$  ( $x = 0, 1$ ). This work provides a further understanding of the process by testing different raw calcareous sources. A high decarbonisation (~80%) of  $\text{CaCO}_3$  was achieved for a silica rich chalk, whereas a lower extent was obtained (~50%) for limestone. To understand the difference in their reaction behaviour, the effect of impurities was studied. The effects of the major impurities (Si, Al, Fe) were found to be marginal, which is advantageous to process industrial grade materials, while the morphology of the raw materials may have a significant impact. The applicability of our technology was also demonstrated on magnesite ( $\text{MgCO}_3$ ).

**Keywords.** Decarbonisation,  $\text{CO}_2$  sequestration, Ambient Conditions, Cement,  $\text{CaCO}_3$ .

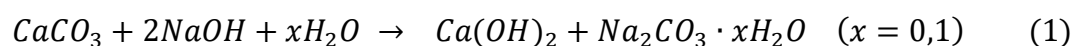
# 1. Introduction

The calcination of calcium carbonate to obtain lime ( $\text{CaCO}_3 \rightarrow \text{CaO} + \text{CO}_2$ ) is currently considered one of the major contributors to the global  $\text{CO}_2$  emissions, due to both the large global demand [1] and the specific carbon footprint ( $1.0\text{--}1.8 \text{ kg}_{\text{CO}_2}/\text{kg}_{\text{CaO}}$ ) [2]. The Portland cement (PC) industry is currently utilising the largest portion of calcined limestone, with a global market size of 4Gt PC per year Survey [3], which makes the cement industry responsible for about the 8% of the total  $\text{CO}_2$  emissions worldwide [4] and 12–15% of global industry energy use [5].

The calcination of calcium carbonate usually involves two distinct emission sources: process- and fuel-derived  $\text{CO}_2$ . The former arises from the calcination stoichiometry ( $0.44 \text{ kg}_{\text{CO}_2}/\text{kg}_{\text{CaCO}_3}$ ) [6], while the latter is linked to the combustion of the hydrocarbon fuels to attain the required pyro-processing temperatures ( $\sim 900^\circ\text{C}$  [2, 7] for lime production and  $1500^\circ\text{C}$  [5] for PC production). Although the fuels represent the largest portion of the overall economic operating costs for both lime and cement industries [8], the process  $\text{CO}_2$  represents the biggest challenge for their sustainable production. The process  $\text{CO}_2$  accounts for majority of  $\text{CO}_2$  emissions from the limestone calcination step, and several solutions have been proposed: Carbon Capture & Storage (CCS) technologies [9], the switch to sustainable fuels [7, 10], the development of low-calcium cements [11]. The CCS technologies are believed to have the highest potential to decarbonise the cement industry, and they might be classified as pre- or post-combustion [12, 13]. The latter ones are usually retrofittable with the conventional cement plants, while the former require a deep modification of the current design. Among the CCS technologies available, the  $\text{CO}_2$  removal through reaction with monoethanolamine (MEA) solutions appears to be the most developed solution so far [9], despite the high operational costs linked to the regeneration of the solvent [14]. The use of waste as fuel is a common practice already, accounting for a significant replacement of fossil sources in the EU, depending on the country [15]; the selection and pre-treatment of the waste are essential to ensure a good quality of the manufactured product. The use of alternative binders with a lower Ca content would reflect a production with limited process  $\text{CO}_2$  emissions. In addition, the re-use of several types of waste as substitutes to the conventional cement chemistry might play a determining role in the waste disposal challenge [16]. These potential solutions are all based on the high temperature calcination process.

In contrast, we recently proposed an alternative technology that exploits the chemical interaction between  $\text{CaCO}_3$  and  $\text{NaOH}$  in aqueous system at ambient conditions [17], so that the high temperature calcination process itself can be avoided. On the other hand, the application of such decarbonisation route would require a drastic modification of the current

plants, with high investment costs associated. Moreover, the significant usage of NaOH would raise concerns in terms of embodied CO<sub>2</sub> and Cl<sub>2</sub> emissions from the chlor-alkali process [18]. Despite this, since the chlor-alkali process is mainly sustained by electric energy [18], the NaOH production would be expected to be carbon neutral by 2050, if the goals set up during the Paris agreement in 2015 will be met [19]. Regarding Cl<sub>2</sub>, its disposal might partially be performed through recycling into Cl-based cements, such as alinite [20, 21]. As shown in Equation 1, the reaction in this process leads to the synthesis of Ca(OH)<sub>2</sub>, which can also be converted to CaO in mild conditions through dehydroxylation Ca(OH)<sub>2</sub>→CaO+H<sub>2</sub>O [7], while sequestrating the process CO<sub>2</sub> into a stable mineral form i.e., Na<sub>2</sub>CO<sub>3</sub>.xH<sub>2</sub>O (x = 0, 1).



For cement clinker production, high temperatures are still required for the formation of clinker phases [1], but such conditions can be achieved through electrical heating [5] and E-fuels [22], concentrated solar power [23], or combustion of waste/biomass [24].

Our previous work [17] demonstrated the feasibility of the proposed decarbonisation technique on reagent grade calcium carbonate and a particular calcium carbonate (chalk) source. For the industrial applications, variabilities in the raw materials source is inevitable, which would affect the process [1, 25]. In the present study, two different industrial grade materials with significantly different compositions, a limestone and a chalk (same as in our previous work[17]) are considered.

Limestone and chalk are mainly calcium carbonate but generally different both at macro and microscopic levels [26], and this allows us to assess the efficiency of our process for varying calcareous sources. Due to the nature of our aqueous process, it is envisaged that the different average porosity (chalk > 25% [27] and limestone <10% [28]) will play a crucial role in the present investigation. A higher or lower permeability and diffusion of foreign elements (e.g., Na+) could make the difference between a more or less reactive material for the scope of this technology; generally, the higher the porosity (ϕ), the higher the permeability (k) [29].

In this work a deeper insight into the mechanisms ruling the reaction is discussed by considering different calcareous sources with varying contents of impurities. The different efficiencies registered could suggest an important effect of varying contents of impurities (Si, Al, Fe, and Mg) in the reactants. For this reason, the effect of each of them was isolated in reagent grade binary systems with increasing contents CaCO<sub>3</sub>, and the outcomes are thoroughly discussed and justified by cross-linking analyses. Finally, in order to detect those parameters, i.e. impurities content or particles morphology, which could mostly influence the reaction efficiency, reagent grade systems simulating the compositions of the chalk and limestone were tested. The authors are well aware that additional considerations must be

done in terms of process design (including the hazards linked to the high concentration of the NaOH solutions used), energy consumption, and carbon balance before even considering a process scale-up; despite this, the outcomes here reported would still provide a valid baseline for further considerations to be done.

## 2. Experimental

### 2.1. Materials

The present work used the following commercial grade chemicals: Sigma-Aldrich  $\text{CaCO}_3$  ( $\geq 99\%$ ), Honeywell Fluka NaOH ( $\geq 97\%$ ), Sigma-Aldrich purum p.a. white quartz as  $\text{SiO}_2$  source ( $\geq 95\%$ ), Acros Organics extra pure  $\text{Al}_2\text{O}_3$  (99%), Fischer Chemical pure  $\text{Fe}_2\text{O}_3$  (99.85%), Honeywell  $\text{MgCO}_3$  basic ( $\text{MgO} > 40\%$ ). Their solubility in water and methanol are reported in Table S1. Industrial grade limestone and chalk used in the present work were provided by CEMEX; their oxide compositions (Table 1) were obtained via X-ray fluorescence (XRF).

Table 1.

	$\text{CaCO}_3$	$\text{SiO}_2$	$\text{Al}_2\text{O}_3$	$\text{Fe}_2\text{O}_3$	$\text{MgCO}_3$	Others (K, Ti, P)	LOI (%)
<b>Limestone</b>	94.4	1.2	0.3	0.5	3.2	<1.0	42.3
<b>Chalk</b>	74.2	19.9	2.8	1.0	0.7	<1.5	29.4

Considering the Loss on Ignition values of 29.4% for the chalk and 42.3% for the limestone, the Ca and Mg content is reported as  $\text{CaCO}_3$  and  $\text{MgCO}_3$  rather than CaO and MgO, respectively. The limestone presented a higher  $\text{CaCO}_3$  content (94.4 wt.%) compared with the chalk (74.2 wt.%). A significant silica content (19.9 wt.%) was detected within the chalk, whereas more  $\text{MgCO}_3$  (3.2 wt.%) were found in the limestone. Traces of  $\text{Fe}_2\text{O}_3$  were also detected in both materials. To compare the results between the reagent and industrial grade calcareous sources, the raw materials were manually sieved below 38  $\mu\text{m}$ . As reported in Figure S1, the dry-state PSD analysis, performed with 10 g of solids and taken as an average of ten measurements, revealed average diameters ( $\text{D}_{x50}$ ) of 6.0  $\mu\text{m}$  and 8.5  $\mu\text{m}$  for the chalk, limestone, respectively. Most of the reagent grade  $\text{CaCO}_3$  solid particles was in the range 20 - 40  $\mu\text{m}$ , with a negligible amount of smaller (5  $\mu\text{m}$ ) ones.

### 2.2. Characterization techniques

#### 2.2.1. X-Ray diffraction (XRD)

X-ray diffraction (XRD) was used to identify the reaction products. The measurements were performed using a Bruker D2 PHASER desktop X-ray diffractometer in Bragg-Brentano geometry, with a Cu-K $\alpha$  radiation source running at 30 kV and 10 mA, a one-dimensional

LYNXEYE detector, and a 1 mm divergence slit. Powdered samples were loaded onto 2.5 cm diameter and 1 mm deep sample holders. Each pattern was recorded between 5° and 80° 2 $\theta$ , with a step size of 0.02° at 0.5 seconds per step, with the stage rotating at 15 rpm. Qualitative phase identification was carried out using the Highscore-Plus software and the PDF-4 2019 database.

### 2.2.2. Thermogravimetry (TG/DTG)

Thermogravimetric analysis (TG) was carried out on the reaction products. Approximately 40 mg of sample was analysed on a PerkinElmer TG 4000 from 30°C to 800°C at a heating rate of 10°C/min with a 40 mL/min N<sub>2</sub> flow. The sample was then held at 800°C for 1 hour to ensure complete loss of CO<sub>2</sub> from CaCO<sub>3</sub> while maintaining Na<sub>2</sub>CO<sub>3</sub> without melting or decomposing. To identify evolving gases, a Hiden mass spectrometer (HPR-20 GIC EGA) was used to record the signals for H<sub>2</sub>O and CO<sub>2</sub>. As shown in Equation 2, the extent of reaction  $\alpha$  was calculated from the weight losses in the temperature ranges corresponding to the thermal decomposition of Ca(OH)<sub>2</sub> (310-470 °C [30]) and CaCO<sub>3</sub> (560-800 °C [31]). The terms w%<sub>[phase]</sub> and MW<sub>phase</sub> refer to the weight loss registered in TG and the molecular weight of the substance considered, respectively. The content of Na<sub>2</sub>CO<sub>3</sub>·H<sub>2</sub>O could similarly be estimated from mass loss in the temperature range 50-130°C [32]. The possible measurement error was estimated, by analysing the same sample six times at the same condition, as  $\pm 0.16$  wt.% Na<sub>2</sub>CO<sub>3</sub>·H<sub>2</sub>O,  $\pm 0.10$  wt.% for Ca(OH)<sub>2</sub> and  $\pm 0.16$  wt.% for CaCO<sub>3</sub>.

$$\alpha = \frac{w\%_{[Ca(OH)_2]}}{MW_{Ca(OH)_2}} \bigg/ \left[ \frac{w\%_{[Ca(OH)_2]}}{MW_{Ca(OH)_2}} + \frac{w\%_{[CaCO_3]}}{MW_{CaCO_3}} \right] \quad (2)$$

### 2.2.3. Scanning Electron Microscopy (SEM)

A Hitachi TM3030 scanning electron microscope with energy-dispersive X-ray spectroscopy (SEM-EDX) was used for microstructural analysis of the starting powders and reaction products at a 15 kV voltage and working distance of approximately 9  $\pm$  0.2 mm. This was fitted with the Bruker Quantax Energy Dispersive X-ray Spectrometer (EDS) for compositional analysis through BSE detectors. The reaction products were mounted, in powder form, in epoxy resin without crushing and left to harden for 72 hours. The analysis surface was ground manually with progressively finer abrasives, up to a 1  $\mu$ m finish [33], and further polished by using diamond pastes of 6, 3, 2, 1 and 0.25  $\mu$ m (MetPrep). The samples then underwent a three-step carbon coating and were back-loaded to a metallic holder. Electrically conductive silver paint (RS Components) was applied at the interface between the metallic base-epoxy-resin to ensure sufficient conductivity and therefore good quality of the SEM micrographs.

### 2.2.4. X-Ray Fluorescence (XRF)

X-Ray Fluorescence was used to quantify the elemental composition of the unreacted and reacted solids; the measurement was performed through a PW4404 AMG Analytical spectrometer, with an Ar/CH<sub>4</sub> gas flow and a Rh X-Ray tube. Samples were crushed and milled to obtain a particle size within the range of 100 – 250µm. The milled materials were dried at 110°C until a constant weight is achieved. The powder was mixed in the fusion vessel with a flux, lithium tetraborate (Li<sub>2</sub>B<sub>4</sub>O<sub>7</sub>), at a 1:10 sample-to-flux weight ratio, and then fired at 1270°C ± 15°C for 12 minutes upon swirling. The detection limit of the XRF analysis depends on both the samples preparation and the atomic number Z of the targeted elements. Generally, detection limits of 20 – 1000 µg g<sup>-1</sup>, 5 – 10 µg g<sup>-1</sup>, and 1 – 20 µg g<sup>-1</sup> are reported for low, medium and high-Z elements, respectively [34]. For this reason, the detection of Mg may be affected by instrumental error, since it belongs to the second group in the period table (Z = 12).

### 2.3. Reaction procedure

Despite the specific conditions stated below for each targeted investigation, all the experiments were conducted according to the same experimental procedure. Upon dissolution of NaOH in water at known molalities, the solutions were left to cool down to room temperature. The solids were dried at 35°C overnight prior to the usage, to remove the weakly bound water which might slightly affect the overall NaOH concentration used. The reaction was carried out in a 250 mL PTFE beaker, to avoid corrosion that may be caused by the hyper-alkaline NaOH solutions, and a stirring rate of 1050 rpm was ensured through a Heidolph R2020 overhead mixer equipped with a PTFE centrifugal stirrer shaft (40 mm diameter). The reaction was carried out at ambient/laboratory conditions (T≈20°C) for a residence time of 300 seconds. To remove the unreacted NaOH after reaction, all the samples discussed above were washed with methanol for 300 seconds. Considering the solubility of NaOH in methanol at 20°C (238 g/L [35]) and the amount of NaOH in the starting mixtures, the complete removal of NaOH was ensured by choosing a methanol to NaOH weight (g/g) ratio of 4. Given the negligible solubility of the targeted phases Ca(OH)<sub>2</sub> [36], Na<sub>2</sub>CO<sub>3</sub>·H<sub>2</sub>O [37], Na<sub>2</sub>CO<sub>3</sub> [37], CaCO<sub>3</sub> [38], SiO<sub>2</sub> [39], Al<sub>2</sub>O<sub>3</sub> [40], Fe<sub>2</sub>O<sub>3</sub> [40] and MgCO<sub>3</sub> [40] in organic solvents, no variation of the solid mixture should have occurred upon washing with methanol. Finally, the reaction products obtained from all the experiments discussed in the present work were collected on a Whatman Grade 1 (90mm) filter paper using vacuum assisted Büchner funnel filtration, dried in an oven at 35 °C for two hours, weighed and ground to below 63 µm for characterization.

### 2.3.1. Decarbonisation of industrial grade calcareous materials

The industrial grade chalk and limestone were reacted with NaOH at the NaOH/CaCO<sub>3</sub> molar ratio of 3, based on the CaCO<sub>3</sub> contents obtained by XRF of the materials (Table 1). This ratio was previously found to positively influence the reaction yield [17]. The systems were tested at increasing water to solids weight ratio, which in return decreases the NaOH molalities in the aqueous solution (4m – 40m). The detailed starting mix compositions are reported in Table 2.

Table 2.

<b>Sample ID</b>	<b>H<sub>2</sub>O (wt.%)</b>	<b>NaOH (wt.%)</b>	<b>Feed Material (wt.%)</b>	<b>NaOH/CaCO<sub>3</sub> (mol/mol)</b>	<b>H<sub>2</sub>O/Feed Material (w/w)</b>	<b>NaOH (mol·kg<sub>H<sub>2</sub>O</sub><sup>-1</sup>)</b>
<b>L_w/s_0.7</b>	24.8	40.3	35.0	3.0	0.7	40.6
<b>L_w/s_1.0</b>	31.8	36.4	31.7	3.0	1.0	28.6
<b>L_w/s_1.5</b>	41.2	31.4	27.4	3.0	1.5	19.0
<b>L_w/s_2.0</b>	48.2	27.7	24.1	3.0	2.0	14.3
<b>L_w/s_3.0</b>	58.2	22.4	19.4	3.0	3.0	9.6
<b>L_w/s_5.0</b>	69.9	16.1	14.0	3.0	5.0	5.7
<b>C_w/s_0.6</b>	24.4	35.1	40.5	3.0	0.6	36.0
<b>C_w/s_0.7</b>	27.4	34.0	38.7	3.0	0.7	31.1
<b>C_w/s_1.0</b>	34.8	30.4	34.8	3.0	1.0	21.8
<b>C_w/s_1.5</b>	44.5	25.8	29.6	3.0	1.5	14.5
<b>C_w/s_2.0</b>	51.7	22.5	25.8	3.0	2.0	10.9
<b>C_w/s_3.0</b>	61.6	18.0	20.4	3.0	3.0	7.3
<b>C_w/s_5.0</b>	72.7	12.7	14.5	3.0	5.0	4.4

### 2.3.2. Effect of impurities (Si, Al, Fe, Mg)

The effect of common impurities in the chalk and limestone (i.e. Si, Al, Fe and Mg) was studied for the decarbonisation reactions. Binary systems of CaCO<sub>3</sub>-SiO<sub>2</sub>, CaCO<sub>3</sub>-Al<sub>2</sub>O<sub>3</sub>, CaCO<sub>3</sub>-Fe<sub>2</sub>O<sub>3</sub>, and CaCO<sub>3</sub>-MgCO<sub>3</sub> were tested using reagent grade chemicals at varying proportions (Table 3), to simulate the oxide compositions of the chalk and the limestone (Table 1). This would isolate the effect of each main impurity and allow the assessment of their effects on the overall reaction.

Table 3.

<b>Sample ID</b>	<b>vCaCO<sub>3</sub> (wt.%)</b>	<b>vSiO<sub>2</sub> (wt.%)</b>	<b>vAl<sub>2</sub>O<sub>3</sub> (wt.%)</b>	<b>vFe<sub>2</sub>O<sub>3</sub> (wt.%)</b>	<b>vMgCO<sub>3</sub> (wt.%)</b>	<b>NaOH/CaCO<sub>3</sub> (mol/mol)</b>	<b>H<sub>2</sub>O/Solids (w/w)</b>
<i>Reference</i>	100.0	0.0	-	-	-	3.9	4.0
<i>SiO<sub>2</sub>_1.0%</i>	99.0	1.0	-	-	-	4.0	4.0
<i>SiO<sub>2</sub>_2.9%</i>	97.1	2.9	-	-	-	4.0	3.9
<i>SiO<sub>2</sub>_4.8%</i>	95.2	4.8	-	-	-	4.0	3.8
<i>SiO<sub>2</sub>_6.5%</i>	93.5	6.5	-	-	-	4.0	3.7
<i>SiO<sub>2</sub>_9.1%</i>	90.9	9.1	-	-	-	4.1	3.6
<i>SiO<sub>2</sub>_13.1%</i>	86.9	13.1	-	-	-	4.0	3.5
<i>SiO<sub>2</sub>_20.0%</i>	80.0	20.0	-	-	-	4.0	3.2
<i>Al<sub>2</sub>O<sub>3</sub>_1.0%</i>	99.0	-	1.0	-	-	4.0	4.0
<i>Al<sub>2</sub>O<sub>3</sub>_2.0%</i>	98.0	-	2.0	-	-	4.0	3.9
<i>Al<sub>2</sub>O<sub>3</sub>_2.9%</i>	97.1	-	2.9	-	-	4.0	3.9
<i>Al<sub>2</sub>O<sub>3</sub>_4.8%</i>	95.2	-	4.8	-	-	4.0	3.8
<i>Fe<sub>2</sub>O<sub>3</sub>_0.5%</i>	99.5	-	-	0.5	-	4.0	4.0
<i>Fe<sub>2</sub>O<sub>3</sub>_1.0%</i>	99.0	-	-	1.0	-	4.0	4.0
<i>Fe<sub>2</sub>O<sub>3</sub>_1.5%</i>	98.5	-	-	1.5	-	4.0	3.9
<i>Fe<sub>2</sub>O<sub>3</sub>_2.0%</i>	98.0	-	-	2.0	-	4.0	3.9
<i>Fe<sub>2</sub>O<sub>3</sub>_4.8%</i>	95.2	-	-	4.8	-	4.0	3.8
<i>Fe<sub>2</sub>O<sub>3</sub>_9.1%</i>	90.9	-	-	9.1	-	4.0	3.6
<i>MgCO<sub>3</sub>_0.6%</i>	99.4	-	-	-	0.6	4.0	4.0
<i>MgCO<sub>3</sub>_1.0%</i>	99.0	-	-	-	1.0	4.0	3.9
<i>MgCO<sub>3</sub>_1.5%</i>	98.5	-	-	-	1.5	4.0	4.0
<i>MgCO<sub>3</sub>_4.8%</i>	95.2	-	-	-	4.8	4.0	3.8
<i>MgCO<sub>3</sub>_9.1%</i>	90.9	-	-	-	9.1	4.0	3.6
<i>MgCO<sub>3</sub>_16.7%</i>	83.3	-	-	-	16.7	4.0	3.3

Prior reaction, the minerals were ground, sieved below 38  $\mu\text{m}$ , and dried at 35°C overnight, to ensure homogeneous particle size and limited presence of water which might lower the overall NaOH concentration used. The 10m NaOH solutions were prepared to ensure a NaOH/CaCO<sub>3</sub> molar ratio of 4 for all the samples. Despite the decreasing w/s ratios used at higher additions of SiO<sub>2</sub>, Al<sub>2</sub>O<sub>3</sub>, Fe<sub>2</sub>O<sub>3</sub>, and MgCO<sub>3</sub> (Table 3), previous investigations revealed that such a parameter would not affect the reaction efficiency in the ranges here considered. A high content of water was chosen for the starting mixture to avoid the agglomeration of solids and therefore error.

To study the effect of the co-existing impurities, reagent grade chemicals were also blended according to the proportions reported in Table 4, simulating the industrial grade chalk and limestone used in the present work (Table 1).

*Table 4.*

<b>Sample ID</b>	<b>vCaCO<sub>3</sub> (wt.%)</b>	<b>vSiO<sub>2</sub> (wt.%)</b>	<b>vAl<sub>2</sub>O<sub>3</sub> (wt.%)</b>	<b>vFe<sub>2</sub>O<sub>3</sub> (wt.%)</b>	<b>vMgCO<sub>3</sub> (wt.%)</b>
<i>Chalk_R.G.</i>	75.2	20.2	2.8	1.1	0.7
<i>Limestone_R.G.</i>	94.9	1.2	0.3	0.4	3.2

These mixtures simulating chalk and limestone were tested in the same way as in the testing of the industrial grade materials (Section 2.3.1) including the starting mix composition (Table 5).

Table 5.

Sample ID	H <sub>2</sub> O (wt.%)	NaOH (wt.%)	Solids (wt.%)	NaOH/CaCO <sub>3</sub> (mol/mol)	H <sub>2</sub> O/Solids (w/w)	NaOH (mol/L)
L_R.G._w/s_0.7	24.8	40.3	34.9	3.0	0.7	40.6
L_R.G._w/s_1.0	31.9	36.5	31.7	3.0	1.0	28.6
L_R.G._w/s_1.5	41.2	31.4	27.4	3.0	1.5	19.0
L_R.G._w/s_2.0	48.2	27.7	24.1	3.0	2.0	14.4
L_R.G._w/s_3.0	58.2	22.4	19.4	3.0	3.0	9.6
L_R.G._w/s_5.0	69.9	16.1	14.0	3.0	5.0	5.7
C_R.G._w/s_0.6	24.4	35.2	40.4	3.0	0.6	36.0
C_R.G._w/s_0.7	27.3	34.0	38.7	3.0	0.7	31.1
C_R.G._w/s_1.0	34.8	30.4	34.8	3.0	1.0	21.8
C_R.G._w/s_1.5	44.5	25.8	29.7	3.0	1.5	14.5
C_R.G._w/s_2.0	51.7	22.5	25.8	3.0	2.0	10.9
C_R.G._w/s_3.0	61.6	18.0	20.5	3.0	3.0	7.3
C_R.G._w/s_5.0	72.7	12.7	14.5	3.0	5.0	4.4

### 3. Results and Discussion

#### 3.1. Industrial grade calcareous materials

The TG analysis (Figure 1) performed on the unreacted raw calcareous materials confirmed the XRF quantification of CaCO<sub>3</sub> reported in Table 1, with slight variations.

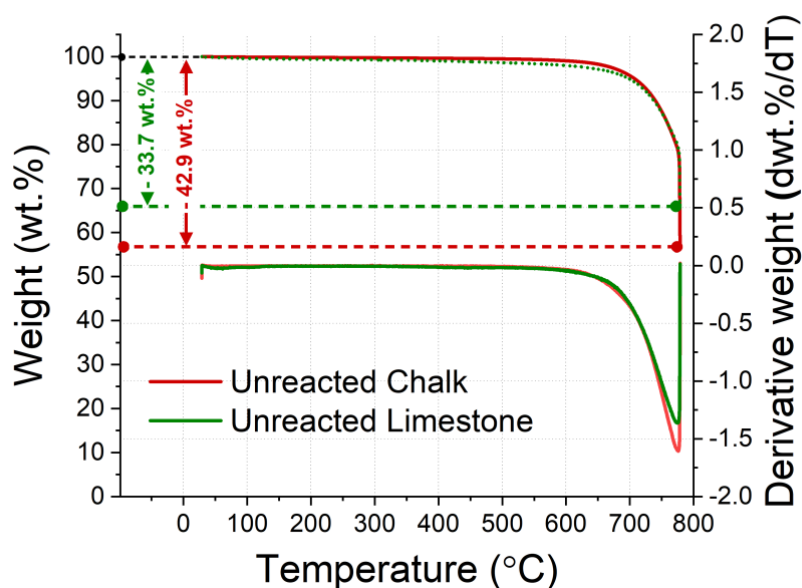


Fig. 1.

CaCO<sub>3</sub> contents of 73.7 wt.% (33.7 % of weight loss) and 96.8 wt.% (42.9 % of weight loss) were detected for the chalk and limestone, respectively. The SEM analysis was used to assess the overall differences of the two materials tested. Firstly, large particles of unreacted chalk and limestone were selected through manual sieving, mounted in epoxy-resin, and analysed (Figures 2A, B), revealing their morphological characteristics. At first sight, the chalk appeared more porous than the limestone, and with a more irregular surface.

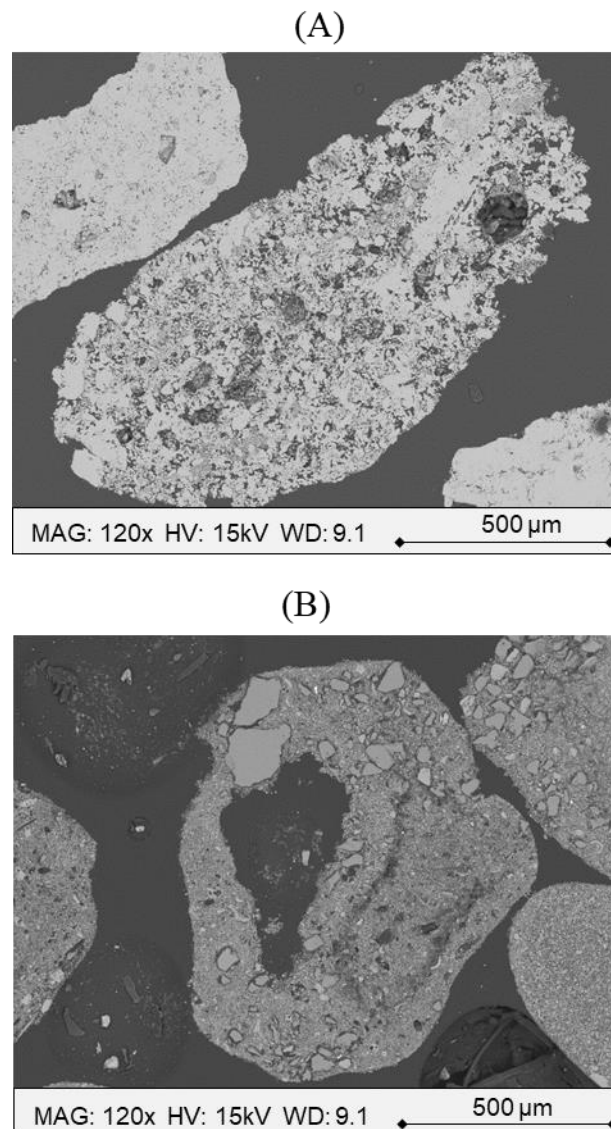


Fig. 2.

The SEM analysis was repeated on the smaller particles (below 38 μm), not epoxy-mounted, but attached to a conductive carbon adhesive tape. The conventional coccolith-like [41] shaped CaCO<sub>3</sub> crystals are observed for the chalk, visible as light-grey circles in Figure 3A. In contrast, a heterogeneous morphology could be observed for the limestone, whose CaCO<sub>3</sub> crystals were showing larger beads of scalenohedral [42] and smaller beads of cubic [43]

geometry (Figure 3B). For completion, the SEM analysis was performed on the reagent grade  $\text{CaCO}_3$  used for comparison with industrial grade materials; as shown in Figure 3C, it was mainly composed of thin plates arranged in spherical agglomerations.

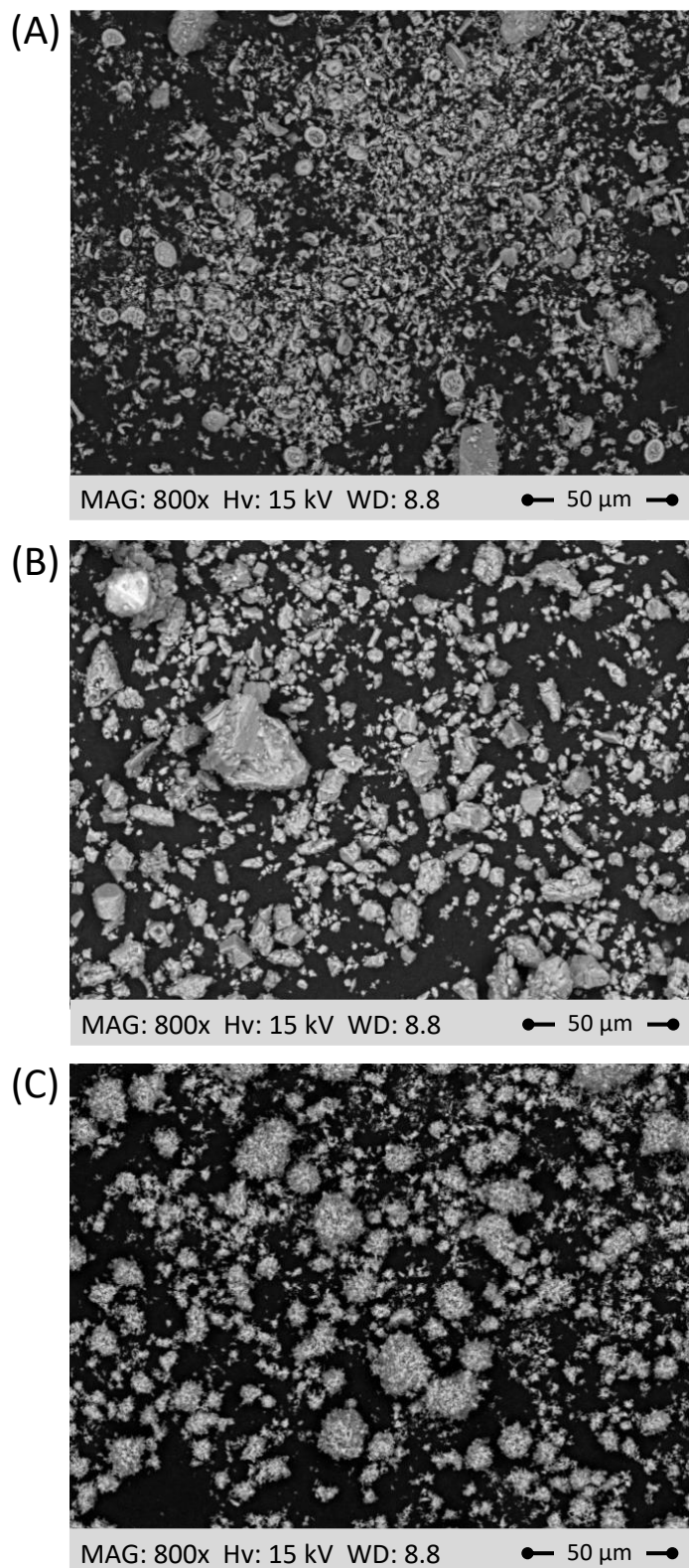


Fig. 3.

### 3.2. Decarbonisation of industrial grade calcareous materials

The industrial grade limestone and chalk were reacted with NaOH solutions at a constant NaOH/CaCO<sub>3</sub> molar ratio of 3 with increasing water to feed material ratio, as reported in Table 2. As shown in the TG/DTG data in Figure 4A, the de-hydroxylation of Na<sub>2</sub>CO<sub>3</sub>·H<sub>2</sub>O and Ca(OH)<sub>2</sub> between 50 – 130°C and 310 – 470°C, respectively, and the decarbonisation of the remaining CaCO<sub>3</sub> between 560 – 800°C could be detected for the chalk samples.

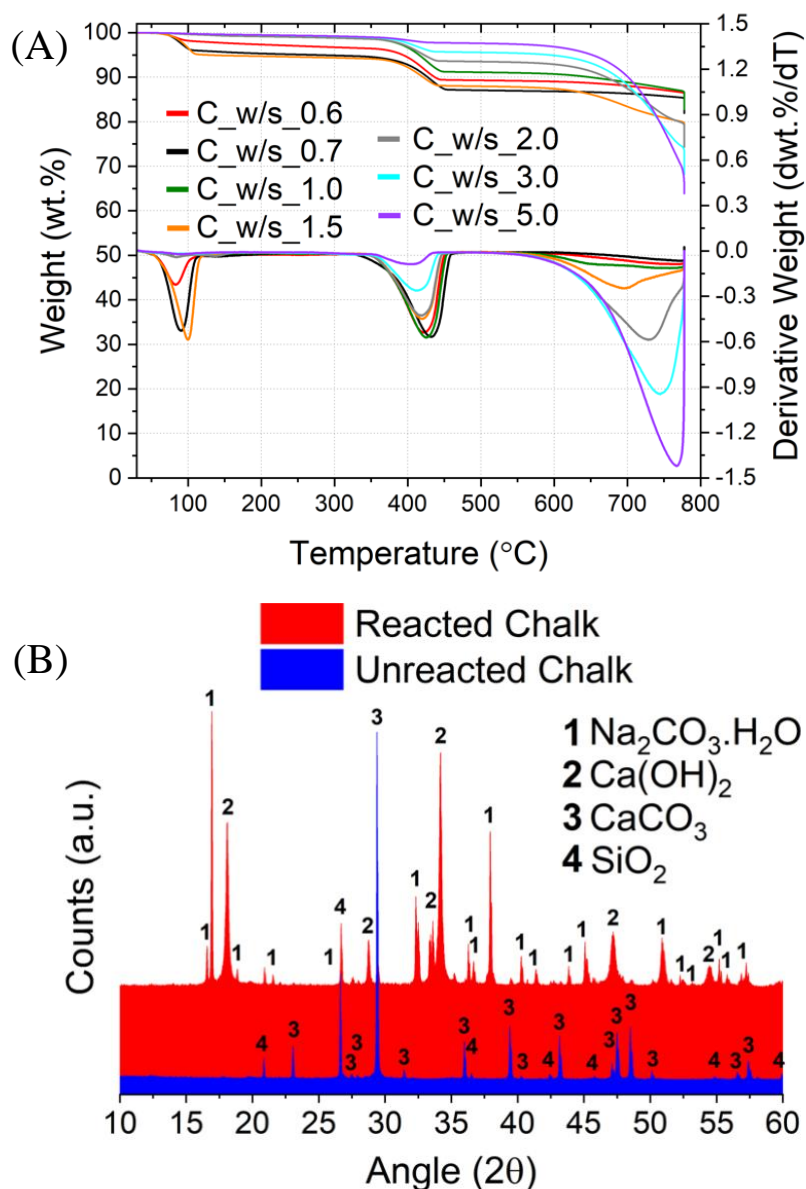


Fig. 4.

The comparison between the XRD patterns for the unreacted and reacted chalk reported in Figure 4B confirmed the outcomes from the TG analysis. Indeed, only Na<sub>2</sub>CO<sub>3</sub>·H<sub>2</sub>O, Ca(OH)<sub>2</sub>, and CaCO<sub>3</sub> could be identified as reaction products. Given the relatively low content in

impurities, their eventual dissolution could not be assessed through XRD analysis, despite the decreasing intensity of the main peak linked to SiO<sub>2</sub> (26.6° 2θ) would suggest that the dissolution of silica would occur upon reaction. To assess that, XRF analysis was conducted on the sample C\_w/s\_0.7, showing the highest capability to convert CaCO<sub>3</sub> to products. Given that the solids would undergo weight increase upon decarbonisation reaction [44], the ratio between the weight percentage of Ca and the specific foreign element was taken as mass balance for the system. These values are reported in Table 6, which show the mass balance performed prior and upon reaction. Apparently, all the foreign elements were dissolving at a certain extent upon reaction, as outlined by the lower Si/Ca, Al/Ca, Fe/Ca, and Mg/Ca ratios with respect to the initial values. Silica was the main component in the chalk, after CaCO<sub>3</sub>, and the SEM micrograph reported in Figure S2 (A) shows an irregular geometry which might be the cause for the dissolution observed.

*Table 6.*

	Si/Ca	Al/Ca	Fe/Ca	Mg/Ca	Si/Ca	Al/Ca	Fe/Ca	Mg/Ca
	Initial				Final			
C_w/s_0.7	3.1E <sup>-01</sup>	5.0E <sup>-02</sup>	2.4E <sup>-02</sup>	6.9E <sup>-03</sup>	1.4E <sup>-01</sup>	3.6E <sup>-02</sup>	1.8E <sup>-02</sup>	5.4E <sup>-03</sup>
L_w/s_2.0	1.5E <sup>-02</sup>	4.2E <sup>-03</sup>	7.5E <sup>-03</sup>	2.5E <sup>-02</sup>	3.2E <sup>-02</sup>	9.9E <sup>-03</sup>	1.3E <sup>-02</sup>	3.4E <sup>-02</sup>

The TG analysis performed on the limestone (Figure 5A) revealed additional signals in the ranges of 140 – 200°C and 250 – 350°C, for the samples reacted at higher w/s ratios; also, the sample L\_w/s\_3.0 showed an anomalous double peak in the region 50 – 130°C.

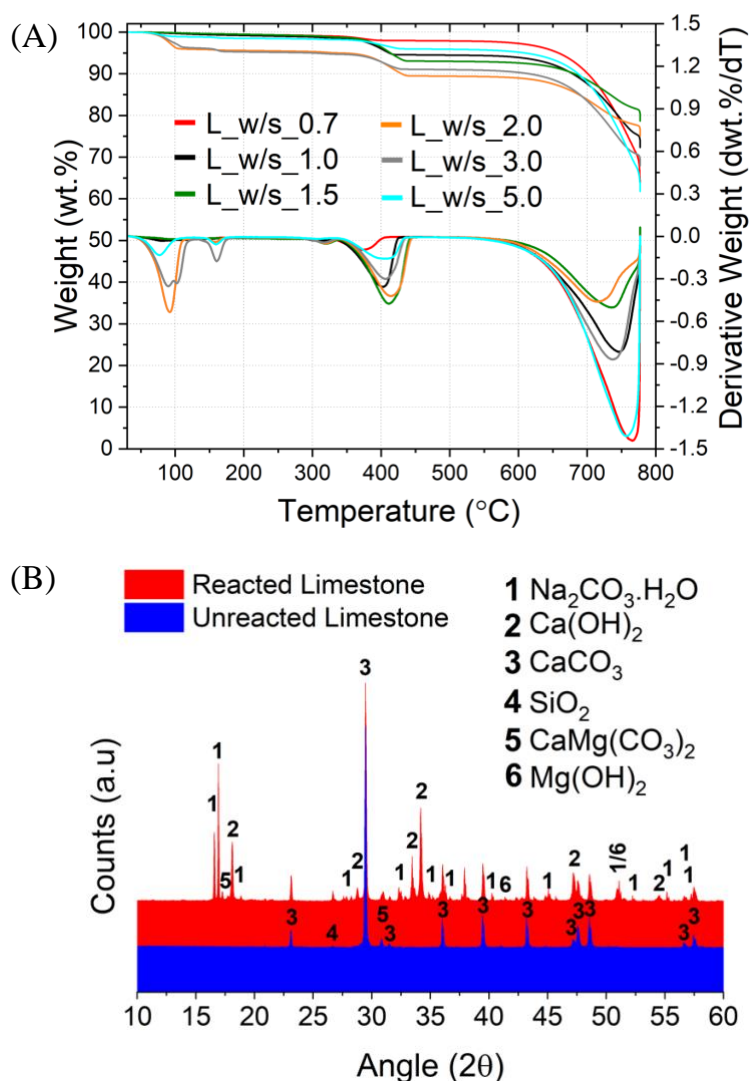


Fig. 5.

Given the higher MgCO<sub>3</sub> content within the limestone (Table 1), the signals between 250 and 350°C were likely attributed to the dehydration of brucite Mg(OH)<sub>2</sub> [45]. The signals between 140 and 200°C may be linked to the dehydration of mono-hydrocalcite CaCO<sub>3</sub>·H<sub>2</sub>O [46], suggesting its formation at generally higher water proportions. The double peak in the temperature region 50 – 130°C, with maximums at 85°C and 102°C, might potentially be due to the two-steps dehydration of Na<sub>2</sub>CO<sub>3</sub>·H<sub>2</sub>O [47], which could not be observed for any other sample here discussed. The comparison between the XRD patterns of unreacted limestone and the sample L\_w/s\_3.0 (Figure 5B) supported the TG analysis. Slight traces of dolomite CaMg(CO<sub>3</sub>)<sub>2</sub> could be observed for the limestone both prior and upon reaction, in accordance with the higher Mg content within the powders identified by XRF (Table 1). A similar intensity of the peaks of CaCO<sub>3</sub> suggest the limited reaction of CaCO<sub>3</sub> to form Ca(OH)<sub>2</sub>, and weak intensities of brucite could also be observed. Again, the eventual dissolution of the foreign

elements could be investigated by exploiting the XRF analysis performed on the sample showing the highest conversion extent (L\_w/s\_2.0). In contrast with the products from the reacted chalk, the Si/Ca, Al/Ca, Mg/Ca, and Fe/Ca ratios were decreasing for the sample L\_w/s\_2.0 upon reaction (Table 6). Such an unexpected outcome would suggest that a portion of the calcium initially introduced would dissolve upon reaction. Likely, the dissolution of dolomite to form brucite (Figure 5B) would contribute to the decreasing final Ca content within the solids. Potentially, given the relatively low content in Mg (Table 1), and therefore dolomite, some of the calcite in the limestone would dissolve too. However, such a fact did not allow to assess the eventual dissolution of the foreign elements Si, Al, Mg, and Fe for the limestone.

Based on the amount of  $\text{Ca(OH)}_2$  and  $\text{CaCO}_3$  estimated through the TG data, the extent of decarbonisation reaction was assessed using Eq. 2. The outcomes of the assessment are plotted against the concentration of NaOH in Figure 6.

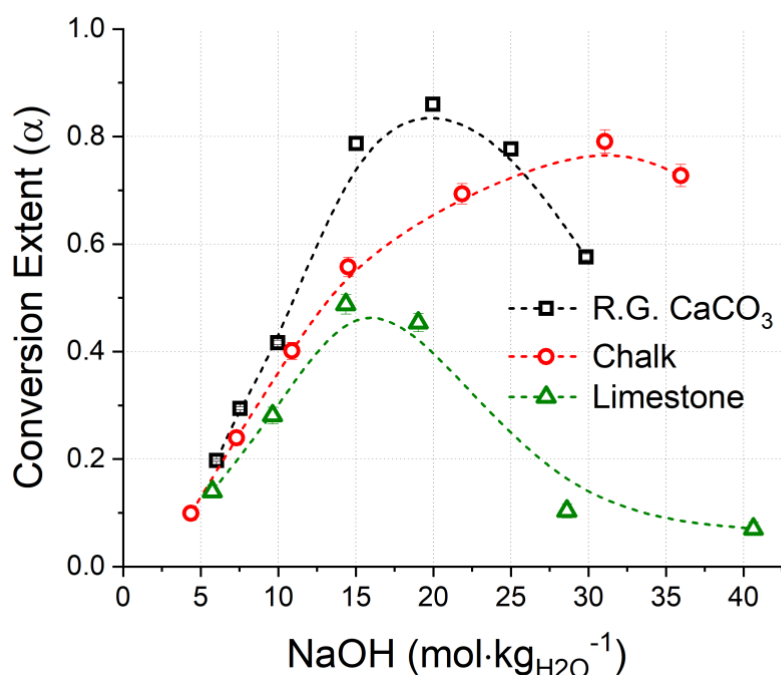


Fig. 6.

Since all samples have a constant NaOH/CaCO<sub>3</sub> ratio, the concentration of NaOH also represents the amount of H<sub>2</sub>O in the system: the higher the NaOH concentration, the less the amount of H<sub>2</sub>O. Despite the higher purity, the chalk appears to be much more reactive than the limestone, resulting in higher extent of decarbonisation (Figure 6). All materials, including the reagent grade CaCO<sub>3</sub> were showing a bell-shaped trend: the chalk indicated the maximum extent of decarbonisation of  $0.79 \pm 0.02$  at a NaOH concentration of 31.1 m, while the limestone achieved the maximum extent of decarbonisation of  $0.49 \pm 0.02$  at a NaOH

concentration of 14.3 m. The reagent grade  $\text{CaCO}_3$  showed the trend like the limestone, registering the maximum extent of decarbonisation of  $0.86 \pm 0.03$  at a 20 m NaOH.

### 3.3. Effect of impurities: individual effect

The effects of major impurities were studied on the decarbonisation reaction of the industrial grade materials. To isolate the effects of individual impurity, reagent grade materials were used to test binary systems of  $\text{CaCO}_3$ - $\text{SiO}_2$ ,  $\text{CaCO}_3$ - $\text{Al}_2\text{O}_3$ ,  $\text{CaCO}_3$ - $\text{Fe}_2\text{O}_3$ , and  $\text{CaCO}_3$ - $\text{MgCO}_3$ , with the varying proportions of impurities (Table 3). It is worth to highlight that the oxides of the targeted element were used here, rather than the corresponding minerals, such as corundum, hematite, and dolomite. For all systems, solid reaction products were recovered and underwent TG and XRD analysis. The quantification of the foreign elements was performed through XRF for those specimens showing the highest and lowest decarbonisation efficiencies in each series. Representatives XRD data for the solid reaction products of each system are shown in Figure 7. The XRD analysis confirms the occurrence of the decarbonisation reaction with clear reflection peaks of  $\text{Ca}(\text{OH})_2$  and  $\text{Na}_2\text{CO}_3 \cdot \text{H}_2\text{O}$ .

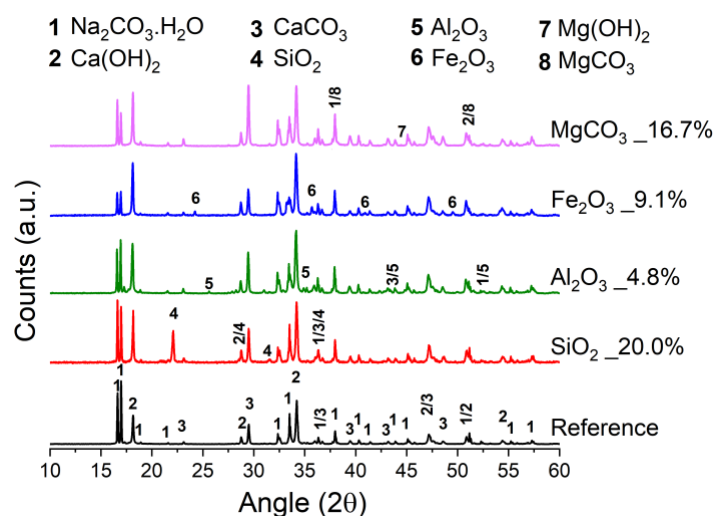


Fig. 7

The TG analysis confirmed the presence of the main phases  $\text{Na}_2\text{CO}_3 \cdot \text{H}_2\text{O}$ ,  $\text{Ca}(\text{OH})_2$  and  $\text{CaCO}_3$ , with no additional signals detected for the  $\text{SiO}_2$ \_n%,  $\text{Al}_2\text{O}_3$ \_n% and  $\text{Fe}_2\text{O}_3$ \_n% series, as reported in Figure S3. Together with the XRD data just discussed (Figure 7), the absence of secondary reactions for these systems was confirmed except brucite formation in the  $\text{CaO}$ - $\text{MgCO}_3$  system. Differently, the weight losses observed between 250 and 350°C for the  $\text{MgCO}_3$ \_n% series (Figure 8) could likely be referring to the dehydration of brucite, as also confirmed by the XRD pattern of the sample  $\text{MgCO}_3$ \_16.7% in Figure 7. Accordingly, the

intensity of the signal was increasing at higher MgCO<sub>3</sub> proportions initially blended with CaCO<sub>3</sub>.

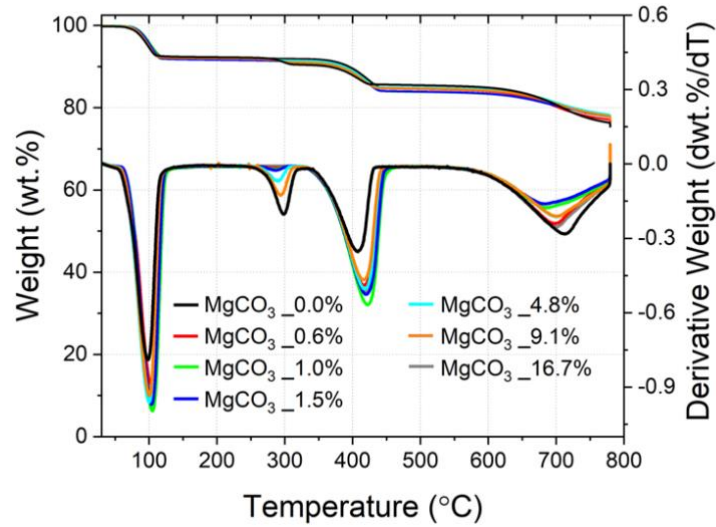


Fig. 8.

The quantification of Na<sub>2</sub>CO<sub>3</sub>.H<sub>2</sub>O, Ca(OH)<sub>2</sub> and CaCO<sub>3</sub>, based on the TG data, allowed to estimate the distributions of Na and Ca in the solid reaction product using Equations 3 and 4, respectively.

$$Na_{wt.\%} = \frac{wt.\%_{Na_2CO_3.H_2O}}{MW_{Na_2CO_3.H_2O}} \times 2MW_{Na} \quad (3)$$

$$Ca_{wt.\%} = \frac{wt.\%_{Ca(OH)_2}}{MW_{Ca(OH)_2}} \times MW_{Ca} + \frac{wt.\%_{CaCO_3}}{MW_{CaCO_3}} \times MW_{Ca} \quad (4)$$

The contents of Na and Ca gained from TG analysis and respective calculations are in good agreement with the XRF analyses conducted on targeted samples, as reported in Figure 9. A slight over-estimation of the Ca-containing species (CaCO<sub>3</sub> and Ca(OH)<sub>2</sub>) was gained from the TG analysis of the samples SiO<sub>2</sub>\_20% and MgCO<sub>3</sub>\_16.7%, with respect to XRF (Figure 9). Despite that, the theoretical Ca content calculated by considering the Na wt.% in the sample, referring to the product Na<sub>2</sub>CO<sub>3</sub>.H<sub>2</sub>O, was higher than the value gained from XRF. Potentially, the higher Si and Mg content in the samples SiO<sub>2</sub>\_20% and MgCO<sub>3</sub>\_16.7%, respectively, could be the cause for a slight under-estimation of Ca through XRF. However, despite these values were slightly off, the overall good correspondence between the TG and XRF data were likely suggesting a high reliability of the phases quantification, and linked conversion efficiency  $\alpha$ , performed through TG analysis.

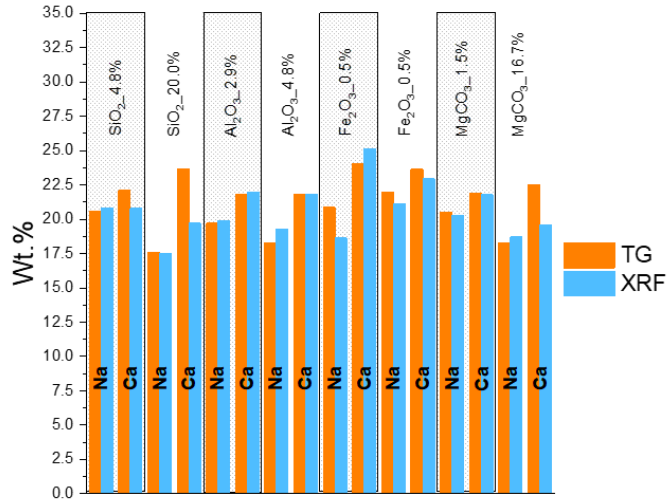


Fig. 9.

Based on the TG data, the amount of Na<sub>2</sub>CO<sub>3</sub>.H<sub>2</sub>O, Ca(OH)<sub>2</sub> and CaCO<sub>3</sub> were calculated for each solid reaction product to estimate the extent of decarbonisation reaction as shown in Figure 10.

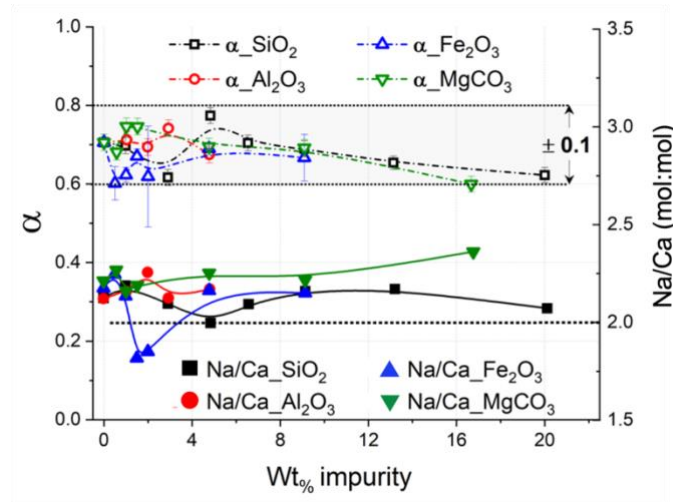


Fig. 10.

Moreover, to gain a better understanding on the precipitation of the main products Ca(OH)<sub>2</sub> and Na<sub>2</sub>CO<sub>3</sub>.H<sub>2</sub>O or Na<sub>2</sub>CO<sub>3</sub>, Na<sub>mol%</sub> and Ca<sub>mol%</sub> were firstly expressed in Equations 5 and 6, respectively.

$$Na_{mol\%} = \frac{Na_{wt.\%}}{MW_{Na}} \times 100 \quad (5)$$

$$Ca_{mol\%} = 100 * \frac{wt.\%_{Ca(OH)_2}}{MW_{Ca(OH)_2}} \times \frac{MW_{Ca}}{MW_{Ca(OH)_2}} \quad (6)$$

While  $N_{mol\%}$  is linearly linked to Equation 3 by the molecular weight of Na ( $MW_{Na}$ ), the  $Ca_{mol\%}$  here only refers to the fraction of Ca present in the system as  $Ca(OH)_2$ . By considering these values, it was possible to highlight a Na/Ca molar ratio slightly above 2 for all the samples discussed (Figure 10), apart from the specimen  $Fe_2O_3_{1.5, 2.0\%}$ . Since the stoichiometric ratio of the reaction products  $Ca(OH)_2$  and  $Na_2CO_3 \cdot H_2O$  or  $Na_2CO_3$  is 1 (Equation 1), the Na/Ca molar ratio should be 2. The slightly exceeding values might indicate a higher kinetic for the precipitation of  $Na_2CO_3 \cdot H_2O$  or  $Na_2CO_3$  with respect to  $Ca(OH)_2$ . Another possibility might relate to a partial loss of  $Ca(OH)_2$  upon dissolution, leading to higher Na/Ca molar ratios, but this is unlikely since the solubility of  $Ca(OH)_2$  is about 220 and 205 times lower than  $Na_2CO_3 \cdot H_2O$  and  $Na_2CO_3$ , respectively (Table S1).

The efficiency of the reaction varies with the type and amount of the impurity, but generally remains at around  $\alpha = 0.71$  with possibly a slight decrease when the amount of impurity increases over 10 wt.%. Specifically, increasing contents of  $Al_2O_3$  and  $MgCO_3$  were not significantly affecting the reaction efficiency, which remained constant throughout the ranges investigated.

The reactions of the systems with  $SiO_2$  and  $Fe_2O_3$  were prepared twice to experimentally confirm the not linear trends detected, and thus their data in Figure 10 indicates the standard deviation. The efficiency of the reaction appears to slightly increase at 4.8wt.%  $SiO_2$  content. Such a silica content may increase the efficiency of the decarbonisation, but additional investigation is required to confirm and elucidate the trend. With  $Fe_2O_3$  impurity, the decarbonisation reaction appeared to be reduced at 0.5wt.% and 2.0wt.%, but that might be due to the significant experimental error (Figure 10).

Based on the initial composition and the XRF data of the reaction products,  $Si_{wt\%}/Ca_{wt\%}$ ,  $Al_{wt\%}/Ca_{wt\%}$ ,  $Fe_{wt\%}/Ca_{wt\%}$ , and  $Mg_{wt\%}/Ca_{wt\%}$  ratios were calculated for the selected systems, as shown in Figure 11. The mass balances prior and upon reaction are not indicating substantial variations for the elements considered, suggesting that the dissolution of those foreign species was not significantly occurring. Such an observation was contradicting the results obtained from the industrial grade chalk and limestone, since silica appeared to dissolve at some extent in those systems (Table 6). Apparently, the reagent grade silica was less reactive than the one within the industrial grade materials, and the reason might be linked to the more irregular surface of the latter (Figure S2). The slight over-estimation of Mg and Fe for the samples  $MgCO_3_{1.5\%}$  and  $Fe_2O_3_{0.5\%}$ , respectively (Figure 11), could possibly be linked to the low Mg and Fe contents and therefore instrumental error.

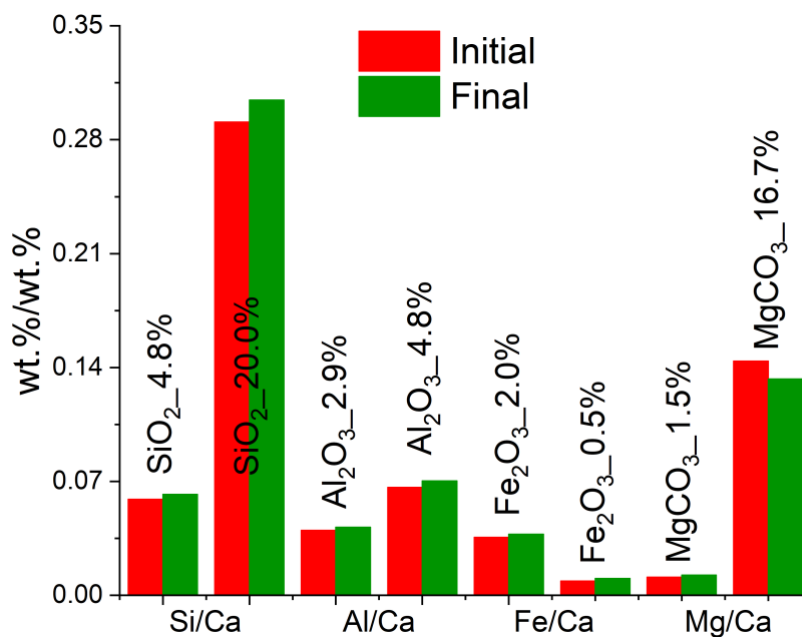


Fig. 11.

The obtained results show that the individual effects of the main impurities of the chalk and limestone tested in the present work are likely minimal on the decarbonisation reaction. Relatively short residence time did not allow for the dissolution of  $\text{SiO}_2$ ,  $\text{Al}_2\text{O}_3$  and  $\text{Fe}_2\text{O}_3$  in the experiments conducted, except the reaction of  $\text{MgCO}_3$  to form  $\text{Mg}(\text{OH})_2$ . These phases remain with the solid reaction products upon washing with methanol (Table S1). In terms of application, for instance for the cement production, the presence of  $\text{SiO}_2$ ,  $\text{Al}_2\text{O}_3$ ,  $\text{Fe}_2\text{O}_3$ , and brucite would not represent a problem, as these are the same “impurities” in raw materials used for traditional cement production. Indeed, the presence of silicates and aluminates is crucial for the synthesis of clinker phases [1].

### 3.4. Effect of impurities: combined effects

To investigate the combined effect of the impurities, samples were prepared by blending reagent grade materials, to simulate the oxide compositions detected for the chalk and limestone (Table 1). Only the main impurity constituents (>1wt.%) detected in the industrial grade materials, such as  $\text{SiO}_2$ ,  $\text{Al}_2\text{O}_3$ ,  $\text{Fe}_2\text{O}_3$ , and  $\text{MgCO}_3$ , were considered and blended with reagent grade  $\text{CaCO}_3$ . The compositions of the reagent grade systems considered are reported in Table 4. These mixtures were tested at the increasing  $\text{H}_2\text{O}/\text{Solids}$  ratios, corresponding to decreasing NaOH molarity, as shown in Table 5; the TG/DTG analysis performed on the reaction products is provided in Figures 12A and B.

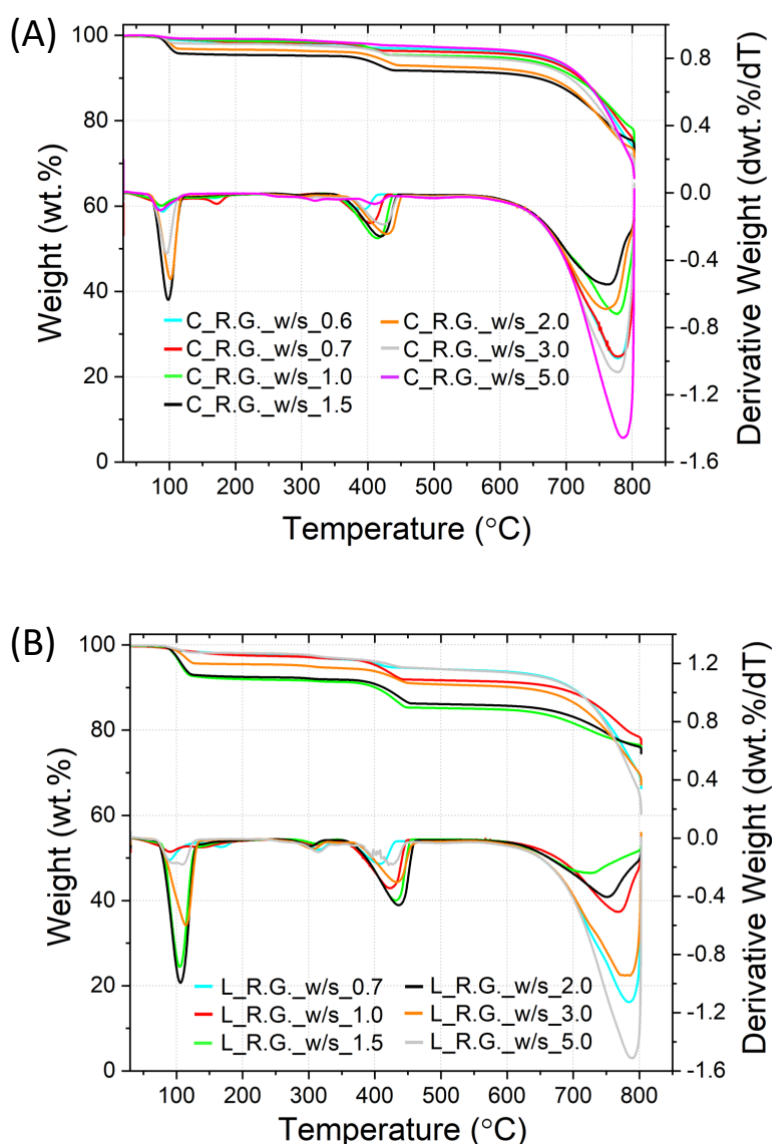


Fig. 12.

Similar to the previous experimental results, the recovered solid reaction products indicated weight loss events attributed to the presence of  $\text{Na}_2\text{CO}_3 \cdot \text{H}_2\text{O}$  (50-130°C),  $\text{Ca}(\text{OH})_2$  (310-470°C) and  $\text{CaCO}_3$  (560-800°C). Both systems indicated a minor formation of monohydrocalcite, reflected by weak weight losses in the region of 150 – 200°C for the samples reacted at a water to solids ratio of 0.7 (Figures 12A, B). A small weight loss observed in the region of 250 – 350°C is likely referred to the dehydration of brucite; more intense signals were detected for the L\_R.G. with respect to C\_R.G., in line with the higher initial  $\text{MgCO}_3$  content (Table 4).

Based on the amount of  $\text{Ca(OH)}_2$  and  $\text{CaCO}_3$  estimated from the TG data, the extent of decarbonisation reaction was assessed and indicated in Figure 13.

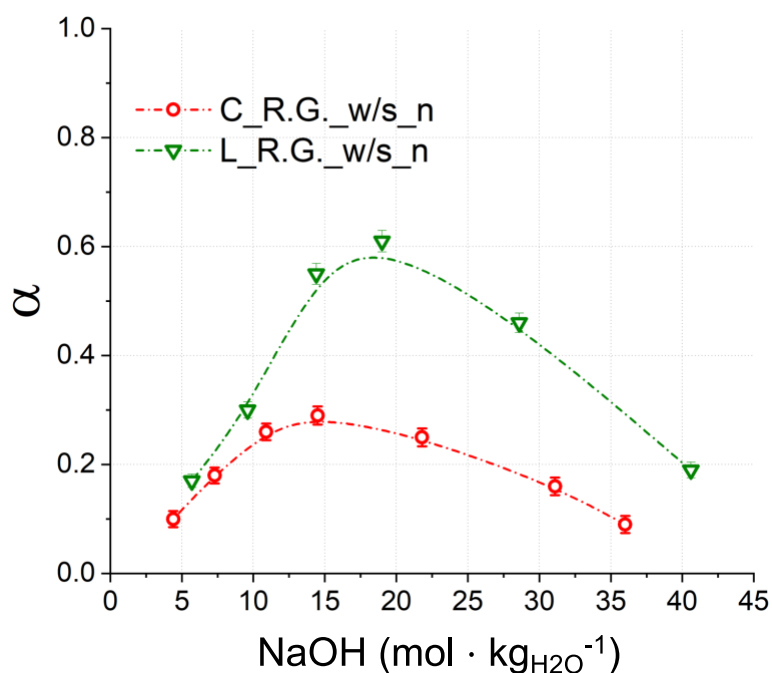


Fig. 13.

As reported, the decarbonisation for the C\_R.G.solid was significantly lower than that for the L\_R.G. for all the NaOH molarities tested. Although the effects of individual impurities were not clearly identified in the former section, it appears that the efficiency of decarbonisation reaction becomes less when the amount of the impurity is larger, as the C\_R.G. system has a larger proportion of the total impurity. This suggests either the potential synergetic effect of the impurities or the effect of the NaOH solution used (as the  $\text{NaOH}/\text{CaCO}_3$  was set to be 3.0 for all reactions, the C\_R.G. system uses less NaOH than the same weight of L\_R.G. system). These results are also in contrast with those obtained from the industrial grade calcareous materials (Figure 6), suggesting that the morphology of the materials has a significant impact on the decarbonisation reaction in the condition investigated in the present work.

XRF analysis was also conducted on the samples showing the highest efficiency of decarbonisation, i.e. C\_R.G.\_w/s\_1.5 (20.0 M NaOH) and L\_R.G.\_w/s\_1.5 (15.0 M NaOH). As reported in Figure 14, the proportion of the impurity components in the reaction products remains constant upon reaction, when assuming that the dissolution of  $\text{CaCO}_3$  and  $\text{Ca(OH)}_2$  is negligible in the alkaline solutions at the residence times considered here [48]. In other words, the XRF data suggests that the impurities are not likely dissolving in the alkaline solution upon reaction.

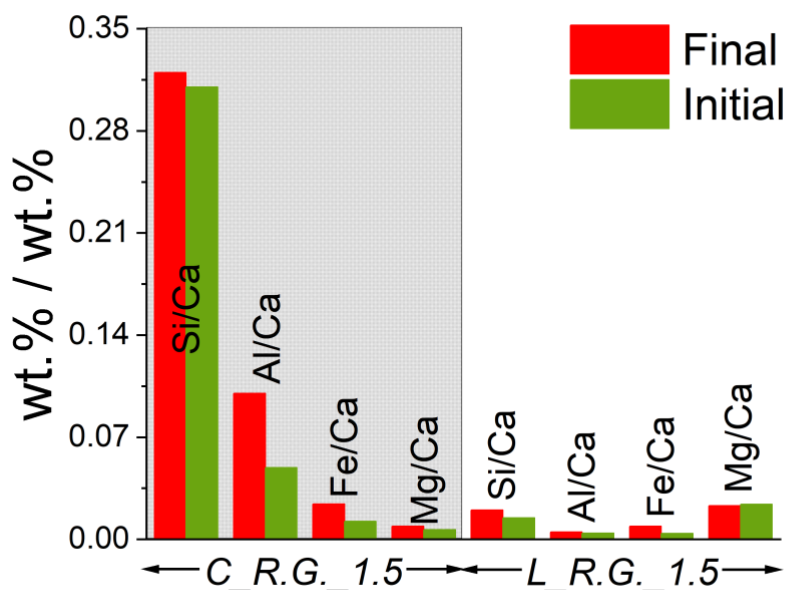


Fig. 14.

## 4. Discussion

In the decarbonisation reaction proposed, the formation of  $\text{Ca}(\text{OH})_2$  and  $\text{Na}_2\text{CO}_3 \cdot x\text{H}_2\text{O}$  should theoretically be 1:1 in moles (Equation 1); that would theoretically correspond to a Na/Ca molar ratio of 2, with Ca only referring to  $\text{Ca}(\text{OH})_2$ . However, slightly more enhanced precipitation of  $\text{Na}_2\text{CO}_3 \cdot x\text{H}_2\text{O}$  was observed with respect to  $\text{Ca}(\text{OH})_2$  when the effect of  $\text{MgCO}_3$  was investigated (Figure 10). That might be explained by considering that the surface of calcite is statistically 27% denser in positively charged ( $\text{Ca}^{2+}$ ) sites than negative ( $\text{CO}_3^{2-}$ ) ones [49], resulting in enhanced tendency to interact with cationic species, such as  $\text{Na}^+$ . Accordingly, a higher affinity should be present for  $\text{Na}^+$  than  $\text{OH}^-$  in the system investigated, which may have resulted in the slightly more enhanced precipitation of  $\text{Na}_2\text{CO}_3 \cdot x\text{H}_2\text{O}$  than  $\text{Ca}(\text{OH})_2$ . The introduction of  $\text{MgCO}_3$  would likely provide additional negative binding sites ( $\text{CO}_3^{2-}$ ) interacting with  $\text{Na}^+$ , leading to a more enhanced precipitation of  $\text{Na}_2\text{CO}_3 \cdot x\text{H}_2\text{O}$  than  $\text{Ca}(\text{OH})_2$ .

Decarbonisation of industrial grade calcareous materials indicated the higher decarbonisation efficiency in the chalk compared with the limestone. This could be likely explained by the higher surface area registered of the chalk, providing a larger number of  $\text{CO}_3^{2-}$  and  $\text{Ca}^{2+}$  binding sites for the interaction with  $\text{Na}^+$  and  $\text{OH}^-$  ionic species in the liquid bulk.

Additionally, the larger content of silica within the chalk (Table 1) might potentially play a significant role in terms of reactivity, since it would provide additional  $\text{Si}^{4+}$  and  $\text{O}^{2-}$  sites which could interact with the ions in the liquid bulk. However, a lower efficiency in decarbonising

$\text{CaCO}_3$  was generally registered for the reagent grade mixture simulating the chalk (Table 4), as reported in Figure 13, suggesting that higher contents of impurities would hinder the reaction at parity of calcareous source used.

The bell-shaped profile was obtained in the decarbonisation efficiency with different NaOH concentration, both with industrial grade and reagent grade calcareous materials (Figures 6 and 13). To understand the reduced decarbonisation efficiency observed at relatively low and high NaOH molarities, it is useful to consider the situation at the solid-liquid interface. In solution, the surface binding sites of the solids are readily saturated with strongly adsorbed layers of water [50] up to four layers below the surface, as shown in Figure 15A. Moreover, it is well known that a diffuse double layer would form at the interface of the solid and liquid bulk, upon incorporation within the solid of a charged species [51]. The double-layer is electrically charged, positive and negative when adsorbed  $\text{CO}_3^{2-}$  and  $\text{Na}^+$  are considered, respectively, to ensure electroneutrality of the surface. Apart from the steric encumbrance linked to the layers of water attached to the surface of calcite, this layer would also contribute to the overall energetic barrier to overcome for the uptake of  $\text{Na}^+$  and  $\text{CO}_3^{2-}$  to occur. With a low NaOH concentration, the chemical potential in the liquid bulk would not be sufficient to overcome the energetic barrier for the nucleation and precipitation to occur. However, the limited reaction efficiencies suggest that the low NaOH concentration was enough to at least saturate the surface binding sites of the solid calcite beneath the layer of water as indicated in Figure 15A. When the NaOH concentration increases, as shown in Figure 15B, its chemical potential in the liquid bulk becomes sufficient both for the saturation of the surface binding sites and to promote the nucleation and precipitation, diffusing towards the inner part of the solids.

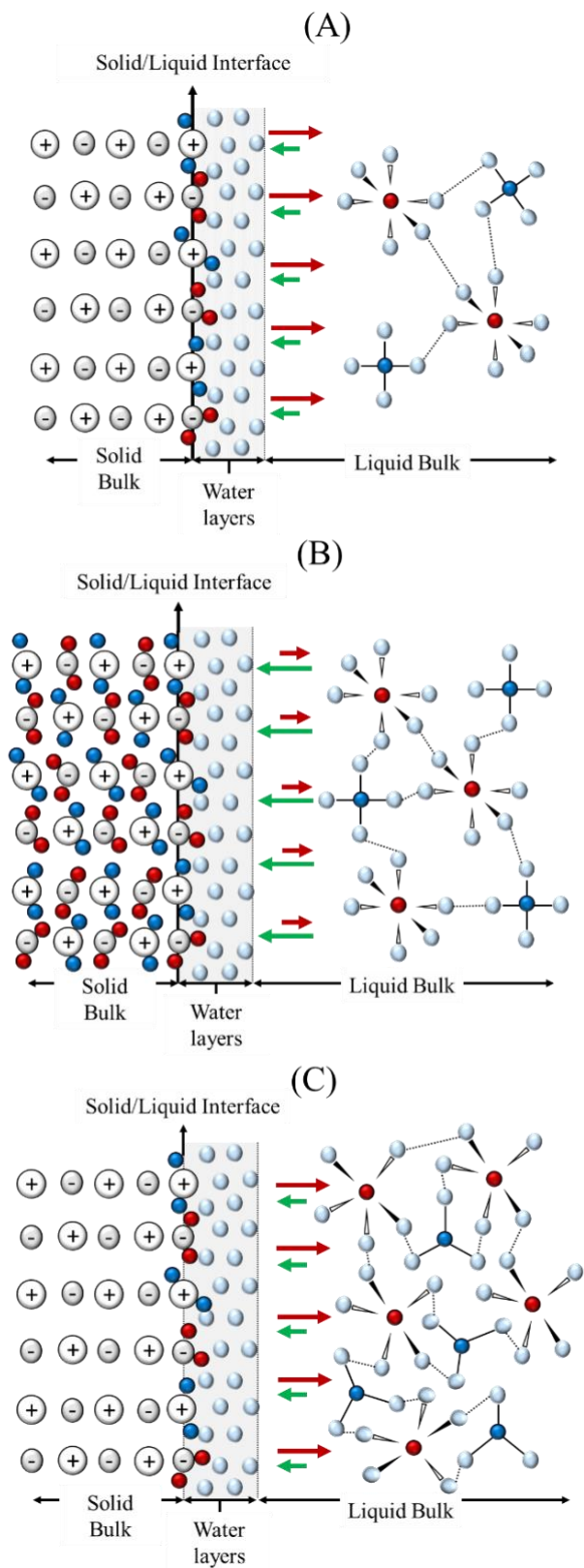


Fig. 15.

However, when the NaOH concentrations becomes too high, as shown in Figure 15C, the nucleation and precipitation of the reaction product becomes harder, likely given the too high

activity of the ions. Moreover, the higher viscosity of the NaOH solution might have lowered the contact with the solid reactants.

## 5. Conclusions

An alternative no-combustion  $\text{CaCO}_3$  decarbonisation route, involving the production of  $\text{Ca}(\text{OH})_2$  and direct capture of the process  $\text{CO}_2$  into  $\text{Na}_2\text{CO}_3 \cdot x\text{H}_2\text{O}$ , on industrial grade calcareous materials was investigated. The reaction efficiency was higher for a type of chalk rich in  $\text{SiO}_2$  (19.9 wt.%) compared with a limestone mostly composed of  $\text{CaCO}_3$  (94.4 wt.%). The maximum decarbonisation efficiencies  $\alpha$  of 0.79 was achieved for the chalk reacting with 31.1 M of NaOH, while a value of 0.49 was obtained for the limestone with 14.3 M of NaOH. The higher irregularity of the chalk surface, likely leading to a larger number of readily available binding sites, is believed to be the main reason behind this efficiency difference. In fact, additional experiments performed with reagent grade reactants highlighted that the solid solution simulating the limestone (rich in  $\text{CaCO}_3$ ) was more reactive, if the same calcareous source was considered.

The bell-shaped trend observed in the decarbonisation efficiency with increasing NaOH molarities was also discussed. Likely, low NaOH concentrations would likely allow only for the saturation of the surface binding sites of calcite, while the subsequent nucleation and precipitation would be increased at higher concentrations (a higher chemical potential) of NaOH within the liquid. However, the lower conversion efficiency observed at too high NaOH molarities was likely linked to the enhanced viscosity of the liquid bulk, hindering the ionic mobility and further interaction with the solid reactants.

The effect of the major impurities was assessed individually with reagent grade materials, and only slight fluctuations in the reaction efficiency were observed at increasing contents of  $\text{SiO}_2$ ,  $\text{Al}_2\text{O}_3$ ,  $\text{Fe}_2\text{O}_3$  and  $\text{MgCO}_3$ . The elemental analysis of the powders prior to and upon the reaction suggested the negligible dissolution of  $\text{SiO}_2$ ,  $\text{Al}_2\text{O}_3$ , and  $\text{Fe}_2\text{O}_3$ , while  $\text{MgCO}_3$  reacts to form brucite  $\text{Mg}(\text{OH})_2$ .

In conclusion, the present study demonstrated the feasibility of the chemical  $\text{CaCO}_3$  decarbonisation route on different industrial sources without combustion. The effect of microscopic morphology and surface of the  $\text{CaCO}_3$  source was more significant than that of impurities. This unconventional route for the decarbonisation of limestone could minimise the  $\text{CO}_2$  emissions both from the conventional calcination of  $\text{CaCO}_3$  and combustion of fuels, simultaneously sequestering  $\text{CO}_2$  in a stable carbonate mineral form. It has a great potential,

with further understanding and development, towards a sustainable future of relevant industries.

## List of captions (order of appearance)

**Table 2.** Oxide composition (wt.%) of the limestone and chalk used, together with the respective Loss On Ignition (LOI) values gained by XRF.

**Table 2.** Compositions inspected for the limestone (L series) and chalk (C series), and the corresponding NaOH/CaCO<sub>3</sub> (mol/mol) and H<sub>2</sub>O/Solids (wt./wt.) ratios.

**Table 3.** Composition of starting solid mixtures (wt.%) of the binary systems, and NaOH/CaCO<sub>3</sub> (mol/mol) and H<sub>2</sub>O/Solids (w/w) ratios used in the reactions.

**Table 4.** CaCO<sub>3</sub>, SiO<sub>2</sub>, Al<sub>2</sub>O<sub>3</sub> and MgCO<sub>3</sub> contents for the Chalk\_R.G. and Limestone\_R.G. powders simulating the industrial grade chalk and limestone.

**Table 5.** Summary of the conditions used for the reaction of the reagent grade powders simulating the industrial grade materials tested and discussed in Section 2.3.1.

**Fig. 1.** TG/DTG analysis performed for both the limestone and the chalk studied.

**Fig. 2.** SEM micrographs of large-sized chalk (A) and limestone (B) unreacted particles, at magnification and working distance of 120x and 9.1 mm, respectively.

**Fig. 3.** SEM micrographs of chalk (A), limestone (B), and reagent grade CaCO<sub>3</sub> (C) unreacted particles sieved below 38 μm, at magnification and working distance of 800x and 8.8, respectively

**Fig. 4.** TG and DTG trends observed for all the chalk samples (A), together with the XRD patterns for C\_w/s\_0.7 and unreacted chalk powders (B).

**Table 6.** Mass balance for each element prior and upon reaction, expressed as Si/Ca, Al/Ca, Fe/Ca, and Mg/Ca ratios.

**Fig. 5.** TG and DTG trends observed for all the limestone samples (A), together with the XRD patterns for L\_w/s\_3.0 and unreacted limestone powders (B).

**Fig. 6.** Overall efficiency of the systems at increasing NaOH molarities for the reacted chalk, limestone and reagent grade CaCO<sub>3</sub>, calculated by substituting the TG data into Equation 2.

**Fig. 7.** XRD patterns of the reference, SiO<sub>2</sub>\_20.0%, Al<sub>2</sub>O<sub>3</sub>\_4.8%, Fe<sub>2</sub>O<sub>3</sub>\_nn%, and MgCO<sub>3</sub>\_16.7% samples with main crystalline phases highlighted (B).

**Fig. 8.** TG and DTG trends observed for the binary systems CaCO<sub>3</sub> : MgCO<sub>3</sub> reported in Table 3.

**Fig. 9.** Effect of impurity contents on the amount of Na and Ca in the solid reaction products (data obtained by XRF and TG): types and quantity of the impurity is indicated at the top.

**Fig. 10.** Conversion extent (α) and Na/Ca (mol%/mol%) ratios, calculated through Equations 5 and 6, for all the binary systems here shown. The lines only work as a guide for the eye.

**Fig. 11.** Change in Si/Ca, Al/Ca, Fe/Ca, and Mg/Ca weight ratios between the initial solid mixtures and the solid reaction products.

**Fig. 12.** TG and DTG trends observed for the C\_R.G.\_w/s\_n (A) and L\_R.G.\_w/s\_n (B) samples.

**Fig. 13.** Overview of the conversion extent  $\alpha$  registered for the C\_R.G. and L\_R.G. samples at increasing NaOH molarities.

**Fig. 14.** Mass balances for Ca, Si, Al and Mg expressed as wt.% Si/Ca, Al/Ca, Fe/Ca, and Mg/Ca ratios, respectively.

**Fig. 15.** Schematic representation of the interactions occurring within the liquid and solid bulk considered for the study, where the red, dark blue, and light blue refer to Na<sup>+</sup>, OH<sup>-</sup> and H<sub>2</sub>O, respectively. Each Na<sup>+</sup> and OH<sup>-</sup> ion is surrounded by a number of water molecules, forming the solvation shell, depending on the NaOH concentration [52]. The hydrogen bonds between the Na<sup>+</sup> and OH<sup>-</sup> ions and the water molecules forming the solvation shell, and between water molecules of adjacent ions are also displayed. The solid/liquid interface is light-grey highlighted, outlining the attachment of those four layers of water, whereas the green and red arrows qualitatively represent the attractive and repulsive forces between the ions in solution and the solid surface. The cases A, B, and C refer to low, medium/optimal, and high NaOH concentrations, respectively.

## Supporting information for publication

<i>Chemical</i>	<i>Solubility in water at 25°C, 1 atm (g L<sup>-1</sup>)</i>	<i>Solubility in methanol at 25°C, 1 atm (g L<sup>-1</sup>)</i>
<i>SiO<sub>2</sub></i>	<i>n.s.<sup>[11]</sup></i>	<i>n.s.<sup>[11]</sup></i>
<i>Al<sub>2</sub>O<sub>3</sub></i>	<i>n.s.<sup>[12]</sup></i>	<i>n.s.<sup>[12]</sup></i>
<i>Fe<sub>2</sub>O<sub>3</sub></i>	<i>n.s.<sup>[12]</sup></i>	<i>n.s.<sup>[12]</sup></i>
<i>MgCO<sub>3</sub></i>	<i>1.1·10<sup>-3</sup><sup>[13]</sup></i>	<i>n.s.<sup>[13]</sup></i>
<i>CaCO<sub>3</sub></i>	<i>1.4·10<sup>-4</sup><sup>[14]</sup></i>	<i>n.s.<sup>[14]</sup></i>
<i>Ca(OH)<sub>2</sub></i>	<i>1.5<sup>[15]</sup></i>	<i>n.s.<sup>[15]</sup></i>
<i>Na<sub>2</sub>CO<sub>3</sub></i>	<i>307.0<sup>[16]</sup></i>	<i>n.s.<sup>[16]</sup></i>
<i>Na<sub>2</sub>CO<sub>3</sub>·H<sub>2</sub>O</i>	<i>330.0<sup>[16]</sup></i>	<i>n.s.<sup>[16]</sup></i>

**Table S1.** Solubility (g L<sup>-1</sup>) of the relevant solid phases in water and methanol at 25°C and 1 atm; n.s. stands for not soluble.

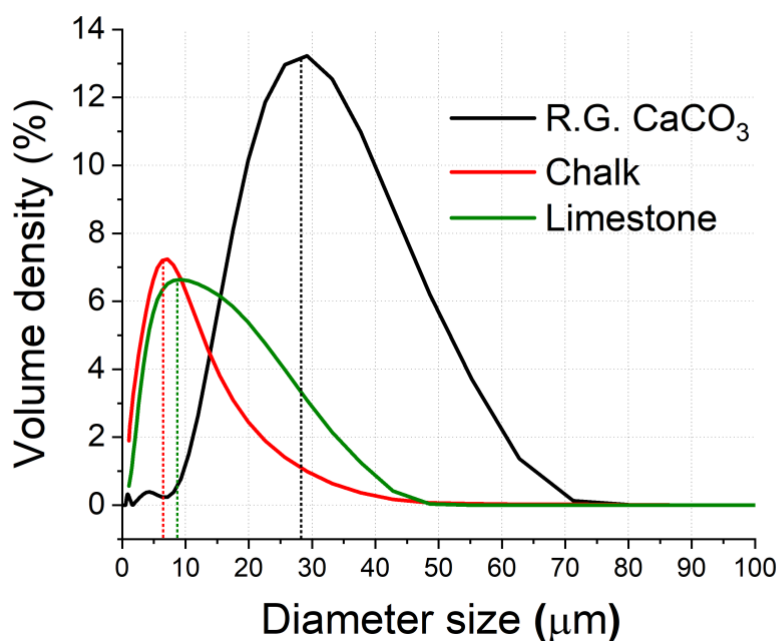


**Figure S1.** Particle Size Distribution (PSD) performed for both the limestone and the chalk studied.

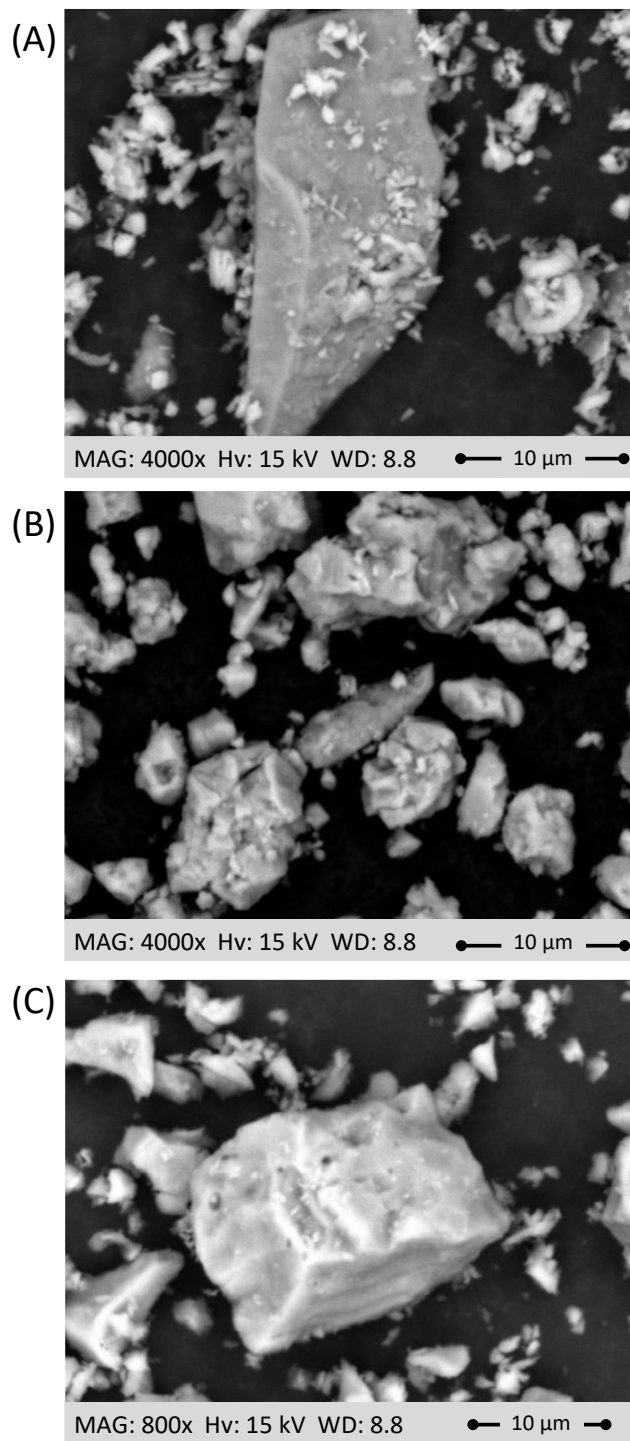


**Figure S2.** SEM micrographs of the silica crystals within the chalk (A) and limestone (B), together with the reagent grade silica (C); the analyses were conducted at 15 kV, magnification and working distance of 800 and 8.8, respectively.

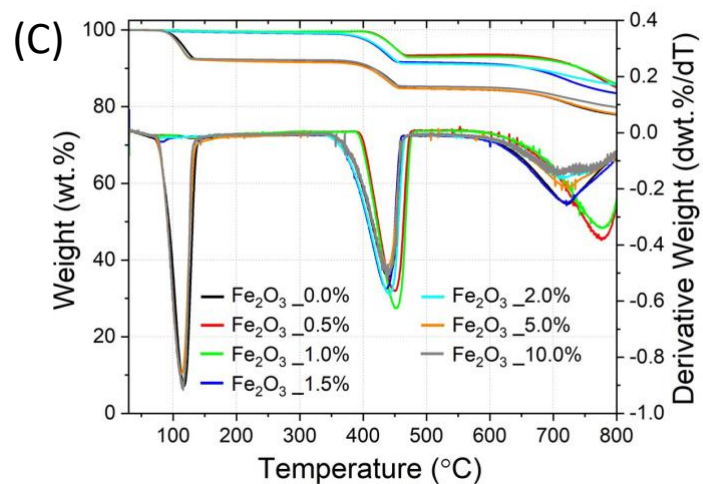
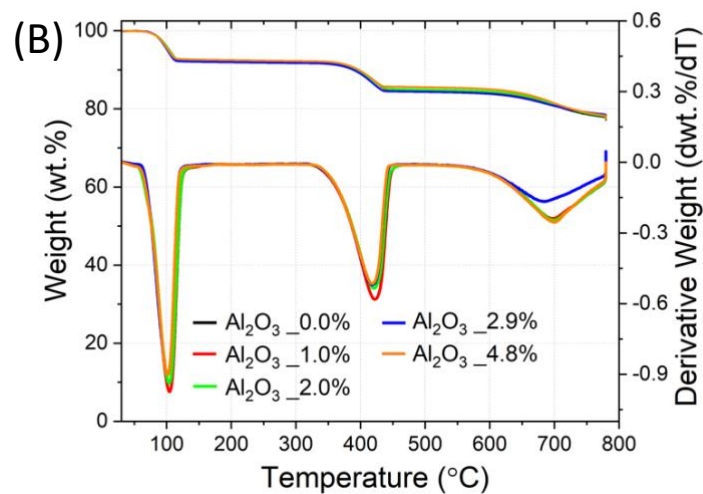
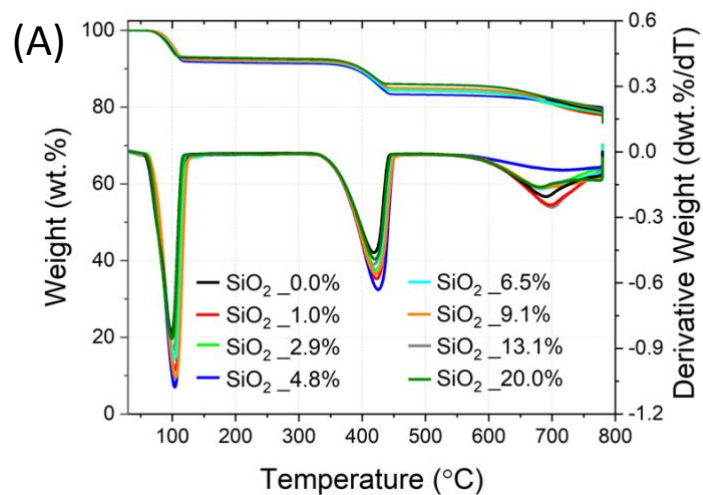
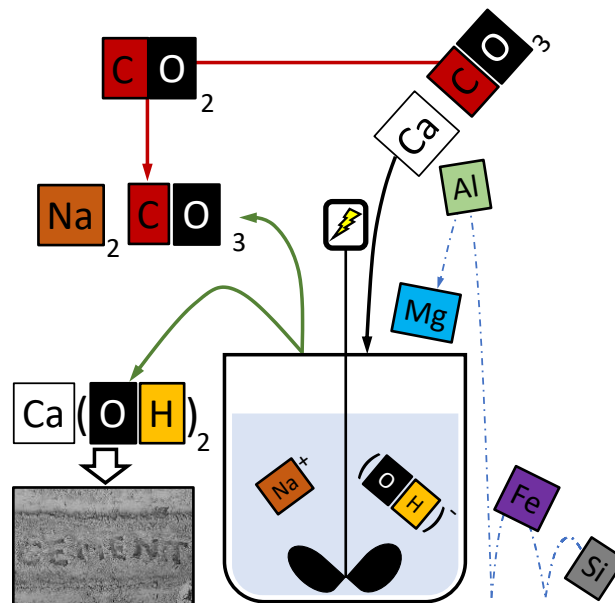


**Figure S3.** TG/DTG trends observed for the binary system  $\text{CaCO}_3\text{:SiO}_2$  (A),  $\text{Al}_2\text{O}_3\text{:SiO}_2$  (B), and  $\text{Fe}_2\text{O}_3\text{:SiO}_2$  (C), reported in Table 4.

## Acknowledgments

This work was funded by the Engineering and Physical Science Research Council (EPSRC) and CEMEX under grant ID EP/R025959/1. This research utilised the HADES/MIDAS facility at the University of Sheffield established with financial support from EPSRC and BEIS, under grant EP/T011424/1. The XRF analysis was performed by AMG Analytical Services, Fullerton Road, Rotherham, South Yorkshire S60 1DL, England. For the purpose of open access, the author has applied a Creative Commons Attribution (CC BY) licence to any Author Accepted Manuscript version arising. The group would also like to express gratitude to Dr. Mark Tyrer for the support and knowledge received.

For Table of contents use only



The impurities within the raw materials did not affect the efficiency of the  $\text{CaCO}_3$  chemical decarbonisation for sustainable cement production.

## References

1. Taylor, H.F.W. *Cement chemistry*. Vol. 2. London, 1997: Thomas Telford, ISBN: 0 7277 2592 0
2. Schorcht, F.; Kourti, I.; Scalet, B. M.; Roudier, S.; Sancho, L. D. *Best available techniques (BAT) reference document for the production of cement, lime and magnesium oxide*. European Commission Joint Research Centre Institute for Prospective Technological Studies (Report EUR 26129 EN). Luxembourg: Publications Office of the European Union, 2013, ISBN 978-92-79-32944-9
3. U.S. Department of the Interior, U.S. Geological Survey, *Mineral commodity summaries 2020*. 2019, National Minerals Information Centre, ISBN 978-1-4113-4283-5
4. Friedlingstein P.; Jones, M.W.; O'sullivan, M.; Andrew, R.M.; Hauck, J.; Peters, G.P.; Peters, W.; Pongratz, J.; Sitch, S.; Le Quéré, C.; Bakker, D.C. *Global carbon budget 2019*. *Earth System Science Data*, 2019. 11(4): p. 1783-1838, DOI:10.5194/essd-11-1783-2019
5. Schneider, M.; Romer, M.; Tschudin, M.; Bolio, H. *Sustainable cement production—present and future*. *Cement and Concrete Research*, 2011. 41(7): p. 642-650, DOI:10.1016/j.cemconres.2011.03.019
6. Blamey, J.; Anthony, E.J.; Wang, J.; Fennell, P.S. *The calcium looping cycle for large-scale CO<sub>2</sub> capture*. *Progress in Energy and Combustion Science*, 2010. 36(2): p. 260-279, DOI: 10.1016/j.peccs.2009.10.001
7. Dowling, A.; O'Dwyer, J.; Adley, C.C. *Lime in the limelight*. *Journal of cleaner production*, 2015. 92: p. 13-22, DOI: 10.1016/j.jclepro.2014.12.047
8. Gutiérrez, A.S.; Martínez, J.B.C.; Vandecasteele, C. *Energy and exergy assessments of a lime shaft kiln*. *Applied Thermal Engineering*, 2013. 51(1-2): p. 273-280, DOI: 10.1016/j.applthermaleng.2012.07.013
9. Bui, M.; Adjiman, C.S.; Bardow, A.; Anthony, E.J.; Boston, A.; Brown, S.; Fennell, P.S.; Fuss, S.; Galindo, A.; Hackett, L.A.; Hallett, J.P. *Carbon capture and storage (CCS): the way forward*. *Energy & Environmental Science*, 2018. 11(5): p. 1062-1176, DOI: 10.1039/C7EE02342A
10. Usón, A.A.; López-Sabirón, A.M.; Ferreira, G.; Sastresa, E.L. *Uses of alternative fuels and raw materials in the cement industry as sustainable waste management options*. *Renewable and Sustainable Energy Reviews*, 2013. 23: p. 242-260, DOI:10.1016/j.applthermaleng.2012.07.013
11. Shi, C.; Jiménez, A.F.; Palomo, A. *New cements for the 21st century: The pursuit of an alternative to Portland cement*. *Cement and concrete research*, 2011. 41(7): p. 750-763, DOI: 10.1016/j.cemconres.2011.03.016
12. Plaza, M.G., Martínez, S.; Rubiera, F. *CO<sub>2</sub> capture, use, and storage in the cement industry: State of the art and expectations*. *Energies*, 2020. 13(21): p. 5692, DOI: 10.3390/en13215692
13. Naranjo, M.; Brownlow, D.T.; Garza, A. *CO<sub>2</sub> capture and sequestration in the cement industry*. *Energy Procedia*, 2011. 4: p. 2716-2723, DOI: 10.1016/j.egypro.2011.02.173
14. Idem, R.; Wilson, M.; Tontiwachwuthikul, P.; Chakma, A.; Veawab, A.; Aroonwilas, A.; Gelowitz, D. *Pilot plant studies of the CO<sub>2</sub> capture performance of aqueous MEA and mixed MEA/MDEA solvents at the University of Regina CO<sub>2</sub> capture technology development plant and the boundary dam CO<sub>2</sub> capture demonstration plant*. *Industrial & engineering chemistry research*, 2006. 45(8): p. 2414-2420, DOI: 10.1021/ie050569e
15. *Bewährtes neu denken, Environmental data of the German cement industry 2020*. Duesseldorf, July, 2021, <https://www.vdz-online.de/en/knowledge-base/publications/environmental-data-of-the-german-cement-industry-2020>, date of access 16.08.2022
16. Busch, P.; Kendall, A.; Murphy, C.W.; Miller, S.A. *Literature review on policies to mitigate GHG emissions for cement and concrete*. *Resources, Conservation and Recycling*, 2022. 182: p. 106278, DOI: 10.1016/j.resconrec.2022.106278
17. Hanein, T.; Simoni, M.; Woo, C.L.; Provis, J.L.; Kinoshita, H. *Decarbonisation of calcium carbonate at atmospheric temperatures and pressures, with simultaneous CO<sub>2</sub> capture, through production of sodium carbonate*. *Energy & Environmental Science*, 14.12 (2021): 6595-6604, DOI: 10.1039/D1EE02637B.
18. Lakshmanan, S.; Murugesan, T. *The chlor-alkali process: work in progress*. *Clean Technologies and Environmental Policy*, 2014. 16(2): p. 225-234, DOI: 10.1007/s10098-013-0630-6
19. Rhodes, C.J. *The 2015 Paris climate change conference: COP21*. *Science progress*, 2016. 99(1): p. 97-104, DOI: 10.3184/003685016X14528569315192
20. Neubauer, J.; Pöllmann, H. *Alinite—Chemical composition, solid solution and hydration behaviour*. *Cement and concrete research*, 1994. 24(8): p. 1413-1422, DOI: 10.1016/0008-8846(94)90154-6
21. Simoni, M.; Hanein, T.; Duvallet, T.Y.; Jewell, R.B.; Provis, J.L.; Kinoshita, H. *Producing cement clinker assemblages in the system: CaO-SiO<sub>2</sub>-Al<sub>2</sub>O<sub>3</sub>-SO<sub>3</sub>-CaCl<sub>2</sub>-MgO*. *Cement and Concrete Research*, 2021. 144, p. 106418, DOI: 10.1016/j.cemconres.2021.106418

22. Ramirez, A.; Sarathy, S.M.; Gascon, J. CO<sub>2</sub> derived E-fuels: research trends, misconceptions, and future directions. *Trends in chemistry*, 2020. 2(9): p. 785-795, DOI: 10.1016/j.trechm.2020.07.005
23. Meier, A.; Bonaldi, E.; Cella, G.M.; Lipinski, W.; Wuillemin, D. Solar chemical reactor technology for industrial production of lime. *Solar Energy*, 2006. 80(10): p. 1355-1362, DOI: 10.1016/j.solener.2005.05.017
24. Murray, A.; Price, L. Use of alternative fuels in cement manufacture: analysis of fuel characteristics and feasibility for use in the Chinese cement sector. 2008, Retrieved from <https://escholarship.org/uc/item/8sf9s522>
25. Manzano, H.; Durgun, E.; Abdolhosseine Qomi, M.J.; Ulm, F.J.; Pellenq, R.J.; Grossman, J.C. Impact of chemical impurities on the crystalline cement clinker phases determined by atomistic simulations. *Crystal Growth & Design*, 2011. 11(7): p. 2964-2972, DOI: 10.1021/cg200212c
26. Palmer, A.N. Origin and morphology of limestone caves. *Geological Society of America Bulletin*, 1991. 103(1): p. 1-21, DOI: 10.1130/0016-7606(1991)103<0001:OAMOLC>2.3.CO;2
27. Fabricius, I.L. Chalk: composition, diagenesis and physical properties. *Bulletin of the Geological Society of Denmark*, 2007. 55: p. 97-128, Retrieved from <http://2dgf.dk/publikationer/bulletin/index.html>
28. Ehrenberg, S.N.; Eberli, G.P.; Keramati, M.; Moallemi, S.A. Porosity-permeability relationships in interlayered limestone-dolostone reservoirs. *AAPG bulletin*, 2006. 90(1): p. 91-114, DOI: 10.1306/08100505087
29. Yang, Y.; Aplin, A.C. A permeability-porosity relationship for mudstones. *Marine and Petroleum Geology*, 2010. 27(8): p. 1692-1697, DOI: 10.1016/j.marpetgeo.2009.07.001
30. Zelić, J.; Rušić, D.; Krstulović, R. Kinetic analysis of thermal decomposition of Ca(OH)<sub>2</sub> formed during hydration of commercial Portland cement by DSC. *Journal of thermal analysis and calorimetry*, 2002. 67(3): p. 613-622, DOI: 10.1023/A:1014348603686
31. Gallagher, P.K.; Johnson Jr, D.W. The effects of sample size and heating rate on the kinetics of the thermal decomposition of CaCO<sub>3</sub>. *Thermochimica Acta*, 1973. 6(1): p. 67-83, DOI: 10.1016/0040-6031(73)80007-3
32. Hartman, M.; Trnka, O.; Vesely, V.; Svoboda, K. Thermal dehydration of the sodium carbonate hydrates. *Chemical Engineering Communications*, 2001. 185(1): p. 1-16, DOI: 10.1080/00986440108912851
33. Kjellsen, K.O.; Monsøy, A.; Isachsen, K.; Detwiler, R.J. Preparation of flat-polished specimens for SEM-backscattered electron imaging and X-ray microanalysis—importance of epoxy impregnation. *Cement and concrete research*, 2003. 33(4): p. 611-616, DOI: 10.1016/S0008-8846(02)01029-3
34. Potts, P.J.; Ellis, A.T.; Kregsamer, P.; Strelci, C.; Vanhoof, C.; West, M.; Wobrauschek, P. Atomic spectrometry update. X-ray fluorescence spectrometry. *Journal of analytical atomic spectrometry*, 2005. 20(10): p. 1124-1154, DOI: 10.1039/B511542F
35. Seidell, A. *Solubilities of inorganic and metal organic compounds*. 1940, Van Nostrand.
36. Farhad, A. and Mohammadi, Z. Calcium hydroxide: a review. *International dental journal*, 2005. 55(5): p. 293-301, DOI: 10.1111/j.1875-595X.2005.tb00326.x
37. Ellingboe, J.L., Runnels, J.H. *Solubilities of Sodium Carbonate and Sodium Bicarbonate in Acetone-Water and Methanol-Water Mixtures*. *Journal of Chemical and Engineering Data*, 1966. 11(3): p. 323-324, DOI: 10.1021/je60030a009
38. Morey, G.W. The action of water on calcite, magnesite and dolomite. *American Mineralogist: Journal of Earth and Planetary Materials*, 1962. 47(11-12): p. 1456-1460, ISSN: 0003-004X
39. Alexander, G.B.; Heston, W.M.; Iler, R.K. The solubility of amorphous silica in water. *The Journal of Physical Chemistry*, 1954. 58(6): p. 453-455, DOI: 10.1021/j150516a002
40. Patnaik, P. *Handbook of inorganic chemicals*. Vol. 529. 2003: McGraw-Hill New York, ISBN: 0-07-049439-8
41. Young, J.R.; Davis, S.A.; Bown, P.R.; Mann, S. Coccolith ultrastructure and biomineralisation. *Journal of structural biology*, 1999. 126(3): p. 195-215, DOI: 10.1006/jsbi.1999.4132.
42. Cizer, Ö.; Rodriguez-Navarro, C.; Ruiz-Agudo, E.; Elsen, J.; Van Gemert, D.; Van Balen, K. Phase and morphology evolution of calcium carbonate precipitated by carbonation of hydrated lime. *Journal of Materials Science*, 2012. 47(16): p. 6151-6165, DOI: 10.1007/s10853-012-6535-7
43. Cheng, B.; Lei, M.; Yu, J.; Zhao, X. Preparation of monodispersed cubic calcium carbonate particles via precipitation reaction. *Materials Letters*, 2004. 58(10): p. 1565-1570, DOI: 10.1016/j.matlet.2003.10.027
44. Simoni, M.; Hanein, T.; Woo, C.L.; Tyrer, M.; Nyberg, M.; Martinez, J.C.; Quintero-Mora, N.I.; Provis, J.L.; Kinoshita, H. Decarbonisation of calcium carbonate in sodium hydroxide solutions under ambient conditions: effect of residence time and mixing rates. *Physical Chemistry Chemical Physics*, 2022, 24(26), pp.16125-16138, DOI:10.1039/D2CP01412B

45. Ball, M.C.; Taylor, H.F.W. *The dehydration of brucite. Mineralogical magazine and journal of the Mineralogical Society*, 1961. 32(253): p. 754-766, DOI:10.1180/minmag.1961.032.253.02
46. Kimura, T.; Koga, N. *Thermal dehydration of monohydrocalcite: overall kinetics and physico-geometrical mechanisms. The Journal of Physical Chemistry A*, 2011. 115(38): p. 10491-10501, DOI: 10.1021/jp206654n
47. Deshpande, D.A.; Ghormare, K.R.; Jawadekar, V.L.; Deshpande, N.D. *Thermal analysis of Na<sub>2</sub>CO<sub>3</sub>·H<sub>2</sub>O crystals. Thermochimica Acta*, 1983. 60(3): p. 295-302, DOI: 10.1016/0040-6031(83)80251-2
48. Duchesne, J.; Reardon, E.J. *Measurement and prediction of portlandite solubility in alkali solutions. Cement and Concrete Research*, 1995. 25(5): p. 1043-1053, DOI: 10.1016/0008-8846(95)00099-X
49. Heberling, F.; Bosbach, D.; Eckhardt, J.D.; Fischer, U.; Glowacky, J.; Haist, M.; Kramar, U.; Loos, S.; Müller, H.S.; Neumann, T.; Pust, C. *Reactivity of the calcite–water-interface, from molecular scale processes to geochemical engineering. Applied geochemistry*, 2014. 45: p. 158-190, DOI: 10.1016/j.apgeochem.2014.03.006
50. Stipp, S.L.; Hochella Jr, M.F. *Structure and bonding environments at the calcite surface as observed with X-ray photoelectron spectroscopy (XPS) and low energy electron diffraction (LEED). Geochimica et Cosmochimica Acta*, 1991. 55(6): p. 1723-1736, DOI: 10.1016/0016-7037(91)90142-R
51. Stillinger Jr, F.H.; Kirkwood, J.G. *Theory of the diffuse double layer. The Journal of Chemical Physics*, 1960. 33(5): p. 1282-1290, DOI: 10.1063/1.1731401
52. Botti, A.; Bruni, F.; Imberti, S.; Ricci, M.A.; Soper, A.K. *Ions in water: The microscopic structure of concentrated NaOH solutions. The Journal of chemical physics*, 2004. 120(21): p. 10154-10162, DOI: 10.1063/1.1705572

## 7. Concluding remarks and recommendations for future work

The chemical decarbonisation of  $\text{CaCO}_3$  proposed here represents a valid alternative to the conventional calcination route, potentially allowing for the avoidance of both the process and combustion  $\text{CO}_2$  emissions. Despite the characterisation was performed at a laboratory-scale, the experimental outcomes suggest that the process is robust and relatively simple. The efficiency of the reaction, based on five minutes of residence time, was greatly affected by the ternary composition used. The adjustment of the three components of the system has been successfully carried out, highlighting those conditions allowing for a wide range of  $\text{CaCO}_3$  conversion extent. Several processing conditions were individually varied to isolate the effect of each of them, i.e. residence time, stirring rate, temperature, impurity content. The outcomes suggested strong potential for the eventual scale-up of the process, since high efficiency was registered at relatively low residence time and stirring rate, while the temperature was not significantly affecting the conversion of  $\text{CaCO}_3$ . Finally, the reaction was successfully tested on industrial grade calcareous sources, i.e. chalk and limestone, and important differences were highlighted and discussed. The material with the higher impurity content was responding more positively than the nearly  $\text{CaCO}_3$ -pure one, suggesting that the morphology of the  $\text{CaCO}_3$  particles would mainly influence the reactivity of the component, rather than the foreign elements in the system. To ensure that, individual experiments were carried out for each impurity detected within the raw materials considered, and the outcomes suggested a minimal influence over the capacity to convert  $\text{CaCO}_3$ .

However, as extensively discussed in the former sections, the reaction occurs at ambient conditions, i.e. no combustion required, to give decarbonised  $\text{CaCO}_3$  as  $\text{Ca}(\text{OH})_2$  and simultaneously sequestering the process  $\text{CO}_2$  into  $\text{Na}_2\text{CO}_3$ . In other words, the carbon footprint of the process itself could be neutral, but different aspects need to be considered and discussed to correctly assess the industrial feasibility of this alternative. Most noticeably, the usage of  $\text{NaOH}$  would be translated into embodied carbon footprint, given the large usage of electrical power for the Chlor-alkali process (Section 7.2). However, as mentioned in Section 2.1., when the electricity is mainly produced from sustainable sources, the emissions arising from the synthesis of  $\text{NaOH}$  could be significantly lowered. Thus, the chemical  $\text{CaCO}_3$  decarbonisation route here discussed here could be close to carbon neutral, and therefore potentially leading to a sustainable cement production. The difference between the cement (Section 1) and  $\text{NaOH}$  (Section 7.2) markets would also represent a crucial issue. In fact, the actual global production of  $\text{NaOH}$  could not fulfil the demand from the cement industry, if this novel decarbonisation route would replace the conventional one, while ensuring the current demand worldwide. This aspect might be mitigated by considering that alternative binders could significantly replace Portland Cement, lowering the demand and therefore the global

production. Also, it must be highlighted that the Chlor-alkali process would provide drinking water as a result of seawater desalination. This last aspect must be highlighted, given the shortage of drinking water expected for the near future; that might lead to an increase of the NaOH market worldwide anyway, to ensure drinkable water for the population. Apart from the convenient co-production of hydrogen, whose role as a future sustainable fuel is widely recognised, the synthesis of significant amounts of chlorine gas must be taken into account too, since the release to the atmosphere of such large amounts would have a critical effect on the environment. The production of Cl-containing binders might offer a good application of such chlorine, and the matter is more extensively discussed in Appendix 2.

For the by-product  $\text{Na}_2\text{CO}_3$ , the actual global market is currently lower than cement, and therefore an over-production is strongly expected if the proposed technique is applied to the cement production globally. However, this can be changed in the future. For instance,  $\text{Na}_2\text{CO}_3$  is used as activator for geo-polymers, whose applicability is already globally accepted and the market expected to expand. In other words, a part of excess  $\text{Na}_2\text{CO}_3$  might feed the cement industry, providing a key component for the synthesis of alternative cements. More importantly, the formation of  $\text{Na}_2\text{CO}_3$  might be seen as a safer alternative to the geological disposal of  $\text{CO}_2$ , which might represent a heavy burden for the future generations to deal with.  $\text{Na}_2\text{CO}_3$  is a stable mineral which can be safely stored at ambient conditions. The regeneration of NaOH could be considered as additional solution. Doing so, the reaction could be performed again with a minimal overall consumption of NaOH, although  $\text{CO}_2$  has to be captured and stored in alternative way.

The possibilities mentioned above require a corresponding life-cycle assessment, which has not been done at this stage yet, precisely assessing the technical and economic feasibility. This is my top-priority recommendation for future work, and the global cement community needs to be made aware of this alternative, alongside the pros and cons linked to a full economic analysis.

In terms of technical aspect, the process needs to be fully optimised, including the successive separation of  $\text{Ca}(\text{OH})_2$  from  $\text{Na}_2\text{CO}_3$  and final clinkering. While the former is currently under investigation as part of another PhD project within the University of Sheffield, the latter has been only briefly tested (Section 9), but a much deeper investigation needs to be done in those terms. For instance, the clinkering kinetics need to be outlined for  $\text{Ca}(\text{OH})_2$  as calcareous source, together with the optimal temperature and residence time. Furthermore, the testing on industrial grade sources reported in Section 6 needs to be enriched with additional materials characterised by varying impurities content and physical properties. Doing so, the feasibility of the reaction on a broad range of starting materials would be demonstrated. As reported in

Sections 3 – 6, the solid powders are washed with methanol to remove the unreacted NaOH and preserve the phase assemblage gained upon reaction; future work might also interest the testing of other solvents, i.e. iso-propanol, acetone, in order to enlarge the range of possible chemicals as alternatives. Finally, the reaction might further be tested by considering other alkalis, i.e. KOH, LiOH, which may lead to a higher system efficiency.

By summarising, the proposed chemical decarbonisation of  $\text{CaCO}_3$  could have the potential to decarbonise the cement/lime industry by avoiding the thermal calcination; its feasibility has been here outlined under several conditions, which revealed promising outcomes from an industrial point of view. It is my belief that this alternative decarbonisation route might represent a valid solution to achieve the carbon neutrality for cement industry, or at least it could inspire the scientific community for further development.

## 8. Appendix

The original plan for this thesis also included some clinkering characterisation from  $\text{Ca}(\text{OH})_2$  as calcareous source rather than  $\text{CaCO}_3$ . In fact, in the case of positive outcomes, it would derive that the  $\text{Ca}(\text{OH})_2$  produced through the chemical decarbonisation of  $\text{CaCO}_3$  here discussed might be directly used for cement production, without passing through a dehydroxylation to  $\text{CaO}$ . Unfortunately, because of the Covid-19 pandemic, the beginning of these experiments has been delayed; following, when the laboratories re-opened again, together with my supervisors we decided not to proceed with the investigation. Anyway, apart from the fact that the suitability of  $\text{Ca}(\text{OH})_2$  for clinkering has been mentioned in Section 2.1., referring to a recent work reported in literature, I could perform three DSC/TG analyses reported below in Figure 3.

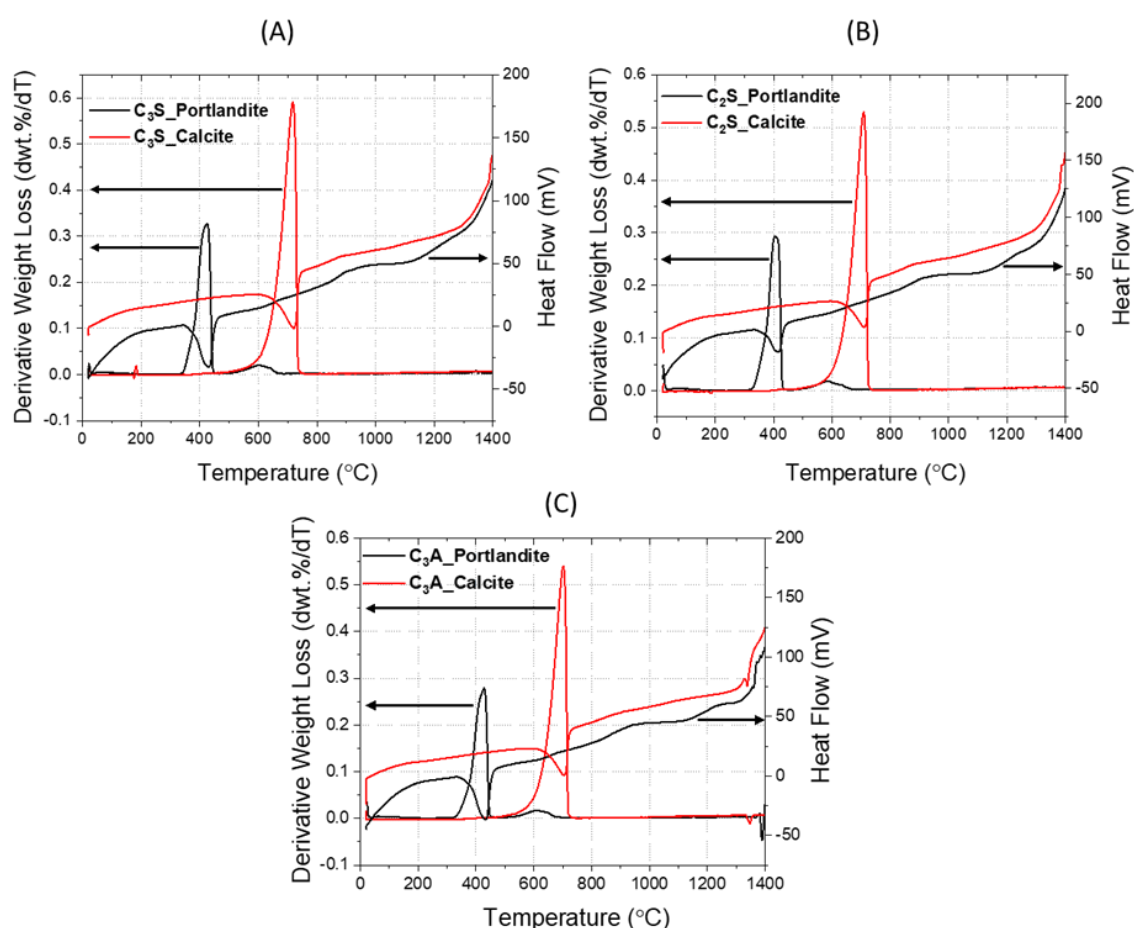


Fig. 3. TG/DTG and DSC data for the powders containing the stoichiometric proportions for the synthesis of  $\text{C}_3\text{S}$  (A),  $\text{C}_2\text{S}$  (B) and  $\text{C}_3\text{A}$  (C) with portlandite  $\text{Ca}(\text{OH})_2$  and calcite  $\text{CaCO}_3$ , black and red-highlighted, respectively, as calcareous sources.

These experiments were aiming to the synthesis of the clinker phases alite  $\text{C}_3\text{S}$ , belite  $\text{C}_2\text{S}$ , and tri-calcium aluminate  $\text{C}_3\text{A}$  from both  $\text{Ca}(\text{OH})_2$  and  $\text{CaCO}_3$ , which could therefore be

compared. Table 4 shows the weight proportion of each phase considered; the solid mixtures were prepared by considering  $\text{Ca(OH)}_2$  (Fischer Scientific, 98%),  $\text{CaCO}_3$  (Sigma-Aldrich,  $\geq 99\%$ ),  $\text{SiO}_2$  (white quartz, Sigma-Aldrich,  $\geq 99\%$ ), and  $\text{Al}_2\text{O}_3$  (Acros Organics, 99%).

Table 3. Weight proportions (wt.%) of  $\text{Ca(OH)}_2$ ,  $\text{CaCO}_3$ ,  $\text{SiO}_2$ , and  $\text{Al}_2\text{O}_3$  aiming to the formation of  $\text{C}_3\text{S}$ ,  $\text{C}_2\text{S}$  and  $\text{C}_3\text{A}$ .

	<b><math>\text{Ca(OH)}_2</math> (wt.%)</b>	<b><math>\text{SiO}_2</math> (wt.%)</b>	<b><math>\text{Al}_2\text{O}_3</math> (wt.%)</b>	<b><math>\text{CaCO}_3</math> (wt.%)</b>	<b><math>\text{SiO}_2</math> (wt.%)</b>	<b><math>\text{Al}_2\text{O}_3</math> (wt.%)</b>
$\text{C}_3\text{S\_Ca(OH)}_2$	<b>78.9</b>	<b>21.1</b>	-	-	-	-
$\text{C}_3\text{S\_CaCO}_3$	-	-	-	<b>83.5</b>	<b>16.5</b>	-
$\text{C}_2\text{S\_Ca(OH)}_2$	<b>71.4</b>	<b>28.6</b>	-	-	-	-
$\text{C}_2\text{S\_CaCO}_3$	-	-	-	<b>77.1</b>	<b>22.9</b>	-
$\text{C}_3\text{A\_Ca(OH)}_2$	<b>68.6</b>	-	<b>31.4</b>	-	-	-
$\text{C}_3\text{A\_CaCO}_3$	-	-	-	<b>74.7</b>	-	<b>25.3</b>

The simultaneous DSC/TG (SDT) analysis was performed on 20 – 40 mg of powder samples in a SDT Q600 (TA Instruments) instrument, operating between 50 °C and 1400 °C in an air atmosphere (flow rate 100 mL/min) at a heating rate of 10 °C / min; the samples were placed in disposable alumina crucibles for measurement. The blending of the powders was operated manually upon addition of enough acetone to make the paste homogeneous and ensure satisfactory mixing of the components. Although, there was no chance to perform XRD analysis in order to retrieve crucial information about the phases formed upon clinkering. We can only certainly say that, based on the outcomes reported in Figure 3, both DTG and DSC showed sharp signals referring to the de-hydroxylation and decarbonisation of  $\text{Ca(OH)}_2$  and  $\text{CaCO}_3$ , respectively. Also,  $\text{Ca(OH)}_2$  was partially converting back to  $\text{CaCO}_3$  upon carbonation from the atmosphere, given the weak DTG signals observed at around 600°C for those samples which were not initially containing any  $\text{CaCO}_3$ . The DSC trend itself could not reveal any certain information, when not coupled with qualitative XRD analysis, but a similarity of the signals in the region 1000 – 1400°C could be observed. That might be related to the formation of those targeted phases in exam, potentially outlining the feasibility of clinkering from  $\text{Ca(OH)}_2$  rather than  $\text{CaCO}_3$ .

## References

1. Voldsund, M., et al., *Comparison of Technologies for CO<sub>2</sub> Capture from Cement Production—Part 1: Technical Evaluation*. Energies, 2019. **12**(3): p. 559.
2. *ECRA CCS Project: Report on Phase IV.A*. 2016, European Cement Research Academy: Duesseldorf, Germany.
3. Gardarsdottir, S.O., et al., *Comparison of Technologies for CO<sub>2</sub> Capture from Cement Production—Part 2: Cost Analysis*. Energies, 2019. **12**(3): p. 542.
4. Nelson, T.O., et al., *RTI's Solid Sorbent-Based CO<sub>2</sub> Capture Process: Technical and Economic Lessons Learned for Application in Coal-fired, NGCC, and Cement Plants*. Energy Procedia, 2017. **114**: p. 2506-2524.
5. Hägg, B., et al., *Pilot Demonstration-reporting on CO<sub>2</sub> Capture from a Cement Plant Using Hollow Fiber Process*. Energy Procedia, 2017. **114**: p. 6150-6165.
6. Plaza, M.G., S. Martínez, and F. Rubiera, *CO<sub>2</sub> capture, use, and storage in the cement industry: State of the art and expectations*. Energies, 2020. **13**(21): p. 5692.
7. Santos, M.P.S., V. Manovic, and D.P. Hanak, *Unlocking the potential of pulp and paper industry to achieve carbon-negative emissions via calcium looping retrofit*. Journal of Cleaner Production, 2021. **280**: p. 124431.
8. Knudsen, J.N., et al., *Pilot plant demonstration of CO<sub>2</sub> capture from cement plant with advanced amine technology*. Energy Procedia, 2014. **63**: p. 6464-6475.
9. Spinelli, M., et al., *Application of Molten Carbonate Fuel Cells in Cement Plants for CO<sub>2</sub> Capture and Clean Power Generation*. Energy Procedia, 2014. **63**: p. 6517-6526.
10. Hanein, T., et al., *Decarbonisation of calcium carbonate at atmospheric temperatures and pressures, with simultaneous CO<sub>2</sub> capture, through production of sodium carbonate*. Energy & Environmental Science, 2021.
11. Iler, K.R., *The chemistry of silica*. Solubility, polymerization, colloid and surface properties and biochemistry of silica, 1979.
12. Patnaik, P., *Handbook of inorganic chemicals*. Vol. 529. 2003: McGraw-Hill New York.
13. Williams, M., *The Merck Index: An Encyclopedia of Chemicals, Drugs, and Biologicals, Edited by MJO'Neil, Royal Society of Chemistry, Cambridge, UK ISBN 9781849736701; 2708 pages. April 2013, \$150 with 1-year free access to The Merck Index Online*. 2013.
14. Morey, G.W., *The action of water on calcite, magnesite and dolomite*. American Mineralogist: Journal of Earth and Planetary Materials, 1962. **47**(11-12): p. 1456-1460.
15. Farhad, A. and Z. Mohammadi, *Calcium hydroxide: a review*. International dental journal, 2005. **55**(5): p. 293-301.
16. Ellingboe, J.L. and J.H. Runnels, *Solubilities of Sodium Carbonate and Sodium Bicarbonate in Acetone-Water and Methanol-Water Mixtures*. Journal of Chemical and Engineering Data, 1966. **11**(3): p. 323-324.